

**School of Electrical Engineering, Computing and  
Mathematical Sciences**

**Curtin Institute of Radio Astronomy**

**Investigating the Links between Radio Pulsar Populations  
that Display Intermittent Emission Phenomena at Low  
Frequencies**

**Bradley Ward Meyers**

This thesis is presented for the Degree of  
**Doctor of Philosophy**  
of  
**Curtin University**

**20 May 2019**



To the best of my knowledge and belief this thesis contains no material previously published by any other person except where due acknowledgement has been made. This thesis contains no material which has been accepted for the award of any other degree or diploma in any university.

Bradley Ward Meyers

20 May 2019



# Acknowledgements

This work was made possible by the continued support of my supervisors, family, and friends. The staff and students of CIRA (newcomers and veterans alike) have had an immeasurable impact on my path. Throughout my undergraduate studies, Honours and, ultimately, my PhD, these people have always provided me with opportunities and support. For that, I thank them. In particular, I would like to express my genuine gratitude to my supervisors: Dr. Steven Tremblay, Dr. Ramesh Bhat, Dr. Ryan Shannon, and Dr. Stephen Ord. Your patience and motivation throughout this part of my life has been, and will continue to be, greatly appreciated. I am proud to have been your student, and to have grown into an independent researcher under your guidance.

To my family, both present and departed, immediate and extended, thank you for your love and support. Your interest in the journey I chose to pursue means more to me than you could know. Even though my Dad and Poppa did not make it to see me finish this chapter of my life, their influence played no small part in my drive to begin it. A special thank-you to my Nanna, whose eagerness to listen to and ask questions about my research was always a highlight (often humorously so). Finally, I thank my Mum and Brother for their unending support and for keeping me sane.

In all sincerity, thank you.



# Abstract

Pulsars are unparalleled astrophysical tools for studying gravity, ultra-dense matter, and plasma physics in extreme electromagnetic environments. Despite this, even after more than 50 years of intense research, we do not fundamentally understand the mechanism responsible for pulsar radio emission. Low-frequency radio observations of pulsars—a scarcely sampled parameter space—have seen a resurgence in popularity in the last decade, and a more robust understanding of these objects is required to achieve the expected science outcomes with the next generation of radio telescopes, such as the Square Kilometre Array. It is, therefore, important to use existing precursor low-frequency radio instruments, like the Murchison Widefield Array (MWA), to investigate pulsar emission properties. We focus on pulsars that exhibit sporadic and/or intermittent emission characteristics, discovered in the last decade, in order to investigate how these objects can further our understanding of the pulsar emission mechanism. This is achieved by conducting a series of systematic, simultaneous, and wideband observations of a subset of pulsars that sample the different sub-populations.

A defining characteristic of pulsar emission is the steep spectral index, where pulsars are typically much brighter at lower frequencies. The pulsar spectral index is broadly expected to be a power law, particularly so for rare giant-pulse emission from pulsars like the Crab (PSR J0534+2200). We found direct evidence that, contrary to this expectation, the spectral index becomes substantially shallower at low radio frequencies, through our analysis of individual giant pulses simultaneously observed at frequencies from 120 MHz to 3 GHz, using the MWA and

Parkes radio telescopes. This is something not predicted by any emission model and, therefore, has substantial implications for theoretical developments of giant-pulse emission physics, the detection of giant-pulse emission at low frequencies, and for the “super-giant” pulse emission model for Fast Radio Bursts.

We also investigated the emission characteristics of an intermittent pulsar and a Rotating Radio Transient (RRAT), specifically examining their single pulse energetics, spectral index and pulse rates. Utilising the the MWA and Molonglo Observatory Synthesis Telescope, we simultaneously captured the active emission state of the intermittent pulsar J1107–5907. This observation was the first detection of an intermittent pulsar below 300 MHz and is a testament that the next generation of low-frequency radio telescopes will be capable of finding and monitoring such pulsars. We also observed that RRAT J2325–0530 with the MWA and Parkes radio telescopes and discovered that the pulsar exhibits signatures of diffractive interstellar scintillation at  $\sim 1$  GHz frequencies. For the first time, we have been able to characterise the scintillation properties of a RRAT. In both cases, we investigated the spectral index and pulse energy distributions of their single pulses and found that they are very similar to those of the normal pulsar population, suggesting that the emission mechanism is likely similar. Furthermore, we showed that the emission from PSR J1107–5907 may be interpreted as RRAT-like emission if it were only a factor of two further from Earth, indicating a possible link between the populations.

Finally, we assert that simultaneous, wideband observations—from  $\sim 100$  MHz to  $\sim$  GHz—are imperative to characterising and comparing the emission properties and energetics of sporadically-emitting pulsars. Additionally, we discuss how strategies developed with precursor instruments will yield high scientific output with next-generation radio telescopes. While the different sub-populations have historically been treated as separate phenomena, our findings strongly support the idea that the sporadic emission behaviour of pulsars is instead due to similar physical mechanisms operating on different time scales.

# Contents

<b>Acknowledgements</b>	<b>v</b>
<b>Abstract</b>	<b>vii</b>
<b>1 Introduction and Background</b>	<b>1</b>
1.1 Neutron stars . . . . .	1
1.2 Pulsars . . . . .	3
1.2.1 Radio emission mechanism . . . . .	9
1.2.2 Observational properties . . . . .	13
1.2.2.1 Pulse profiles and individual pulses . . . . .	13
1.2.2.2 Profile frequency evolution . . . . .	14
1.2.2.3 Spectral index . . . . .	14
1.2.3 Sporadic and intermittent emission . . . . .	15
1.3 Signal propagation effects . . . . .	18
1.3.1 Cold plasma dispersion . . . . .	18
1.3.2 Interstellar scintillation . . . . .	20
1.3.2.1 Weak scintillation . . . . .	23
1.3.2.2 Diffractive scintillation . . . . .	24
1.3.2.3 Pulse broadening . . . . .	26
1.3.2.4 Refractive scintillation . . . . .	30

1.4	Giant pulse emitters . . . . .	31
1.5	Mode changing . . . . .	33
1.6	Nulling . . . . .	35
1.7	Rotating Radio Transients . . . . .	36
1.8	Intermittent pulsars . . . . .	39
1.9	Fast Radio Bursts . . . . .	42
1.10	Pulsars at low frequencies . . . . .	44
1.10.1	Pulsar science with the Murchison Widefield Array . . . . .	45
1.11	Motivation for this Thesis . . . . .	46
1.12	Statement of Originality . . . . .	47
<b>2</b>	<b>Instruments and Methods</b>	<b>51</b>
2.1	The Murchison Widefield Array . . . . .	51
2.1.1	The MWA Voltage Capture System . . . . .	54
2.1.2	Processing MWA VCS data . . . . .	54
2.1.2.1	Incoherent summation . . . . .	56
2.1.2.2	Coherent summation . . . . .	57
2.1.3	Flux density calibration of VCS data . . . . .	60
2.1.3.1	Applying the solutions . . . . .	61
2.1.3.2	Polarisation calibration . . . . .	62
2.2	The Parkes radio telescope . . . . .	63
2.2.1	Flux density and polarisation calibration . . . . .	65
2.3	The Molonglo Observatory Synthesis Telescope . . . . .	65
2.3.1	Flux density calibration . . . . .	67
2.4	Multi-telescope considerations . . . . .	68
2.4.1	Calibration and RFI considerations . . . . .	68

2.5	General pulsar data processing . . . . .	70
2.5.1	Pulsar ephemerides . . . . .	70
2.5.2	De-dispersion . . . . .	71
2.5.3	Sub-integrations and folding . . . . .	73
2.5.4	Software . . . . .	74
2.5.4.1	DSPSR . . . . .	74
2.5.4.2	PSRCHIVE . . . . .	75
2.5.4.3	PRESTO . . . . .	78
<b>3</b>	<b>Spectral Flattening at Low Frequencies in Crab Giant Pulses</b>	<b>81</b>
3.1	Summary . . . . .	81
3.2	Introduction . . . . .	82
3.3	Observations . . . . .	84
3.3.1	Parkes . . . . .	84
3.3.2	Murchison Widefield Array . . . . .	86
3.4	Data processing and calibration . . . . .	86
3.4.1	Parkes . . . . .	86
3.4.2	Murchison Widefield Array . . . . .	87
3.4.2.1	Tied-array beamforming . . . . .	88
3.4.2.2	Tied-array system temperature and gain . . . . .	88
3.4.2.3	Flux density estimation . . . . .	91
3.5	Analysis and Results . . . . .	93
3.5.1	Detecting giant pulses . . . . .	94
3.5.1.1	Parkes . . . . .	94
3.5.1.2	MWA . . . . .	97
3.5.2	Pulse broadening . . . . .	101

3.5.3	Simultaneous giant pulses . . . . .	101
3.5.4	Giant pulse fluence distributions . . . . .	106
3.5.5	Spectral index distributions . . . . .	110
3.5.6	Non-giant pulse emission . . . . .	119
3.6	Discussion . . . . .	120
3.6.1	Spectral flattening . . . . .	120
3.6.2	Emission mechanism . . . . .	122
3.6.3	FRBs as extragalactic super-giant pulses . . . . .	124
3.7	Conclusions . . . . .	125

## **4 Hunting for Radio Emission from the Intermittent Pulsar J1107–5907 at Low Frequencies 129**

4.1	Summary . . . . .	129
4.2	Introduction . . . . .	131
4.3	Observations and Data Processing . . . . .	134
4.3.1	UTMOST . . . . .	137
4.3.2	MWA . . . . .	137
4.3.2.1	Buffered VCS recording . . . . .	138
4.3.2.2	Tied-array beamforming . . . . .	138
4.3.2.3	Flux density calibration . . . . .	139
4.4	Results and Discussion . . . . .	140
4.4.1	Pulse finding and cross-matching . . . . .	140
4.4.2	Dispersion measure . . . . .	142
4.4.3	Pulse profile . . . . .	144
4.4.4	Spectral index . . . . .	145
4.4.5	Pulse energy distributions . . . . .	149

4.4.6	Single pulses and nulls . . . . .	153
4.4.7	Pulse rates and intermittency . . . . .	156
4.4.8	Rotation measure . . . . .	159
4.5	Low-frequency detection prospects . . . . .	160
4.6	Summary and Conclusions . . . . .	161
4.6.1	Acknowledgements . . . . .	162
<b>5</b>	<b>The emission and scintillation properties of RRAT J2325–0530 at 154 MHz and 1.4 GHz</b>	<b>165</b>
5.1	Introduction . . . . .	166
5.2	Observations and Calibration . . . . .	168
5.2.1	MWA . . . . .	168
5.2.1.1	Tied-array beamforming . . . . .	168
5.2.1.2	Flux density calibration . . . . .	169
5.2.2	Parkes . . . . .	169
5.2.2.1	Flux density and polarisation calibration . . . . .	169
5.3	Analysis and Results . . . . .	170
5.3.1	Single pulse detection . . . . .	170
5.3.2	Profiles and polarisation . . . . .	172
5.3.3	Scintillation . . . . .	174
5.3.3.1	Scintillation bandwidth . . . . .	174
5.3.3.2	Scintillation time scale . . . . .	178
5.3.3.3	Scintillation velocity and turbulence strength . .	179
5.3.4	Spectral index . . . . .	181
5.3.5	Fluence distributions . . . . .	181
5.3.6	Pulse rates and clustering . . . . .	183

5.3.7	Rotation measure . . . . .	188
5.4	Discussion . . . . .	190
5.4.1	Scintillation characteristics compared to normal pulsars .	190
5.4.2	Spectral index . . . . .	192
5.4.3	Fluence distributions . . . . .	193
5.4.4	Pulse rates and clustering . . . . .	194
5.4.5	Pulse peak misalignment . . . . .	195
5.5	Concluding remarks . . . . .	196
5.5.1	Acknowledgements . . . . .	197
<b>6</b>	<b>Linking the sub-populations of intermittent and sporadically emitting pulsars</b>	<b>199</b>
6.1	Distinguishing properties . . . . .	201
6.2	Similarities between populations . . . . .	204
6.2.1	Broadband emission . . . . .	204
6.2.2	Spectral index . . . . .	205
6.2.3	Pulse energy distributions . . . . .	208
6.3	Detection and characterisation in the future . . . . .	211
<b>Appendices</b>	<b>215</b>	
<b>A</b>	<b>Co-author agreements</b>	<b>217</b>
A.1	Statement of Originality . . . . .	217
A.2	Co-author responses . . . . .	219
<b>B</b>	<b>Simulating the MWA Tied-array Beam and Determining System Parameters</b>	<b>229</b>
B.1	Array factor calculation . . . . .	229

B.2	Antenna temperature . . . . .	232
B.3	Tied-array gain . . . . .	232
<b>C</b>	<b>Correcting UTMOST Flux Density Measurements of a Polarised Source</b>	<b>235</b>
<b>D</b>	<b>Copyright Information</b>	<b>237</b>
D.1	Chapter 3 & 4 copyright . . . . .	237
	<b>Bibliography</b>	<b>241</b>



# List of Figures

1.1	Simple schematic of a pulsar . . . . .	5
1.2	The $P$ – $\dot{P}$ diagram . . . . .	8
1.3	Single pulse variability in PSR J1136+1551 at 185 MHz . . . . .	12
1.4	Sub-populations on the $P$ – $\dot{P}$ diagram . . . . .	17
1.5	Dispersion sweep of PSR J1136+1551 at 185 MHz . . . . .	21
1.6	Dynamic spectrum of PSR J1136+1551 at 185 MHz . . . . .	25
1.7	Pulse broadening of the Crab pulsar . . . . .	28
1.8	Crab giant pulses observed on a nanosecond time scale . . . . .	32
1.9	Mode changing in six pulsars at 1.4 GHz . . . . .	34
1.10	RRAT to nulling mode switching in PSR J0941–3941 . . . . .	38
1.11	Spin-down rate for the intermittent pulsar PSR J1841–0500 . . . . .	41
2.1	An MWA tile at the MRO . . . . .	52
2.2	The MWA signal chain . . . . .	55
2.3	The Parkes radio telescope . . . . .	63
2.4	The Parkes signal path (pre-2019) . . . . .	64
2.5	The MOST East-West arm . . . . .	66
2.6	Incoherent dedispersion . . . . .	72
3.1	MWA and Parkes frequency band coverage . . . . .	89
3.2	System temperature, gain and SEFD information for the MWA . .	92

3.3	A giant pulse simultaneously detected with across all five frequency bands . . . . .	95
3.4	Sample noise distributions for coherently beamformed, dedispersed MWA data . . . . .	100
3.5	Pulse broadening times and scaling relation for MWA giant pulses	102
3.6	Giant pulse cumulative fluence distributions . . . . .	108
3.7	Example fluence distribution models for giant pulses at 184.96 MHz	111
3.8	Spectral index distributions for simultaneous giant pulses . . . . .	113
3.9	Selected samples of giant pulses based on simultaneity of detection	115
3.10	A “synthetic” spectrum of Crab giant pulses from MWA and Parkes data . . . . .	116
3.11	A comparison of Crab giant pulse spectral indices from the literature	118
4.1	Frequency vs. phase waterfall plot of the PSR J1107–5907 signal arriving at the MWA and UTMOST . . . . .	143
4.2	Pseudo-integrated pulse profile of PSR J1107–5907 . . . . .	146
4.3	An exceptionally bright PC component pulse at the 154 MHz . . .	147
4.4	Single-pulse spectral index distributions between the MWA and UTMOST for the MP and PR components . . . . .	148
4.5	Normalised fluence distributions for PSR J1107–5907 . . . . .	152
4.6	Single pulses from PSR J1107–5907 . . . . .	155
4.7	A timeline of the detections and sensitivity of UTMOST when observing PSR J1107–5907 . . . . .	158
5.1	Example coincident single pulses from RRAT J2325–0530 . . . .	171
5.2	Pseudo-integrated polarisation profile of RRAT J2325–0530 . . .	173
5.3	Dynamic spectra of RRAT J2325–0530 at 154 MHz and 1.4 GHz .	175
5.4	Spectral autocorrelation functions and best-fit models . . . . .	177
5.5	Mean temporal correlation coefficients . . . . .	179

5.6	Single pulse spectral index distribution . . . . .	182
5.7	Pulse energy distributions and models . . . . .	185
5.8	Wait-time distributions from MWA and Parkes detections . . . . .	187
6.1	Emission intermittency time scales . . . . .	203
B.1	The MWA tile and tied-array beam patterns . . . . .	234



## **Statement of Contribution by Others**

The content of Chapter 3 is my own work, excepting the following. The MWA data for this project were reduced by F. Kirsten, and the developed flux density calibration technique was aided by A. Sutinjo, D. Ung, and M. Sokolowski. R. Shannon facilitated the Parkes observations and provided the data acquisition and processing details. S. Tremblay, R. Bhat and R. Shannon provided input in terms of the structure and contextual discussion.

The content of Chapter 4 is my own work, excepting the following. The development of the MWA buffered triggering system was led by B. Crosse and A. Williams with input from myself and S. Tremblay for testing and configuration. The corresponding UTMOST observations were facilitated by C. Flynn, W. Farah and V. Gupta. Archival UTMOST data, flux density calibration information and observing details were provided by C. Flynn and V. Gupta. S. Tremblay, R. Bhat and R. Shannon provided detailed input on the scope and structure of the article, S. Murray provided input regarding the fluence distribution analysis, and C. Sobey provided ionospheric rotation measure estimates.

The content of Chapter 5 is my own work, excepting the following. The Parkes observations were carried out by R. Bhat. R. Shannon provided advice for the Parkes flux density and polarisation calibration. C. Sobey provided ionospheric rotation measure estimates for both telescopes. S. Tremblay, R. Bhat, R. Shannon and S. Ord provided initial input into the scope of the analysis.

(Signature of Candidate)

(Signature of Supervisor)

# Chapter 1

## Introduction and Background

### 1.1 Neutron stars

Neutron stars were first proposed to explain the large energy release from supernovae through gravitational collapse of an ordinary progenitor star (Baade & Zwicky, 1934). It is now accepted that when the core of an ordinary star of mass  $\approx 10\text{--}30 M_{\odot}$  can no longer support itself against gravity, it will undergo gravitational collapse to potentially create a neutron star. The neutron star is supported against further gravitational collapse by the strong nuclear force and quantum degeneracy pressure (a manifestation of the Pauli exclusion principle). The composition and theoretical mass limits of neutron stars were first explored by Oppenheimer & Volkoff (1939), though even today, these aspects remain poorly understood (see e.g. Lattimer, 2012 for a review). There are a variety of limits placed on neutron star masses, derived from assumptions about the sound speed within a neutron star, the internal density transitions defined by an equation of state, and the requirement that the neutron star be stable against disintegration due to the rotation (see e.g. Lattimer et al., 1990; Glendenning, 1990; Lattimer & Prakash, 2001; Lattimer, 2012). Ultimately the minimum and maximum possible masses are unknown, thus, one typically takes the mass of a neutron star to be within  $M_{\star} \approx 1.3\text{--}2.5 M_{\odot}$  and the radius to be  $R_{\star} \approx 10 \text{ km}$ .

After the collapse, the neutron star retains much of the angular momentum of the progenitor star. The dramatic reduction in stellar radius results in the neutron star having a much smaller moment of inertia ( $I \propto M_\star R_\star^2$ ) compared to the progenitor. To conserve angular momentum, the neutron star is born with a high angular velocity, with birth rotation periods ( $P$ ) estimated to be  $\sim 5$  ms via models based on supernovae physics (Heger et al., 2004). Contrary to the model predictions, the observationally derived initial spin periods for some neutron stars suggests  $P \approx 10\text{--}150$  ms (e.g. Migliazzo et al., 2002; Kramer et al., 2003b; Faucher-Giguère & Kaspi, 2006). This implies that either our supernova and neutron star creation models are incomplete or the observationally constrained parameters are missing information about some significant event in the early stages of the neutron star life-cycle which drastically slows the rotation rate. While not (necessarily) directly related to the stellar spin properties, we know that asymmetries within the supernova event also give rise to a wide distribution of neutron star space-velocities<sup>1</sup> (e.g. Cordes & Rickett, 1998; Sartore et al., 2010; Gonzalez et al., 2011; Deller et al., 2018), often ranging from  $v_{\text{psr}} \sim 1\text{--}1000$  km s<sup>-1</sup>. Given the complex physics involved in a supernova and subsequent neutron star formation, it is difficult to give any confident answer to this issue.

Besides the extreme rotation rates, neutron stars have strong magnetic fields (often assumed to be dipolar) that are locked (or “frozen”) in and co-rotate with the star (Reisenegger, 2013). The first direct measurements of neutron star magnetic fields came from cyclotron radiation features in X-ray binaries (Trümper et al., 1978; Wheaton et al., 1979). At the surface, the magnetic field strengths are estimated to be between  $B_\star \sim 10^8\text{--}10^{14}$  G. The origin of these magnetic fields is not fully understood, but could be due to conservation of magnetic flux of the progenitor star (see e.g. Urpin & Yakovlev, 1980; Blandford et al., 1983 for discussion). Whether or not the internal structure of the neutron star allows for

---

<sup>1</sup>Though the exact form and physics behind these distribution is still debated within the literature.

the creation of a dynamo effect ( $|B_\star| \propto P^{-1/2}$ ) is still unclear (though there is evidence to the contrary, given some neutron stars spin much faster than normal, but have substantially weaker magnetic fields; see §1.2), as we do not yet have a satisfactory understanding of the equation of state for a neutron star. These strong magnetic fields, in combination with the rotation, play an important role in our detecting these compact objects by facilitating the creation of electromagnetic radiation.

Many neutron stars can be detected by emission across the electromagnetic spectrum, ranging from radio emission to X-rays and  $\gamma$ -rays. It is expected that most, if not all, neutron stars have a plasma-filled atmosphere (Goldreich & Julian, 1969; Pavlov & Shibanov, 1978; Romani, 1987; Shibanov et al., 1992). This plasma is somehow producing some fraction of the detectable emission via interaction with the magnetic fields and neutron star rotation. Thermal emission from the surface of the neutron stars is sometimes seen in the X-ray regime (e.g. Chiu & Salpeter, 1964; Helfand et al., 1980; Zavlin, 2009), whereas the radio emission likely originates from collimated, relativistic beams of particles along the magnetic axes (e.g. Gold, 1968; Pacini, 1968). If the neutron star emits strongly in the radio, and we have the correct viewing angle, we can observe radio pulses as the radiation passes through our line-of-sight every rotation period. This subset of rotating neutron stars was discovered in 1967 by Jocelyn Bell and Antony Hewish (Hewish et al., 1968) at radio frequencies ( $\approx 80$  MHz). These objects are now known as pulsars, stemming from the pattern: *puls(ating st)ars*.

## 1.2 Pulsars

Pulsars are excellent astrophysical probes that allow us to study topics ranging from plasma micro-physics (e.g. Eilek & Hankins, 2016) to gravitational waves (e.g. Shannon et al., 2013). The combination of strong electric and magnetic fields (accelerating charged particles), fast rotation (inducing electro-dynamical forces) and a plasma-filled atmosphere (a charged particle source) creates bi-polar

beams of coherent radiation along the magnetic axes.

The rotation and magnetic axes of the neutron star are often misaligned, making the emission beam sweep around, much like a lighthouse (see Figure 1.1). If the beam intersects our line-of-sight on Earth then, once per rotation (typically), we detect a pulse of radiation. If the rotation and magnetic axes are close to orthogonal, and both beams pass through our line-of-sight, then we can see a pulse from each beam, separated by  $\sim 180^\circ$  in rotation phase. The second, often weaker, pulse is called an “interpulse” and can look very different (in time and frequency) to the “main pulse”.

Viewing geometry is a major factor in detection of pulsars; if the emission beam never intersects our line-of-sight, then we don’t see the pulsar at radio frequencies. Even though numerous surveys over the past decades have led to the discovery of more than 2613 pulsars<sup>2</sup> (Manchester et al., 2005) that emit at radio frequencies, and we know at least some of the salient details of the pulsar population within our Galaxy (e.g. pulsar formation follows star formations, older pulsars tend to exist further from the plane), there is still much we do not understand. This is partially due to the fact that their detection depends on the viewing geometry and their birth rates, which are both difficult problems to approach. Fundamentally, these issues are also related to the estimation of neutron star birth rates and supernova rates, which continues to be an active subject of research.

Several quantities that characterise a pulsar can be calculated from some basic observables, such as the spin period and period derivative, assumptions about the magnetic field structure (i.e. assumed to be dipolar) and the mass of neutron stars ( $M_\star \sim 1.4 M_\odot$ ). For instance, the total power output of the neutron star can be measured from the loss of rotational kinetic energy over time, commonly referred to as the spin down luminosity, assuming a canonical moment of inertia,

---

<sup>2</sup>ATNF Pulsar Database v1.56; <http://www.atnf.csiro.au/people/pulsar/psrcat/>

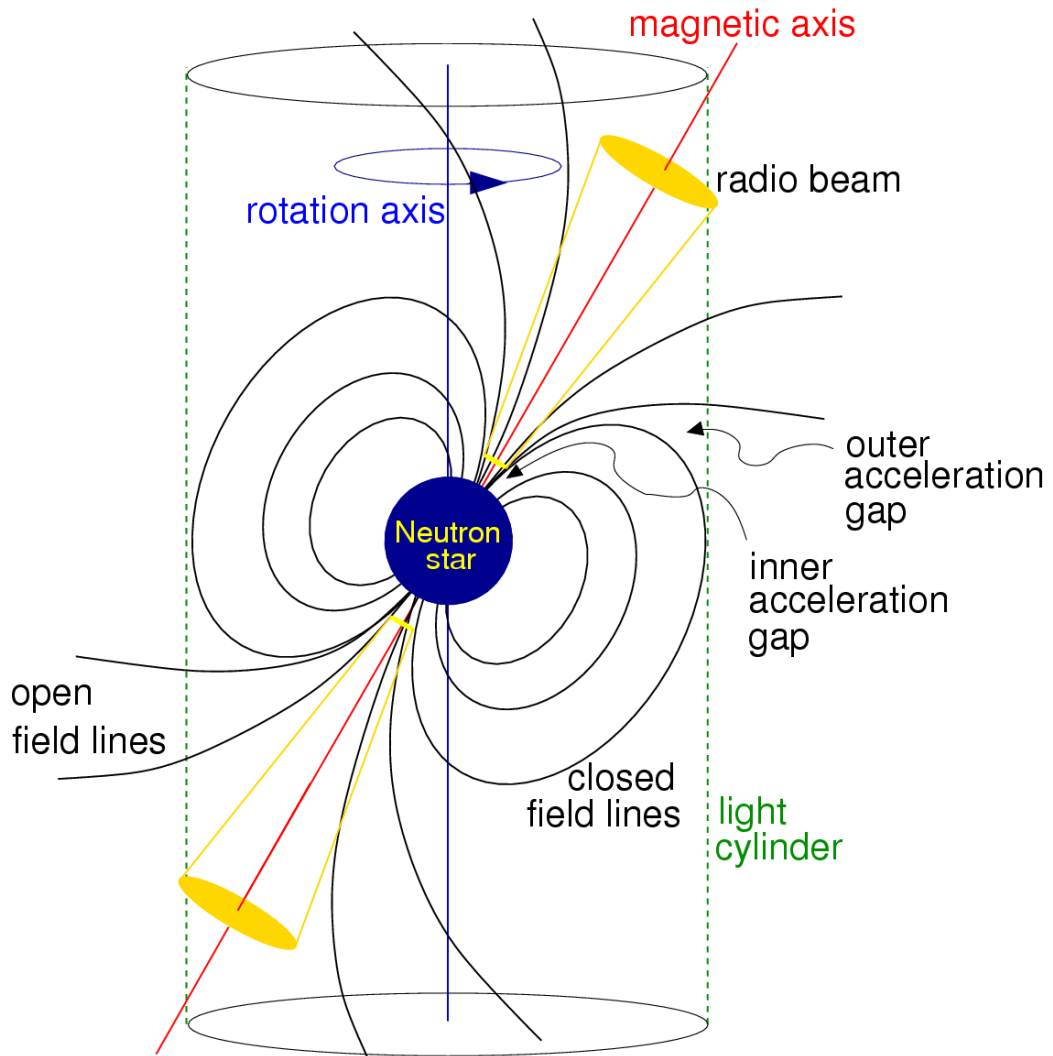


Figure 1.1: Schematic diagram of the dipolar model for a canonical radio pulsar. The rotation and magnetic axes are misaligned, causing the radiation beam to sweep across the sky. Different acceleration regions for particles are marked here as “gaps”. The light-cylinder is a boundary at which the magnetic field lines attached to the neutron star are rotating at the speed of light. Field lines that extend beyond this boundary are “open” (but likely close somewhere in the local interstellar medium), while those within the boundary are considered closed. Image from Lorimer & Kramer, 2004.

$I = 10^{45} \text{ g cm}^{-2}$ , is

$$\dot{E} = 4\pi I \dot{P} P^{-3} \simeq 3.95 \times 10^{31} \text{ erg s}^{-1} \left( \frac{\dot{P}}{10^{-15}} \right) \left( \frac{P}{\text{s}} \right)^{-3}, \quad (1.1)$$

where  $P$  is the rotation period as previously defined, and  $\dot{P} = dP/dt$  is the first time-derivative of the rotation period. Only a small fraction ( $\lesssim 1\%$ ) of the total emitted power is converted into radio emission. From the measurements of  $P$  and  $\dot{P}$ , it is also possible to estimate the characteristic age of the pulsar, which is given by

$$\tau = \frac{P}{2\dot{P}} \simeq 15.8 \text{ Myr} \left( \frac{P}{\text{s}} \right) \left( \frac{\dot{P}}{10^{-15}} \right)^{-1}, \quad (1.2)$$

under the assumption that the initial spin period was much shorter than what is observed, and that the spin-down is entirely due to magnetic dipole radiation. The observables  $P$  and  $\dot{P}$  are vitally important in characterising the most basic properties of a pulsar.

A more accurate age estimate is possible, but is difficult to calculate as it requires knowledge of the initial spin period,  $P_0$ , and the so-called braking index,  $n$ , which depends on the energy dissipation mechanism that is causing the spin-down of the pulsar. Typically it is assumed that  $n = 3$ , which is the case for pure vacuum dipolar radiation. The presence of a magnetosphere (surrounding plasma) and/or outflowing particle winds are other possible mechanisms which would present braking indices of  $n \neq 3$ , especially if the physical properties of the plasma or particle wind change (see e.g. Sections 1.5 and 1.8). In the rare cases where measurements are precise enough, it is possible to estimate the braking index using

$$n = 2 - \frac{P \ddot{P}}{\dot{P}^2}, \quad (1.3)$$

where  $P$  and  $\dot{P}$  are as previously defined, and  $\ddot{P} = d^2P/dt^2$  is the second time-derivative of the rotation period. In the cases where these measurements are possible, the recorded braking indices are within the range  $n = 0.9\text{--}2.8$  (Lyne

et al., 1993, 1996; Livingstone et al., 2007; Weltevrede et al., 2011; Espinoza et al., 2011; Roy et al., 2012; Lyne et al., 2015). Measurements of braking indices are typically very difficult due to the effects of “timing noise” (see §1.5). The handful of successfully measured braking indices imply that the common assumption of a vacuum dipolar radiation mechanism as the primary source of energy dissipation is not entirely correct. Other physical parameters, though often excluded, have been suggested as critically important in understanding pulsar braking indices (e.g. a changing inclination angle between magnetic and rotation axes, Johnston & Karastergiou, 2017), for the majority of the pulsar population.

The braking mechanism, which defines how pulsars expend their rotational energy, also has important implications for the evolution of  $P$  and  $\dot{P}$  and therefore how pulsars track through the  $P$ – $\dot{P}$  parameter space. Figure 1.2, referred to as the  $P$ – $\dot{P}$  diagram, highlights the bimodal distribution of pulsars as a function of the spin period and the period time-derivative. The “slow” or “normal” pulsar population is the larger clump in the top-right region of the diagram, with  $P \sim 1$  s. The special class of millisecond pulsars reside in the bottom-left region, with rotation rates  $P \sim 1\text{--}10$  ms and very small spin down rates ( $\dot{P} \sim 10^{-20}$  ss $^{-1}$ ), making them extremely stable rotators.

The magnetic fields of pulsars are also linked to their period and period derivative. Again, assuming vacuum dipolar radiation as the sole energy dissipation mechanism, the surface magnetic field strength can be estimated as

$$B_\star = \sqrt{\frac{3c^3}{8\pi^2} \frac{I}{R_\star^6 \sin^2 \alpha} P \dot{P}} \simeq 10^{12} \text{ G} \left( \frac{\dot{P}}{10^{-15}} \right)^{1/2} \left( \frac{P}{\text{s}} \right)^{1/2}, \quad (1.4)$$

where  $c$  is the speed of light, and we have assumed  $I = 10^{45}$  g cm $^{-2}$ ,  $R_\star \approx 10$  km and  $\alpha = \pi/2$  is the angle between the magnetic and rotation axes (i.e. an oblique rotator). Typically,  $\alpha$  is unknown, and almost certainly not  $\pi/2$ , though this value is used as a simplifying assumption. Moreover,  $I$  is unknown and we do not understand the dissipative mechanism. Tauris et al. (2012) obtain a

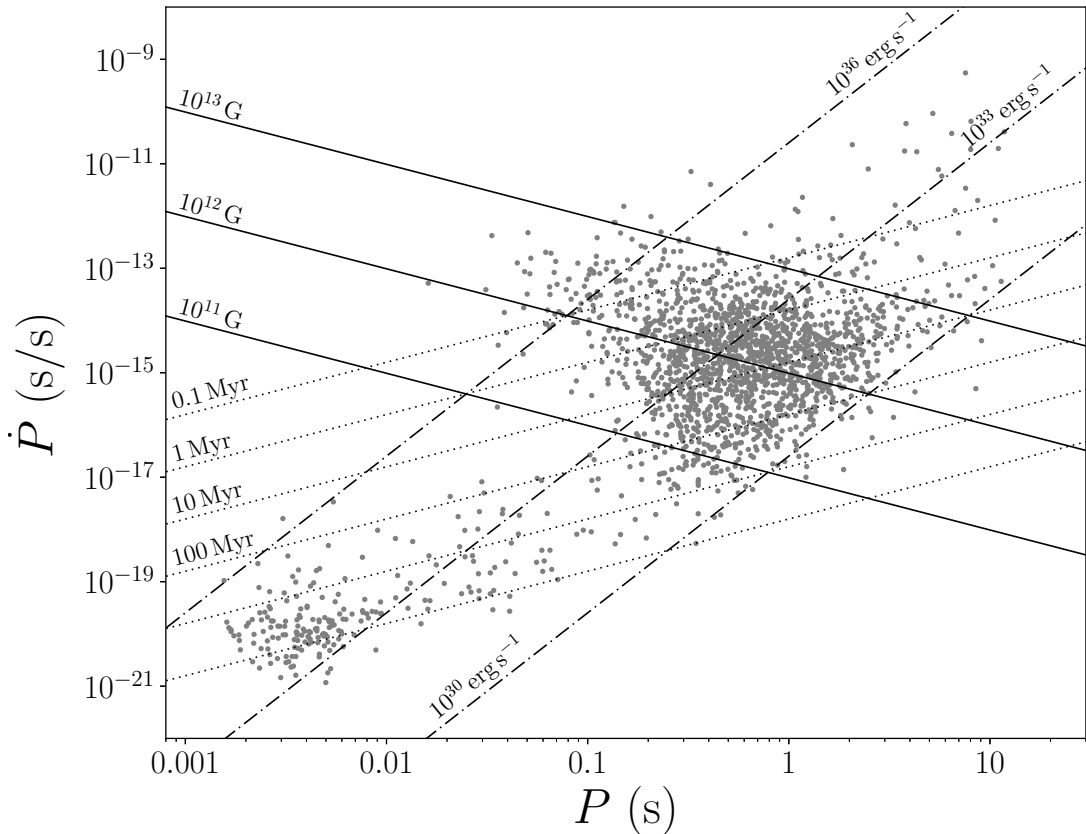


Figure 1.2: The  $P-\dot{P}$  diagram for radio pulsars with available period and period derivative measurements. The canonical long-period pulsars (central clump) and millisecond pulsars (bottom-left clump) are plotted as grey points. Lines of constant magnetic field strength (solid), characteristic age (dotted) and spin-down energy (dot-dashes) are drawn and labelled.

slightly altered version of equation (1.4), which makes use of the three-dimensional magnetosphere model as detailed by Spitkovsky (2006), which includes several, often ignored, plasma related effects. In light of the discovery of new classes of pulsars that deviate significantly from the simple model (e.g. intermittent pulsars, Kramer et al. (2006), §1.8), equation (1.4) can only be taken as an order of magnitude estimate for the magnetic field strength at the pulsar equator. The interaction between rotation and magnetic field is a fundamental part of understanding how pulsars produce the coherent radio emission we observe.

### 1.2.1 Radio emission mechanism

The conditions required to generate pulsar radio emission are understood only in a general sense. Typically, pair production of positrons and electrons is invoked to create a charged particle cascade *in situ* near the pulsar surface. These charges are then accelerated by an electric field in some “acceleration region”, which forces the charges away from the surface (e.g. Ruderman & Sutherland, 1975; Arons & Scharlemann, 1979). Some of the expelled charges maintain a plasma around the pulsar and form what is commonly called the magnetosphere, and the remaining charges escape to produce the pulsar wind.

Two of the earliest pulsar models were derived from previously developed electrodynamics. The vacuum dipole model, which was developed in the context of rotating magnetised stars (Deutsch, 1955), was applied to pulsars by Pacini (1968). It related the observational properties (i.e.  $P$  and  $\dot{P}$ ) to the physical properties of the star. While the vacuum dipole model is still commonly used to estimate basic parameters (see e.g. equations 1.1 and 1.4), it neglects the magnetospheric plasma entirely. The rotating magnetospheres model, which was developed to explain rotating planetary magnetospheres (Hones & Bergeson, 1965), was developed in the context of pulsars by Goldreich & Julian (1969). It is often used as a basic framework for modern magnetospheric and emission theories. The main principle is that the pulsar magnetosphere exists in a “force-free”

state, which requires an interior electric field,  $\mathbf{E}$ , that satisfies

$$\mathbf{E} + \frac{1}{c} (\boldsymbol{\Omega} \times \mathbf{x}) \times \mathbf{B} = 0, \quad (1.5)$$

where  $\mathbf{x}$  is a position vector in the star-centred coordinate system.

It is now typically thought that the magnetosphere does co-rotate with the pulsar. Notably, the co-rotation is limited to the distance where the magnetic field lines and plasma would be required to travel faster than light. This boundary is called the light-cylinder radius,  $R_{\text{LC}} = c/\Omega$ , where the rotational velocity  $\Omega = 2\pi/P$  (refer to Figure 1.1).

If we assume the pulsar is initially surrounded by a vacuum (i.e. that the vacuum dipole model is correct), then there will be a surface charge on the neutron star. This charge density induces an exterior quadrupolar electric field with a component,  $E_{\parallel}$ , parallel to the magnetic field lines. This creates a Lorentz force,  $F = qE_{\parallel}$ , felt by the charged particles at the neutron surface. With some assumption of typical pulsar parameters, Goldreich & Julian (1969) showed that the magnitude of the Lorentz force exceeds the magnitude of the gravitational force experienced by several orders of magnitude. Charges are pulled away from the neutron star surface, thus the vacuum surrounding the pulsar cannot be maintained and eventually the neutron star is surrounded by a dense plasma. Hence the vacuum dipole model cannot be sustained.

The charge density distribution for the plasma in the rotating magnetosphere model is given by Goldreich & Julian (1969),

$$\rho_{\text{GJ}} = \epsilon_0 (\nabla \cdot \mathbf{E}) = -\frac{\epsilon_0 B_* \Omega R_*^3}{cr^3} (3 \cos^2 \theta - 1), \quad (1.6)$$

where  $r$  is the radial distance from the neutron star,  $\theta$  is the colatitude (or polar angle) and  $\epsilon_0$  is the permittivity of free space. Once the charges are arranged to produce such a distribution, the parallel electric field ( $E_{\parallel}$ ) is shielded and a force-free state is obtained. The required particle number density at the magnetic pole

$(\theta = 0, r = R_\star)$  to maintain a force-free magnetosphere, assuming only electrons are present, is known as the Goldreich-Julian density, and is given by

$$n_{\text{GJ}} = \frac{\rho_{\text{GJ}}}{-e} = \frac{2\epsilon_0\Omega B_\star}{ec}, \quad (1.7)$$

where  $e \approx 1.602 \times 10^{-19}$  C is the elementary charge. The  $\mathbf{E} \times \mathbf{B}$  field within the interior of the neutron star is also experienced by the surrounding plasma, and thus it will co-rotate with the star out to the light-cylinder radius.

This simple model, while physically conceivable and elegant, is widely considered to be unrealistic due to the many assumptions folded into its original formulation (see e.g. Beskin et al., 1993; Michel & Li, 1999 for critical reviews). For example, the frequency of the radio emission should be close to the plasma emission frequency, which is predicted to be  $\nu_p \gtrsim 1$  GHz. But pulsars are strong radio sources at observing frequencies well below even 100 MHz. To explain this, one can invoke a plasma density in the magnetosphere significantly lower in some regions than expected, which therefore implies that a steady co-rotation of the magnetosphere is not possible.

Even after a half-century of intense studies, we still do not have a consistent model for the pulsar magnetosphere, nor the coherent emission mechanism required to explain observations (see e.g. Melrose, 1995, 2004, 2017 for reviews). There has, however, been recent progress in constructing more realistic three-dimensional pulsar magnetosphere models (see e.g. Spitkovsky, 2006; Li et al., 2012c; Kalapotharakos et al., 2012; Timokhin & Arons, 2013; Tchekhovskoy et al., 2013; Kisaka et al., 2016). To complicate the matter further, individual pulses from pulsars display a remarkable amount of pulse-to-pulse variability (see Figure 1.3). This is not necessarily surprising given the dynamic nature of the emission plasma that is typically invoked, however, no single model has been able to explain such observed features of pulsar emission in satisfactory detail.

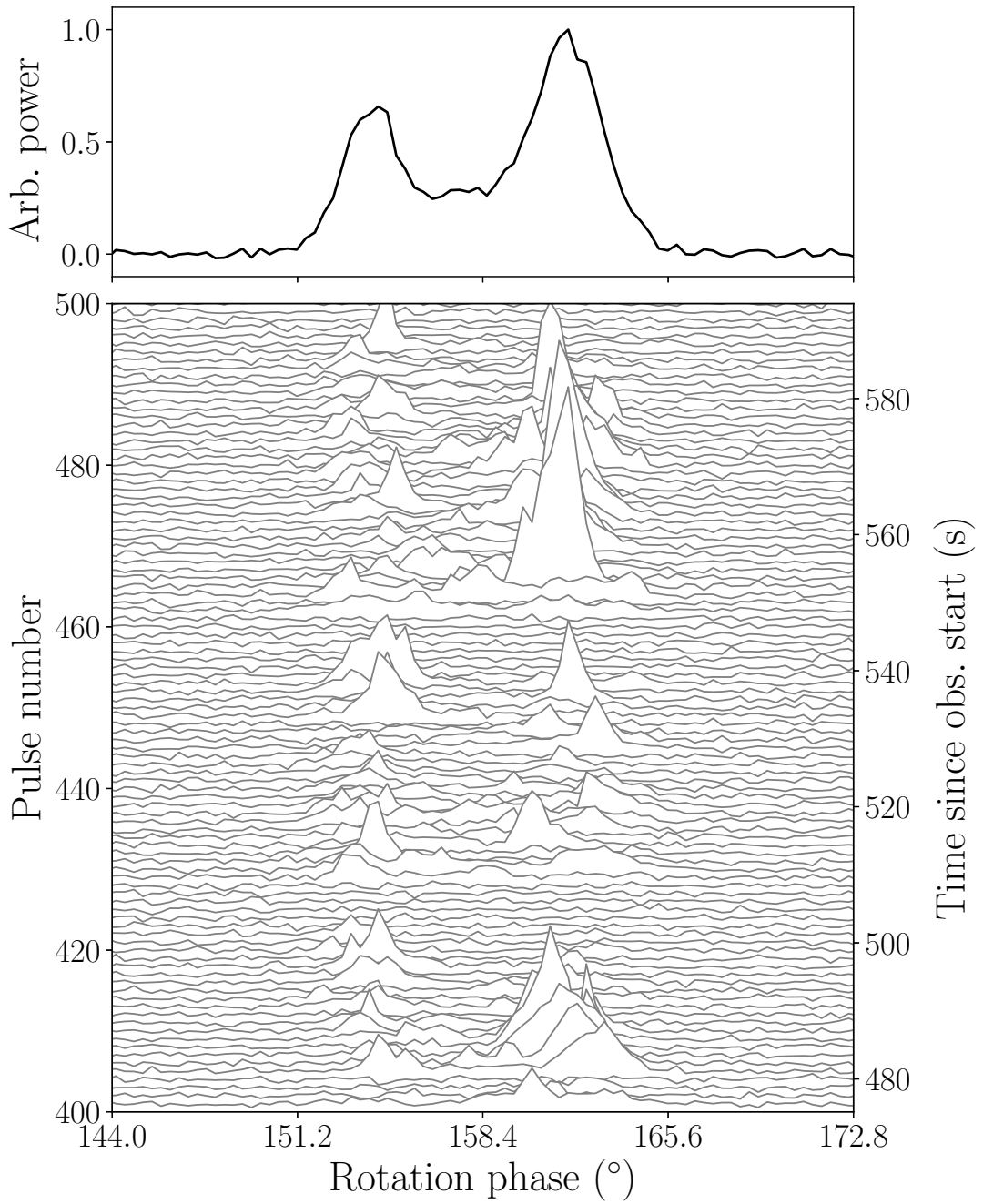


Figure 1.3: An example of the pulse-to-pulse variability observed in PSR J1136+1551 ( $P \approx 1.18$  s) from the Murchison Widefield Array at 185 MHz. Traces for 100 consecutive pulses are shown in the bottom pane and the collapsed average of these pulses (the integrated profile) is shown in the top pane. This pulsar is known to scintillate (see §1.3.2), which contributes to the apparent variability, and is a well studied nulling pulsar (see §1.6). This pulse stack includes several instances of nulling (see pulse numbers  $\sim 424$ – $430$ ,  $455$ – $461$ ), where the detectable radio emission ceases.

## 1.2.2 Observational properties

Besides the emission mechanism, there are several more salient properties associated with radio pulsar emission. These properties, while not ubiquitous, are relatively standard across the entire pulsar population.

### 1.2.2.1 Pulse profiles and individual pulses

By averaging over hundreds or thousands of rotations an integrated pulse profile is produced. The integrated profile can be treated as the unique probability envelope of where individual pulses arrive as a function of rotation phase, and is found to be very stable for most pulsars. Integrated pulse profiles exhibit a wide morphology, from simple narrow Gaussian-like structure to complicated, wide multi-component profiles. These can be explained by different models of the emission beam geometry (e.g. Rankin, 1993; Lyne & Manchester, 1988; Karastergiou & Johnston, 2007), which attempt to explain how the one-dimensional cross-section we observe (the profile) is related to the three-dimensional beam structure.

In terms of rotation, pulsars are generally extremely stable. This rotation stability, combined with the profile stability over an appropriate amount of time (typically minutes), makes pulsars particularly good astrophysical clocks. In fact, the emission can be so regular, especially in the case of millisecond pulsars, that some pulsars can be used to define a time standard rivalling even the best atomic clocks on Earth (Hobbs et al., 2012).

On an individual pulse basis, the radio emission varies drastically between rotations, likely due to the complex nature of the emission mechanism (which we do not fully understand). This is an intrinsic property in *all* radio pulsar emission. Variability between a series of pulses can range from a rotational phase shift or difference in intensity, to a complete cessation of observable emission for one or more rotations. An example of this can be found in Figure 1.3. This phenomenon, where emission stops and the pulsar radio emission mechanism appears “off”, is called “nulling” (see §1.6). For at least one pulsar, very faint emission has been

detected during a null (Esamdin et al., 2005), though for the majority it appears that the emission has actually ceased.

### 1.2.2.2 Profile frequency evolution

While, at any given observing frequency, an integrated pulse profile is generally found to be relatively stable, observations indicate that the profile changes significantly as a function of the observing frequency (see e.g. Komesaroff, 1970; Gould & Lyne, 1998; Johnston et al., 2008). For some pulsars, this profile evolution with frequency can be understood in terms of the radius-to-frequency mapping (RFM) model, which was first observationally demonstrated by Cordes (1978). RFM predicts that low-frequency radio emission originates from higher altitude regions in the magnetosphere, while high-frequency emission is produced closer to the neutron star surface. This comes from the consideration that pulsar emission is primarily a consequence of ultra-relativistic charged particles moving along magnetic field lines. In turn this implies that the emission frequency is dependent on the local plasma conditions, which vary as a function of time and altitude. The magnetic field lines are more separated at higher altitudes, thus the low-frequency emission produces a wider beam, hence a broader pulse profile.

There are of course exceptions (discussed briefly in §1.5), and many pulsar integrated profiles do not show a strong frequency evolution. In some cases, the opposite behaviour is observed, where the profile becomes narrower at low frequencies (e.g. Gould & Lyne, 1998). RFM is obviously not universal and, at times, can be difficult to disentangle from other frequency-dependent effects (see §1.3) especially in the cases of relatively complicated integrated profiles.

### 1.2.2.3 Spectral index

Measurements of flux density and spectral index are critically important for understanding the pulsar emission mechanism. Pulsars typically exhibit power law spectra,  $S_\nu \propto \nu^\alpha$  (Sieber, 1973a), where  $S_\nu$  is the flux density measured at fre-

quency  $\nu$  and  $\alpha$  is the spectral index. For the majority of pulsars,  $\alpha < 0$  and thus they are much brighter at low frequencies. Lorimer et al. (1995) measured the spectral indices for 280 pulsars using observations at 0.4 and 1.6 GHz, and estimated the mean spectral index to be  $\alpha = -1.6 \pm 0.3$ . This sample was later extended with the addition of several new pulsars and higher frequency information by Maron et al., 2000a, who estimated a mean spectral index of  $\alpha = -1.8 \pm 0.2$ . They also found that a small fraction of pulsars that have a relatively flat spectrum ( $\alpha \gtrsim -1$ ) between 0.3–20 GHz. Approximately 5% of the sample were better represented by a broken power law, with  $\alpha_{\text{low}} = -0.9 \pm 0.5$  and  $\alpha_{\text{high}} = -2.2 \pm 0.9$ . Between 100–400 MHz, Malofeev et al. (2000) determined a shallower mean spectral index of  $\alpha = -1.47 \pm 0.76$ . More recently, Bates et al. (2013) employed a population synthesis analysis to show that the underlying, as opposed to the observed, spectral index distribution for pulsars can be modelled with a Gaussian distribution with a mean of  $-1.41$  and a standard deviation of  $0.96$ .

Ultimately this is an active area of research important for constraining pulsar emission mechanism models. Eventually, the spectrum must flatten and turn over at low radio frequencies (i.e.  $\lesssim 100$  MHz), which has been shown to be the case for many pulsars (e.g. Sieber, 1973a; Izvekova et al., 1981; Maron et al., 2000a; Bilous et al., 2016).

### 1.2.3 Sporadic and intermittent emission

In the literature, several sub-groups of pulsars are identified and often treated separately based on their emission characteristics. All of these sub-groups contain pulsars that share the trait of emission intermittency over a wide range of time scales. It is possible that each of these groups share the same emission mechanism, which is active on different time scales, that in turn creates seemingly distinct populations. Understanding the sporadic emission and how the populations are linked is crucial for creating a consistent emission model.

The intermittency of pulsar emission can be broadly categorised into two regimes: giant pulses, where the pulses of interest are *brighter* than the normal pulses that are typically observed (see §1.4) and; sporadic emission, where the emission either ceases for extended amounts of time (e.g. nullers, see §1.6) or the emission is generally not observed except for occasional bursts (e.g. Rotating Radio Transients (RRATS; McLaughlin et al., 2006); and intermittent pulsars (Kramer et al., 2006); see §1.7 and §1.8 respectively).

Four of the six *bona fide* giant-pulse emitters are “millisecond pulsars”, making two well separated clusters of giant pulse emitters (see Figure 1.4). In this case, a “*bona fide* giant-pulse emitter” is a pulsar which has intrinsically short duration bursts that occur within a narrow rotation phase range, as well as displaying a power law pulse intensity distribution. Given we only have a handful of giant pulse emitting pulsars, it is difficult to draw any real conclusions from that separation. A commonly shared trait of the giant pulse emitters is that they all have high magnetic field strengths at the light cylinder and high spin-down energies, which could mean that the (giant pulse) emission is generated from the outer magnetosphere.

There is an insufficient number of the so-called intermittent pulsars to truly see a restriction in this parameter space, but they appear to reside within the “normal pulsar” clump ( $P \sim 1$  s, see Figure 1.4). Nulling pulsars and RRATs also occupy the “normal pulsar” area of the  $P-\dot{P}$  diagram. Some RRATs extend to the top-right which corresponds to a pulsar population with particularly strong magnetic fields (magnetars) that also tend to have associated X-ray emission. Overall, the nullers and RRATs occupy a wide distribution in period and period derivative. RRATs are a relatively newly discovered population and, while “nulling” is not a recent phenomenon, not all pulsars have been scrutinised for nulling (and many are too weak to rule out nulling). This suggests that these sub-groups may not represent truly distinct populations of pulsars, at least from the perspective of a  $P-\dot{P}$  parameter space. It should be noted, however, that the nulling phenomenon

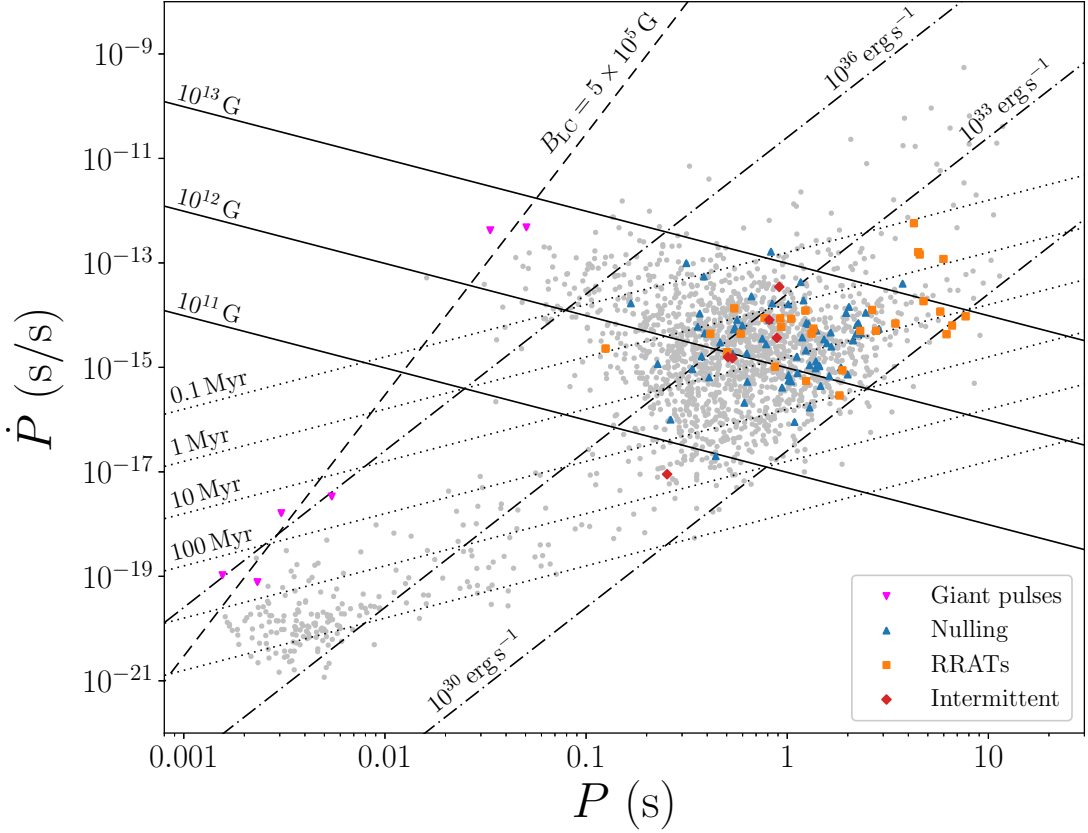


Figure 1.4: A modified  $P$ - $\dot{P}$  diagram with four sub-populations highlighted. The canonical long-period and millisecond pulsar populations are in the background (light grey points). Nulling pulsars are depicted as blue triangles, RRATs as orange squares, giant pulse emitters as magenta triangles and intermittent pulsars as red diamonds. A large fraction of the RRAT population is not plotted here due to no available timing solution (i.e.  $\dot{P}$  is unknown). Lines of constant magnetic field strength, characteristic age and spin-down energy are drawn and labelled as in Figure 1.2. For giant pulses, the magnetic field strength at the light cylinder is an important quantity, thus a (dashed) line indicating  $B_{LC} = 5 \times 10^5$  G is also included.

is (marginally) correlated with the near alignment of the pulsar spin and magnetic axes (Biggs, 1992), which has not been shown for RRATs.

Models for the sporadic nature of these sub-populations range from in-falling asteroidal material disrupting the emission process (Cordes & Shannon, 2008) to resistive plasmas that can (at least in simulation) produce long-duration inactive emission phases (Li et al., 2012c). If we want to link the sub-populations quantitatively, we need to study them in terms of properties that directly relate to the physical process producing the radiation and the emission geometry. Low frequencies offer an opportunity to study different regions of the pulsar magnetosphere and will provide vital clues for the nature of the radio emission mechanism, including what is causing the sporadic state change.

## 1.3 Signal propagation effects

The radio signal from a pulsar traverses the interstellar medium (ISM), which imprints signatures on, and distorts, the intrinsic properties of pulsar signals. These propagation effects give us information on the structure and content of the ISM and the Galactic magnetic field, but they also obfuscate the intrinsic pulsed emission. Understanding these effects is particularly important at low frequencies, where they tend to be much stronger (compared to high frequencies) and can be more easily characterised.

### 1.3.1 Cold plasma dispersion

The most common ISM propagation effect is formulated if we assume the ISM can be treated as a cold plasma that disperses the signal as a function of frequency (Davidson & Terzian, 1969; Manchester & Taylor, 1972). The ISM has a refractive index,

$$\mu = \sqrt{1 - \left(\frac{\nu_p}{\nu}\right)^2}, \quad (1.8)$$

where  $\nu_p$  is the plasma frequency and  $\nu$  is the observing frequency. The plasma frequency depends on the equivalent mass of the electron,  $m_e$ , and the number density of electrons,  $n_e$ , such that

$$\nu_p = \sqrt{\frac{n_e e^2}{4\pi^2 m_e \epsilon_0}}, \quad (1.9)$$

where  $e$  is the charge of an electron and  $\epsilon_0$  is the permittivity of free-space. Assuming a typical Galactic value of  $\langle n_e \rangle \approx 0.03 \text{ cm}^{-3}$ , we find that  $\nu_p \simeq 1.5 \text{ kHz}$ . The group velocity of a wave,  $v_g = \mu c$ , travelling through the ISM is therefore less than the speed of light (except for  $\nu = \infty$ ), since equation (1.8) implies  $\mu < 1$ . With respect to infinite frequency, after the propagating wave travels a distance  $L$ , it will have been delayed, compared to a wave with  $v_g = c$ , by an amount

$$t_d = \int_0^L \frac{dz}{v_g} - \frac{L}{c},$$

where  $t_d$  is commonly known as the absolute dispersion delay. Substituting  $v_g = \mu c$  and evaluating the binomial expansion of equation (1.8) we find that the dispersion delay can be written as

$$t_d = \frac{1}{c} \int_0^L \frac{dz}{\mu} - \frac{L}{c} \approx \frac{1}{c} \int_0^L \left(1 + \frac{\nu_p^2}{2\nu^2}\right) dz - \frac{L}{c},$$

where we assume  $\nu_p \ll \nu$ . Substituting equation (1.9), we find that the dispersion delay depends on several constants, the inverse-square of observing frequency and the integrated electron density along the line-of-sight,

$$t_d = \frac{e^2}{8\pi^2 c \epsilon_0 m_e \nu^2} \int_0^L n_e(z) dz. \quad (1.10)$$

If we define the dispersion measure, DM, as the integrated electron density along the line-of-sight, then

$$\text{DM} \equiv \int_0^L n_e(z) dz, \quad (1.11)$$

and equation (1.10) then becomes

$$\Delta t_d = \frac{e^2}{8\pi^2 c \epsilon_0 m_e \nu^2} \times \text{DM}. \quad (1.12)$$

If, instead of absolute delays, we are concerned with the differential dispersion delay (i.e. between frequencies  $\nu_{\text{lo}}$  and  $\nu_{\text{hi}}$ ), then equation (1.12) becomes

$$\Delta t_d = \frac{e^2}{8\pi^2 c \epsilon_0 m_e} \times \text{DM} \times \left( \frac{1}{\nu_{\text{lo}}^2} - \frac{1}{\nu_{\text{hi}}^2} \right), \quad (1.13)$$

with DM and the frequencies ( $\nu_{\text{lo}}, \nu_{\text{hi}}$ ) in SI units of  $\text{m}^{-2}$  and Hz respectively. Converting into more typical units by expressing the DM in units of  $\text{pc cm}^{-3}$  and frequencies in GHz, equation (1.13) can be written as

$$\left( \frac{\Delta t_d}{\text{ms}} \right) \approx 4.148808 \times \left( \frac{\text{DM}}{\text{pc cm}^{-3}} \right) \times \left[ \left( \frac{\nu_{\text{lo}}}{\text{GHz}} \right)^{-2} - \left( \frac{\nu_{\text{hi}}}{\text{GHz}} \right)^{-2} \right]. \quad (1.14)$$

The signature of dispersion is a characteristic quadratic sweep in power across the observing bandwidth, such that lower-frequency components arrive later than higher-frequency components. An example of this effect is shown in Figure 1.5.

### 1.3.2 Interstellar scintillation

In addition to intrinsic pulse-to-pulse variation, the ISM can also induce short-term variability through a process termed scintillation. This scintillation is caused by variations in electron density within the interstellar medium (ISM), or more specifically; the distribution of turbulence scale sizes in the ISM and the relative motions of the Earth, pulsar and scattering screen. Interference between elements of a wavefront that travel different paths through the ISM from the pulsar creates a time and frequency dependent pattern on the observer's plane, similar to Young's two-slit experiment<sup>3</sup>. These patterns are made of "patches" of bright emission, often referred to as scintles.

---

<sup>3</sup>The condition for constructive interference is that the signal phases do not differ by more than  $\approx 1$  radian.

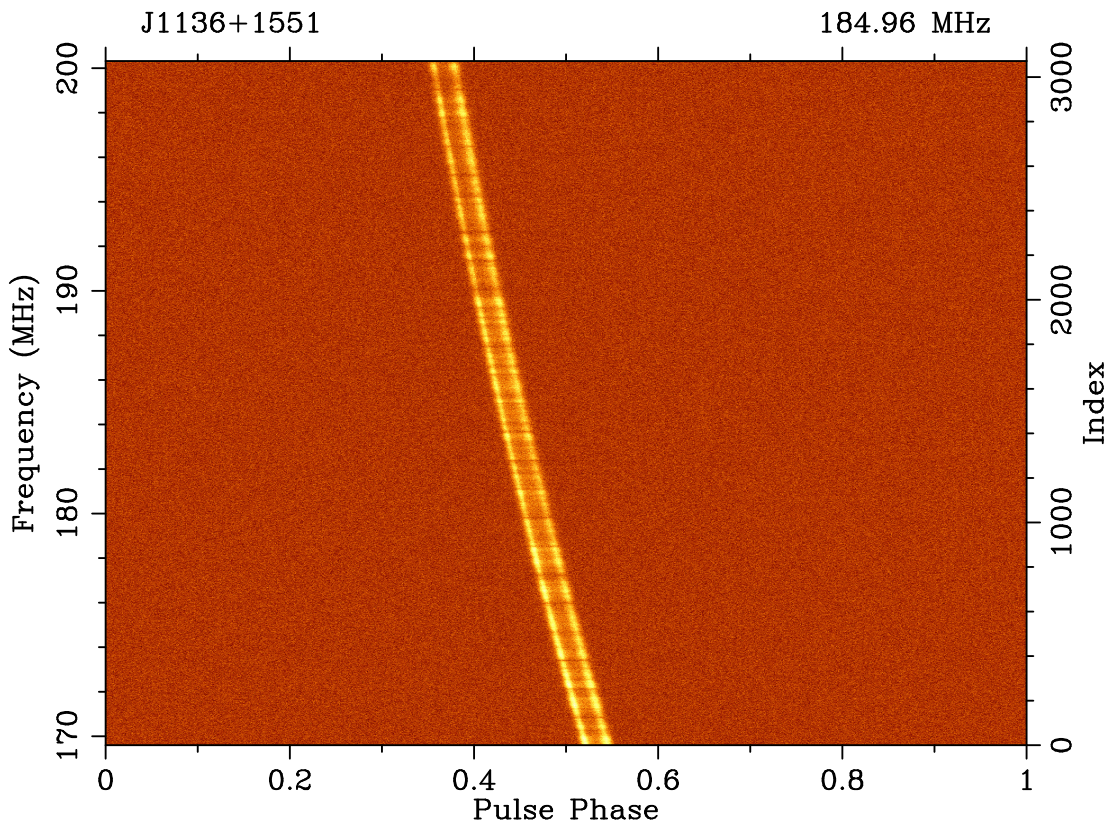


Figure 1.5: The effects of cold plasma dispersion from the interstellar medium on the radio signal from PSR J1136+1551 observed at 185 MHz using the Murchison Widefield Array Voltage Capture System. The pulsar signal is plotted as a function of frequency and pulse phase. The dispersion measure of PSR J1136+1551 is  $4.84 \text{ pc cm}^{-3}$ . This causes a dispersion delay time across the 30.72 MHz bandwidth of  $\Delta t_d \approx 198 \text{ ms}$ .

Interstellar scintillation is split into two regimes: weak and strong. The two regimes scale differently with frequency and distance due to the intrinsically different physics causing the modulation (e.g. Rickett, 1990; Narayan, 1992). The definition is based on the root-mean-square phase variations,  $\phi_{\text{rms}}$ , across the scattering screen, and is closely linked to the dominating physical scales of the turbulence within the ISM. In reality,  $\phi_{\text{rms}}$  and the associated physical scales are not directly measurable, however, the scintillation strength parameter,  $u$ , can be calculated from observable properties. It can be used to determine which regime is dominating, where if  $u < 1$  we are in the weak regime, and if  $u > 1$  we are in the strong regime. The scintillation strength can also be determined by comparing the field coherence scale  $s_0$  and the first Fresnel zone radius  $r_F$ . The field coherence scale ( $s_0$ ) is a measure of the size of a source-centred circular region on the scattering screen that results in phase differences of  $\leq 1$  radian. If the screen scatters the wave phase fronts into an angular spectrum with scale size  $\theta_d$ , then  $s_0 = \lambda/2\pi\theta_d$ , which, in the case of a Kolmogorov spectrum, means that  $s_0 \propto \nu^{1.2} d^{-0.6}$ . The first Fresnel zone radius (as in diffractive optics) is typically expressed as  $r_F = (\lambda d/2\pi)^{1/2}$  where  $\lambda$  is the observing wavelength and  $d$  is the distance to the scattering screen. The scintillation strength can be expressed as:

$$u = \frac{s_0}{r_F} \equiv \sqrt{\frac{\nu}{\nu_{\text{diss}}}}, \quad (1.15)$$

where  $\nu_{\text{diss}}$  is known as the scintillation bandwidth. For a centre frequency  $\nu$ , signals at frequencies outside  $\nu \pm \nu_{\text{diss}}$  do not contribute to the interference pattern.

Theoretically, the distribution of turbulence scale sizes is the three-dimensional Fourier transform of the electron density autocovariance function (Rickett, 1977). Based on observational evidence, the distribution is commonly described using an extended power law model (Rickett, 1990; Armstrong et al., 1995), which is given by

$$P_{n_e}(\kappa) = \frac{C_n^2}{(\kappa^2 + \kappa_o^2)^{\beta/2}} \exp\left[-\frac{\kappa^2}{4\kappa_i^2}\right] \quad (1.16)$$

where  $\kappa = \kappa_x^2 + \kappa_y^2 + \kappa_z^2$  is the magnitude of the three-dimensional wavenumber,  $\kappa_o$  and  $\kappa_i$  are the “outer” and “inner” turbulence scales respectively,  $\beta$  is the power density spectral index, and  $C_n^2$  is a structure coefficient that gives the turbulence strength along a given line-of-sight. In the instance where  $\kappa_o \ll \kappa \ll \kappa_i$ , which is almost always the case, equation (1.16) simplifies to

$$P_{n_e}(\kappa) = C_n^2 \kappa^{-\beta}. \quad (1.17)$$

Assuming this model, the scintillation bandwidth and scattering time scale,  $\tau_s$ , depend on the observing frequency as

$$\Delta\nu_{\text{diss}} \propto \nu^\alpha, \quad \tau_s \propto \nu^{-\alpha}$$

where  $\alpha = 2\beta/(\beta - 2)$  is the frequency scaling parameter. In general it is assumed  $\beta = 11/3$ , corresponding to a Kolmogorov spectrum where energy cascades down from larger to smaller scales within the medium. There are a number of cases for and against a purely Kolmogorov spectrum, but in general it appears suitable on scales  $\lesssim 10^{11}$  m (Gupta, 2000). At larger spatial scales the turbulence spectrum either steepens ( $\beta \approx 4$ ) or has other components that become prominent.

### 1.3.2.1 Weak scintillation

Weak scintillation occurs when the phase perturbations within the Fresnel zone of radius  $r_F$  (near field) at the position of the observer are small. This corresponds to the regime where  $s_0 \gg r_F$ . The relative motion of the pulsar and the ISM results in intensity modulations as the patches within the scattering screen pass by the line-of-sight. Weak scintillation therefore occurs due to the motion of the pulsar, and has a time scale of

$$\Delta t_{\text{weak}} = \frac{r_F}{V_{\text{ISS}}} \propto \nu^{-0.5} d^{0.5}, \quad (1.18)$$

where  $V_{\text{ISS}}$  is the relative speed of the pulsar with respect to the ISM, and acts to move the interference pattern on the observer's plane. In the weak scintillation regime, the scintillation bandwidth is  $\nu_{\text{diss}} \sim \nu$ .

In the case where the source can no longer be considered a point source, these results are modified slightly by a factor of  $\theta_S/\theta_F$ , where  $\theta_S$  is the angular size of the source and  $\theta_F = r_F/d$ . At a critical frequency, estimated by setting equation (1.15) equal to unity, the scintillation regime transitions to the strong regime where diffractive and refractive effects dominate the observed scintillation behaviour.

### 1.3.2.2 Diffractive scintillation

Diffractive scintillation was first recognised by Lyne & Rickett (1968a,b) while observing five pulsars soon after their initial discovery. This branch of strong scintillation occurs when the phase perturbations at the position of the observer are large, where multi-path propagation dominates. In this regime, Fraunhofer (far field) diffraction dominates, and  $s_0 \ll r_F$ . It is typically observed as strong intensity variations in both time *and* frequency. Diffractive scintillation also depends on the relative velocity of the pulsar and the ISM, however the dominating length scale is now  $s_0$  (and  $u > 1$ ). The diffractive time scale is

$$\Delta t_{\text{diss}} = \frac{s_0}{V_{\text{ISS}}} \propto \nu^{1.2} d^{-0.6}. \quad (1.19)$$

The diffractive scintillation bandwidth is approximately

$$\nu_{\text{diss}} \approx \frac{1.16}{2\pi\tau_s} \propto \nu^{4.4} d^{-2.2}, \quad (1.20)$$

assuming a Kolmogorov turbulence spectrum (Cordes et al., 1985; Cordes & Rickett, 1998). These scales represent the size of a scintle, and can often be measured directly by creating a dynamic spectrum (Figure 1.6). In practise, this means that some averaging in time or frequency is required in order for a reliable flux

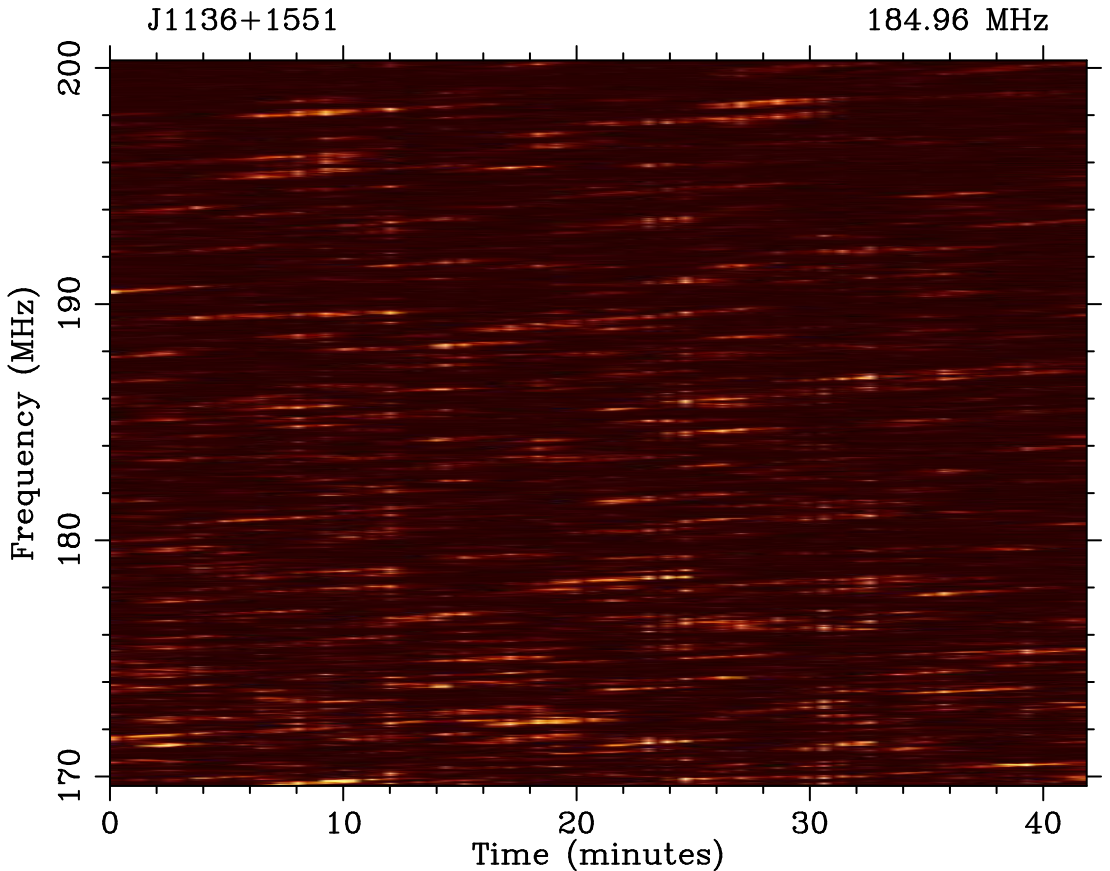


Figure 1.6: An example dynamic spectrum of PSR J1136+1551 from the MWA at 185 MHz. The vertical barred structure is due to the pulsar nulling, thus the sub-integrations which contain nulls are visibly fainter. The horizontal/diagonal structures are the scintles. Measuring the width in frequency and time can give us estimates of the relevant scintillation bandwidths and time scales.

density estimate to be made, to average intrinsic pulse-to-pulse variations. These effects become more prominent at high frequencies ( $\nu \gtrsim 1$  GHz) when the fractional bandwidth is small (which is less of an issue with modern pulsar backends and receivers).

In some cases, where there are high signal-to-noise measurements of many scintles, diffractive scintillation causes particular patterns in the dynamic spectrum, which in turn produce distinct arc-like features in the two-dimensional Fourier transform (e.g. Stinebring et al., 2001; Hill et al., 2003; Stinebring et al., 2019). The characteristics of these arcs appear to be frequency dependent, and the curvature can be used to estimate the precise location of the effective scat-

tering screen along the line-of-sight to the pulsar (e.g. Bhat et al., 2016). The arcs are also useful tools for studying scattering screen models, and for probing the emission regions in pulsar magnetospheres (Cordes et al., 2006).

Diffractive scintillation provides many ways to characterise the ISM as well as the kinematics (i.e. velocities) of pulsars where these effects are measurable. Another observable manifestation of diffractive scintillation is a distortion of the intrinsic pulse shape. This is commonly known as pulse broadening and is characterised by the previously introduced scattering time scale  $\tau_s$ .

### 1.3.2.3 Pulse broadening

The same ISM inhomogeneities and physics that cause diffractive scintillation effects also scatter the emitted radiation from a pulsar, such that it travels along various paths, of differing length, to the observer (Scheuer, 1968; Salpeter, 1969). The phenomenon was first observed in the Crab pulsar (Staelin & Sutton, 1970a), the Vela pulsar (Ables et al., 1970) and a handful of others, which allowed Lang (1971a,b) to theorise that the characteristic scattering time scale,  $\tau_s$ , scales with the observing frequency as  $\tau_s \propto \nu^{-4}$ .

The scattering time scale depends on the observing frequency and the form of turbulence spectrum assumed (see e.g. Lee & Jokipii, 1975; Cordes et al., 1986; Romani et al., 1986). For example, assuming a Kolmogorov energy spectrum we have  $\alpha = 22/5 = 4.4$  (where  $\alpha$  is as discussed in §1.3.2) and thus we would theoretically expect  $\tau_s \propto \nu^{-4.4}$ . In some cases, measurements indicate that the observed scattering time scales are consistent with a purely Kolmogorov spectrum (e.g. Löhmer et al., 2004), while in others, particularly for high-DM pulsars, the scattering time scales are observed to diverge significantly from the theoretical limit, to both shallower and steeper values of  $\alpha$  (e.g. Löhmer et al., 2001; Bhat et al., 2004; Lewandowski et al., 2013; Spitler et al., 2014b). A well known example of divergence from the theorised scaling is the Crab pulsar which typically exhibits a shallower than expected power law index (see e.g. Popov et al., 2006a; Bhat

et al., 2007b; Ellingson et al., 2013; Eftekhari et al., 2016; F. Kirsten et al., submitted).

The shape of the broadened pulse depends on: the choice of “screen” that is assumed to be causing the scattering (e.g. spatially thick or thin, finite or infinite in extent, etc.), the intrinsic pulse shape and the instrumental response. In fact, the observed pulse shape will be a convolution of these factors. The shapes of the scattered pulses are described by pulse broadening functions (PBFs), some of which are defined analytically. The simplest example of a PBF ( $g_0$ ) is that of a one-sided exponential decay,

$$g_0(t; \tau_s) \propto \left( \frac{1}{\tau_s} \right) \exp \left[ -\frac{t - t_0}{\tau_s} \right] u(t), \quad (1.21)$$

where  $t_0$  is the rising edge start time and  $u(t)$  is a unit step function defined as

$$u(t) = \begin{cases} 1, & t > t_0, \\ 0, & t \leq t_0. \end{cases}$$

This corresponds to a geometrically thin (i.e. two-dimensional), finite screen causing the multi-path scattering events. Williamson (1972, 1973, 1974) determined analytic approximations for more realistic screen models based on optics arguments. Specifically, geometrically thick screens that are finite ( $g_1$ ) and infinite ( $g_2$ ) in extent, with functional forms

$$g_1(t; \tau_s) \propto \left( \frac{\pi \tau_s}{4(t - t_0)^3} \right)^{1/2} \exp \left[ -\frac{\pi^2 \tau_s}{16(t - t_0)} \right], \quad (1.22)$$

$$g_2(t; \tau_s) \propto \left( \frac{\pi^5 \tau_s^3}{8(t - t_0)^5} \right)^{1/2} \exp \left[ -\frac{\pi^2 \tau_s}{4(t - t_0)} \right], \quad (1.23)$$

where  $\tau_s$  is the characteristic scattering time scale. One can also find modified versions of these PBFs (which are not necessarily physically motivated), such as an exponentially truncated power law (thin screen) Karuppusamy et al. (2012a)

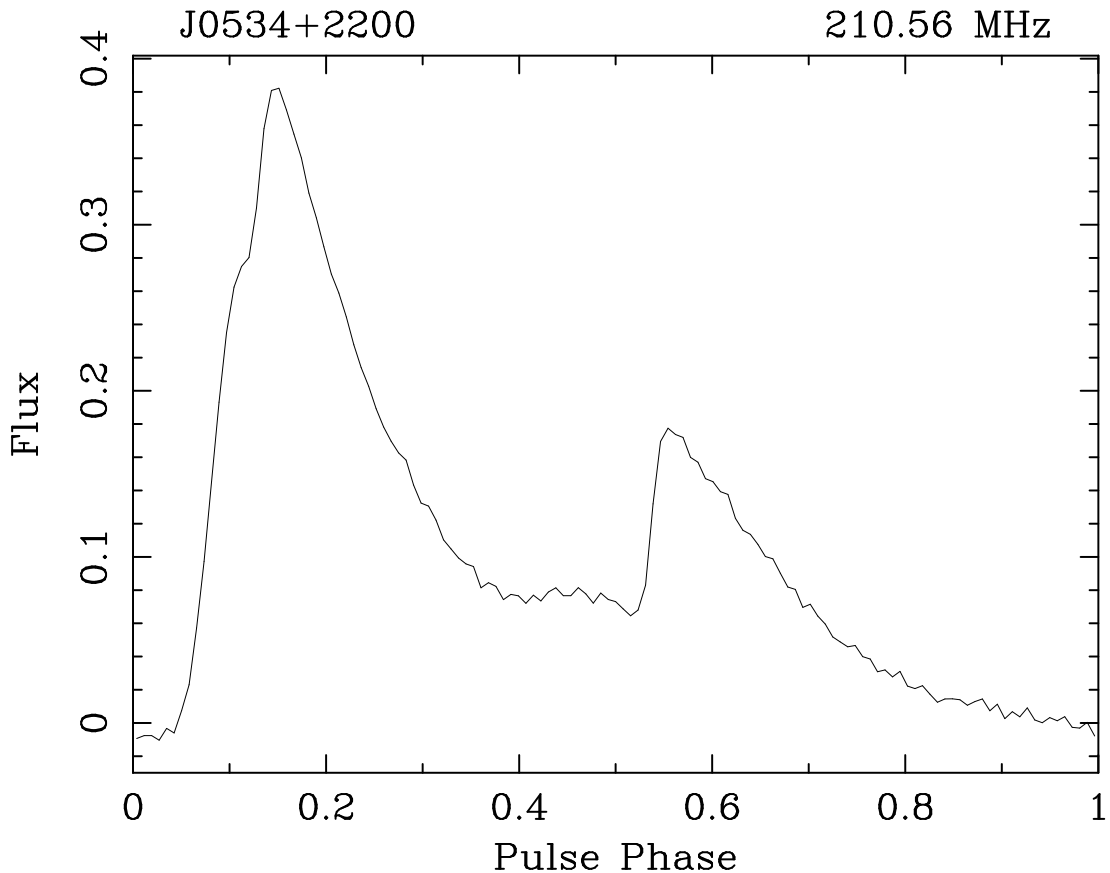


Figure 1.7: The Crab pulsar (PSR J0534+2200) has a multi-component profile. At 210 MHz with the MWA, the pulse broadening has smeared these components into each other such that there is no longer an “off-pulse” window (where there is no astrophysical emission present). In this case, the pulse broadening time scale is  $\tau_s = 3.4 \pm 0.7$  ms (see Chapter 3), which is approximately 10% of the pulse period (33 ms). The components are principally broadened at the leading edge (i.e. right hand side of the pulse) with an exponentially decaying tail, however at lower frequencies it becomes clear that the rise-time (i.e. the left edge of the pulse) is also extended.

that takes the form

$$g_3(t; \tau_s) \propto (t - t_0)^\beta \exp\left[-\frac{t - t_0}{\tau_s}\right]. \quad (1.24)$$

In reality, these functions are not always analytical, especially when attempting to solve in the fully-diffractive regime and/or with the inclusion of multiple scattering screens along the line-of-sight. For these cases, one must use the formalism of Lee & Jokipii (1975) to numerically determine the characteristics of the scattering kernel (see e.g. Kirsten et al., 2019).

In the literature, almost all cases are treated with a thin screen model. At high frequencies this is appropriate, however, at low frequencies, where the scattering effects are extreme, a significant departure from the classical thin screen model is observed (see e.g. Karuppusamy et al., 2012a; Ellingson et al., 2013; Geyer et al., 2017). At these frequencies, the thick screen and/or modified PBFs are required in order to fit the rise-time and extended scattering tail.

It is important to note that the pulse broadening functions described by equations (1.21–1.24) are isotropic, in that they assume that the turbulence is such that light rays are scattered equally in all directions perpendicular to the line-of-sight. Some recent work has been conducted to examine the effects of an anisotropic scattering medium in the context of a thin screen model (Geyer & Karastergiou, 2016). The authors identify that using an anisotropic scattering screen and the appropriate fitting methodology, certain geometries and scattering configurations can cause significant deviations from the predicted models, at least from the simulated data. It is unclear how successful this approach is at low frequencies, given that in general the thin screen model appears to not be favoured. In terms of translating the idea of an anisotropic scattering medium to the thick screen regime, it is not clear what level of improvement would be achieved, given that one can consider a thick screen as an incoherent superposition of thin screens, which would average out any anisotropies.

Removing or mitigating multipath scattering is exceptionally difficult, typ-

ically requiring deconvolution techniques (e.g. Bhat et al., 2004) or advanced signal-processing techniques such as cyclic-spectroscopy (e.g. Demorest, 2011; Walker et al., 2013). Neither of these techniques work in all cases, nor are they commonly used in either the literature or standard pulsar processing pipelines. While often providing improvements over the original data, these techniques and their subtleties can sometimes be difficult to use.

#### 1.3.2.4 Refractive scintillation

Flux density variations on time scales of  $\sim$  days to weeks (or longer) observed in pulsars were long assumed to be an intrinsic property of pulsars. However, Sieber (1982) noticed that these modulations increased as the source distance increased. Such a relationship cannot be explained as an intrinsic property of pulsars, thus Rickett et al. (1984) proposed refractive interstellar scintillation as the cause of the long term flux density variations.

Refractive scintillation is typically understood in terms of focussing and defocussing of rays by the scattering screen. The refractive time scales are much longer than those of diffractive scintillation, and are determined by a characteristic refractive scale  $r_R = r_F^2/s_0$ , such that

$$\Delta t_{\text{riss}} = \frac{r_R}{V_{\text{ISS}}} \equiv u^2 \Delta t_{\text{diss}} \propto \nu^{-2.2} d^{1.6}, \quad (1.25)$$

where  $u$  is the scintillation strength as in equation (1.15). This scaling is consistent with the observations of Sieber (1982), that the effect increases with distance. Like diffractive scintillation, this effect is clearly seen as a variety of different phenomena in pulsar dynamic spectra (see e.g. Gupta et al., 1994). Occasionally, dynamic spectra can exhibit features such as criss-cross patterns, which are clear identifiers of refractive scintillation.

## 1.4 Giant pulse emitters

As the name implies, giant pulses are extremely bright, with typical equivalent blackbody emission temperature of  $T_b \gtrsim 10^{31}$  K and intrinsically short duration ( $\delta t \sim 1$  ns) bursts of coherent radio emission that have been observed in only a handful of pulsars. The Crab pulsar (PSR J0534+2200) is a giant pulse emitter and is the best studied example (e.g. Comella et al., 1969; Hankins et al., 2003; Cordes et al., 2004; Bhat et al., 2007b, 2008; Karuppusamy et al., 2010a; Oronsaye et al., 2015; Lyne et al., 2015; Hankins et al., 2015, 2016). In fact, the giant pulse emission from the Crab is how the pulsar was first discovered (Staelin & Reifenstein, 1968).

There are six known giant pulse emitting pulsars (refer to Figure 1.4), four of which have periods of less than 10 ms. All six occasionally display extremely bright pulses that follow a different pulse energy distribution to typically-observed pulsar emission (e.g. Cognard et al., 1996; Knight et al., 2006; Knight, 2007). Normal pulsar emission is characterised by an exponential or log-normal pulse energy distribution (Burke-Spolaor et al., 2011), whereas giant pulses appear to follow a power law relation (e.g. Cordes et al., 2004; Bhat et al., 2008; Karuppusamy et al., 2010a; Oronsaye et al., 2015).

Giant pulse emission, as an example of sporadic pulsar emission, appears to be produced by a distinct, non-linear process in the magnetosphere separate from the standard pulsar emission. At least for the Crab pulsar, it is suggested that the emission region is well above the pulsar surface (Eilek & Hankins, 2016), closer to the typically high-energy (X-ray and  $\gamma$ -ray) emission zones. The Crab giant pulses also show interesting temporal structure and spectral behaviour (Figure 1.8). If giant pulse emission is produced by the standard pulsar emission mechanism, then they are an example of extreme and/or catastrophic changes in the local plasma conditions.

Simultaneous observations across a wide frequency range are sparse for most giant pulse emitting pulsars. Being able to track the same single giant pulse

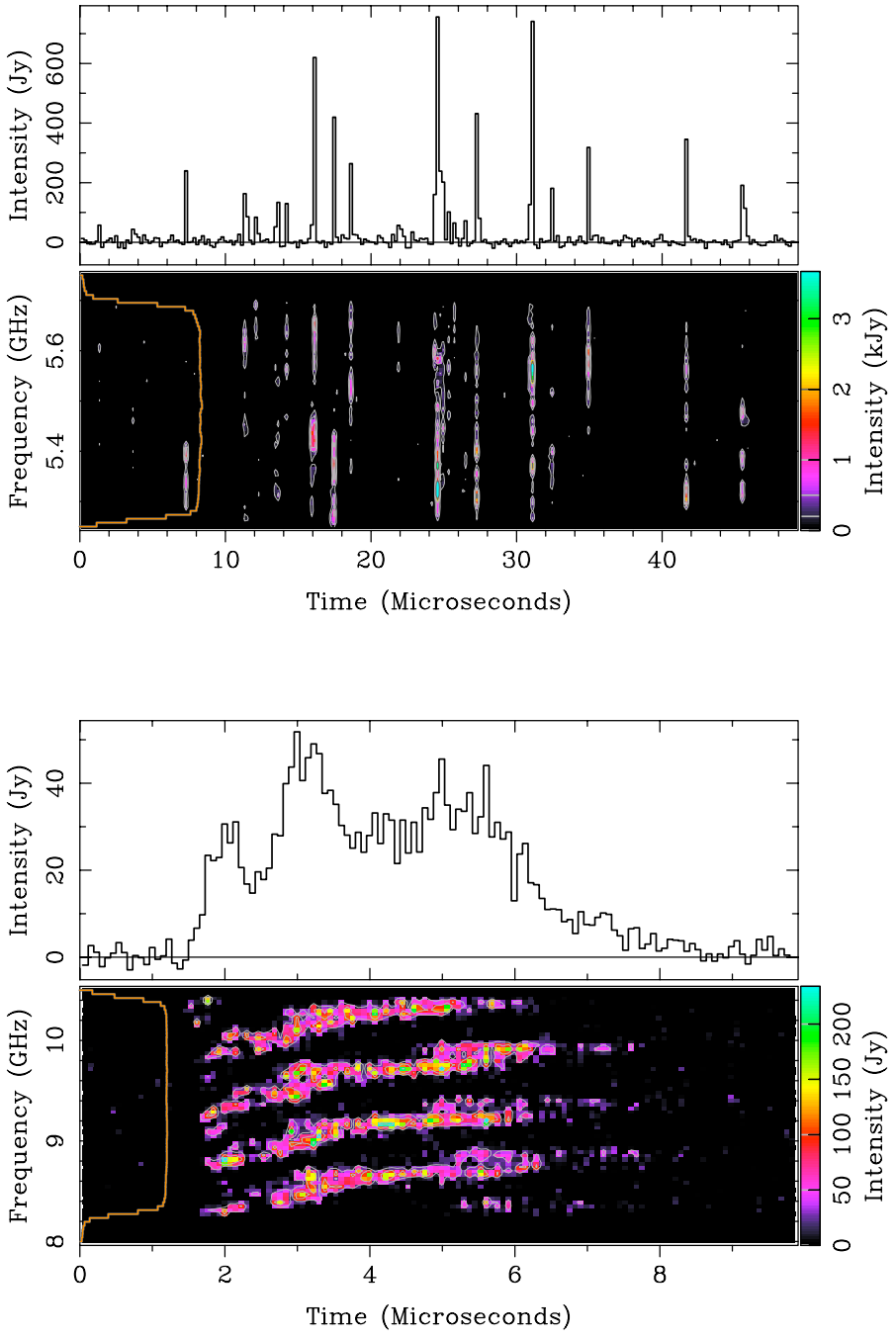


Figure 1.8: *Top:* A series of separated “nanoshots” from the Crab pulsar. They are relatively narrowband and last  $\sim 1$  ns. When combined, these nanoshots create a broadband, microsecond-long burst. *Bottom:* An example of a giant pulse occurring at high-frequency ( $> 8$  GHz) during the interpulse for the Crab. These zebra stripe patterns are completely unexpected, but resemble phenomena observed from the Sun. Figures from Eilek & Hankins (2016).

across a wide low-frequency range would provide new information for the emission characteristics (see e.g. Oronsaye et al., 2015) and possibly prompt further development of a possible emission model. Filling in the low-frequency regime with simultaneous multi-frequency observations will allow theoretical physicists to model the emission mechanism with data from  $\lesssim 300$  MHz in the radio to  $\sim 1$  MeV in the  $\gamma$ -ray regime (see e.g. Machabeli & Chkheidze, 2014).

## 1.5 Mode changing

Mode changing was first observed by Backer (1970a), who suggested the phenomenon as an explanation for some of the pulse variability observed in pulsars in the early years of pulsar science, especially “nulling” (§1.6). At the most basic level, mode changing is the phenomenon where an integrated pulse profile changes between two or more morphologies. Wang et al. (2007) found that the nulling phenomenon and mode changes were correlated for some pulsars. An illustrative example is PSR J1701–3726, which is a mode changing pulsar that has two distinct emission modes and always exhibits nulling when switching between these modes. Furthermore, Lyne et al. (2010) found that for six pulsars, the observed changes in the spin-down rate directly mapped to a change in the pulse profile shape (see Figure 1.9).

Mode changing is thought to be associated with some fraction of “timing noise” (see e.g. Hobbs et al., 2010; Shannon & Cordes, 2010), and appears to be a manifestation of two (or more) different spin-down modes that are switched between quasi-periodically. When a pulsar switches modes, it is suggested that a significant change occurs in the magnetosphere and therefore the emission profile also changes (Lyne et al., 2010). In addition to radio profiles changing, PSR B0943+10 was shown to “mode switch” between correlated radio and X-ray emission states (Hermsen et al., 2013). For this pulsar, the (pulsed) radio-loud state coincides with unpulsed, non-thermal X-ray emission, while bright, 100% pulsed thermal X-ray emission occurs in the radio-quiet state. The explanation

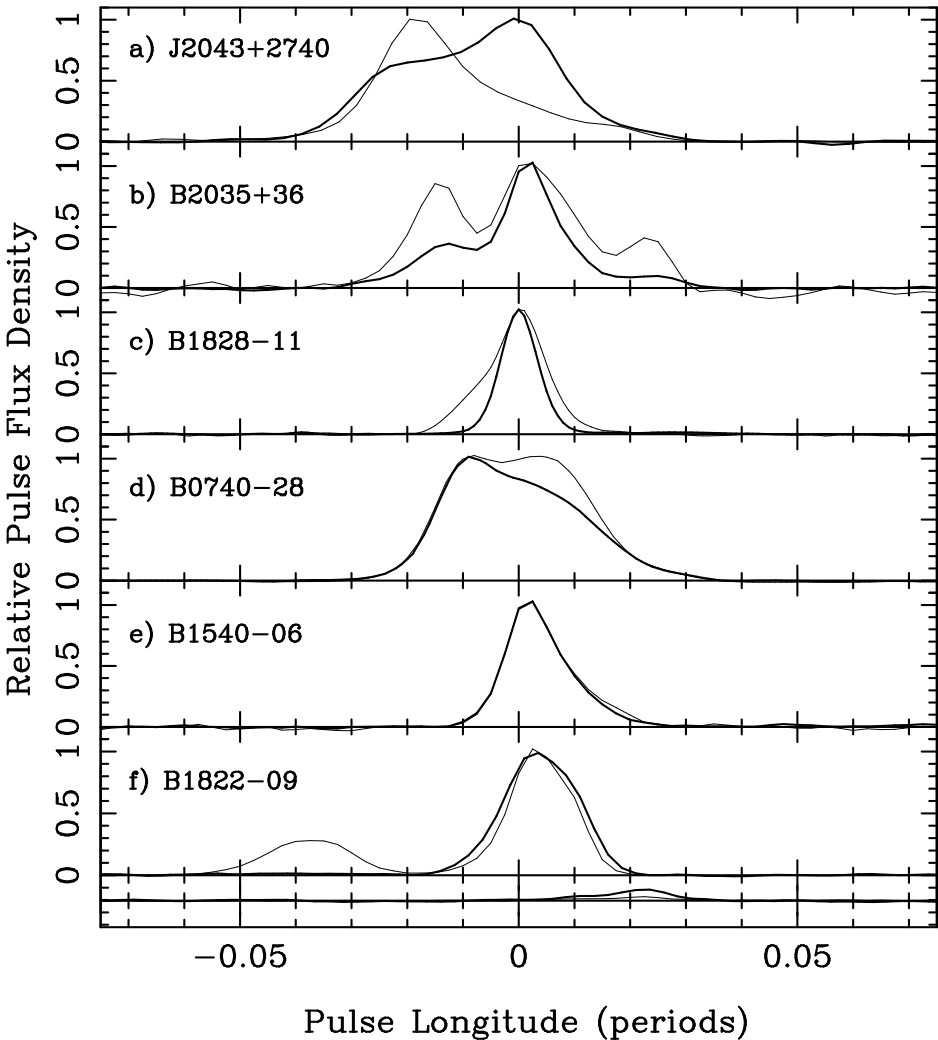


Figure 1.9: Integrated pulse profiles at 1.4 GHz of six pulsars that exhibit long-term shape changes. Each pulsar has two traces which are examples of the most extreme observed pulse shapes. The profile drawn with a thick line corresponds to the largest spin down rate (i.e.  $|\dot{\nu}| = -\dot{P}/P^2$ ). The final, smaller panel is the interpulse of PSR B1822-09 shifted by half a pulse period. Figure from Lyne et al. (2010).

for these emission modes again involves rapid, large-scale changes in the pulsar magnetosphere. In both of these circumstances, the magnetospheric configuration is significantly altered by some event (either external or from instabilities in the plasma itself). This directly affects the currents flowing within the emitting plasma and therefore affects the spin-down torque applied to the magnetosphere (and by extension the pulsar, since the magnetosphere and pulsar are co-rotating) as well as the emission region location and characteristics. Mode changing challenges most, if not all, current pulsar emission theories, particularly in the case of PSR B0943+10. How, or if, mode changing is linked to other forms of emission intermittency (see below) is not explicitly obvious, though it is conceivable for a pulsar to have a mode where, for instance, no detectable radio emission is produced.

## 1.6 Nulling

Nulling pulsars generally emit like “normal” pulsars, however, they occasionally cease to emit above the observing sensitivity limit for several rotations. This phenomenon was first noticed by Backer (1970b) in four pulsars. The duration and frequency of nulling events varies between pulsars. The nulling fraction (NF) describes the amount of time the pulsar spends “off” for the duration of an observation. Observationally, this value ranges from 0% (always “on”) to  $> 50\%$ , but is typically between  $\sim 1\text{--}20\%$  for pulsars that do null. In most cases, nulling happens abruptly, in that the pulsar changes from emitting to nulling within a single pulse period (Deich et al., 1986). For a handful of well-studied pulsars, a roll-off in flux density is observed before nulling, taking anywhere from  $\sim 1\text{--}50$  rotation periods to enter a null (e.g. PSR B1944+17, Deich et al., 1986; and PSR J1752+2359, Lewandowski et al., 2004). An example of nulling can be found in Figure 1.3, showing 100 consecutive single pulses from PSR J1136+1551.

Early studies of nulling pulsars suggested that there was a correlation between NF and the pulsar characteristic age (Ritchings, 1976) and the spin period (Biggs,

1992). These correlations suggest the emission mechanism begins to fail as the pulsar approaches the end of its radio emission lifetime. However, there is a large scatter in the observed nulling fractions of pulsars (Rankin, 1986), making it difficult to see any obvious or direct relationship between nulling fraction and age or spin period. In fact, observations of millisecond pulsars (MSPs; old pulsars that have been “spun up” or recycled, likely by an accretion event) tend to show very little, if any, nulling activity (e.g. PSR J0437–4715, Vivekanand et al., 1998). This is not surprising, given that there are only a handful of MSPs that have been studied on a single-pulse level, most are very faint compared to young pulsars, and that MSPs are a truly distinct population of pulsars with different rotational properties.

The radio emission observed (or not) during a null is usually limited by signal-to-noise and does not necessarily indicate that the emission process has completely stopped. By stacking the data (i.e. summing the time series modulo the pulse period and calculating the average) during the nulls of PSR B0826–34, Esamdin et al. (2005) found weak radio emission on the order of 2% of the “on” flux density and that the pulse profile changed from that of the normal “on” profile (which is reminiscent of mode changing, §1.5). Results from a study of 23 pulsars (6 of which showed both nulling and mode changing) with Parkes (Wang et al., 2007) suggest that nulling could be a manifestation of mode changing. Ultimately, the nulling phenomenon is still a very active area of research and there is no consensus on what nulling represents, how it occurs, nor how it relates to the pulsar emission mechanism.

## 1.7 Rotating Radio Transients

Discovered in 2006 by single-pulse detection algorithms run on archival Parkes data (McLaughlin et al., 2006), Rotating Radio Transients (RRATs) are a recently discovered population of pulsars, now with over 100 members or candidates<sup>4</sup>.

---

<sup>4</sup>See the RRATatalog here:<http://astro.phys.wvu.edu/rratalog/>

RRATs are a manifestation of sporadic pulsar emission operating on time scales of minutes to hours and are best detected by single-pulse searching techniques (Keane & McLaughlin, 2011).

The emission mechanism for these objects is also unknown, though likely the same as “normal” pulsars. With the assumption that the RRATs were not emitting at all during the “off” periods, several theories were proposed. The problem with these “solutions” is that they invoke the idea that the observed emission is a re-activation of the normal pulsar emission mechanism, even though RRATs are only objects that satisfy observationally dependent selection criteria. RRATs could be a manifestation of long-duration nulling (i.e. nulling fractions  $\gtrsim 90\%$ ) or even distant/weak pulsars that exhibit large brightness fluctuations making the RRAT only detectable via single bright bursts of radiation (Keane et al., 2011). Naturally the idea of mode changing is appealing, however the relationship between RRATs and mode changing is, as with nulling, unknown. The emission mechanism may be that of normal pulsars in a different magnetospheric configuration or it may be that the RRAT phenomenon is a selection effect.

It is important to note that, as already mentioned, the definition of a RRAT is arbitrary in that separate surveys with different observing properties may detect the same pulsar as being, e.g., a nullder and a RRAT (e.g. Weltevrede et al., 2006a,b). Keane & McLaughlin (2011) proposed the definition: “*A RRAT is a repeating radio source, with underlying periodicity, which is more significantly detectable via its single pulses than in periodicity searches.*” This definition is not the only one in the literature and thus far there is no consensus on how to best concisely define a RRAT.

Another way to determine whether a pulsar is a RRAT would be to use the intermittency ratio, introduced by McLaughlin & Cordes (2003),

$$r = \frac{(S/N)_{SP}}{(S/N)_{FFT}} = \frac{A}{\sqrt{N}} \frac{S_{peak}}{S_{av}}, \quad (1.26)$$

where the subscripts SP and FFT correspond to “Single Pulse” and “Fast Fourier

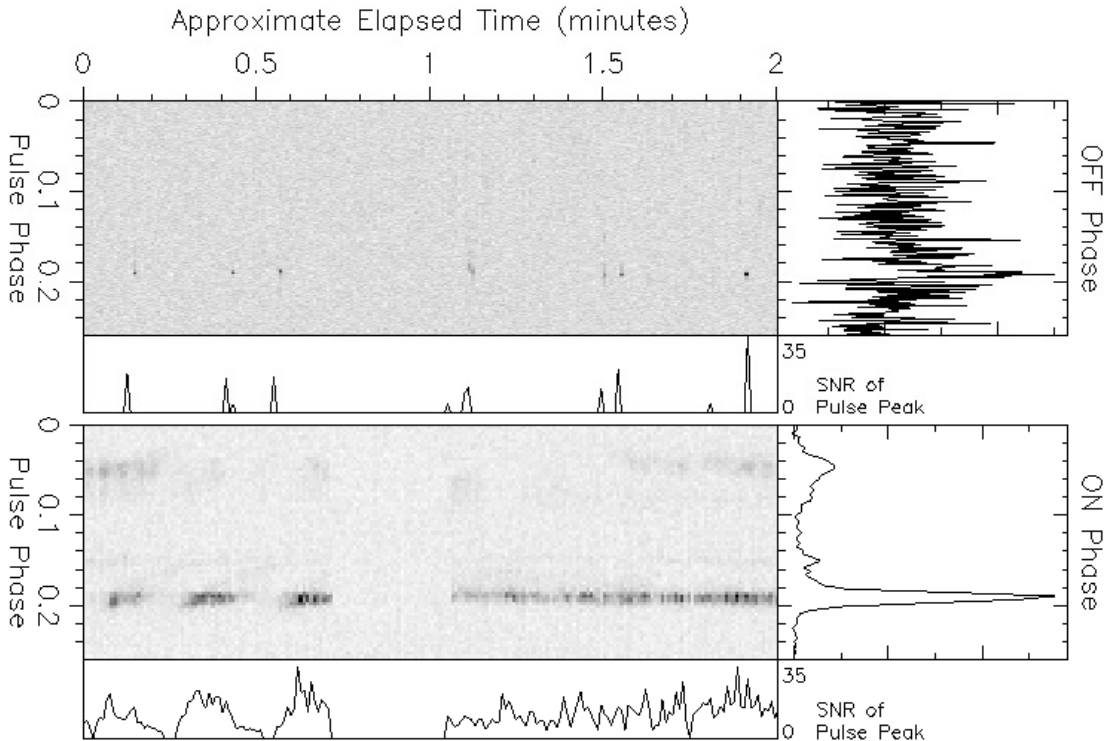


Figure 1.10: PSR J0941–3941 in RRAT mode (top) and nulling pulsar mode (bottom) at 1372 MHz. The integrated pulse profile is appended to the right of each panel. Below each panel is a trace of the signal-to-noise (S/N) for each pulse. The peak S/N is comparable in both modes, implying that the difference is not due to scintillation. Figures from Burke-Spoloar & Bailes (2010).

Transform” search methods,  $A \approx 2$ ,  $N$  is the number of pulse periods in an observation and  $S_{\text{peak}}/S_{\text{av}}$  is the ratio of the peak flux-density and the average flux-density. If  $r > 1$  then one could classify the object as being a RRAT. Clearly this is an observational effect and thus it is difficult to claim that RRATs are actually different at all from standard pulsars.

Observations of RRATs below 300 MHz are sparse, however, the Green Bank Telescope (GBT) is producing promising results at 350 MHz (Karako-Argaman et al., 2013; Karako-Argaman et al., 2015a). The LWA has recently detected RRATs below 100 MHz (Taylor et al., 2016) and LOFAR has found at least two new RRATs from the LOFAR Tied-Array Survey (LOTAS,  $\sim 150$  MHz; Coenen et al., 2014a). The overall lack of low-frequency coverage, especially in the southern hemisphere, is a problem when trying to model a potentially broadband emission

process. When emitting (“on”), RRATs look very much like normal pulsars and even tend to have similar spectral indices ( $S \propto \nu^{-1.7}$ ; Miller et al., 2011) – though these estimates are based on observations for frequencies  $\nu > 700$  MHz. The same underlying physics could be producing both normal pulsar and RRAT radio emission, given the similarity of RRAT pulse characteristics to normal pulsars in terms of pulse width, duration and single-pulse structure.

Links between RRATs and nulling (or mode changing) pulsars are already observed, e.g. PSR J0941–3941 (see Figure 1.10, Burke-Spolaor & Bailes, 2010) and PSR B0826–34 (Esamdin et al., 2012). Interestingly, RRATs make a reasonably distinct population on the  $P-\dot{P}$  diagram, which has been suggested as an indication of an evolutionary relationship between RRATs and isolated X-ray pulsars or magnetars (Popov et al., 2006b). It is proposed that at least some RRATs may be extreme nulling pulsars (Burke-Spolaor & Bailes, 2010), which is not unexpected given the arbitrary definition of a RRAT. There are also some RRATs that seem to better fit the idea that the pulsar is weak and/or distant with large amplitude brightness modulations.

The issues of selection bias and emission modes still stand for the RRAT population as a whole. What makes the pulsar switch between modes, and is it even some form of mode switching or just a selection effect? Do all RRATs exhibit this behaviour, and is it observing frequency dependent? In order to link RRATs to any other sub-group, like nullers or intermittent pulsars, we need to study properties that directly affect the emission process and can answer some of these questions. In particular, the low-frequency ( $\lesssim 100$  MHz) information is lacking for the majority of these pulsars, and could provide crucial evidence for a sound explanation of the RRAT phenomenon.

## 1.8 Intermittent pulsars

As the newest identified class in the sporadic-emission group of pulsars, the aptly-named intermittent pulsars spend a large fraction of time in an “off” state, lasting

anywhere from weeks to years. The prototypical example of an intermittent pulsar is PSR J1933+2421 which was discovered by Stokes et al. (1985a). It was not until much later that it was actually classified as an intermittent pulsar, with an active period of 5–10 days that also exhibits “normal” nulling behaviour, and an inactive period of 25–35 days, where no emission is detected (Kramer et al., 2006).

Since then, there have been at least six more pulsars of this kind discovered (PSRs J1841–0500; Camilo et al., 2012, J1832+0029; Lorimer et al., 2012, J1107–5907; Young et al., 2014, J1717–4054; Kerr et al., 2014, J1910+0517 and J1929+1357; Lyne et al., 2017), each with “off” stages lasting for between a few hours to more than 800 days. It is important to recognise that, due to their extreme time scales, it is much more difficult to detect these pulsars, compared to normal pulsars, and there could be (and likely are) a significant number of intermittent pulsars that have not yet been discovered.

For at least three of these pulsars, we know that the spin-down rate ( $\dot{P}$ ) changes by a factor of  $\sim$ 1.5–2.5 between “on” and “off” states, indicating a drastic change in the magnetosphere (see Figure 1.11). For the other two, the transition from “on” to “off” has only been published once, thus we do not know the active-to-inactive state duty cycle, nor can we compare two of the same states to determine if the spin-down rate changed.

This phenomenon is similar to that of mode changing and nulling, except that the different state durations operate on entirely different time scales (months to years). Intermittent pulsars seem unlikely to just be pulsars with large nulling fractions, given the amount of time that the emission mechanism remains inactive exceeds that of even the longest nulling pulsar by five orders of magnitude. In fact, PSR J1841–0500 has a modest nulling fraction of 20–40% during the active emission state, but the time between active and inactive states is extreme ( $\approx$  1 yr, Camilo et al., 2012). During the “off” state, many observations of PSR J1841–0500 were made (squares in Figure 1.11), but no detectable emission was observed,

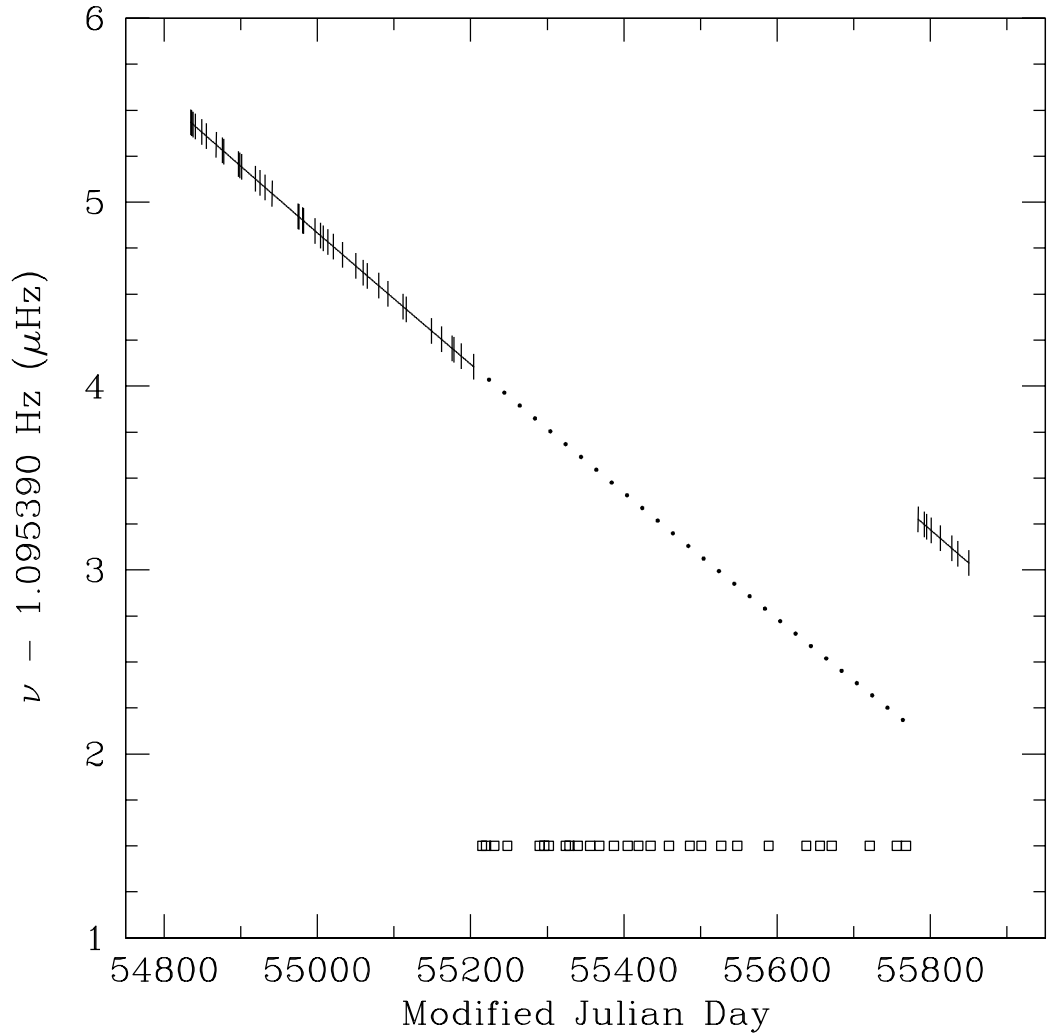


Figure 1.11: Spin frequency evolution for PSR J1841–0500. The first (from left) solid line represents the timing solution obtained in 2009, before the inactive state switch. The second, shorter solid line represents the timing solution from 2011 after the pulsar went into an active state. The dotted line shows the extrapolation based on the 2009 timing solution. Observations were made during the inactive period, displayed here as squares. Figure from Camilo et al. (2012).

thus the “off” duration is not simply due to a lack of observation.

Naturally, pulsars of this type are difficult to detect, which hints at a potentially large population of intermittent pulsars in the Galaxy (i.e. a non-detection due to being in the “off” state during a survey). A large proportion of known pulsars are not monitored regularly, thus it is not clear what fraction of pulsars exhibit long-term intermittency (e.g. PSR J1933+2421 was not recognised as a peculiar case for  $\sim 20$  years; Stokes et al., 1985b).

In terms of a pulsar emission mechanism allowing for this extreme intermittency, models range from a plasma-free magnetosphere (Manchester & Taylor, 1977) to an idealised magneto-hydrodynamics plasma-filled magnetosphere (Spitkovsky, 2006). Neither of the models can explain pulsar emission on their own. Even when considering a switching between a plasma-free and a plasma-filled magnetospheric state, theory is inconsistent with observations, given that the predicted active-to-inactive state spin-down rate ratio is  $> 300\%$ , while the observed ratio is  $< 250\%$ . More recently, models of the magnetosphere where conduction currents are suppressed by some resistive mechanism can produce results similar to observation (Li et al., 2012a; Kalapotharakos et al., 2012).

Intermittent pulsars are argued to be a distinct phenomenon and not RRAT/nulling behaviour (Burke-Spolaor et al., 2011). They do not appear to form an obvious group on the  $P-\dot{P}$  diagram, unlike nulling pulsars or RRATs, however, there must be something similar occurring in the magnetosphere in order to see such long duration inactive states. Again, in order to link this phenomenon with RRATs or nulling pulsars (or indeed show that they are entirely separate), low-frequency studies that will reveal more information about the actual emission mechanism are required.

## 1.9 Fast Radio Bursts

Fast Radio Bursts (FRBs, e.g. Lorimer et al., 2007; Thornton et al., 2013) are bright, millisecond-duration bursts of radio emission known to originate at cos-

mological distances (Bannister et al., 2019). Their discovery and the similarities in emission to what we see from pulsars is a tantalising prospect that has since birthed a new and rapidly maturing area of transient astrophysics. The physics driving FRB emission is, as in the case of pulsars, somewhat of a mystery, thus many of the questions asked in the context of pulsar intermittency and the mechanisms behind it are also valid for FRBs. For an extensive review of the field, see Petroff et al. (2019).

Since their initial discovery, there have been major efforts to expand the population from only a handful to now over 70 examples (the most prolific contributors recently being CHIME/FRB Collaboration et al., 2019b; Shannon et al., 2018), which are catalogued in the FRB Catalogue<sup>5</sup> (Petroff et al., 2016). The discovery of repeating FRBs (Spitler et al., 2016; CHIME/FRB Collaboration et al., 2019a) is yet another phenomenon within the FRB population. In the literature, repeating FRB sources have often been theorised to be a consequence of either pulsar emission or related to compact object interactions. A link to giant pulse emission, like that from the Crab, was quickly drawn (Connor et al., 2016; Cordes et al., 2016; Lyutikov et al., 2016) and still remains a plausible scenario. In total, there are at least 55 FRB progenitor theories<sup>6</sup> (Platts et al., 2018), the vast majority of which involve neutron stars.

In the context of this thesis, the salient features of FRBs are the short-duration, bright single pulses, the spectral index, and the paucity of detections below a frequency of 400 MHz. There have been myriad attempts to detect FRBs at low frequencies (Coenen et al., 2014b; Tingay et al., 2015; Karastergiou et al., 2015a; Rowlinson et al., 2016; Burke-Spolaor et al., 2016a; Amiri et al., 2017; Chawla et al., 2017) with no success. Thus far, Sokolowski et al. (2018) have provided the strongest limits on low-frequency FRB radio emission by simultaneously observing (in imaging mode) when the Commensal Realtime ASKAP Fast Transients (CRAFT) survey (Macquart et al., 2010) detected several bright

---

<sup>5</sup><http://www.frbcat.org/>

<sup>6</sup><https://frbtheorycat.org/>

FRBs. Generally speaking, the connection between pulsars and FRBs is a (very) open question, but sporadic emission from pulsars could hold important clues to understanding FRB emission (and vice versa), especially at low frequencies.

## 1.10 Pulsars at low frequencies

Most radio observations of pulsars in the last few decades have been at frequencies above 300 MHz. Originally, pulsars were discovered at  $\approx 80$  MHz (Hewish et al., 1968), and in the early stages of the field, low-frequency observations were prevalent. The initial detections at low frequencies are not surprising, given the typical pulsar emission spectral index (see §1.2.2). Low frequency pulsar observations are also more strongly affected by the propagation effects discussed in §1.3 and thus allow us to study these processes in more detail than at high frequencies.

Observations of pulsars originally moved to high-frequencies due to, at least in part:

- higher telescope sensitivity (generally speaking),
- less severe propagation effects (e.g. dispersion and scattering),
- suppressed background/diffuse emission from the Galaxy,
- less frequency-dependent time and phase delays due to the Earth's ionosphere, and
- less prominent radio frequency interference (RFI).

On the last point, it is important to realise that as RFI becomes more problematic with technology taking up more of the frequency spectrum for high-power broadcasting of signals (e.g. digital television and mobile/cellular networks), a low-frequency approach is becoming more appealing. Furthermore, with recent improvements in technology, engineering developments and signal-processing, there is now a paradigm shift in pulsar astronomy to move to low

frequencies once again. Some of the most prominent low-frequency telescopes include: the Murchison Widefield Array (MWA, Tingay et al., 2013; Wayth et al. in prep.), the LOw Frequency ARray in the Netherlands (LOFAR, van Haarlem et al., 2013), the Long Wavelength Array (LWA1, Taylor et al., 2012) and the Giant Metre-wave Radio Telescope (GMRT, Swarup, 1990; Swarup et al., 1991). These instruments now regularly study pulsars, providing valuable profile, flux density and dispersion measure information at low frequencies (see e.g. Stovall et al., 2015; Bhattacharyya et al., 2016; Bilous et al., 2016; Xue et al., 2017).

### 1.10.1 Pulsar science with the Murchison Widefield Array

The Murchison Widefield Array (MWA) is a low-frequency precursor (80–300 MHz) to the upcoming Square Kilometre Array (SKA) low-frequency component (SKA-Low, 50–350 MHz). Pulsar astronomy is a key science topic for the SKA (e.g. Karastergiou et al., 2015b), thus pulsar studies with the MWA will provide insight into the detectability of pulsars and inform on SKA observing and processing strategies.

The MWA is the only low-frequency telescope that can observe 500-600 known radio pulsars below declination  $\delta \approx -50^\circ$  below 300 MHz. The high time resolution capability required for time-domain pulsar astronomy is provided by the Voltage Capture System (VCS, Tremblay et al., 2015). The VCS allows for a wide variety of pulsar science, including: single-pulse studies of pulsars (e.g. Oronsaye et al., 2015; McSweeney et al., 2017; Meyers et al., 2017), low-frequency censuses and characterisation of ISM effects (see e.g. Bhat et al., 2016, 2018; F. Kirsten et al., submitted).

The VCS records the voltages before they reach the MWA correlator, with 10 kHz frequency resolution and  $100\,\mu\text{s}$  time resolution. This corresponds to a data rate of  $\approx 28\,\text{TB}$  per hour. Voltages can be combined incoherently, where we calculate the power for each MWA receiving element (a “tile”) and sum, providing maximum field-of-view ( $\approx 1200\,\text{deg}^2$  at 150 MHz), but limited sensitivity

(theoretically  $\sqrt{N}$  times the individual tile sensitivity, where  $N$  is the number of tiles summed). The raw voltages can also be combined coherently (i.e. rotate and sum complex voltages from each tile, then calculate the power; Ord et al., 2019), which provides maximum sensitivity (theoretically another factor of  $\sqrt{N}$  over the incoherent sum), but at the cost of significant compute overheads and a reduced field-of-view ( $\approx 8 \text{ arcmin}^2$  at 150 MHz, assuming a maximum baseline of 3 km). See Section 2.1 for an in-depth description of the pertinent signal processing and telescope design details.

## 1.11 Motivation for this Thesis

The pulsar emission mechanism is one of the most prominent unanswered questions in radio astronomy today. We are able to interpret a significant amount of information about some physical pulsar quantities from effectively a one-dimensional signal, however the wide variety of emission phenomenology observed poses a complex problem. Studying pulsars over a wide range of frequencies provides another dimension in which to solve this problem. The majority of catalogued pulsars are not well studied at frequencies below 300 MHz, especially in the southern hemisphere. Low-frequency pulsar astronomy has seen a resurgence in the past decade, and is now a key science area for the next generation of radio telescopes. The MWA offers a unique perspective for southern pulsars below 300 MHz, particularly with the VCS.

Populations of pulsars with intermittent/sporadic emission properties are comparatively recent discoveries (with the exception of Crab giant pulses and “nulling”). These newer groups of pulsars have not had the same low-frequency coverage as the earliest pulsars, thus we are missing crucial information for a significant fraction of the pulsar population. By using the MWA and other telescopes to study these objects over wide frequency ranges, with wide fractional bandwidths, we will be able to provide valuable insight into the emission mechanism and whether or not the sporadic populations are truly distinct from each other. The broadband

nature of the emission from these populations of pulsars, in particular at low radio frequencies, is generally uncertain. The work forming this thesis aims to address some of these issues by characterising emission from at least one target of each population (namely: giant pulses, intermittent pulsars and RRATs) over a wide spread in frequencies, especially  $< 300$  MHz. Thorough observational characterisation further prompts the exploration of sporadic pulsar radio emission from a phenomenological and theoretical basis, and will ultimately lead to a stronger understanding of the pulsar emission mechanism, and the Galactic pulsar (and neutron star) population.

Ultimately, this work aims to provide new evidence that can propel our understanding of the pulsar emission mechanism. The coherent emission physics implied by a number of observational qualities of pulsar emission is something for which we do not have a solid theoretical basis. This issue is tightly connected to relativistic electrodynamics that are impossible to recreate and study in terrestrial laboratories, ergo, pulsars provide the best possible probe into these fundamental questions. In addition to its importance in understanding pulsars, the coherent emission mechanism that produces the observed radio emission may also be at play in other astrophysical contexts, a clear example being Fast Radio Bursts, which are thought to be extragalactic in origin and are the most powerful radio transient events currently known. While not directly addressed, the analysis presented here highlights a number of interesting and new results that will provide another stepping stone towards a more holistic understanding of pulsars.

## 1.12 Statement of Originality

This section is to comply with the requirement that all co-authors of work included in this thesis outline their contributions. In communicating this statement to the co-authors, they were also informed that the lack of a response would be taken as unconditional tacit approval. Otherwise, all co-authors have read and agreed to the following statement, and their responses can be found in

## Appendix A.

In Chapter 3, we investigated giant pulses from the Crab pulsar (PSR J0534+2200) with the MWA using the then newly implemented “coherent beamforming” pipeline. The MWA data for this project were reduced by F. Kirsten, and the analysis was carried out by myself under the supervision of S. Tremblay, R. Bhat and R. Shannon. The flux density calibration technique and application detailed in this work (which is also used in subsequent chapters) was also developed by myself with significant input from A. Sutinjo and D. Ung regarding the theoretical aspects of the design, and from M. Sokolowski regarding the practical application of the simulation results to the data. R. Shannon provided the nominal Parkes observing and data processing procedure description included in the published article (which I edited to fit into the paper), and I wrote the other sections of the paper. S. Tremblay, R. Bhat and R. Shannon aided in the article writing process by providing guidance in terms of the structure and contextual discussion, both before and after referee comments were received. Additional co-authors for this paper provided comments on the paper drafts and contributed to the planning and execution of the experiment prior to the beginning of my PhD.

I led the proposal and organisational aspect of simultaneous MWA and UTMOST observations of the intermittent pulsar PSR J1107–5907 in 2017 (Chapter 4). The development of the MWA buffered triggering system was led by B. Crosse and A. Williams with input from myself and S. Tremblay in terms of testing and configuration. The corresponding observations with UTMOST were facilitated by C. Flynn, W. Farah and V. Gupta. Archival UTMOST data were retrieved and provided by C. Flynn and V. Gupta, as well as the relevant information required for the UTMOST flux density calculation. I conducted the processing and analysis of both data sets, and wrote the resulting paper, except for the text describing the UTMOST observations and technical details which was initially provided by C. Flynn and V. Gupta (and subsequently altered by me to fit into the paper). S. Tremblay, R. Bhat and R. Shannon provided detailed input on

the scope and structure of the article, S. Murray provided input regarding the fluence distribution analysis and C. Sobey provided ionospheric rotation measure estimates used to correct the observed value. Other co-authors are members of the UTMOST or MWA telescope collaborations, and provided comments on the paper drafts and/or made contributions to the funding, development, management, and maintenance of their respective instrument.

Finally, in Chapter 5, we used the MWA and Parkes radio telescope to simultaneously observe the Rotating Radio Transient J2325–0530. Observations were provided through Director’s Time proposals submitted by myself to both the MWA Director and Parkes time allocation/scheduling manager. I led the analysis of both data sets, and wrote the entirety of the article. Flux density and polarisation calibration advice for the Parkes data was provided by R. Shannon. C. Sobey provided ionospheric rotation measure estimates in order to correct both Parkes and MWA polarimetric profiles. S. Tremblay, R. Bhat, R. Shannon and S. Ord provided initial input into the scope of the analysis, with R. Bhat and R. Shannon providing particular input on the scintillation analysis. Additional co-authors provided comments and helped to shape the final published work, which has been submitted to the Publications of the Astronomical Society of Australia (PASA) journal.



# Chapter 2

## Instruments and Methods

### 2.1 The Murchison Widefield Array

The Murchison Widefield Array (MWA; Tingay et al., 2013) is a low-frequency (80–300 MHz) precursor to the next generation of radio telescopes, specifically the Square Kilometre Array (SKA). It is located at the Murchison Radio-astronomy Observatory (MRO) in Western Australia. Its primary goals are (Bowman et al., 2013): to make a statistical detection of the Epoch of Reionisation (EoR); to survey the Galactic and Extragalactic sky at low radio frequencies; to investigate time-domain astrophysics at centimetre wavelengths (both fast and slow transients), and; to study the Sun, heliosphere and ionosphere. The MWA Phase I was an aperture array imaging interferometer with 128 “tiles”, each approximately  $5\text{ m} \times 5\text{ m}$  and host to 16 dual-polarisation dipole elements in a  $4 \times 4$  grid (dipole centres separated by  $\sim 1.1\text{ m}$  each), as in Figure 2.1. These tiles are distributed pseudo-randomly across the MRO, with maximum baselines of  $\sim 3\text{ km}$  in Phase I. The MWA Phase I tile beam is strongly frequency-dependent and, over the observing frequency range, has a full-width at half-maximum (FWHM) of 62–16 deg, with a resolution element (equivalent to the naturally weighted synthesised beam) of 6–1.5 arcmin.

During the period from late 2016 to early 2017, an additional 128 tiles were



Figure 2.1: An MWA tile at the Murchison Radioastronomy Observatory. The centres of each dipole are equally spaced by  $\approx 1.1$  m over the  $5\text{ m} \times 5\text{ m}$  ground screen (metal mesh), thus the observing element has a physical size of  $\approx 4.4$  m. A total of 256 of these tiles are spread over a 6 km radius area (as of the Phase II upgrade). Credit: N. Hurley-Walker.

deployed at the MRO to form the MWA Phase II upgrade (Wayth et al., 2018). The current MWA software correlator (Ord et al., 2015) only supports the ingest of data from 128 tiles (i.e. 256 signal feeds as there are two polarisations per tile). Therefore, the telescope is periodically reconfigured between two array footprints that each have particular benefits for different science cases (A. Beardsley et al. in prep.). The *compact* configuration, primarily for EoR science, is designed such that the vast majority of connected tiles are within  $\sim 300$  m of the array core. This configuration also purposefully introduced many redundant baselines which are considered to be helpful during calibration procedures (e.g. Wieringa, 1992; Liu et al., 2010), though this remains to be robustly shown in practice (Li et al., 2018). The short baselines provided in this configuration are also preferable for pulsar science in many cases, particularly regarding survey speed, because a decrease in maximum baseline length acts to increase the simultaneous

field of view of the instrument (since the angular resolution of a telescope is proportional to  $1/D$ , where  $D$  is the diameter of the observing element in the case of a tile, and is the maximum baseline length when considering the full array). The *extended* configuration disconnects the majority of the closely-spaced core tiles and instead uses tiles distributed out to a  $\sim 6$  km radius, which allows for sub-arcminute imaging, ideal for extragalactic survey science. This configuration is also acceptable for pulsar science, however the ionospheric effects introduced can lead to reduced “coherence” of the calibration solutions, adversely affecting the quality of the beamformed pulsar data (see Section 2.1.2.2). In Phase II, the tile primary beam width (i.e. the field of view) is unchanged, but the synthesised beam width changes with the array reconfigurations (e.g. the synthesised beam width over the observing frequency band ranges from 55–15 arcmin in the compact configuration, and from 3–0.7 arcmin in the extended configuration).

The details of MWA signal chain are beyond the scope of this thesis, however there are some salient features that affect time-domain astrophysics, especially for pulsar science. The MWA signal chain has two channelisation stages: “coarse” and “fine”. Coarse channels are produced by a polyphase filterbank (PFB) within the receiver enclosures, which receive complex voltages from 8 tiles each, digitise, and channelise the baseband data into 256 “coarse channels”, each 1.28 MHz wide, from 0–327.68 MHz. The second stage feeds 24 user-selected coarse channels into another set of PFBs that further channelise each coarse channel into  $128 \times 10$  kHz “fine channels”. This results in an instantaneous bandwidth of up to 30.72 MHz (for contiguous coarse channel selection). The coarse channels selected need not be adjacent, so it is possible to create 1–24 subbands, spread across the observable frequency range (80–300 MHz). At this stage in the MWA signal path the channelised voltages are usually then sent to the correlator to be averaged and converted into complex visibilities, which capture all the information describing the interferometer response to the sky brightness distribution for individual baselines. Typically, the visibilities are then converted into a sky brightness map (an

image) via a Fourier transform operation<sup>1</sup>. In order to capture the higher time and frequency resolution data required to facilitate pulsar science, we instead record the voltage data to disk before it is sent to the correlator (see Figure 2.2).

### 2.1.1 The MWA Voltage Capture System

The original design for the MWA did not include a way to directly record tile voltages (i.e. after the fine-PFB stage), however, the flexibility of the MWA correlator signal path allows us to retrieve the voltages before they are averaged and converted into visibilities. The Voltage Capture System (VCS; Tremblay et al., 2015) is an alternative telescope mode that does this by recording the channelised, critically sampled voltages (i.e. 10 kHz frequency channels, 100  $\mu$ s time samples) on media conversion servers (henceforth VCS servers), where, in the normal signal chain, the bespoke PFB output data formats are converted for reading by the MWA correlator (this section is highlighted by a dashed box in Figure 2.2). The VCS servers generate  $32 \times 242$  MB files per second from the post-PFB output, totalling  $\sim 7.7$  GB/s ( $\sim 28$  TB/hr). This data rate fills all of the disks ( $\sim 50$  TB) in the VCS servers within  $\sim 100$  minutes.

### 2.1.2 Processing MWA VCS data

Observations using the VCS result in enormous amounts of data, where the typical data rates are  $\sim 28$  TB per hour (truly in the regime of “Big Data”). To process these data in any meaningful sense, we require the resources of high performance computing, including large data storage capabilities. The MWA has a direct fibre-optic connection to the Pawsey Supercomputing Centre in Perth, Western Australia, where data are downloaded from the site, archived and subsequently analysed.

---

<sup>1</sup>Naturally, the process in reality is far more complicated, however that is beyond the scope of this thesis as we do not directly use visibility or imaging data for pulsar science with the MWA.

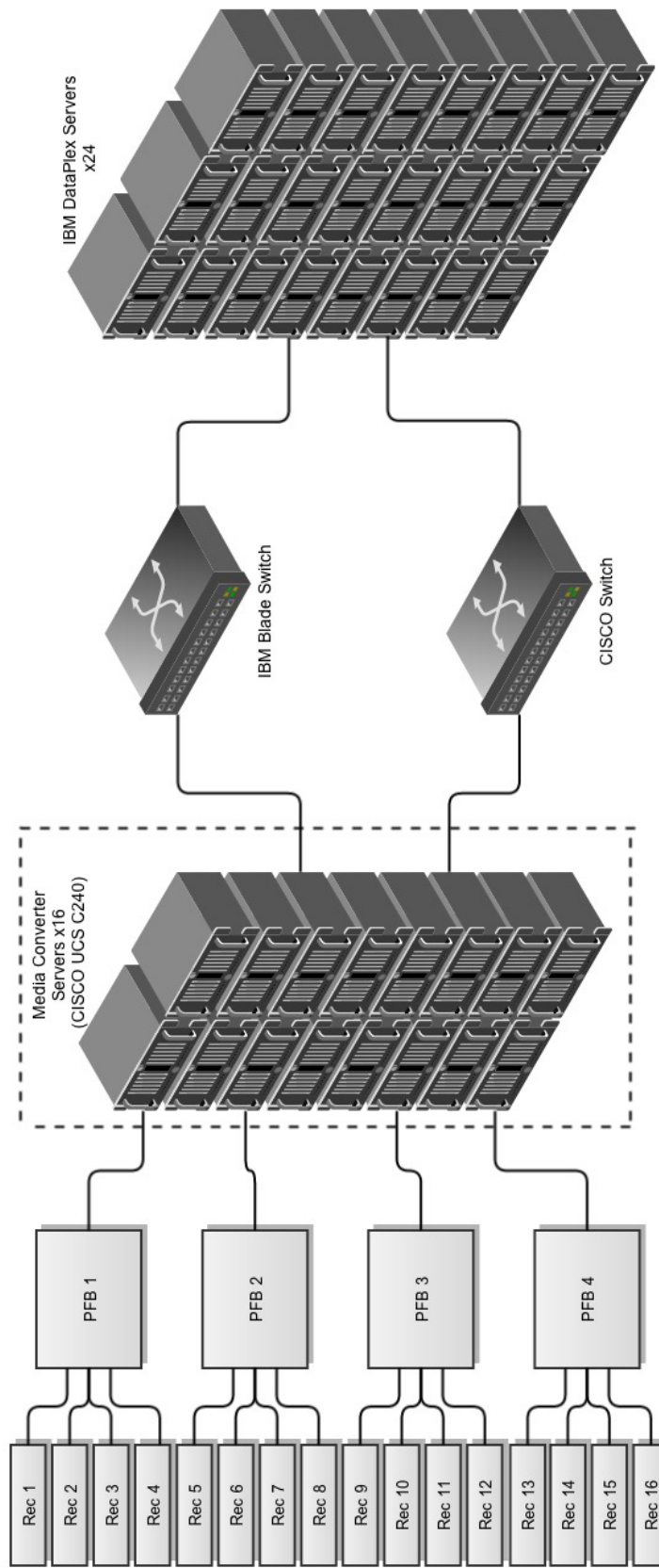


Figure 2.2: A schematic of the nominal MWA signal chain, from the output of the receivers, through the polyphase filter bank channelisation stage, media conversion and correlator. The 16 “Media Converter Servers” normally convert the output of the polyphase filter banks to a format recognised by the software correlator, but are also where the voltages are recorded to disks during high-time resolution observations. Figure from Tremblay et al. (2015).

Processing VCS observations in a reasonable time is also challenging from a software and pipeline perspective. For pulsar science, there are different ways in which we can post-process the recorded voltages to maximise the required science outcome. The different processing procedures are outlined in the following sections (for more details, see Ord et al. (2019)).

### 2.1.2.1 Incoherent summation

To preserve the wide field of view of an MWA tile, one can combine the voltage data “incoherently”. An incoherent summation amounts to calculating the power from each MWA tile and summing them together. Mathematically, we can write this as

$$\mathcal{I}(t, \nu) = \sum_{k=1}^{N_{\text{tile}}} |\mathcal{V}_k(t, \nu)|^2 \quad (2.1)$$

where  $N_{\text{tile}}$  is the number of tiles to be included in the summation and  $\mathcal{V}_k(t, \nu)$  is the voltage sample from the  $k$ th tile at time  $t$  for the channel with centre frequency  $\nu$ . For convenience, we omit the  $t$  and  $\nu$  dependence for the remainder of this section, making it implicit throughout.

In more detail, consider a voltage sample  $\mathcal{V}$  that consists of two polarisation measurements,

$$\mathcal{V} = \begin{bmatrix} v_x \\ v_y \end{bmatrix}. \quad (2.2)$$

The incoherent sum is then

$$\mathcal{I} = \sum_{k=1}^{N_{\text{tile}}} \mathcal{V}_k^\dagger \mathcal{V}_k \equiv \sum_{k=1}^{N_{\text{tile}}} |\mathcal{V}_k|^2 = \sum_{k=1}^{N_{\text{tile}}} (|v_{x,k}|^2 + |v_{y,k}|^2), \quad (2.3)$$

where  $\mathcal{V}_k^\dagger$  is the conjugate transpose of  $\mathcal{V}_k$ . This acts to increase the sensitivity over that of an individual tile by a factor  $\sqrt{N_{\text{tile}}}$ . The detected incoherent beam is then written to a PSRFITS format (Hotan et al., 2004) file for further post-processing and analysis by standard pulsar software packages.

An incoherent sum is a computationally inexpensive operation and thus pro-

vides a quickly producible, reasonably sensitive data set to search for pulsars over a large fraction of the visible sky in a relatively small amount of observing time (e.g. Xue et al., 2017). It is unfortunately prone to corruption due to RFI, even at the MRO which is an exceptionally radio quiet zone. As the dipole elements of each tile essentially see the entire sky (horizon to horizon), bright RFI can still negatively affect the data quality. These problems can sometimes be reduced when searching for pulsars as the RFI may only corrupt dispersion measure trials where  $DM \sim 0 \text{ pc cm}^{-3}$  (i.e. terrestrial signals). It is still necessary to conduct careful examination of data for RFI even in the dedispersed data, since time-dependant RFI in distinct frequency channels can conspire to mimic high-DM (i.e. non-zero DM) signals. This is especially true when searching for single pulses. It is, therefore, important to note that dedispersion does not necessarily completely remove the effects of RFI, especially if the interference is bright or the pulsar has a low DM, since the RFI can leak through into many non-zero DM trials (often tens of DM units in the case of the MWA).

### 2.1.2.2 Coherent summation

To further increase sensitivity, we can instead coherently sum the tile voltages. This process amounts to applying a phase correction to the complex voltages on a per-tile basis, summing voltages of all tiles and computing the power. Mathematically, we can write the coherent voltage beam as

$$\mathcal{C}(t, \nu) = \sum_{k=1}^{N_{\text{tile}}} \mathcal{V}_k(t, \nu) e^{-i\phi_k(t, \nu)}, \quad (2.4)$$

where  $\phi_k(t, \nu)$  is a phase introduced to point the beam in the desired direction. As in Section 2.1.2.1, we omit the  $t$  and  $\nu$  dependence for convenience in the remainder of the section.

In more detail, the coherent voltage beam is

$$\mathcal{C}_k = J_k^{-1}(\nu) W_k(\tau, \nu) \mathcal{V}_k = \begin{bmatrix} c_{x,k} \\ c_{y,k} \end{bmatrix}, \quad (2.5)$$

$$\mathcal{C} = \sum_{k=1}^{N_{\text{tile}}} \mathcal{C}_k = \begin{bmatrix} c_x \\ c_y \end{bmatrix}, \quad (2.6)$$

where  $J_k^{-1}(\nu)$  is the appropriate inverse Jones matrix for the relevant coarse channel and  $W_k(\tau, \nu)$  is a complex weighting matrix that is frequency dependent and recomputed on a time scale of  $\tau$  seconds to ensure the desired target is tracked appropriately with the synthesised beam. The Jones matrices,  $J_k$ , are calculated via the Real Time System (RTS) calibration software, which was designed specifically for the MWA (Mitchell et al., 2008), and are fully polarimetric (i.e. they capture the response of both  $x$  and  $y$  polarisations of the tiles). The combination of  $J_k$  and  $W_k$  acting on the voltage samples effectively constitutes the  $e^{-i\phi_k}$  phase turn in eq. (2.4). Given that  $W_k$  is re-calculated every  $\tau$  seconds, this means that all voltage samples within  $\tau$  seconds<sup>2</sup> are rotated by the same amount per frequency channel. In terms of eq. (2.4), the phase term is modified such that  $e^{-i\phi_k(t,\nu)} \Rightarrow e^{-i\phi_k(\tau,\nu)}$ . Ultimately, eqs. (2.5) and (2.6) act to minimise the difference between the computed sky model from the RTS (the calibration solution) and the data by applying tile and frequency dependent phase corrections to every sample.

The noise in each polarisation associated with this voltage beam is then

$$n_{\mathcal{C}} = \sum_{k=1}^{N_{\text{tile}}} \mathcal{C}_k \mathcal{C}_k^\dagger = \begin{bmatrix} n_{xx} & n_{xy} \\ n_{yx} & n_{yy} \end{bmatrix} \quad (2.7)$$

where  $\mathcal{C}_k^\dagger$  is the conjugate transpose of  $\mathcal{C}_k$ , the matrix components  $n_{xx}$  and  $n_{yy}$

---

<sup>2</sup>Currently,  $\tau = 1$  s, thus the same weights are applied to  $10000 \times 100 \mu\text{s}$ , but  $\tau$  can be changed arbitrarily so the weights can be calculated on any time scale that is an integer multiple of the  $100 \mu\text{s}$  sample time.

are real valued, and  $n_{xy} = n_{yx}$ . Through this process, we theoretically gain an additional factor of  $\sqrt{N_{\text{tile}}}$  over the incoherent sum (i.e. collectively a factor of  $N_{\text{tile}}$  more than a single MWA tile). As a consequence, we lose the wide field of view provided by the incoherent sum, and instead have data from a single “pixel” on the sky, where that pixel is effectively a synthesised MWA beam.

The voltage beam  $\mathcal{C}$  is then converted into Stokes parameters (e.g. McMaster, 1954, 1961) via

$$I = \frac{1}{N_{\text{tile}}} \left[ (|c_x|^2 - n_{xx}) + (|c_y|^2 - n_{yy}) \right], \quad (2.8)$$

$$Q = \frac{1}{N_{\text{tile}}} \left[ (|c_x|^2 - n_{xx}) - (|c_y|^2 - n_{yy}) \right], \quad (2.9)$$

$$U = 2\text{Re} \left[ \frac{1}{N_{\text{tile}}} \left( c_x c_y^* - n_{xy} \right) \right], \quad (2.10)$$

$$V = -2\text{Im} \left[ \frac{1}{N_{\text{tile}}} \left( c_x c_y^* - n_{xy} \right) \right], \quad (2.11)$$

where  $c^*$  is the complex conjugate of  $c$ . Once in this form, the data are considered “detected”. The detected Stokes parameters can then be written to a PSRFITS file, which is equivalent in format to the incoherent sum output (but  $4\times$  larger given that the incoherent sum is Stokes  $I$  only). The coherent beamforming process is described in detail by Ord et al. (2019).

An important aspect which we have so far ignored is the effect of the ionosphere, both in terms of the calibration and beamforming process. The RTS solutions used in the beamformer software correct for the bulk ionospheric positional shifts (which is important when calculating the correct delay to add in eq. 2.5), however the small scale turbulence is not corrected in the pipeline. This is one reason why the coherent beamformed data do not usually reach the theoretically expected signal-to-noise ratio. Furthermore, the ionosphere is capable of drastically changing the polarisation signatures of sources, and consequently their rotation measures. This effect can be corrected in post-processing by using a model of the Earth’s ionosphere and magnetic field (e.g. Hernández-Pajares

et al., 2009; Thébault et al., 2015) to estimate how the ionosphere has affected the polarisation properties of the source given the line of sight (e.g. the IONFR software package is able to do this; Sotomayor-Beltran et al., 2013). In Xue et al. (2019) we conducted an in-depth analysis of these effects, specifically focusing on the stability and reliability of MWA-VCS polarisation. We found that generally speaking the polarimetry is good, assuming an appropriate calibration source was chosen (i.e. nearby on the sky and within a few hours of the target observations).

Finally, a modified version of the beamforming software allows for the complex voltage beam to be written as a VDIF<sup>3</sup> file. This output is created only on user-request and requires several further operations within the beamforming software. Briefly, the software re-synthesises the 1.28 MHz coarse channel data by inverting the hardware implementation of the fine (second stage) PFB. This additional inversion step is a compute-intensive operation, but it allows for coherent dedispersion of the re-synthesised 1.28 MHz channels, effectively giving arbitrary time resolution (up to the 1.28 MHz sampling rate, which corresponds to a time resolution of  $\approx 0.78125 \mu\text{s}$ ). Currently, this mode is still being tested, though preliminary results seem promising, especially for millisecond pulsar work (Kaur et al., 2019).

### 2.1.3 Flux density calibration of VCS data

Flux density calibrating an aperture array is a non-trivial activity. For the MWA, this is particularly true for VCS data. An estimated scaling can be applied by using a reliable Global Sky Model (GSM; e.g. Haslam et al., 1981, 1982; de Oliveira-Costa et al., 2008; Zheng et al., 2017; Dowell et al., 2017) and a model of the instrument beam response (beam pattern). We are able to simulate the incoherent and coherent beam response. The MWA beam pattern for an individual tile beam (see e.g. Sutinjo et al., 2015; Sokolowski et al., 2017) is the beam response expected for the incoherent sum procedure explained in the previ-

---

<sup>3</sup>See <http://www.vlbi.org/vdif/> for format definitions.

ous section. The computation for the coherent (tied-array) beam is significantly more expensive, particularly due to the scale of the structures being simulated:  $\sim 1$  deg scales for the tile beam, but  $\lesssim 0.01$  deg for the tied-array beam. This is even more of an issue for MWA Phase II extended configuration data. It is now possible to create these coherently summed beam patterns which are effectively equivalent to the naturally weighted synthesised beam of the MWA. For details, see Appendix B.

### 2.1.3.1 Applying the solutions

A detailed summary of the application of the simulation outputs to real data is given in the publication included in Chapter 3 (Sections 3.4.2.2 and 3.4.2.3). Here we provide an abridged version.

The tied-array beam simulations assume perfect coherency (i.e.  $\sqrt{N_{\text{co}}}$  improvement in sensitivity, for  $N_{\text{co}}$  tiles used to form the coherent beam). In reality this is never true, thus, we compensate by applying another scaling factor that accounts for the real versus expected improvement, which we call a “coherency factor”, denoted  $f_c$ . The coherency factor is determined by evaluating

$$f_c = \sqrt{N_{\text{co}}} \left( \frac{(\text{S/N})_{\text{co}}}{(\text{S/N})_{\text{inco}}} \right)^{-1}, \quad (2.12)$$

where  $(\text{S/N})_{\text{co}}$  is the signal-to-noise ratio of a bright pulse in the coherently beamformed data and  $(\text{S/N})_{\text{inco}}$  is the signal-to-noise ratio of the same pulse in the incoherently summed data.

The system temperature and gain calculations from the simulations are used to convert the voltage time series data from arbitrary power units to flux density units by

$$S = (\text{S/N}) \times \frac{f_c T_{\text{sys}}}{G \sqrt{n \Delta \nu \Delta t}}, \quad (2.13)$$

where  $\text{S/N}$  is the sample signal-to-noise ratio,  $f_c$  is the coherency factor as in eq. (2.12),  $n$  is the number of polarisations summed (for the MWA,  $n = 2$ ),  $\Delta \nu$

is the observing bandwidth,  $\Delta t$  is the sample integration time, and  $S$  is the flux density in Jy.

### 2.1.3.2 Polarisation calibration

For incoherently summed data, polarisation estimation for a pulsar is nonsensical, as the field of view is so large that the instrumental polarisation response will drastically change across as a function of sky position and will be a combination of all sources within the field. Attempting to then assign accurate polarisation characteristics to a point source within that field of view is infeasible.

In the case of coherently summed data, we are able to directly form the Stokes parameters during the beamforming process (see Section 2.1.2.2). Theoretically, we then need only to account for the instrumental polarisation and can then apply the same solutions from the Stokes  $I$  data. To first order, this will provide us with polarised flux density measurements for the target object.

The critical assumption is that we understand our instrumental polarisation response well, though in reality this is not necessarily true. Preliminary analysis for the internal stability of the polarisation response (Xue et al., 2019) clearly indicates changes that significantly depend on several factors, including frequency, pointing direction (i.e. azimuth and elevation), and to a lesser extent the target object position relative to calibrator object position. Additionally, external checks with other low-frequency telescopes (e.g. LOFAR) to vet the absolute polarisation calibration are under way by observing common-sky pulsars (Tremblay et al. in prep.). Furthermore, the ionosphere can also cause large discrepancies in the observed polarisation properties. Given that the rotation measure scales with the square of the observing wavelength (i.e.  $\lambda^2$ ), this causes significant Faraday rotation of the polarised radiation (e.g. Noutsos et al., 2008; Han et al., 2018).

For the analysis herein we are generally only interested in the Stokes  $I$  emission, thus did not conduct any rigorous polarimetric calibration.

## 2.2 The Parkes radio telescope

The Parkes radio telescope is a premiere Australian radio astronomy instrument with a wide variety of science capabilities, not least the study of pulsars. The telescope is a 64-m fully-steerable “classical” paraboloid dish, able to point between 0–360 deg in azimuth, and between  $\sim 30$ –89 deg in elevation. Parkes hosts a large fleet of receivers and backends<sup>4</sup>, including high time resolution modes ideal for pulsar science. The observable bands depend on the receiver in place, but ranges from 0.7–22 GHz, where the system temperature is typically between 20–150 K, and the gain between 1–2 K Jy<sup>-1</sup>.

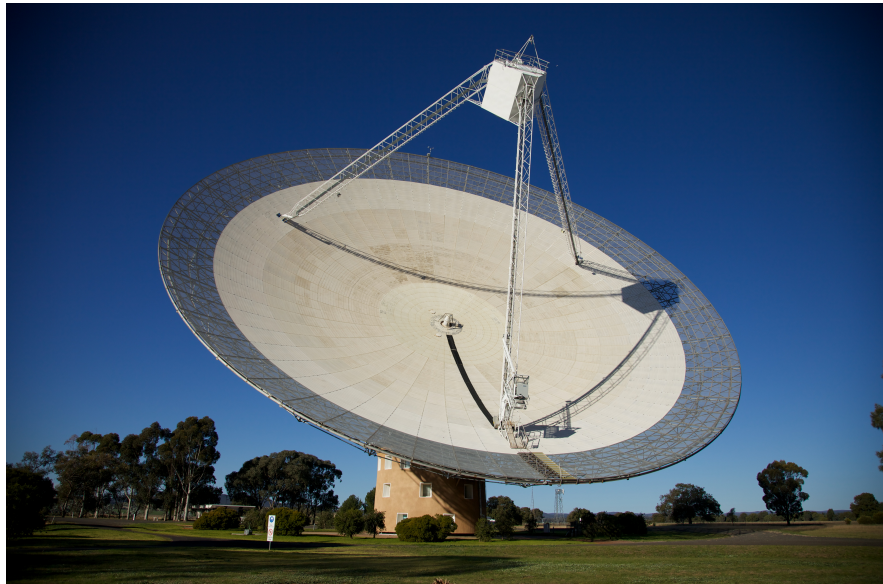


Figure 2.3: The Parkes radio telescope. A textbook example of a radio telescope, the dish is 64 m in diameter and, in combination with its receiver fleet and signal processing backend, is a world-renowned pulsar finding machine. Credit: E. Lenc (SIfA).

The majority of Parkes digital backends allow some level of pulsar observation capability. These backends can provide either: baseband data that is coherently dedispersed online (for maximum time resolution and complete removal of dispersive effects); or what is commonly called *search mode* data, which is effectively a

---

<sup>4</sup>For details, please see the Parkes user’s guide here: [http://www.parkes.atnf.csiro.au/observing/documentation/user\\_guide/pks\\_ug.html](http://www.parkes.atnf.csiro.au/observing/documentation/user_guide/pks_ug.html)

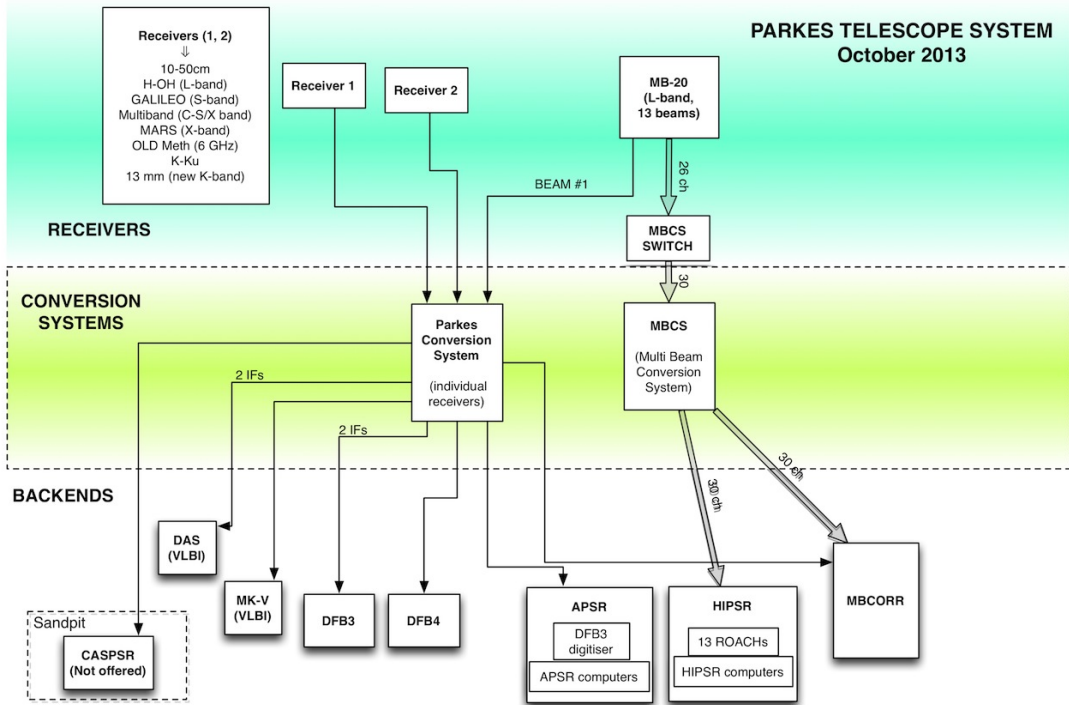


Figure 2.4: An overview of the Parkes observing system (prior to the installation and commissioning of the Ultra-Wide-Band receiver in late 2018, which began operations in 2019). Credit: CSIRO, Parkes User Guide.

channelised filter bank data stream that is then processed offline.

In the context of this thesis, we make use of the Digital Filter Bank Mark III and IV (DFB3 and DFB4, respectively) and the HI-Pulsar (HIPS; Price et al., 2016) digital signal processing system, particularly the high time resolution pulsar modes. The receivers of interest are: the so-called “1050cm” receiver, a dual-band coaxial receiver with centre frequencies 732 and 3100 MHz, and the Multibeam receiver, which records data from its 13 beams simultaneously at a centre frequency of  $\sim 1.4$  GHz (Staveley-Smith et al., 1996). A general overview of the Parkes observing and signal chain is shown in Figure 2.4. A new Ultra-Wide-Band receiver and backend digital system (called “Medusa”), which records and processes data over a contiguous frequency range of  $\sim 700\text{--}4000$  MHz, has recently been installed at Parkes, and will take over from the legacy 1050cm receiver and PDFB backends from 2019.

### 2.2.1 Flux density and polarisation calibration

Parkes is a well understood telescope and can be calibrated in terms of flux and polarisation in a textbook manner (see e.g. Lorimer & Kramer, 2004 for details in the pulsar context). Flux density calibration is typically achieved by observing Hydra A (3C 218), as described in Manchester et al. (2013). Briefly, Hydra A is assumed to have a flux density of 43.1 Jy at 1.4 GHz with a spectral index of  $\alpha = -0.91$  over the nominal observing frequency range. The calibration scans are taken (typically) once per observing session and consist of five individual 2-minute observations as follows: off-source (north), on-source, off-source (south), on-source, off-source (north). These scans are then combined and converted into calibration solutions for each frequency band, using tools in the PSRCHIVE software suite (see e.g. Hotan et al., 2004; van Straten et al., 2012 for examples).

Polarisation calibration is conducted by injecting a calibrated, 100% linearly polarised signal into the system, which allows accurate measurement of the differential gain and phase of the receiver feeds as a function of frequency (i.e. across the observing bandwidth). This also provides the ability to measure and correct for the cross-coupling of the two orthogonal polarised receptors, and their relative positions with respect to the telescope axis (van Straten, 2004, 2006).

## 2.3 The Molonglo Observatory Synthesis Telescope

The recently refurbished Molonglo Observatory Synthesis Telescope (UTMOST, Bailes et al., 2017) is an East-West aligned cylindrical paraboloid located  $\sim 40$  km east of Canberra, Australia. UTMOST has an effective collecting area of  $18000\text{ m}^2$  and operates between 820–850 MHz, observing only a single polarisation (right-hand circular, according to the PSR/IEEE standard). The telescope has a highly elliptical beam pattern due to it being a linear array in only one direction.

Prior to the recent upgrade, the telescope was prolific in the early years of

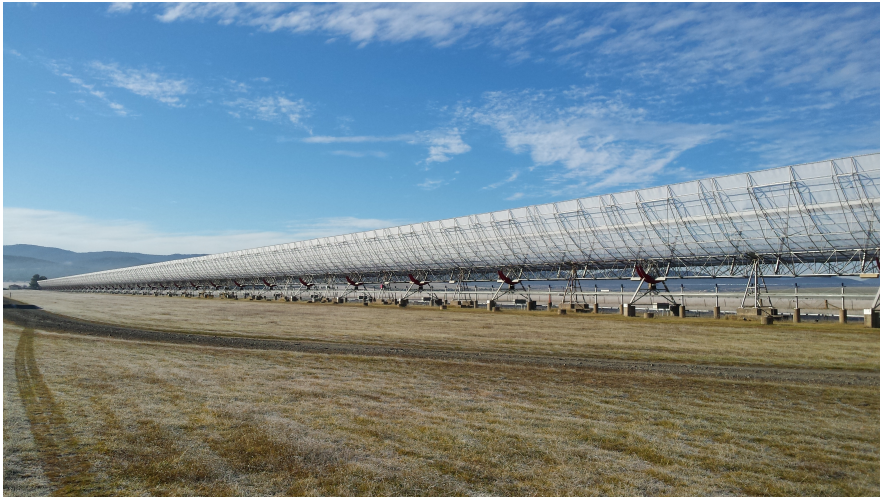


Figure 2.5: The Molonglo Observatory Synthesis Telescope (owned by the University of Sydney), a 12-m wide cylindrical paraboloid telescope, looking along the East-West arm which is  $\sim 1.5$  km long. Credit: Swinburne University of Technology.

pulsars (e.g. Large et al., 1968; Manchester et al., 1978), produced a number of important southern sky survey catalogues (e.g. the Sydney University Molonglo Sky Survey, Bock et al., 1999; Mauch et al., 2003), and was instrumental in rapid radio follow-up observations of transients (e.g. the detection of prompt radio emission from supernova SN1987A, Turtle et al., 1987).

UTMOST is now a fixed transit instrument that has been transformed into a pulsar and fast radio burst machine. The hardware is being updated, with the East-West arm upgrade now complete, and the North-South arm upgrade proceeding rapidly, but the biggest improvement in terms of the ability to detect pulsars and other radio transient is the new backend infrastructure. Details are given by Bailes et al. (2017), thus here we only summarise some of the most important aspects.

The backend is a fully automated pipeline that can be operated in several different modes depending on the science requirement. For our purposes, we are interested in the high time resolution “pulsar” mode. In this mode, UTMOST processes voltages from the telescope in real time on multiple GPU nodes and records decimated data products, including diagnostic plots, folded profiles and

pulse stacks. If required, it is also possible to keep the filterbank data at a higher time and frequency resolution ( $327\,\mu\text{s}$ , 97 kHz), which aids in single-pulse studies. The pipeline is able to monitor and process multiple targets (typically pulsars) simultaneously within the relatively wide field of view and does so continuously. This ability allows UTMOST to accurately and regularly time many pulsars (Jankowski et al., 2018a), which has meant that the telescope was able to detect several pulsar glitches (e.g. Jankowski et al., 2015, 2016, 2017). It also concurrently conducts a FRB search which has resulted in 9 discoveries to date, including the first interferometric detection (Caleb et al., 2016, 2017), and the first FRB seen at very high time resolution allowing analysis of micro-structure within the burst (Farah et al., 2018).

### 2.3.1 Flux density calibration

The MOST consists of 352 elements, known as “modules”, and the performance of these modules varies with time. These variations are regularly monitored as part of the standard operation of the telescope on a daily basis and therefore allows the full system performance to be characterised. The system equivalent flux density is measured regularly by observing a sample of bright pulsars with well-defined flux densities (Jankowski et al., 2018b). From these measurements, the gain and system temperature are extracted.

The UTMOST system measures only a single circular polarisation (IEEE right-hand circular) between 820–850 MHz. This means extra care must be taken when computing the flux density scale, especially if the target sources are polarised, which is often true for pulsars. When measuring the system parameters using pulsars, it is assumed that they are unpolarised<sup>5</sup>, thus there is a polarisation compensation factor implicit within those measurements. This acts to effectively ensure that, when converted from S/N to flux densities, the resulting scale is the total intensity (Stoke  $I$ ). It is important to note that the pulsars used to create

---

<sup>5</sup>While this is not necessarily true for all pulsars, the targets used for this calibration are preferentially selected to have very low polarisation fractions.

the flux density scale are not well measured in the UTMOST band, though the overlap with the recently commissioned Ultra-Wide-Band receiver (0.7–4 GHz) at Parkes will help with comparative testing.

The system performance and therefore ability to calibrate accurately has improved with the hardware upgrades. The uncertainty in flux density measurements is  $\sim 30\%$ . Additional details, particularly regarding the work in Chapter 4 and how to correct flux densities for moderately to highly polarised pulsars, can be found in Appendix C.

## 2.4 Multi-telescope considerations

Using multiple telescopes simultaneously always comes with logistical and technical challenges. At some point throughout this work, all four telescopes described above are used, sometimes simultaneously. Given the significant differences between telescope operation, data analysis and calibration procedures, it is worth noting some of the difficulties encountered. Using data from these telescopes together means dealing both with the individual challenges and the added complexity of ensuring consistency between the instruments. In terms of pulsar data, the major issue is typically timing offsets (e.g. difference in the observatory clock, errors/inaccuracies in time stamps and metadata, etc.), which can be solved by using, for instance, correlation analysis or more standard pulsar timing techniques.

### 2.4.1 Calibration and RFI considerations

The Parkes radio telescope is a well-calibrated instrument and a national facility, thus from a data-user perspective, the pulsar data analysis and calibration procedures are straightforward. There is a documented standard procedure for pre-processing and calibration (both flux density and polarisation) of pulsar data that for all but the most specific science cases is sufficient (see e.g. van Straten

et al., 2012). One of the difficulties in working with Parkes data is the RFI environment, which has become more severe over recent years, particularly due to digital television and new mobile network systems. This RFI environment often requires the excision of a large fraction of the observed bandwidth, and consists of constant and time-variable interference sources<sup>6</sup>.

As with Parkes, the RFI environment around UTMOST is also relatively contaminated, with the most sensitive part of the observing band (around 840 MHz) often requiring sophisticated amelioration techniques to mitigate or remove signals from nearby mobile network activity. In order to reduce the impact of RFI on UTMOST data, the mitigation method is to evaluate the spectral kurtosis of the voltage streams on a per-module basis and to then replace those samples that deviate significantly from Gaussianity (within a reasonable threshold) with random noise generated with the same statistics as the uncorrupted data (Bailes et al., 2017). An additional complexity to using UTMOST is that the telescope only samples a single polarisation (PSR/IEEE right-hand circular; see e.g. van Straten et al., 2010), which means flux density and polarisation calibration is difficult (see Appendix C). More than the single polarisation sampling, the large number (352) of antenna modules have widely varying sensitivities (usually a factor of 10 or more between the best and worst performing modules). This level of inhomogeneity in the basic observing elements of an array is unusual and difficult to correct. The telescope is also a transit instrument (i.e. it does not point in an East-West directions, but can point in the North-South direction) so, in general, the best case scenario will be that a source stays within the UTMOST primary beam for  $\sim 30$  min.

The RFI environment for the MWA is extremely clean in general, owing to its radio quiet location. For VCS data we nominally flag edge channels in every coarse channel to avoid the non-trivial effects of aliasing, which can reduce the

---

<sup>6</sup>A compendium of various studies conducted to examine the RFI environment surrounding Parkes can be found here: [http://www.parkes.atnf.csiro.au/observing/rfi/parkes\\_rfi\\_studies.html](http://www.parkes.atnf.csiro.au/observing/rfi/parkes_rfi_studies.html)

usable effective bandwidth by  $\sim 30\%$  when employing a particularly brutal flagging scheme. The MWA high-time resolution capabilities enabled by the VCS are continually evolving, primarily in terms of software capability and efficiency. The pulsar data processing pipeline is steadily maturing, with the capability to estimate flux densities (using simulations of the tied-array beam pattern; see Appendix B) and, in the near-future, low-frequency polarimetric measurements of pulsars. The major processing bottleneck (“the beamformer”; see Section 2.1.2) has recently been GPU-accelerated, making the process more efficient. There is scope for further improvements such as simultaneous multi-directional beam-forming and a more optimised usage of GPU resources (particularly in high-performance computing environments).

## 2.5 General pulsar data processing

Typically, there are a number of steps after beamforming and/or pre-processing of the telescope data required to examine the pulsar emission and its properties. This includes removal/mitigation of RFI, correcting for propagation effects and dissecting the time series data.

### 2.5.1 Pulsar ephemerides

The parameters that define the rotation of the pulsar and characterise the ISM propagation effects along the line-of-sight (via DM and RM measurements, for example) are kept in an ephemeris. General parameters include the pulsar period and period derivatives, Right Ascension and Declination, dispersion measure, rotation measure, and important reference times (such as when quantities were measured or when rotational glitches occurred). For binary pulsar systems, additional parameters such as the orbital eccentricity, orbital period and projected semi-major axis are included. In combination, the parameters within an ephemeris model the rotation of the pulsar with a high degree of precision.

## 2.5.2 De-dispersion

One of the first steps in processing pulsar data is to remove the effects of the ISM. As detailed in Section 1.3.1, a pulsar signal is dispersed when travelling through the ISM, causing the higher frequency components arrives earlier than the corresponding low frequency components. This acts to smear the emission in time, creating a parabolic sweep in frequency (see Figure 1.5). This can be corrected by processing the time series data different ways, depending on how the data was recorded.

If the data are pre-channelised, where there is an individual time series for each channel, then we “incoherently dedisperse” the data. This involves calculating the appropriate dispersion delays using eq. (1.13) for *every* channel, and shifting the samples in that channel by the calculated amount. Figure 2.6 depicts this process. Ultimately, as the dispersion delay across the individual channels is not corrected, this is an approximate correction. This approximation is such that, due to the finite channel widths, the resulting signal is smeared by an amount that is proportional to the DM. While narrower channels alleviate this smearing, it is always the case that for any given DM and channel width there will be a limit to how narrow a pulse will appear (consider eq. (1.13) where the upper and lower frequencies are the channel edges).

If, on the other hand, the data is in the form of a voltage stream (i.e. no channelisation has occurred), then we can “coherently dedisperse” the data. This involves applying the inverse of a phase-only filter (transfer function) to the voltage stream which completely removes the effects of dispersion (Hankins, 1971; Hankins & Rickett, 1975; see also Section 5.3 of Lorimer & Kramer, 2004). In principle, coherent dedispersion works as follows. We record the voltage  $V(t)$  at a centre frequency  $\nu_0$ , which is a combination of the intrinsically emitted voltage  $V_{\text{int}}(t)$  and ISM effects (i.e. dispersion). We can describe this interaction in Fourier space as

$$\hat{V}(\nu_0 + \nu) = \hat{V}_{\text{int}}(\nu_0 + \nu)H(\nu_0 + \nu),$$

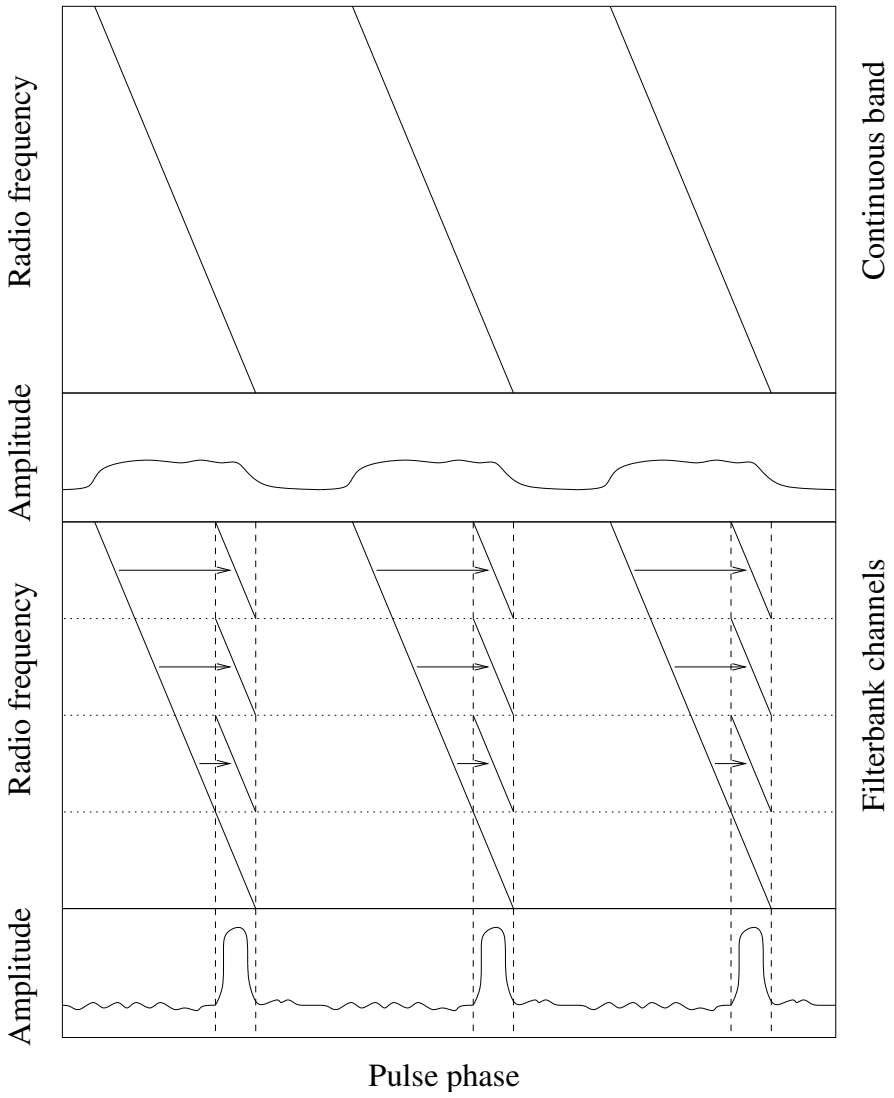


Figure 2.6: The incoherent dedispersion process, where each frequency channel is bulk-shifted an amount equal to the corresponding dispersion delay. This does not remove the dispersion delay across the channels. Credit: Lorimer & Kramer (2004), thanks to D. Lorimer for providing a publication quality figure.

where  $\hat{V}(\nu) = \mathcal{F}(V(t))$  is the Fourier transform of the raw voltage time series.

The transfer function,  $H$ , is defined as

$$H(\nu_0 + \nu) = \exp \left[ +i \frac{2\pi \mathcal{D} \nu^2}{(\nu_0 + \nu) \nu_0^2} \times \text{DM} \right], \quad (2.14)$$

where  $\mathcal{D} = e^2/(8\pi^2 c \epsilon_0 m_e) \approx 4.148808 \times 10^3 \text{ MHz}^2 \text{ pc}^{-1} \text{ cm}^3 \text{ s}$  is the dispersion constant and  $\nu_0$  is the centre frequency of the signal. It is then possible to recover

the intrinsic voltages by evaluating

$$V_{\text{int}}(t) = \mathcal{F}^{-1} \left( \hat{V} H^{-1} \right),$$

where  $\mathcal{F}^{-1}$  is the inverse Fourier transform operator. The implementation of coherent dedispersion in software can vary slightly, but is generally approached as described above (see e.g. van Straten & Bailes, 2011). At this stage, the signal can be channelised and will have no residual dispersion delays present (assuming the DM is known exactly).

### 2.5.3 Sub-integrations and folding

Once the effects of dispersion have been removed from the time series, the next stage is to dissect the time series into a number of “sub-integrations”. These sub-integrations can consist of any number of pulsar rotations, or indeed any arbitrary time up to the total time series length. This subset of data is typically created using an ephemeris (see Section 2.5.1), and is thus cyclic on the pulsar period (see Section 2.6 of van Straten & Bailes (2011) for a mathematical description of “folding” in the context of pulsar data).

Combining many of these sub-integrations, or constructing only one sub-integration from the entire time series, results in a time-integrated emission profile. One can also average across all frequency channels and polarisations to create what is commonly referred to as the “folded profile”. While the emission from the pulsar changes with time (i.e. any individual pulse will be unique), the folded profile is typically very stable if enough pulses have been averaged (typically thousands of pulses must be averaged to attain profile stability). There are exceptions to this assumption in reality, as described in Sections 1.5–1.8.

Creating sub-integrations which are of length equal to the pulsar period provides a more in-depth look at the emission at the cost of creating far more data products (e.g. a 1 hr observation of a 30 ms pulsar would create 120000 single-

pulse sub-integrations). The ability to observe the emission for every pulsar rotation is extremely powerful and can often reveal features of the emission that are obscured when inspecting the folded profile. The single pulses can be averaged to recover the folded profile using the information in the ephemeris.

### 2.5.4 Software

Sophisticated software is employed to process the time series data as described above, and these tools were used to perform a significant amount of the post-processing analysis. The following sections describe the primary software packages and associated tools, and the basic applications relevant to this thesis.

#### 2.5.4.1 DSPSR

The Digital Signal Processing Software for Pulsar Astronomy, hereafter DSPSR, was originally designed to reduce the data recorded by the ATNF Parkes Swinburne Recorder (APSR), which produced baseband data over a relatively large bandwidth in real-time. Since the initial development, the DSPSR software has evolved significantly, and is now a widely used pulsar processing software package (see van Straten & Bailes, 2011 for the software description), in both real-time (online) and offline processing regimes.

DSPSR is used in this thesis to reduce the post-beamformer data into sub-integrations, while correctly accounting for the pulsar rotation models and removing the dispersion caused by the ISM. In particular, DSPSR provides the ability to create single-pulse sub-integrations, which are vital when comparing simultaneously recorded data at different telescopes and frequencies.

A typical DSPSR command to reduce a MWA data set into single pulse time series would resemble:

---

```
dspsr -E ephem.par -K -s -b 128 data.fits
```

---

From left to right, the above command line options specify the following behaviour:

- **-E `ephem.par`:** read the required pulsar parameters (e.g. spin period, DM, position, etc.) to create a rotation model from the file named `ephem.par`
- **-K:** remove the dispersion delay between channels (inter-channel delays)
- **-s:** make single-pulse sub-integrations (time series) and store in separate files on disk (by default, these files are named `pulse_N.ar`, where `N` is the corresponding rotation number since the reference date as read from the ephemeris file, assuming the constructed model)
- **-b 128:** ensure each sub-integration has 128 time samples<sup>7</sup> (i.e. each sample will be 1/128th of the pulsar period)
- **data.fits:** read the raw data from `data.fits`

After processing in this way, a number of multi-dimensional data containers, colloquially called “archives”, are produced (with the file name suffix `.ar`), which contain time, frequency, polarisation and other auxiliary information regarding the processed data properties. These archives are highly structured and contain a relatively large amount of metadata on top of the processed time series data. A description of the archive file format can be found online<sup>8</sup> as part of the PSRCHIVE software suite.

#### 2.5.4.2 PSRCHIVE

PSRCHIVE is a set of software applications designed for the analysis of pulsar data (Hotan et al., 2004; van Straten et al., 2012). This suite includes routines

---

<sup>7</sup>This will often require resampling of the input data, as the data time resolution will almost never divide evenly into the pulsar rotation period.

<sup>8</sup><http://psrrchive.sourceforge.net/tutorial/structure.shtml>

that interact with the archives created by DSPSR and modify them where appropriate (e.g. when calibrating polarisation or flux density, removing RFI, searching for single-pulse events, etc.), as well as providing general visualisation capabilities.

The most commonly used routines in this thesis are designed to remove RFI, perform averaging over time/frequency/polarisation, search for pulses within the time series, or write the contents of an archive to a more easily accessible format (e.g. ASCII text). Examples of these commands are included below.

## RFI mitigation

To remove/mitigate RFI from the data housed in the archives, we use the **paz** routine. A typical example for MWA data would be:

---

```
paz -r -k edgechans.txt -e .zap example.ar
```

---

The above command line specifies the following behaviour:

- **-r**: perform a median smoothed difference filtering algorithm to excise RFI in time and frequency
- **-k edgechannels.txt**: zero-weight the frequency channels corresponding to those listed in **edgechannels.txt** (which is a single column, one channel number per line)
- **-e .zap**: after flagging the required channels/sub-integrations, write the output to a copy of the original archive and replace the suffix with **.zap**
- **example.ar**: the archive to process

After which, if additional RFI removal is required, the interactive tool **pazi**<sup>9</sup>.

---

<sup>9</sup><http://psrchive.sourceforge.net/manuals/pazi/>; also **psrzap**, which is a newer/updated version of **pazi**, with very similar interactions, can be used.

## Time, frequency, and polarisation averaging

To average in time/frequency/polarisation we use the `pam` routine. In the case of polarisation, there can be multiple different representations of polarisation information, but generally these are stored as Stokes parameters ( $I$ ,  $Q$ ,  $U$ , and  $V$ ). When we say “average in polarisation” what is actually meant is that only the total power  $I$  is kept. A typical example for MWA data would be:

---

```
pam -F -T -p -e .ftp example.ar
```

---

The above command line specifies the following behaviour:

- `-F`: average over all frequency channels
- `-T`: average over all sub-integrations (time)
- `-p`: average over all polarisations
- `-e .ftp`: write the output to a copy of the input file, but replace the suffix with `.ftp`
- `example.ar`: the archive to process

## Searching for single pulse events

To perform a single-pulse search, we can use the `psrspa` routine. A typical example, assuming that single-pulse archives have been created and that they have been averaged in frequency and polarisation, would be:

---

```
psrspa -a above:threshold=6 -N 127 -e 6sigma *.ar
```

---

The above command line specifies the following behaviour:

- `-a above:threshold=6`: select the algorithm<sup>10</sup> to search for peaks above 6

<sup>10</sup>See the help text produced by `psrspa -help=a` for a description of the different algorithms available. For details of each algorithm implementation the user will need to examine the code base.

times the local noise

- **-N 127:** the minimum number of bins to average and search across (i.e. for a 128-bin archive, **-N 127** means search over the entire pulsar rotation, but do no bin averaging)
- **-e 6sigma:** list the output in a file with a suffix **.6sigma** (the default output will be **psrspa\_pulses.6sigma** in this case)
- **\*.ar:** find pulses in all archives that satisfy the wildcard expression (i.e. all files that end in **.ar**)

With the above three commands, a large fraction of the work required to analyse and cross-match single-pulse events is done for us. From this point, customised scripts are written to further reduce, sort and characterise the data (e.g. calculate spectral indices between pulses, determine pulse energies, create publication-ready plots, etc.).

#### 2.5.4.3 PRESTO

A separate software package that is designed to search for new pulsars is PRESTO<sup>11</sup>, which includes Fourier-domain searches with a particular focus on accelerated systems (Ransom et al., 2002; Andersen & Ransom, 2018) and binary systems (Ransom et al., 2003). PRESTO is also able to perform a single-pulse search for various trial DMs which is particularly useful for finding objects such as RRATs.

Nominally, the standard PRESTO single-pulse search pipeline used for MWA data in this thesis is as follows.

- compute an RFI mask by Fourier analysis and user-input (i.e. flag certain channels/times) using the **rfifind** routine
- create dedispersed time series by using the **prepsubband** routine with many ( $\geq 1$ ) trial DMs (i.e. one dedispersed time series per trial DM)

---

<sup>11</sup><https://github.com/scottransom/presto>

- search all dedispersed time series using a boxcar filter-based method for significant candidate bursts that are above a user-defined threshold using the `single_pulse_search.py` script

The output of the single-pulse search can then be visually inspected and algorithmically explored as each event and its properties (i.e. time of occurrence, DM, significance, etc.) is recorded. The use of software such as RRATtrap<sup>12</sup> (Karako-Argaman et al., 2015a) can further characterise the single-pulse events using other information, such as event clustering as a function of DM.

---

<sup>12</sup>The original code can be found here: <https://github.com/ckarako/RRATtrap>. However, RRATtrap is now included as part of the PRESTO software package.



# Chapter 3

## Spectral Flattening at Low Frequencies in Crab Giant Pulses

This work was published by:

Meyers, B. W., Tremblay, S. E., Bhat, N. D. R., Shannon, R. M., Kirsten, F., Sokolowski, M., Tingay, S. J., Oronsaye, S. I., and Ord, S. M., “Spectral Flattening at Low Frequencies in Crab Giant Pulses”, 2017, *The Astrophysical Journal*, 851, 1

### 3.1 Summary

In this paper, we examine simultaneous, wideband observations of giant pulses from the Crab pulsar (PSR J0534+2200) with the MWA and Parkes, covering a frequency range of 120 MHz to 3.1 GHz. We found that the spectral index of giant pulses becomes significantly shallower at lower frequencies. This is the first direct evidence of this for the Crab and is contrary to the general expectation of a steep power law. We also studied:

- the pulse broadening times of giant pulses and the frequency scaling of this effect, finding that the frequency evolution is in-line with previous literature, but difficult to explain with current ISM plasma turbulence theories;

- the giant pulse fluence (pulse energy) distribution as a function of frequency, finding that the previously observed power law is appropriate for both the main pulse (MP) and interpulse (IP) emission; and
- the non-giant pulse emission from Parkes data, finding an extremely steep spectral index for both MP and IP emission, consistent with the limited literature available on this aspect.

Finally, we discuss the implications that the spectral flattening has for giant pulse emission models as well as the detectability of Fast Radio Bursts, assuming theories that rely on “super-giant” pulse emission from extragalactic pulsars to explain the observed energetics of the bursts. Fundamentally, the current generation of giant pulse emission models are unable to readily predict spectral index properties, let alone the observed frequency-dependence. Therefore, further theoretical investigations are required. Such efforts will ultimately also aid in furthering our understanding of the pulsar emission mechanism in general.

Minor alterations have been made to the published work in the following sections in order to enforce consistent formatting. Some details, especially regarding the introductory material and observations, have already been discussed at length in Chapter 2, thus the respective sections have been removed or reduced significantly. Some additional text has been added to clarify certain points at the request of the thesis reviewers, though this has not changed to science or outcomes presented. The conclusions have also been shortened and edited to enhance the thesis flow between chapters, and citations have been updated where necessary to reflect their current status.

## 3.2 Introduction

The Crab pulsar (PSR J0534+2200) was discovered through its giant pulse emission (Staelin & Reifenstein, 1968). Individual giant pulses are observed to have brightness temperatures in the range  $T_b \sim 10^{30-32}$  K, implying a coherent emis-

sion mechanism. At extremely high time resolution, Crab giant pulses have been observed to reach brightness temperatures of  $10^{41}$  K, corresponding to a peak flux density of  $S_{\text{peak}} = 2.2 \text{ MJy}$  at 9 GHz (Hankins & Eilek, 2007). Giant pulses are therefore invaluable tools for understanding pulsar emission and, more generally, astrophysical coherent emission mechanisms from a variety of objects.

There are six pulsars known to exhibit giant pulses. These include: two young pulsars (PSRs J0534+2200 and J0540-6919) and four millisecond pulsars (PSRs J0218+4232, J1823-3021A, J1824-2452A, J1939+2134; Knight et al., 2006), all of which have high magnetic field strengths at the light-cylinder radius ( $B_{\text{LC}} \sim 10^{5-6} \text{ G}$ ). The giant pulses from these six objects occur within a confined phase location, are intrinsically short duration (microseconds or less) and exhibit a power-law pulse energy distribution.

Multi-frequency simultaneous observations of the Crab have previously been undertaken, though typically only between two frequencies (e.g. Bhat et al., 2008; Oronsaye et al., 2015) or over a narrow frequency range (e.g Karuppusamy et al., 2012b; Eftekhari et al., 2016). In order to further constrain the giant pulse emission mechanism, wideband simultaneous observations with intermediate frequency coverage such as that conducted by Mikami et al. (2016) are required to uncover the broadband spectral behaviour.

With the advent of the Fast Radio Burst (FRB) phenomenon, especially the repeating FRB 121102 (Spitler et al., 2014a, 2016; Scholz et al., 2016), several theories have been put forth suggesting that at least some FRBs may originate from extragalactic giant pulses (e.g. Cordes & Wasserman, 2016; Lyutikov et al., 2016; Connor et al., 2016). Determining the spectral behaviour<sup>1</sup> of simultaneously detected Crab giant pulses over a wide frequency range will also provide clues regarding a giant pulse origin of FRBs, especially given the paucity of low frequency detections.

---

<sup>1</sup>Throughout, we adopt  $S_{\nu}$  to represent flux densities and  $F_{\nu}$  to represent fluences at frequency  $\nu$ .

### 3.3 Observations

The Crab pulsar was observed simultaneously with Parkes and the MWA on 7 November 2014. Parkes observed the pulsar at 732 and 3100 MHz for 1.4 hours. The MWA-VCS data collection was split into two distinct observations, totalling 1.3 hours. The first 20 minute observation was conducted at a central frequency of 184.96 MHz. Immediately following this, the second observation lasted for 1 hour and was designed such that the MWA bandwidth was split into four subbands distributed between 120.96–278.40 MHz. Observation details are summarised in Table 3.1.

#### 3.3.1 Parkes

We observed the Crab pulsar using the coaxial 1050cm receiver on the 64-m Parkes radio telescope, which is capable of simultaneously recording signals at 732 MHz (64 MHz bandwidth) and 3100 MHz (1024 MHz bandwidth). Both systems are sensitive to linear polarisation. Data were recorded with the mark-3 and mark-4 versions of the Parkes digital filterbank spectrometers (PDFB3 and PDFB4) for a duration of  $\approx 5060$  s. The spectrometers employ polyphase digital filters, with PDFB3 recording data with 512 channels across the 64 MHz low-frequency band, and PDFB4 recording data with 512 channels across the 1024 MHz high-frequency band. Data were recorded in polarimetric search mode. For each channel four coherency products (the power from each probe and the complex-valued correlated power between the two) were detected and averaged over 256  $\mu$ s before being written to disk with 8-bit precision.

The decorrelation bandwidths ( $\Delta\nu_{\text{DISS}}$ ) due to diffractive scintillation at 732 and 3100 MHz are 35 kHz and 6 MHz respectively, assuming  $\Delta\nu_{\text{DISS}} = 2.3$  MHz at 2.33 GHz (Cordes et al., 2004) and a scaling of  $\Delta\nu_{\text{DISS}} \propto \nu^{3.6}$  (e.g. Ellingson et al., 2013; Eftekhari et al., 2016, Kirsten et al. in prep.). Over the respective bandwidths of the observing frequency bands, these contributions are negligible. The refractive time scales are 2 days and  $\sim 7$  hours respectively. On the time

Table 3.1: Observation parameters.

Parameters		MWA <sup>a</sup>		Parkes
Center frequency (MHz)	120.96	165.76	184.96	210.56
Bandwidth (MHz)	7.68	7.68	30.72	7.68
FWHM (arcmin)	3.60	2.63	2.36	2.07
Time resolution ( $\mu$ s)	100	100	100	100
Frequency resolution (MHz)	0.01	0.01	0.01	0.01
Dispersion delay across bandwidth <sup>b</sup> (ms)	2048.48	795.26	2319.09	387.83
Dispersion delay in lowest channel <sup>b</sup> (ms)	2.93	1.10	0.96	0.53
Start time (UTC)	17:14:00	17:14:00	16:53:40	17:14:00
Observation duration (s)	3663	3663	1163	3663
				5065
				5055

<sup>a</sup>The 278.4 MHz subband was excluded due to poor quality calibration solutions (see text).

<sup>b</sup>Assuming a nominal dispersion measure of  $56.7762 \text{ pc cm}^{-3}$ .

scales we are probing, we do not expect any significant contribution from scintillation to the giant pulse flux densities in the 732 MHz band. In the 3100 MHz band we expect that the small contribution from scintillation will be dominated by the measurement scatter in giant pulsar flux densities.

### 3.3.2 Murchison Widefield Array

Using the MWA-VCS, we recorded  $\approx 4826$  s of data from the array pointed towards the Crab pulsar (see Table 3.2). As previously mentioned, this observing run was split into two observations. The first 20 minutes with the full 30.72 MHz of bandwidth, centred at 184.96 MHz. The remaining 60 minutes were observed with the bandwidth split into four 7.68 MHz subbands, distributed to centre frequencies of 120.96, 165.76, 210.56 and 278.40 MHz.

At MWA frequencies, the decorrelation bandwidths due to diffractive scintillation range between  $\Delta\nu_{\text{DISS}} \approx 50\text{--}1000$  Hz at the observed MWA bands. The refractive time scales are between 8 and 25 days. Therefore, we do not expect any contribution from scintillation to be significant in our intensity estimates for the Crab giant pulses at MWA frequencies.

## 3.4 Data processing and calibration

### 3.4.1 Parkes

Absolute flux density calibration was performed using the standard procedures as outlined in Section 2.2.1. This allowed us to measure the frequency-dependent differential gain and phase of the two feeds. We did not correct for feed ellipticity or cross coupling.

The 732 MHz data were incoherently dedispersed and folded using DSPSR (van Straten & Bailes, 2011) with an ephemeris from the Jodrell Bank monthly monitoring<sup>2</sup>. A more accurate pulsar ephemeris was produced from these data, fitting

---

<sup>2</sup><http://www.jb.man.ac.uk/pulsar/crab.html>

for the optimum period, period derivative and dispersion measure with TEMPO2 (Hobbs et al., 2006). The dispersion measure calculated by this process was  $56.7762 \text{ pc cm}^{-3}$  and is henceforth taken as the nominal dispersion measure for the Crab pulsar.

Data from both Parkes bands were then re-processed using DSPSR and the updated ephemeris, subdividing the data streams into individual pulses. The pulses were flux density and polarisation calibrated using PSRCHIVE (Hotan et al., 2004) routines. RFI was removed using the PAZ routine, flagging the edge 5% of each band and running the inbuilt median smoothed difference excision algorithm.

### 3.4.2 Murchison Widefield Array

Calibrating the MWA data is non-trivial, especially in the case of VCS recorded data for which there is currently no dedicated automatic calibration pipeline. The Crab nebula was selected as the calibrator source for both the 184.96 MHz full-bandwidth observation and the split-bandwidth observation. Visibilities for each observation were created using an offline version of the MWA correlator (which performs the same function as the online version; Ord et al., 2015). For each band, a calibration solution (amplitude and phase) for each tile was calculated from the visibilities using the Real Time System (RTS; Mitchell et al., 2008). The output from the RTS is a calibration solution for each coarse channel containing the calibration information for each MWA tile, thus there is a set of 24 solutions per observation. Due to poor quality calibration solutions, data from 8 of the 128 tiles for the full bandwidth observation were discarded, while 21 of the 128 tiles were discarded for the split-bandwidth observation.

The MWA tiles and beam models are less well characterised at higher frequencies ( $\nu \sim 300 \text{ MHz}$ ) and moreover there are increased levels of satellite-based radio frequency interference (RFI), making calibration significantly more difficult. Owing to the poor calibration solution quality at the 278.40 MHz band, the data were discarded leaving us with three usable subbands (120.96–210.56 MHz) and

one band at 184.96 MHz (see Figure 3.1).

The MWA uses analogue beamformers to set the pointing direction of each tile, thus there are a discrete set of delays available. For our observations, this means that the tile beam is never pointed directly at the Crab and so we are never at full sensitivity. The MWA tile beam is very complex, thus in some cases the Crab is not within a well-understood region of the beam. Throughout the 120.96 and 165.76 MHz and 184.96 MHz observations, the Crab is always within the half-power point of the beam, for which we have the most confidence in the beam modelling. At 210 MHz, the beam is such that the Crab is only barely within the half-power point for  $\sim 1/3$  of the full observation. We therefore have less confidence in the ability to accurately flux calibrate the data at that particular frequency band, using the method outlined here.

### 3.4.2.1 Tied-array beamforming

The tied-array beam is formed by coherently summing individual tile voltages (see Section 2.1.2.2). Theoretically, this process yields a factor of  $\sqrt{N_{\text{co}}}$  improvement in sensitivity over an incoherent sum (i.e. detect tile power and sum, see Oronsaye et al., 2015), where  $N_{\text{co}}$  is the number of tiles used to create the tied-array beam. In reality, this is not the case and we see an improvement by a factor of between 4.2–5.4, depending on the frequency. The discrepancy is primarily due to the pointing of the telescope (i.e. the MWA beam pattern is less well characterised as we diverge from a zenith pointing) and the calibration solution quality.

### 3.4.2.2 Tied-array system temperature and gain

For a tied-array beam, the field-of-view is significantly smaller than that of the tile beam, approximating the naturally weighted synthesised beam of the array – nominally FWHM  $\sim 1.27\lambda/D$ , where  $\lambda$  is the observing wavelength and  $D$  is the maximum baseline of the array. The scaling factor of 1.27 derives from the MWA being dominated by shorter baselines. This means that neither the integrated

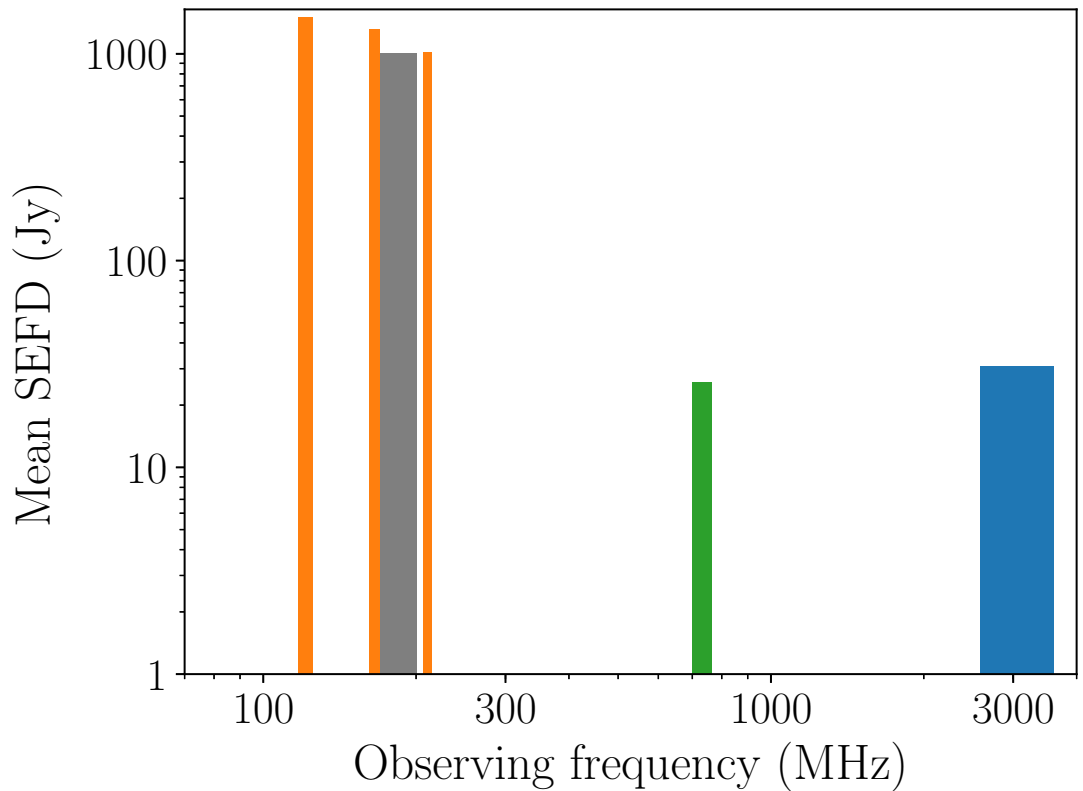


Figure 3.1: Schematic of the MWA and Parkes frequency coverage versus the mean system equivalent flux density (SEFD). The orange bars correspond to the split-bandwidth observations with 7.69 MHz bandwidth. The gray is the full-bandwidth observation with 30.72 MHz bandwidth. The green bar represents the 732 MHz Parkes band with 64 MHz bandwidth and the blue bar represents the 3100 MHz Parkes band with 1024 MHz bandwidth.

sky temperature nor the system gain will be the same as for the tile beam.

The overall system temperature ( $T_{\text{sys}}$ ) for each frequency band, is a combination of the receiver temperatures ( $T_{\text{rec}}$ ), antenna temperatures ( $T_{\text{ant}}$ ), and the ambient temperature ( $T_0$ ), and is calculated as

$$T_{\text{sys}} = \eta T_{\text{ant}} + (1 - \eta)T_0 + T_{\text{rec}}, \quad (3.1)$$

where  $\eta$  is the frequency and direction dependent radiation efficiency of the array. Efficiencies and receiver temperatures for each subband are given in Table 3.2. The receiver temperatures are well characterised across the nominal observing frequency range of the MWA. The ambient temperature weighting of  $1 - \eta$  where  $\eta \simeq 1$  means that the contribution is negligible compared to the sky, and we therefore assume the ambient temperature is  $T_0 \approx 290$  K. This contributes  $\simeq 5\text{--}7$  K to the total system temperature.

Table 3.2: Frequency and direction dependent radiation efficiencies and receiver temperatures for the MWA.

Pointing center (Az., El.) (deg, deg)	Center frequency (MHz)	Radiation efficiency $\eta$	Receiver temperature $T_{\text{rec}}$ (K)
(18.43, 41.42)	120.96	0.980	39
(18.43, 41.42)	165.76	0.976	32
(26.56, 37.31)	184.96	0.980	23
(18.43, 41.42)	210.56	0.981	34

In order to calculate the antenna temperature in equation (3.1) we require an adequate understanding of the tied-array synthesised beam pattern. In this case, the tied-array beam power pattern is the product of an individual MWA tile power pattern and the array factor. The tile pattern is simulated using the formalism set out by Sutinjo et al. (2015), while the array factor encapsulates the phase information required to point the tied-array at the target source. For a full

description of the formulation of the array factor, see Appendix B. This procedure was used to create the tied-array beam pattern at multiple times throughout the observation.

We use the Global Sky Model (GSM; de Oliveira-Costa et al., 2008) as our sky map and scale it to our observing frequencies. The GSM was modified in the region of the Crab nebula with the scaling  $S_{\text{CN}} = 955\nu^{-0.27}$  Jy (Apparao, 1973; Bietenholz et al., 1997) to more accurately represent the contribution from the nebula. Convolving the tied-array beam pattern with the GSM and integrating over the sky (see e.g. Sokolowski et al., 2015), we produce an estimate of the antenna temperature (see Appendix B.2). Using these antenna temperatures and equation (3.1), we calculate a system temperature estimate multiple times during the observation for each band. Fitting a second-order polynomial to the results from the separate evaluations of  $T_{\text{sys}}$ , we estimate a system temperature curve as a function of time.

We also calculate the gain,  $G$ , (see Appendix B.3) at the same intervals as calculating the system temperature. The gains are relatively stable over the duration of the observation, thus we fit a linear slope to create a gain curve as a function of time for the entire observation. The system temperature and tied-array gain curves are shown in Figure 3.2. Note that these estimates have included in them the assumption of ideal sensitivity increase (i.e. by a factor of  $\sqrt{N_{\text{co}}}$ ). This is corrected, given that we do not see the theoretical increase in sensitivity, in the following Section.

### 3.4.2.3 Flux density estimation

The output of the coherent beamforming pipeline (see Section 3.4.2.1) is a set of PSRFITS files (Hotan et al., 2004), one file per 200 seconds per 1.28 MHz coarse channel. The individual channels can be combined into one 200 second file, reducing the number of data files by a factor of 24. These PSRFITS data were then incoherently dedispersed and subdivided into single-pulse archives using

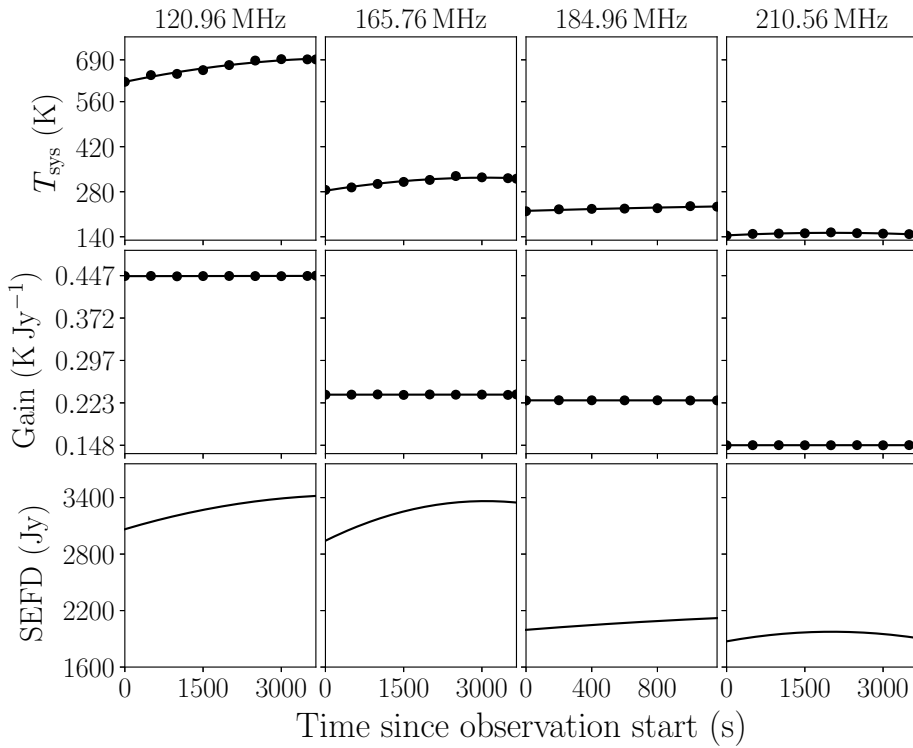


Figure 3.2: System temperature, gain and SEFD estimates as a function of time for the full-bandwidth and split-bandwidth MWA observations. The black points are the measurements made from the simulated tied-array beam patterns and the black lines are fits to the measurements. The system temperatures are fitted with a second order polynomial and the gains described by a linear fit. The SEFD is calculated as  $f_c T_{\text{sys}}/G$ , using the polynomial fits, and  $f_c$  is defined in equation (2.12).

DSPSR and the ephemeris derived from the Parkes 732 MHz data. Each coarse channel’s edges were flagged (fine channels 0–19 and 108–127) to mitigate the effects of aliasing introduced during the channelisation process, and the PSRCHIVE routine PAZ was used to apply the inbuilt median smoothed difference excision algorithm. Finally, the archives were collapsed in polarisation and frequency and written to a time series using PDV, without automatic baseline removal.

The system temperature and gain calculations are used to convert the time series data from arbitrary power units to flux density units using

$$S = (\text{S}/\text{N}) \times \frac{f_c T_{\text{sys}}}{G\sqrt{n\Delta\nu\Delta t}}, \quad (3.2)$$

where S/N is the sample signal-to-noise ratio,  $f_c$  is the coherency factor as in equation (2.12),  $n$  is the number of polarisations summed (in this case  $n = 2$ ),  $\Delta\nu$  is the observing bandwidth, and  $\Delta t$  is the sample integration time. For an individual MWA tile, the SEFD is typically  $\sim 2 \times 10^4$  Jy, however, for the coherently beamformed we find (for this set of subbands and pointings) the SEFD to be  $\sim 2\text{--}3 \times 10^3$  Jy.

### 3.5 Analysis and Results

After post-processing, we produced five time series with  $\Delta t = 261.241\,\mu\text{s}$  time resolution. This was achieved by re-binning the data into 129 phase bins per pulse period, ensuring that both the MWA and Parkes data had a sample time greater than the Parkes intrinsic sampling time  $256\,\mu\text{s}$ . We use fluence (integrated flux density over the pulse width) as a direct measure of the pulse energy, given that peak or mean flux densities are less informative at MWA frequencies where giant pulses are typically scattered over several pulse periods.

### 3.5.1 Detecting giant pulses

Due to frequency dependent propagation effects, the Parkes and MWA data were processed differently. As the data were incoherently dedispersed, the dispersive smearing across individual channels was not removed. While this delay is large at MWA frequencies ( $\sim 1\text{--}10\%$  of a pulse period), the dominating factor is still the multipath scattering which broadens an individual giant pulse across several pulse periods (see Section 3.5.2). Not only does this scattering make pulse detection and cross-matching more difficult, it also requires a more complicated method of measuring the pulse fluences. An example of a giant pulse detected simultaneously across all five subbands, shown in Figure 3.3, illustrates the pulse-shape evolution with frequency due to multipath scattering.

A summary of the detected main pulse (MP) and interpulse (IP) giant pulses from each frequency band is presented in Table 3.3. Every giant pulse detected is recorded in a table format including the pulse number, phase position, and fluence estimate.

Table 3.3: Number of detected giant pulses per frequency.

Centre frequency (MHz)	$N_{\text{total}}$	$N_{\text{MP}}$	$N_{\text{IP}}$
120.96	90	79	11
165.76	386	336	50
184.96	407	341	66
210.56	648	560	88
732	6344	5306	1038
3100	231	217	14

#### 3.5.1.1 Parkes

The calibrated single-pulse archives for both the 732 and 3100 MHz data were summed in polarisation and frequency to produce total intensity profiles. To

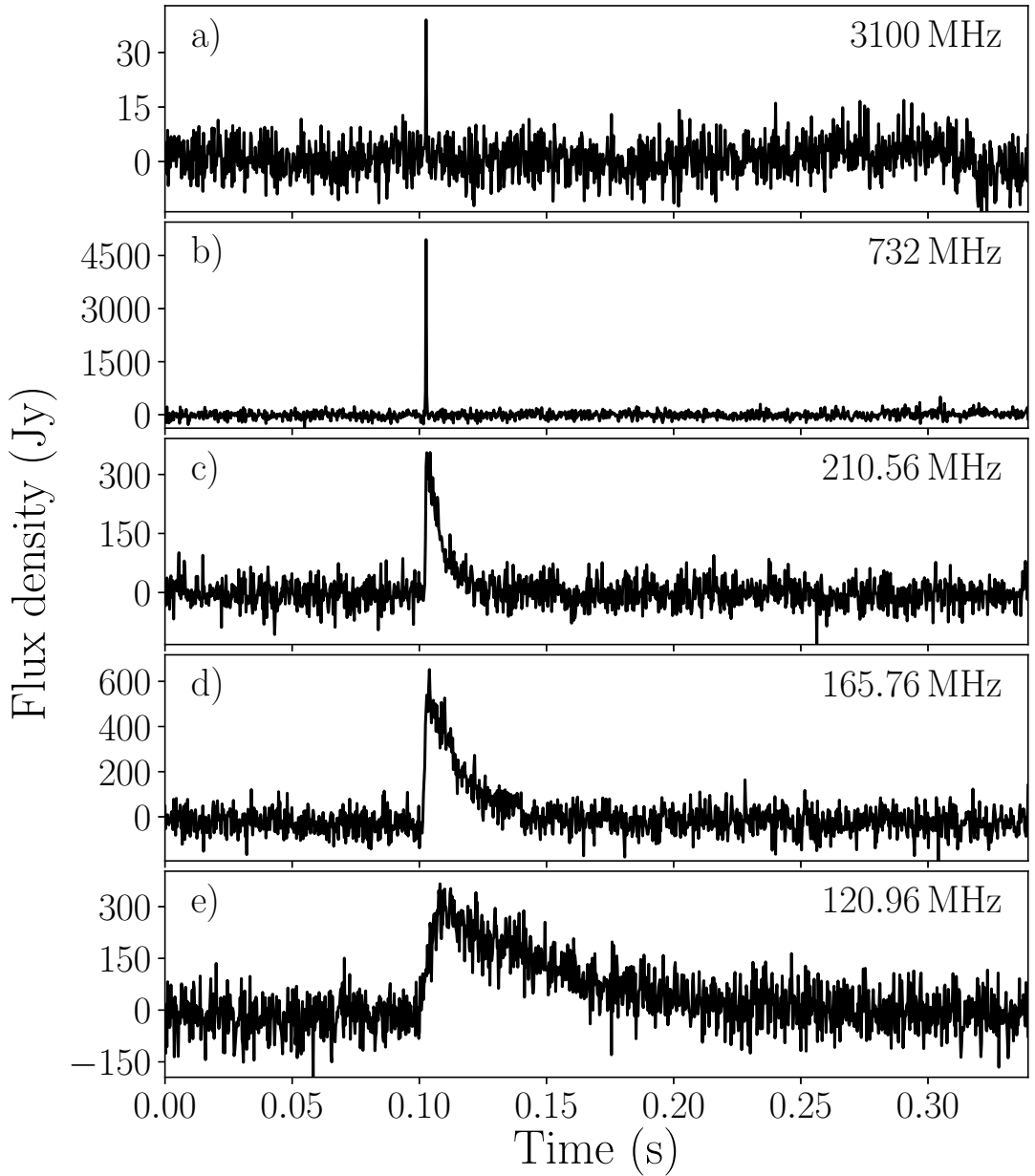


Figure 3.3: A simultaneous giant pulse detected in all five observing bands: a) 3100 MHz, b) 732 MHz, c) 210.56 MHz, d) 165.76 MHz, and e) 120.96 MHz. The effect of multipath scattering are most obvious at MWA frequencies, introducing a significant exponential tail to each giant pulse, while the Parkes pulses are delta-functions with the recorded time resolution. The 120.96 MHz pulse also has a visible rise time compared to the other frequencies.

find giant pulses in the single-pulse archives we used PSRCHIVE’s single-pulse analysis routine PSRSPA to search for candidate events with a signal-to-noise ratio  $\text{SNR} \geq 6$ . The candidate lists were filtered to remove events with large pulse widths<sup>3</sup>. The time-of-arrival (TOA) was calculated for each giant pulse candidate with the ephemeris used during the folding process. The giant pulse positions in rotation phase were then examined using TEMPO2. At 732 and 3100 MHz, there were 179 and 39 outliers (main pulse and interpulse combined) discarded, respectively.

This produced a list of 231 pulses at 3100 MHz and 6344 pulses at 732 MHz. From the finalised list of candidates, on-pulse peak flux densities were recorded for each single-pulse archive. The giant pulse fluences were then calculated as the product of the peak flux density and the time series bin width. The fluence errors were calculated from the off-pulse root-mean-square (RMS) value. The reduced number of detections at 3100 MHz is at least partly due to the sub-optimal time sampling, since at those frequencies the typical width of giant pulses is on the order of microseconds. Naturally then, only the particularly bright examples are detected in the high band (and, to a lesser extent, the 732 MHz band). For this reason, we elect to use the fluence (pulse energy) to measure the energetics of the giant pulses, rather than their flux densities directly.

Assuming Gaussian noise, the probability,  $P_n$ , of a false detection above some signal-to-noise ratio  $n\sigma$  is,

$$P_n(x > n\sigma) = \int_{\mu+n\sigma}^{\infty} P(x) dx = \frac{1}{2} \operatorname{erfc}\left(\frac{n}{\sqrt{2}}\right), \quad (3.3)$$

where  $\mu$  is the mean noise level,  $\sigma$  is the root-mean-square noise, and  $\operatorname{erfc}(x)$  is the complementary error function. The signal-to-noise ratio threshold when searching for single pulses in both the 732 and 3100 MHz bands was  $6\sigma$ , which corresponds to a false detection likelihood of  $P_6 \approx 1 \times 10^{-9}$ . The number of

---

<sup>3</sup>The Parkes data is limited by the time resolution, thus giant pulses appear as events with a width of 1 sample only.

false positives ( $N_{f,pks}$ ) is then the product of  $P_6$  and the number of observed pulsar rotations ( $\approx 1.5 \times 10^5$ ). We calculate this number to be significantly less than unity ( $N_{f,pks} \approx 1.5 \times 10^{-4}$ ) and therefore do not expect any giant pulse candidates with  $\text{SNR} \geq 6$  to be spurious. After removing the RFI, ensuring pulses were recorded only if they occur in the main pulse and interpulse phase windows and by excluding candidates with pulse widths greater than 1 sample, we assert that all Parkes giant pulse candidates used in the following analysis are real. An implicit assumption in this estimate is that we are searching for an event in one particular bin for every pulsar rotation. In the case of the Parkes data, this is true given the time sampling and also because we know that giant pulses only appear in very confined phase locations (for the Crab).

### 3.5.1.2 MWA

As MWA giant pulses are severely scattered, some custom software was developed specifically for searching for scattered pulses in the time series. The input to this code is the time series created in Section 3.3.2. For each time series, the data were smoothed using a Savitzky-Golay low-pass filter with a window length of 9 samples and a 3rd order fitting polynomial. Typical pulse widths are  $> 40$  samples, thus the smoothing window length will not adversely affect the local pulse shape. This mitigated the high-frequency noise without reducing the fidelity of the individual pulses. The baselines for each time series were then removed by subtracting a linear fit over adjacent  $10^4$  sample windows.

Local peaks were detected above a threshold of  $5.5\sigma^4$  in partially overlapping sections of the time series. Any new candidate peaks recorded with the same sample number as a previously detected peak were discarded. Around each of the peaks, between 500 and 1000 samples (from the highest to the lowest frequency, respectively) were retrieved before and after the peak to ensure the entire

---

<sup>4</sup>A lower threshold than that used for the Parkes observations is enforced for the MWA data because of the significantly quieter RFI environment at the Murchison Radio-astronomy Observatory.

scattered pulse is captured in the time series window.

In order to further constrain the pulse position and extent, we fitted a pulse broadening function (PBF) to each time series windows. The thick, finite extent scattering screen PBF proposed by Williamson (1972) was chosen, as it models both the significant rise-time and exponential scattering tail present at low frequencies. The sample selections were fitted with the corresponding PBF form,

$$g(t) = A \left( \frac{\pi \tau_d}{4(t - t_0)^3} \right)^{1/2} \exp \left[ -\frac{\pi^2 \tau_d}{16(t - t_0)} \right] \quad (3.4)$$

where  $A$  is a constant amplitude scaling,  $t_0$  is the start time of the leading edge of the pulse and  $\tau_d$  is the characteristic scattering time. Pulse numbers and phase were calculated based on the best-fitting pulse starting time,  $t_0$ . The pulse candidates were then selected based on whether their fitted  $\tau_d$  values fell within a predetermined range, based on the approximate scattering time measured at each frequency (see Section 3.5.2). This distinguishes bona fide candidates with sensible scattering time estimates from spurious detections. We note that the fitting was used only as a filtering process, and because we know that, for the Crab, none of the standard PBFs fit correctly (see e.g. Kirsten et al., 2019) the resulting scattering times may be somewhat less reliable. Each fitted pulse was also inspected by eye so that any questionable candidates were removed. For the full-bandwidth observation (184.96 MHz), this produced a list of 407 pulses. For the split-bandwidth observation, we record: 90 pulses at 120.96 MHz; 386 pulses at 165.76 MHz; and 648 pulses at 210.56 MHz.

For each real candidate pulse, we define the start of the pulse as the best-fitted  $t_0$ , and the end of the pulse as 6  $e$ -folds past the PBF peak (i.e.  $t_0 + \pi^2 \tau_d / 4 + 6\hat{\tau}_d$ ). In this case,  $\hat{\tau}_d$  is the median scattering timescale as in Table 3.4 while  $\tau_d$  is the best-fitting scattering time for the individual pulse. We define this window as the actual pulse from which to calculate the fluence. For each candidate we then integrate over the pulse window and record that as the pulse fluence, along with the fluence from the fitted PBF. The fluence uncertainty for each pulse was

calculated by integrating under the fitted PBF model, scaled such that the peak amplitude was equal to the local RMS value.

Detections near the threshold limit may have underestimated fluences, given that the giant pulses (specifically the scattered tail) would be dominated by noise and fall within the baseline RMS well before a brighter counterpart pulse at a different frequency. Fluence estimates, and consequently the calculated spectral indices (see Section 3.5.5), in those cases may be less reliable, especially for weaker pulses. Additionally, the software searches only for simple PBF forms, thus giant pulses with significantly different structure (e.g. a second pulse within the scattering tail) may be discarded, especially if the structure is such that the estimated scattering time scales are outside the nominally expected range. At 210.56, 184.96, 165.76 and 120.96 MHz, this results in  $\sim 7\%$ ,  $\sim 0.4\%$ ,  $\sim 10\%$  and  $\sim 1\%$  of candidates being flagged, respectively. The 184.96 MHz fraction is significantly smaller due to both the sensitivity (i.e. the noise characteristics are typically better behaved) and the observation duration (i.e. we are less likely to observe, for instance, a giant pulse within the scattering tail of another).

We tested the noise statistics for coherently beamformed, dedispersed, baseline-removed MWA data for normality. This was achieved by selecting five evenly spaced samples, each containing 1000 data points, from each subband time series and fitting a normal distribution. From these samples, the noise statistics are consistent with Gaussian noise (see Figure 3.4 for an example), therefore we can use equation (3.3) to calculate the false detection likelihood for MWA data. The signal-to-noise ratio threshold when searching through MWA data was  $5.5\sigma$ , thus the false detection probability is  $P_{5.5} \approx 2 \times 10^{-8}$ . The number of pulsar rotations during the MWA split-bandwidth observations is  $\approx 1.1 \times 10^5$ , thus the number of false detections expected is again significantly less than unity ( $N_{f,mwa,\text{split}} \approx 2.2 \times 10^{-3}$ ). For the full-bandwidth observation, the number of pulsar rotations is  $\approx 3.5 \times 10^4$ , and the number of expected false detections is  $N_{f,mwa,\text{full}} \approx 7 \times 10^{-4}$  – again much less than unity. We claim that no MWA giant

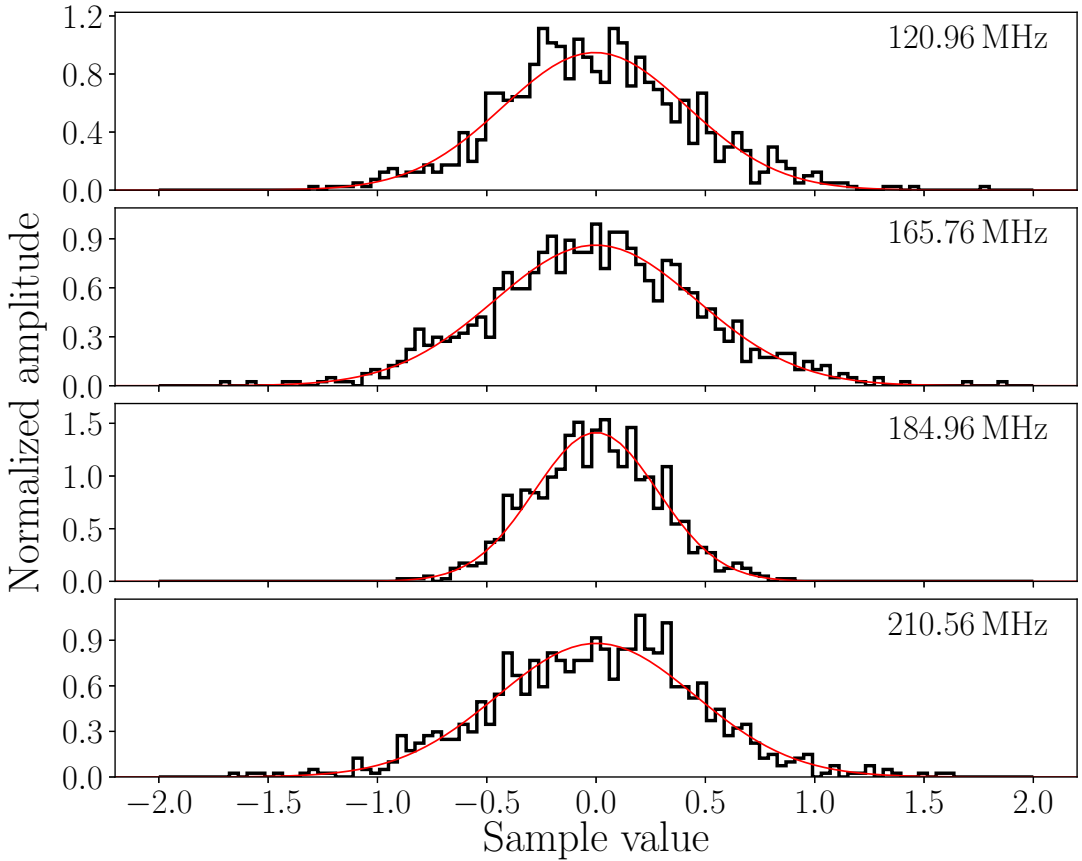


Figure 3.4: A 1000 sample example of the noise characteristics for coherently beamformed, dedispersed, baseline-removed MWA data. The red solid line is a fitted normal probability density function.

pulses are spurious detections, given the statistics and the filtering performed during the candidate selection process. We also acknowledge that the implicit assumption which was valid for the Parkes data (i.e. that we are searching for a single-bin event in each pulsar rotation) does not hold in the case of the MWA time series, since the giant pulses are scatter broadened over many rotations. In reality, one would need to rigorously model the probability distributions involved, accounting for the intrinsic pulse shape, scattering kernel and instrumental statistics to robustly estimate an equivalent false detection rate. The saving grace in this case is the distinct scattered pulse shape, which allows for a more sophisticated matched filter-like approach when detecting the pulses.

### 3.5.2 Pulse broadening

At both Parkes subbands, we cannot directly determine the scattering time scale ( $\tau_d$ ) since we are limited by the time resolution ( $261.241\,\mu\text{s}$ ) of our recorded data. At MWA frequencies, from the rudimentary fitting performed when detecting the pulses we can estimate the pulse broadening. We report the median scattering time scales in Table 3.4. Furthermore, we calculated the scattering spectral index ( $\alpha_d$ ) using the MWA data. Using a least-squares minimisation approach, we fitted a power-law ( $\tau_d \propto \nu^{\alpha_d}$ ) to the MWA scattering time scales (see Figure 3.5). The determined scaling index is  $\alpha_d = -3.73 \pm 0.45$ , significantly shallower than what is predicted from a Kolmogorov model, which is  $\alpha_d = -4.4$ . This results is consistent with what is reported in the literature at low frequencies (e.g. Bhat et al., 2007b; Ellingson et al., 2013; Eftekhari et al., 2016). Extrapolating using the above scaling index, we also estimate the scattering expected in the Parkes subbands in Table 3.4.

Given the time-variability of characteristic scattering times observed for the Crab, and the dependence of the estimated scattering time on the chosen PBF, discrepancies as much as by a factor of  $\sim 2$  are not uncommon between similar frequencies. Our values from the MWA subbands are roughly consistent with those quoted in the literature (e.g. Staelin & Sutton, 1970b; Popov et al., 2006a; Oronsaye et al., 2015). A more detailed examination of the scattering behaviour of the Crab and other pulsars within the MWA observing frequency range is reported by Kirsten et al. (2019). In particular, there is discussion of the difficulties in correctly characterising the pulse broadening seen in Crab giant pulses at low frequencies and reconciling this with a variety of theoretical scattering screen models.

### 3.5.3 Simultaneous giant pulses

For every giant pulse found in Sections 3.5.1.1 and 3.5.1.2, a pulse number was recorded. We use those pulse numbers and the phase (to discriminate between MP

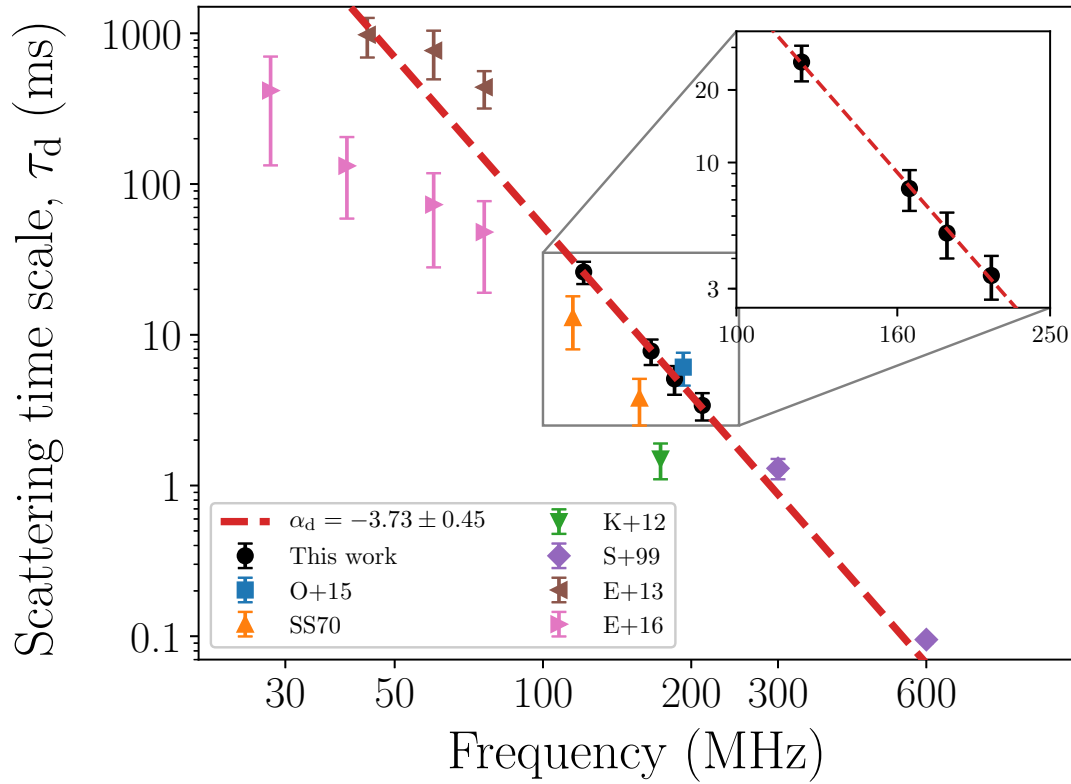


Figure 3.5: Pulse broadening times from the four MWA bands. The median scattering time scales (circles), their respective errors and the fitted power-law (red dashed line), are plotted on a log-log scale. The scaling index,  $\alpha_d = -3.73 \pm 0.45$  is significantly shallower than what is expected from a Kolmogorov model, but consistent with other estimates at similar frequencies in the literature. Given the variability of Crab pulse broadening, it is not surprising that many of the scattering times from the literature do not fall on the fitted power-law. The scattering times legend keys are as in Table 3.4.

Table 3.4: Pulse broadening time scales in the literature, including this work.

Centre frequency (MHz)	$\tau_d$ (ms)	Reference	Key
28	$417 \pm 284$	Eftekhari et al. (2016)	E+16
40	$132 \pm 73$	Eftekhari et al. (2016)	E+16
44	$978 \pm 287$	Ellingson et al. (2013)	E+13
60	$768 \pm 273$	Ellingson et al. (2013)	E+13
60	$73 \pm 45$	Eftekhari et al. (2016)	E+16
76	$48 \pm 29$	Eftekhari et al. (2016)	E+16
76	$439 \pm 122$	Ellingson et al. (2013)	E+13
115	$13 \pm 5$	Staelin & Sutton (1970b)	SS70
120.96	$26.1 \pm 4.4$	<i>This work</i>	
157	$3.8 \pm 1.3$	Staelin & Sutton (1970b)	SS70
165.76	$7.8 \pm 1.5$	<i>This work</i>	
173.25 <sup>a</sup>	$1.5 \pm 0.4$	Karuppusamy et al. (2012b)	K+12
184.96	$5.1 \pm 1.1$	<i>This work</i>	
192.64	$6.1 \pm 1.5$	Oronsaye et al. (2015)	O+15
210.56	$3.4 \pm 0.7$	<i>This work</i>	
300	$1.3 \pm 0.2$	Sallmen et al. (1999)	S+99
600	$0.095 \pm 0.005$	Sallmen et al. (1999)	S+99
732	$\sim 0.03^b$	<i>This work</i>	
3100	$\sim 0.0002^b$	<i>This work</i>	

<sup>a</sup>Scattering time estimated from Figure 6 in Karuppusamy et al. (2012b).

<sup>b</sup>Extrapolated from 184.96 MHz, assuming  $\tau_d \propto \nu^{-3.7}$ .

and IP giant pulses) of each giant pulse to cross-match across the five frequency bands. The cross-matching was achieved by using routines from the Starlink Tables Infrastructure Library Tool Set (STILTS; Taylor, 2006), which is designed for robust and efficient processing of tabular data. The tools are implemented for generic manipulation of tabulated data sets, though are typically used for astronomical object catalog analysis, in particular cross-matching of large data sets based on user-specified selection criteria. The results of cross-matching the giant pulse samples from each subband are summarised in Table 3.5.

Between the two Parkes frequencies, we find that there are 157 simultaneous main pulses and 9 simultaneous interpulses. These numbers correspond to approximately 72% and 64% coincidence for main pulses and interpulses respectively, based on the number of pulses detected in the 3100 MHz band.

Between the MWA full-bandwidth observation and the 732 MHz Parkes band, there are 140 simultaneous main pulses and 33 simultaneous interpulses, corresponding to 41% and 50% based on the total numbers from the 184.96 MHz band. Across all three bands, we detected 10 simultaneous main pulse giant pulses and 2 simultaneous interpulse giant pulses.

Within the MWA bands (Table 3.1), the full-bandwidth and split-bandwidth observations have no overlap in time, thus we focus only on the three subbands at 120.96, 165.7, and 210.56 MHz. Between the highest and middle bands, there are 269 simultaneous main pulses and 42 interpulses, corresponding to 80% and 84% based on the number of pulses detected in the 165.76 MHz band. Between the lowest and middle bands there are 68 simultaneous main pulses and 8 interpulses, corresponding to 87% and 72% correlation based on the number of pulses detected in the 120.96 MHz band. There are 7 giant pulses detected simultaneously across all five bands, 6 main pulses and 1 interpulse.

For the brightest  $\sim 10\%$  of pulses (combining main pulses and interpulses) in each band, we checked for pulses that had no counterpart in adjacent frequency bands. At 210.56 MHz, there are 68 pulses with fluences greater than

Table 3.5: Number of simultaneous pulses between different frequency bands. The table is split by the diagonal (left-to-right): numbers in white cells represent simultaneous main pulses, while numbers in gray cells represent simultaneous interpulses. The values along the diagonal (in light blue), separated by a backslash ( $\backslash$ ) are the number of main pulses (left) and interpulses (right) for each band. Columns marked with a dash (–) indicates no cross-matching was possible.

Frequency (MHz)	120.96	120.96	165.76	184.96	210.56	732	3100
120.96	79 \ 11	8	–	7	4	1	1
165.76	72	336 \ 50	–	42	25	5	5
184.96	–	–	341 \ 66	–	33	2	2
210.56	66	269	–	560 \ 88	56	5	5
732	38	173	141	326	5306 \ 1038	9	9
3100	6	16	10	22	157	217 \ 14	14

1.5 Jy s, of which there are only 42 counterparts at 732 MHz and 67 counterparts at 165.76 MHz. Inspecting the MWA time series, we found that the missing giant pulse in the 165.76 MHz band is below the detection threshold. At 165.76 MHz, there are 38 pulses with fluences greater than 5 Jy s, with 37 counterparts at 210.56 MHz and 26 counterparts at 120.96 MHz. The missing counterpart at 210.56 MHz is relatively clear in the time series, however it is actually two giant pulses combined (and therefore discarded during the candidate processing) – a main pulse and interpulse in adjacent rotations. At 732 MHz, the main pulse is detected, but the interpulse in the subsequent rotation is not. For the 12 missing counterparts at 120.96 MHz, in 8 of those cases, there is a visible counterpart below the  $5.5\sigma$  detection threshold. For another 3, there are no visible counterparts. For one pulse, there is no 120.96 MHz data at the corresponding time because of the dispersion delay.

In light of the “double giant pulse” (i.e. a main pulse and interpulse occurring within one rotation), we searched for other examples across all frequency bands. At 3100 MHz, there is one marginal case ( $\sim 0.4\%$  of detected pulses), while at 732 MHz there are 85 clear examples ( $\sim 1\%$  of detected pulses). Within the MWA bands, the pulse broadening makes robustly identifying double giant pulses difficult, however, we find  $\sim 1\text{--}2$  marginal examples per MWA band. The double giant pulses at one band do not necessarily coincide with double giant pulses at any other.

### 3.5.4 Giant pulse fluence distributions

In Figure 3.6 we plot the complementary cumulative distribution function (CCDF), also known as the survival function, of pulses as a function of fluence for each subband. The clustering at low frequencies suggests that there is some degree of flattening of the spectral indices occurring at the lowest frequencies. This also provides estimates for sub-populations of giant pulses and rates of occurrence as a function of frequency and fluence. Listed in Table 3.6 are some basic quantities

describing the fluences of all detected giant pulses in each observed band.

Typically, the fluence distributions are assumed to follow a power-law,  $N(> F_\nu) \propto F_\nu^{-\beta}$ . In the literature, the standard approach is to estimate a power-law cut-off ( $x_{\min}$ , see Figure 3.7) by eye and use a least-squares approach to only fit data beyond that limit. This approach may introduce significant biases in the power-law index estimation and assumes that the data are independent and identically sampled.

To avoid subjectivity, we chose to use the `powerlaw` Python module (Alstott et al., 2014), which appropriately treats several heavy-tailed distributions, particularly focusing on power-laws. The best-fitting power-law distribution index ( $\hat{\beta}$ ) and power-law cut-off ( $x_{\min}$ ) are determined by finding the minimum Kolmogorov-Smirnov distance between the data and model (see e.g. Figure 3.7). The data are used to evaluate multiple distribution models, including truncated power-laws (where  $N(> F_\nu) \propto F_\nu^{-\Gamma} e^{-\lambda\nu}$ ), log-normal, and exponential distributions. This provides the ability to statistically test which distribution is a better representation of the data based on the likelihood ratios and  $p$ -values. In general, we find that a power-law distribution is the most likely, however the significance of that distinction varies drastically between bands and the compared distributions. Therefore, we cannot say for certain that a power-law is the best-fitting distribution for all of our data. Table 3.7 summarises the fitting results assuming a power-law distribution.

Our results in terms of  $\hat{\beta}$  for the two Parkes subbands are within the range of those reported by Mickaliger et al. (2012) between 330 and 1200 MHz ( $\hat{\beta}_{\text{MP}} \sim 2.1\text{--}3.1$ ,  $\hat{\beta}_{\text{IP}} \sim 2.4\text{--}3.1$ ), but steeper than reported by Bhat et al. (2008) between 1300 and 1470 MHz ( $\hat{\beta} = 2.33 \pm 0.15$ , where the MP and IP are combined), except in the case of our 3100 MHz Parkes IP exponent. For the MWA subbands, results are typically steeper than the estimated value at 325 MHz ( $\hat{\beta}_{\text{MP}} = 2.61 \pm 0.14$ ,  $\hat{\beta}_{\text{IP}} = 2.7 \pm 0.7$ ) reported by Mikami et al. (2016), and are also steeper than the slopes calculated by Karuppusamy et al. (2012a) between 110–180 MHz ( $\hat{\beta}_{\text{MP}} \sim$

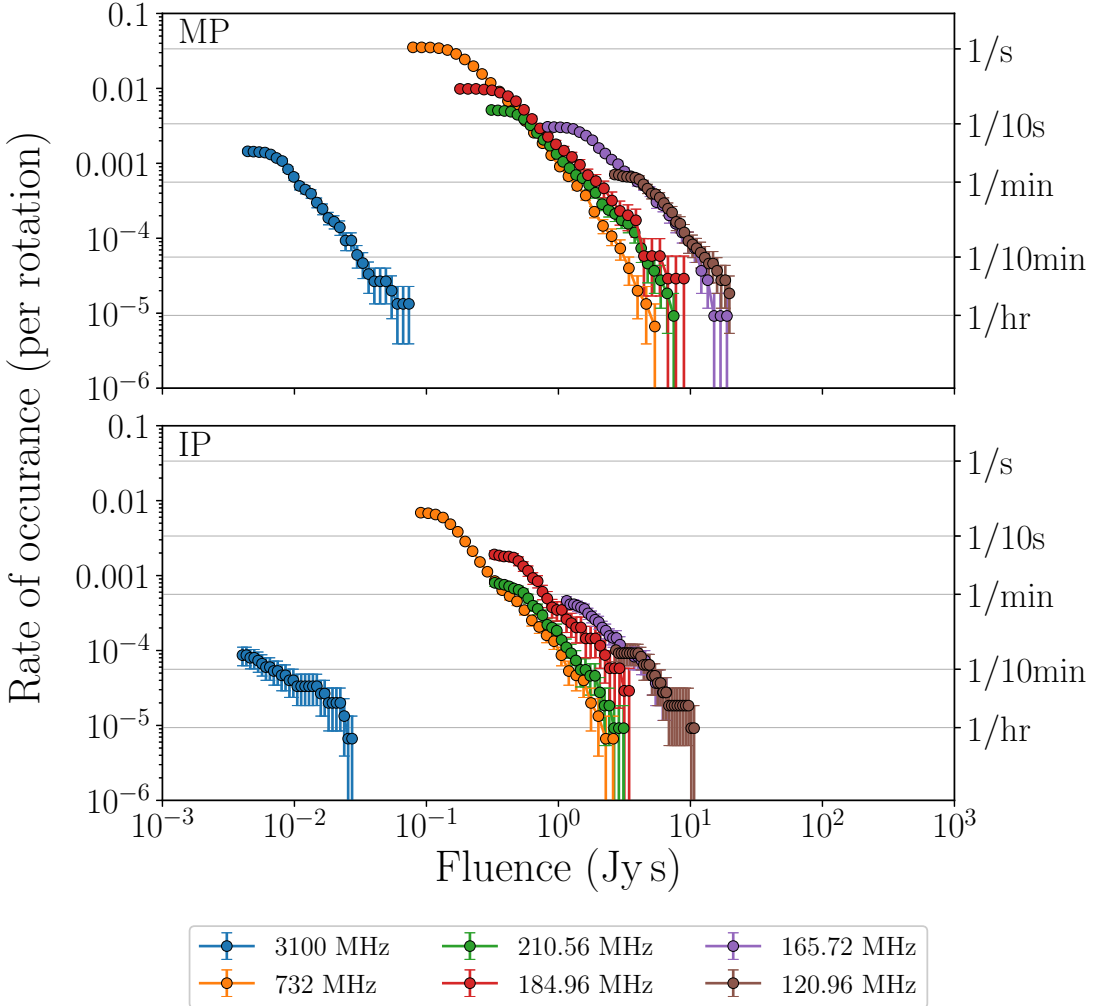


Figure 3.6: Giant pulse rates versus fluence for each observed frequency. The left vertical axis effectively denotes the probability of detecting one giant pulse per rotation, while on the right these are translated into rates. The clustering of the low-frequency bands (120.96, 165.76, 185.96 and 210.56 MHz) hints that the spectral index is flattening for both main pulses (top) and interpulses (bottom).

Table 3.6: General statistics of the full sample of giant pulse fluences from each subband.

Center frequency (MHz)	Main pulse $F_\nu$				Interpulse $F_\nu$			
	Median (Jy s)	Std. dev. (Jy s)	Min. (Jy s)	Max. (Jy s)	Median (Jy s)	Std. dev. (Jy s)	Min. (Jy s)	Max. (Jy s)
120.96	5.62	3.71	2.57	20.42	4.91	2.34	2.66	10.91
165.76	1.99	2.46	0.78	19.96	2.01	1.52	1.12	6.77
184.96 <sup>a</sup>	0.52	0.78	0.16	9.54	0.61	0.58	0.31	3.57
210.56	0.64	0.80	0.29	7.89	0.61	0.54	0.31	3.53
732	0.22	0.28	0.07	5.77	0.17	0.22	0.08	3.58
3100	0.009	0.009	0.004	0.077	0.008	0.008	0.004	0.028

<sup>a</sup> Adjusting to account for the bandwidth difference produces a median of 1.7 Jy s for main pulses and 1.5 Jy s for interpulses.

1.5–2.4,  $\hat{\beta}_{\text{IP}} \sim 0.7$ –2.7, with errors typically around  $\pm 0.1$  for main pulses and  $\pm 0.5$  for interpulses). The MWA main pulse indices are shallower (except for the 120.96 MHz band) than reported by Oronsaye et al. (2015), where  $\hat{\beta} = 3.35 \pm 0.35$  (main pulses and interpulses combined), though interpulse indices for all MWA bands are consistent.

Table 3.7: Best-fit parameters for the fluence distributions in each band.

Frequency (MHz)	Main pulse			Interpulse		
	$\hat{\beta}^a$	$x_{\min}$	$N > x_{\min}$	$\hat{\beta}^a$	$x_{\min}$	$N > x_{\min}$
120.96	$3.73 \pm 0.54$	6.81	24	$3.70 \pm 0.86$	3.94	10
165.76	$2.69 \pm 0.11$	1.60	242	$2.84 \pm 0.29$	1.47	40
184.96	$2.88 \pm 0.12$	0.44	234	$3.10 \pm 0.29$	0.49	52
210.56	$2.90 \pm 0.09$	0.51	434	$3.14 \pm 0.25$	0.49	71
732 <sup>b</sup>	$3.30 \pm 0.09$	0.46	719	$3.16 \pm 0.09$	0.15	658
3100	$3.19 \pm 0.17$	0.01	82	$2.15 \pm 0.31$	0.004	13

<sup>a</sup>The uncertainties quoted are the standard error in the power-law index estimation.

<sup>b</sup>In this case, the evaluated  $x_{\min}$  for the main pulses is relatively high, excluding  $\sim 85\%$  of detected pulses. See text for details.

For main pulses at 732, 210.56, and 165.76 MHz, the distribution appears more likely to be log-normal or a truncated power-law, and the significance ( $p > 0.05$ ) is such that we cannot entirely reject that hypothesis. In each of the three bands, only a handful of pulses (i.e. less than 10) contribute to the non-standard power-law shape. Notably, the determined power-law cut-off for the 732 MHz data is relatively high compared to the other bands, such that only  $\sim 15\%$  of pulses are being fit. If we set an upper limit of 1 Jy s (of which only 2% of main pulses are brighter) then the re-evaluated power-law fit is such that  $\hat{\beta} = 3.12 \pm 0.04$  and  $x_{\min} = 0.21$  Jy s and  $> 53\%$  of main pulses are included in the fitted distribution.

### 3.5.5 Spectral index distributions

The spectral index for giant pulse emission is typically assumed to be a power-law, where  $S_\nu \propto \nu^\alpha$ , which will also apply to fluences, such that  $F_\nu \propto \nu^\alpha$ . We find

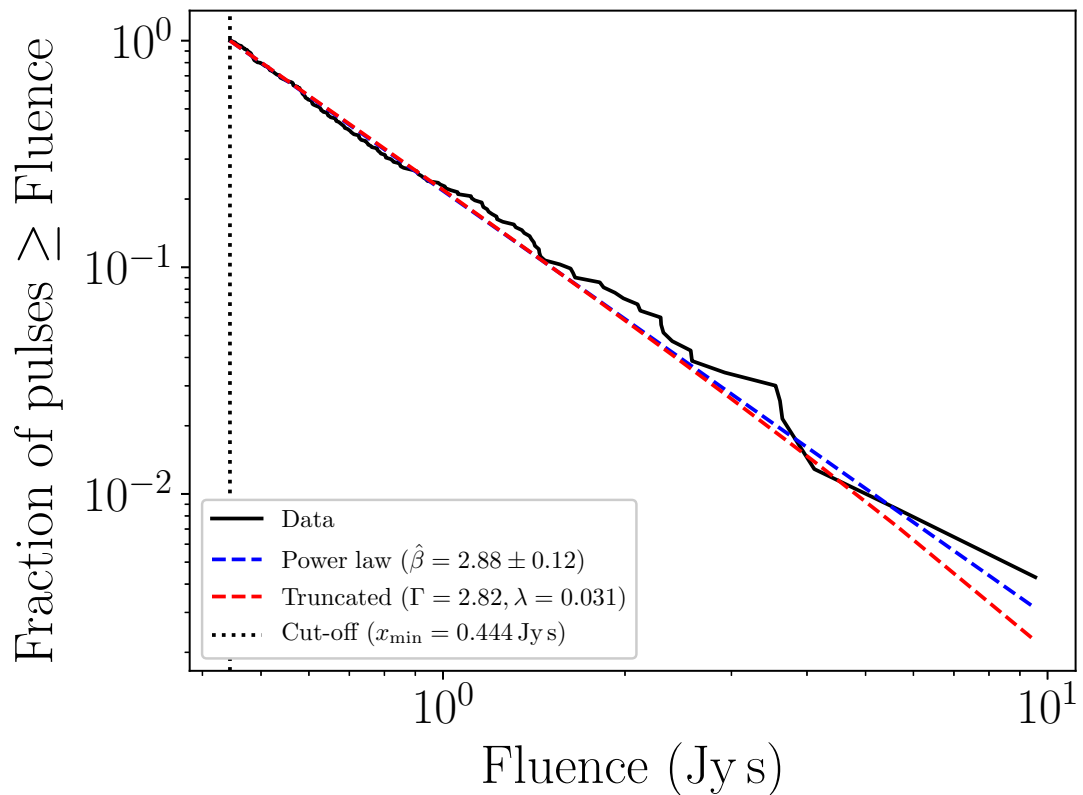


Figure 3.7: The normalised fluence distribution fits for MWA 184.96 MHz main pulses, where the  $y$ -axis now represents the fraction of pulses observed greater than a given fluence value up to the power-law cut-off.

that a simple power-law is unable to accurately model the observed giant pulse spectrum between 120.96 and 3100 MHz. In Figure 3.8 we plot the spectral index distributions between each consecutive frequency pair, separated into main pulses and interpulses. From 732–3100 MHz, 75% of simultaneous main pulses have a spectral index between  $-3.3$  and  $-2.1$ . Between 732 and 165.76 MHz, the same fraction of the giant pulses exhibit a spectral index in the range  $-1.8$  to  $-0.4$ . The distribution between the two lowest MWA bands is wider and flatter, with 75% of pulses within  $-2.5$  to  $0.7$ . Using the 184.96 MHz data, we also calculated the spectral index distribution for a similar sample of giant pulses (with a signal-to-noise ratio  $\geq 11$  which accounts for the factor of 2 sensitivity improvement provided by 4 times the bandwidth). This produces a distribution with a mean  $\alpha = -0.8$  and a width of 0.6, with 75% of the pulses between  $-1.5$  and  $-0.1$ . Given the sparse interpulse distributions, we did not calculate the above intervals, though we can say that they appear to follow a similar trend of flattening.

As discussed in Section 3.4.2, the trustworthiness of the 210.56 MHz beam, and hence the fluence estimates, are questionable. We calculate a spectral index from the data in Table 3.6 between 210.56 and 732 MHz to be  $\alpha \approx -0.6$  with a width of 0.5, while between 210.56 and 165.76 MHz  $\alpha \approx -4.7$  with a distribution width of  $\sim 3$ . The 210.56 MHz data is therefore not used in the following analysis. Additionally, as discussed in Section 3.5.1.1, the time sampling of the data is significantly longer than the typical giant pulse widths at both Parkes bands. Nevertheless, this does not affect the overall fluence of the pulse (assuming it is bright enough), but does mean that the spectral index distributions would be slightly biased towards bright giant pulses.

Karuppusamy et al. (2010b) report spectral index distributions between 1300–1450 MHz centred around  $-1.44 \pm 3.3$  and  $-0.6 \pm 3.5$  for main pulse and interpulse giant pulses respectively, though the distribution width ranges from approximately  $-15$  to  $+10$ . Mikami et al. (2016) also estimate spectral indices in the range  $-15$  to  $+10$  based on their fluence calculations between 1586–1696 MHz.

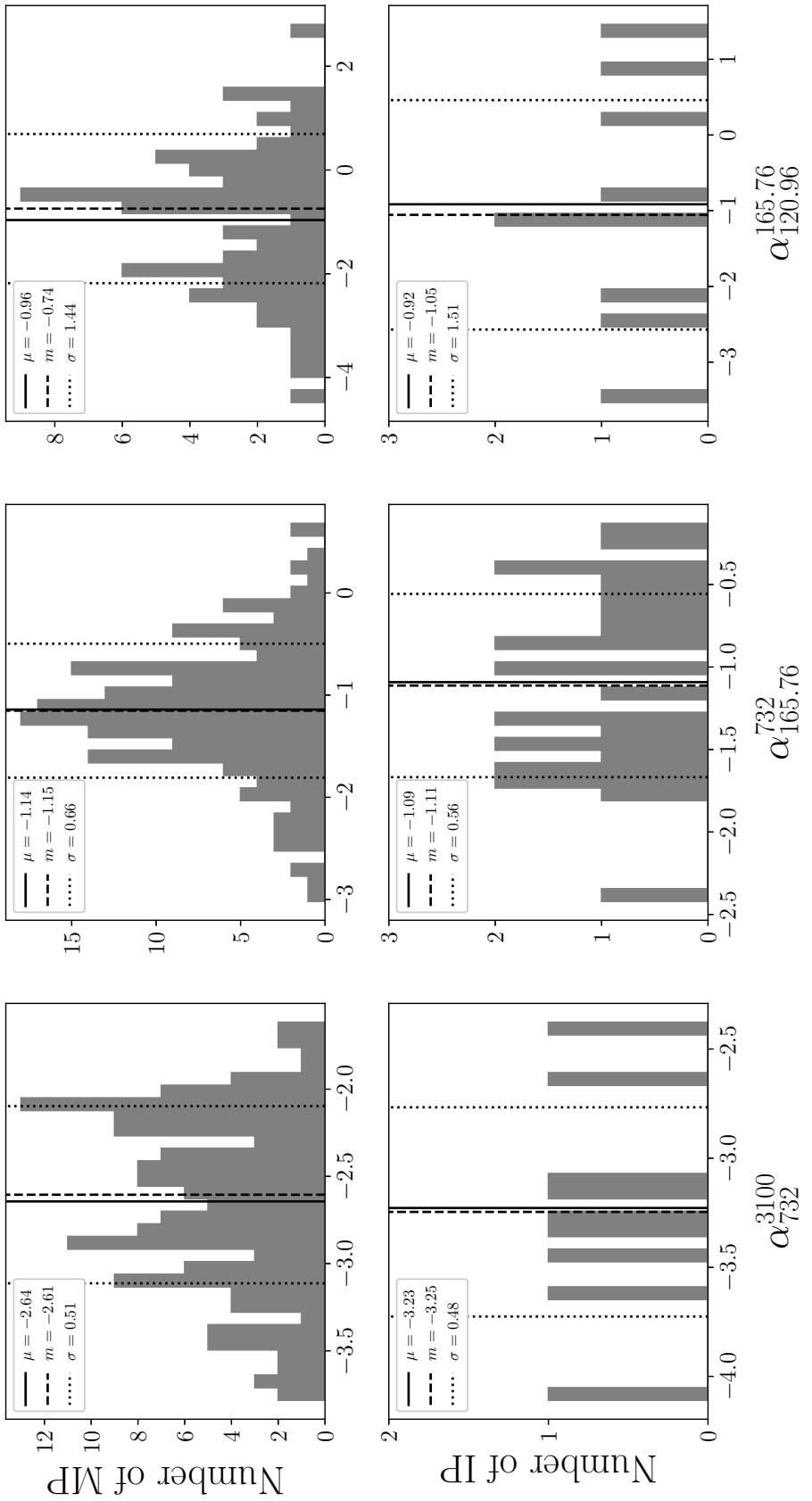


Figure 3.8: Distributions of spectral indices for each combination of giant pulses with the mean ( $\mu$ ), median ( $m$ ) and standard deviation ( $\sigma$ ) included. The top row contains only the main pulse simultaneous matches and the bottom row contains only the interpulse matches. The spectrum of the simultaneous giant pulses appears to be flattening at low frequencies. There are only a handful of interpulses, thus the mean and median estimates are not as meaningful, but tend to be steeper between the Parkes bands and similar to the main pulses at the lower frequencies.

We therefore do not find it surprising that our spectral index distributions are relatively wide, especially between MWA subbands.

Our observations indicate that the spectral index for simultaneous giant pulses is flattening over the sampled frequency range. If we use the median fluences from Table 3.6, the computed main pulse spectral index is  $\approx -1.4$  across most bands, except for between 120.96 and 165.76 MHz where it steepens to  $\approx -3.3$  and between the Parkes bands. In part this is due to the smaller lever-arm available between MWA bands, however it also indicates that the detected simultaneous pulses (which have a slightly shallower spectral index) are more consistent tracers of the spectral flattening.

In Figure 3.9 we plot three different samples of giant pulses, based on the frequency bands in which they were detected. In general, these spectra also show a tendency of flattening at the lower frequencies. An archetypal synthetic giant pulse spectrum based on the spectral index distributions is shown in Figure 3.10, which demonstrates the expected pulse spectral shape given a 3100 MHz fluence of 0.013 Jy s. The shaded error region is calculated using the median absolute deviation of the spectral index distribution, instead of the standard deviation, as it is less sensitive to the existence of extreme values (see Figure 3.8). The power-laws drawn are fits to the two Parkes bands and the 165.76 and 120.96 MHz MWA subbands.

The mean spectral index between 3100 and 732 MHz from the synthetic spectrum is  $\alpha_{732}^{3100} = -2.7$  with a width of 0.4. Between 732 and 165.76 MHz the synthetic spectral index becomes shallower with  $\alpha_{165}^{732} = -1.1$  and a width of 0.4. Between 165.76 and 120.96 MHz is estimated to be  $\alpha_{120}^{165} = -0.8$  with a distribution width of 2.5. The large error in  $\alpha_{120}^{165}$  is due to a combination of relatively large errors in fluence estimates and that the frequencies are relatively close together, hence there is a wide distribution of spectral indices and therefore a less well constrained mean. Spectral index information between each of the bands and from the synthetic spectrum are shown in Table 3.8.

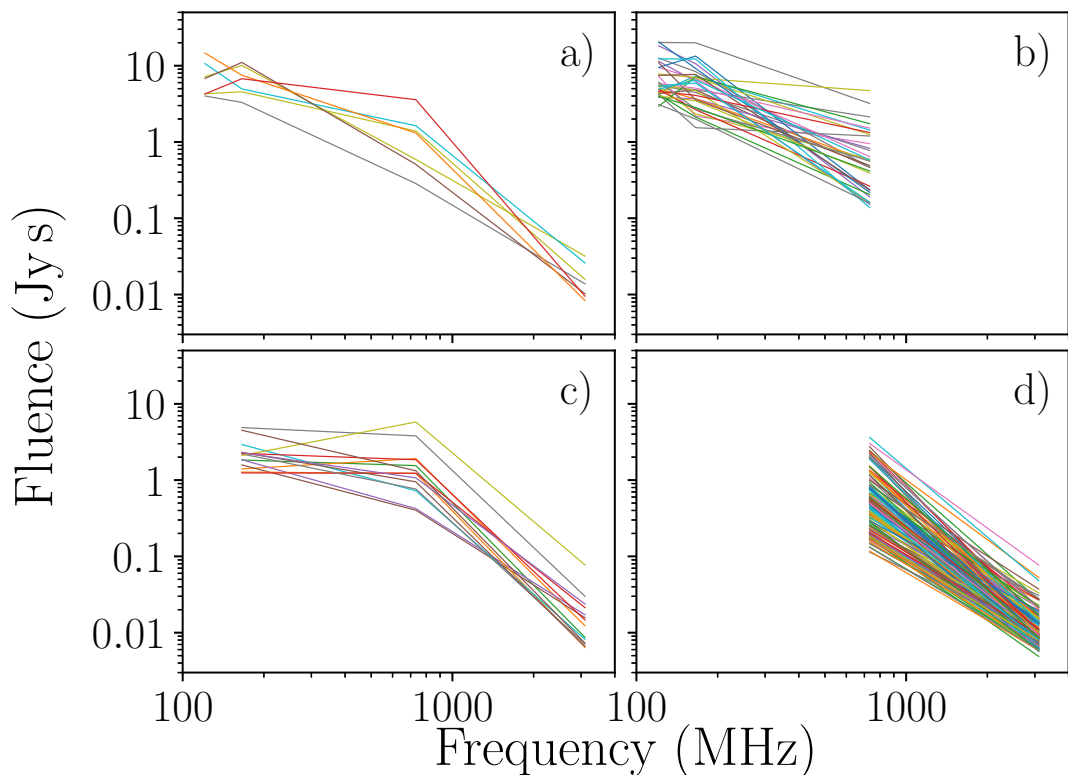


Figure 3.9: Selected samples of giant pulses based on their simultaneous detections. Giant pulses with simultaneous detections in all four bands are plotted in a). Giant pulses detected simultaneously without a 3100 MHz detection are shown in b), while those pulses with only a 3100, 732 and 165.76 MHz simultaneous detection are shown in c). Panel d) contains giant pulses only detected between 732 and 3100 MHz.

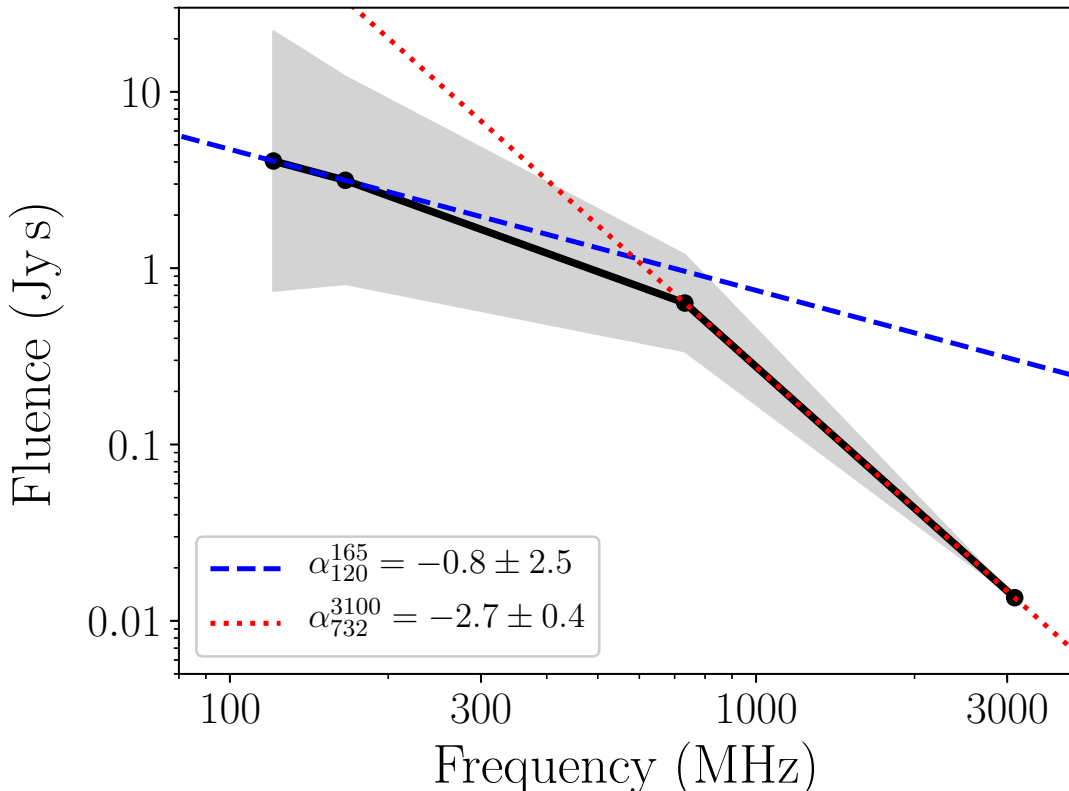


Figure 3.10: An archetypal average spectrum of the detected giant pulses. Each spectral point is calculated based on the mean spectral index between the two frequencies. This is the expected shape of a giant pulse spectrum, for a reference value of 0.013 Jys at 3100 MHz. The gray shaded error region represents the median absolute deviation for each spectral index distribution. The power-law fits are based on only the two Parkes bands (red dotted) and on the two lowest MWA bands (blue dashed).

The synthetic spectrum, in addition to the spectral index histograms and fluence distribution clustering, is evidence for a flattening spectrum for giant pulses at low frequencies. Moreover, we gathered measurements of spectral indices from the literature (Sieber, 1973b; Lorimer et al., 1995; Sallmen et al., 1999; Karuppusamy et al., 2012b; Eftekhari et al., 2016; Mikami et al., 2016) and compared them to our measurements (see Figure 3.11). We find that our results are consistent with previous measurements of the giant pulse spectral index.

Table 3.8: Spectral index distribution and synthetic spectrum parameters.

	Measured <sup>a</sup>	Synthetic <sup>b</sup>
$\alpha_{120}^{165}$	$-0.74^{+1.4}_{-1.8}$	$-0.79 \pm 2.5$
$\alpha_{165}^{732}$	$-1.15^{+0.8}_{-0.6}$	$-1.07 \pm 0.4$
$\alpha_{732}^{3100}$	$-2.61^{+0.5}_{-0.7}$	$-2.66 \pm 0.4$
$\alpha_{185}^{732}$	$-0.78^{+0.73}_{-0.72}$	—

<sup>a</sup>The quoted uncertainties represent the 12.5 and 87.5 percentile (i.e. where 75% of pulses are present about the mean).

<sup>b</sup>The errors represent the distribution width only.

The average main pulse spectral index we find between the two Parkes bands (Figure 3.8) is consistent with the value ( $\alpha = -2.4 \pm 0.5$ ) computed by Mikami et al. (2016), however the interpulse spectral index is difficult to compare given the small number of pulses detected simultaneously. The spectral index we calculate between the Parkes 732 and MWA 165.76 MHz subbands is consistent with the shallower value ( $\alpha = -1.7 \pm 0.5$ ) calculated by Karuppusamy et al. (2010b).

As a test, we supposed our fluence estimates were significantly in error and that the spectral index is in reality  $\alpha = -2.7$ , even over our low frequency subbands. With a reference fluence of 0.013 Jy s at 3100 MHz, as in Figure 3.10, this would require a mean fluence of  $\sim 83$  Jy s at 120.96 MHz,  $\sim 35$  Jy s at 165.76 MHz, and  $\sim 19$  Jy s at 210.56 MHz, overestimating the average fluences by a factor of  $\sim 10$  based on the values recorded in Table 3.6. Additionally, if we assume the distributions follow the same power-law behaviour and that our noise statistics

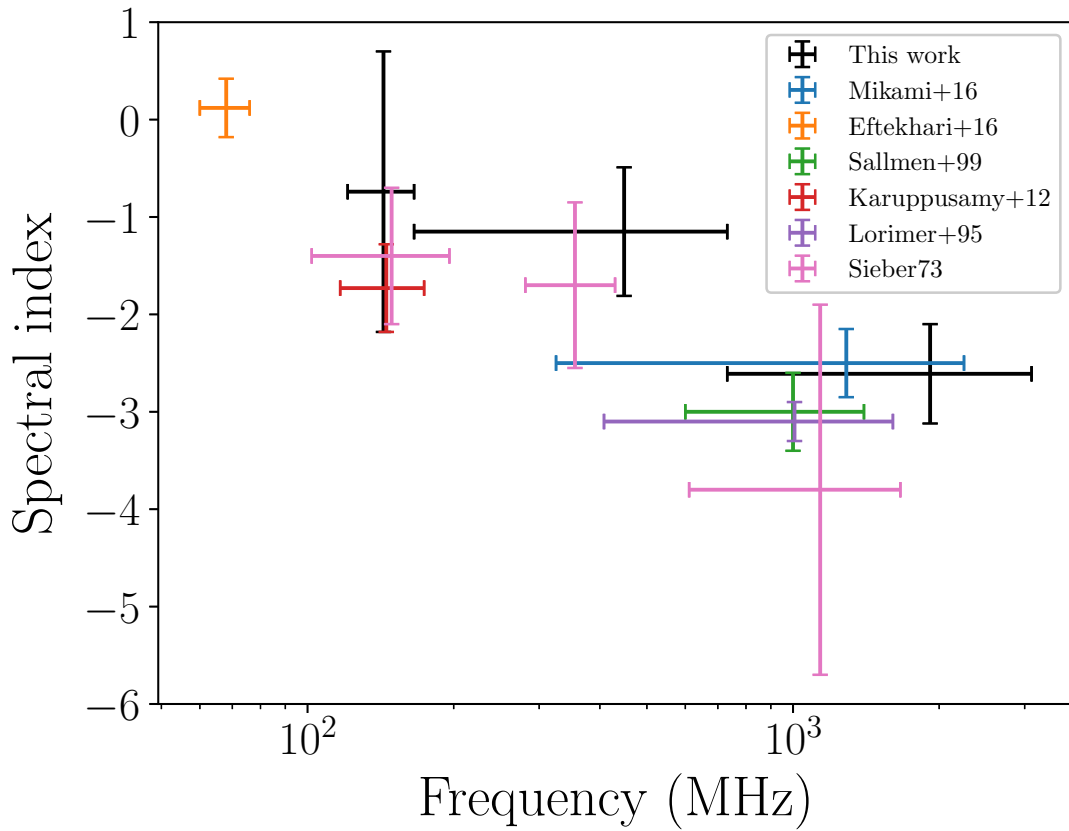


Figure 3.11: A comparison of our measured spectral indices with those reported in the literature. Our data (black) are from simultaneous observations and shows the spectral behaviour over a wide frequency range. The spectral indices from the literature, by and large, are consistent with the spectral flattening that is indicated by our observations. The horizontal bars represent the frequency range over which the spectral indices were calculated. The vertical bars represent the errors reported by the sources, which in most cases corresponds to the range of indices possible based on flux density errors. The distribution widths, or  $\pm 50\%$ , were used in the cases where no error/range information was available.

would remain unchanged, then we can calculate the number of detectable giant pulses ( $N_1$ ) above the extrapolated median fluences ( $F_1$ ) using

$$N_1 = N_0 \left( \frac{F_0}{F_1} \right)^{-\hat{\beta}}, \quad (3.5)$$

where  $N_0$  is the measured number of pulses above the measured median fluence  $F_0$ , and  $\hat{\beta}$  is the measured power-law exponent. Computing this for each of the three MWA subbands, for main pulses only, yields an expected  $\sim 5 \times 10^6$  detectable pulses at 210.56 MHz,  $\sim 4 \times 10^5$  at 165.76 MHz, and  $\sim 9 \times 10^5$  at 120.96 MHz. These predictions are between a factor of  $\sim 10^{3-4}$  times larger than the recorded numbers of main pulses. It is therefore implausible that the spectrum continues with the steep index to low frequencies.

### 3.5.6 Non-giant pulse emission

For the Parkes data, we also attempted to recover the non-giant pulse emission from the Crab. For this, we essentially treated all pulses with a detection below a  $3.5\sigma$  threshold as being “non-giant pulse” emission. All such pulses were synchronously averaged to construct an “integrated profile”. At 732 MHz, the MP and IP components of such a profile are approximately equal in amplitude ( $S_{\text{peak}} \sim 19$  Jy), whereas in the constructed giant pulse profile (detections  $\geq 6\sigma$ ), the MP is  $\sim 6$  times brighter than the IP. At 3100 MHz, the giant pulse profile is dominated by the MP emission, and there is only a marginal peak at the IP phase. The non-giant pulse profile at this frequency contains both MP and IP components, though the MP ( $S_{\text{peak}} \sim 150$  mJy) is only  $\sim 2$  times brighter than the IP. Based on this, if we calculate the spectral index for the MP ( $\alpha_{\text{MP}}$ ) and IP ( $\alpha_{\text{IP}}$ ) non-giant pulse emission, we find that  $\alpha_{\text{MP}} \approx -3.3 \pm 0.1$  and  $\alpha_{\text{IP}} \approx -3.8 \pm 0.1$ . In comparison with the published estimates of the normal emission spectral behaviour (e.g. Moffett & Hankins, 1999;  $\alpha_{\text{MP}} = -3.0$  and  $\alpha_{\text{IP}} = -4.1$ ), we find that our results appear consistent.

We, however, did not carry out such an analysis on the MWA subbands because of the severity of the pulse broadening (see Section 3.5.2), which makes it extremely difficult to disentangle the non-giant pulse emission from weak, scattered giant pulses.

## 3.6 Discussion

### 3.6.1 Spectral flattening

Our analysis identifies a spectral flattening at low frequencies in Crab giant pulses. A flattening spectrum was also hinted at by Oronsaye et al. (2015), whose analysis showed the spectrum becomes shallower by  $\sim 5\%$  at lower frequencies based on Monte Carlo simulations of observations at 193 MHz and 1382 MHz. We note, however, that the fluences presented by Oronsaye et al. (2015) are significantly different (by orders of magnitude) to those we calculate here. Re-examining the Parkes data used, we estimate that the flux densities are a factor of  $\sim 10\text{--}100$  larger than quoted and attribute this to an error in the flux density calibration in the original processing. This discrepancy is also noted by Mikami et al. (2016), whose observing bands are at a similar frequency to those used by Oronsaye et al. (2015). The MWA fluences we calculate herein are roughly consistent with the estimates made by Oronsaye et al. (2015), which together with the re-evaluated Parkes fluences implies that the flattening observed is more significant than the authors stated.

The two power-law slopes we identify behave similarly to those broken-type spectra (Maron et al., 2000b; Bates et al., 2013), where  $|\alpha_{\text{low}}| < |\alpha_{\text{high}}|$ . The average spectral indices we see from our giant pulse sample ( $\alpha_{120}^{165} = -0.7 \pm 1.4$ ,  $\alpha_{165}^{732} = -1.1 \pm 0.7$  and  $\alpha_{732}^{3100} = -2.6 \pm 0.5$ ) are consistent with the estimates of Maron et al. (2000b) for normal pulsar emission,  $\langle \alpha_{\text{low}} \rangle = -0.9 \pm 0.5$  and  $\langle \alpha_{\text{high}} \rangle = -2.2 \pm 0.9$ . Mikami et al. (2016) report a main pulse spectral index between 325 and 2250 MHz of  $\alpha_{325}^{2250} = -2.44 \pm 0.47$ , which is consistent with our

estimated main pulse high-frequency spectral index.

We acknowledge that given we have only 4 spectral points, thus there is not enough information to robustly determine the actual spectral index values and associated uncertainties in the synthetic spectrum. The uncertainty in the MWA fluences is generally the most significant source of error, especially at the lowest frequency where the pulses tend to be scattered, and appropriately characterising the pulses is difficult.

There is an increasing amount of evidence for a slightly flatter, or even an inverted spectrum at low frequencies (e.g. Bhat et al., 2007b; Karuppusamy et al., 2010b; Oronsaye et al., 2015; Eftekhari et al., 2016). In contrast, Popov et al. (2006a) calculate giant pulse spectral indices between  $-3.1$  and  $-1.6$  for 111–600 MHz and  $-3.1$  to  $-2.5$  for 23–111 MHz, both with a mean of  $-2.7 \pm 0.1$ , however note that these values are subject to selection effects. In addition to this, their errors in fluence and spectral index are likely optimistic given that at 23 MHz the giant pulse rise time alone would be several tens or hundreds of pulse periods.

While there is indeed a wide spread in the spectral indices quoted in the literature, the general trend is a shallower spectral index at low frequencies. (see Figure 3.11). Since our data are from simultaneous observations, we are able to confidently assert that the spectral index tends to be shallower at low frequencies. If we only use the values from the literature, a direct comparison is difficult as they are from different instruments and measured at widely separated epochs (sometimes spanning decades).

The implications for the giant pulse emission mechanism is that we would need some process or propagation effect (possibly within the magnetosphere) that allows for a flattening and eventual turn-over (which likely occurs at  $\nu \ll 100$  MHz) in the spectrum. As with the GPS pulsars, this effect is perhaps caused by the surrounding environment of the pulsar (i.e. the Crab nebula in this case). However, Oronsaye et al. (2015) showed that at MWA frequencies, free-free absorption from

within the nebula (e.g. Bietenholz et al., 1997) is not able to explain the flattening they observe, with free-free absorption coefficients on the order of  $\sim 10^{-23} \text{ cm}^{-1}$ . Given our flattening is more apparent than represented previously, free-free absorption alone causing the flattening is unlikely. Structures in the nebula and the intervening ISM (e.g. Smith & Terry, 2011) may be capable of attenuating the fluence estimates by a few percent, but would require 10–100 such filaments to be intercepted. Not only is the chance alignment of filaments unlikely, but the DM of the pulsar would be increased by  $\sim$  few  $\text{pc cm}^{-3}$  which is unphysical.

### 3.6.2 Emission mechanism

The giant pulse fluence dependence on frequency, particularly the flattening at low frequencies, is not predicted in detail in any of the current models. The spectral behavior provides important information about what physical processes are producing the emission.

The coherent radio emission mechanism for pulsars is still unknown (see e.g. Melrose, 1995 for a review), especially given the complexity of modelling pulsar magnetospheres (e.g. Spitkovsky, 2006; Li et al., 2012b; Tchekhovskoy et al., 2013) and the myriad emission models in the literature. There are several models that are able to address individual aspects of giant pulse emission (Eilek & Hankins, 2016), though none are able to explain all of the characteristics alone, possibly because they are not fully explored in the non-linear regime (see e.g. Eilek et al., 2002).

Main pulse emission from the Crab is comprised of narrow-band nanoshots (e.g. Hankins & Eilek, 2007; Hankins et al., 2016). The emission we observe is the average of many of these nanoshots, where the centre frequency depends on which emission model is selected. We examine two plasma emission models, following Eilek & Hankins (2016).

Strong plasma turbulence (Weatherall, 1997, 1998) relies on relativistic particles driving the production of plasma waves which are converted into electro-

magnetic radiation and escape to potentially produce nanoshots. The emission is produced at a frequency  $\nu_{\text{SPT}} \sim 2\gamma_s^{1/2}\nu_p$ , where  $\gamma_s$  is the Lorentz factor describing the streaming speed of the pair plasma and  $\nu_p$  is the plasma frequency. In order for this emission be observed in the radio, the plasma densities must be enhanced by a factor of  $10^2 \lesssim \lambda\gamma_s \lesssim 10^5$ , where  $\lambda = n/n_{\text{GJ}}$  and  $n_{\text{GJ}} \sim 10^6\text{--}10^7 \text{ cm}^{-3}$  is the Goldreich-Julian (GJ) density. The flux densities of the nanoshots are predicted to scale with frequency as  $S_\nu \propto \nu^{-1}$ , assuming radius-to-frequency mapping and ignoring effects related to polar cap current flow.

A free-electron maser model involves the interaction of relativistic particle beams with plasma waves to induce charge bunching, leading to strong coherent bursts of radiation. The emission frequency, assuming the plasma is at rest (e.g. Benford, 1992), is  $\nu_{\text{FEM}} \sim 2\gamma_b^2\nu_p$ , where  $\gamma_b$  describes the speed of the driving particle beam. For radio frequency emission, this requires a density enhancement similar to that of the strong plasma turbulence,  $10^2 \lesssim \lambda\gamma_b^4 \lesssim 10^5$ .

The flattening spectrum then raises the question of what is driving the nanoshot emission in the regions where conditions translate to emission at low frequencies. Crab giant pulse radio emission is suspected to originate higher in the magnetosphere, perhaps near the light-cylinder. This is based on the relative enhancements required for radio emission in comparison to pair-production plasma models (e.g. Arendt & Eilek, 2002; Eilek & Hankins, 2016). High-altitude emission is also supported by multi-wavelength observations of the Crab identifying that the high-energy and radio profiles are very close in pulse longitude, implying they originate from similar regions within the magnetosphere (Abdo et al., 2010). While the strong plasma turbulence model has a shallow predicted scaling for nanoshot flux density which supports a flatter spectrum, it is unclear how that scaling translates into the regime where we are observing the superposition of many nanoshots. If  $S_\nu \propto \nu^{-1}$  is representative for unresolved emission, then the model is unable to explain the steep spectral index typically observed above  $\sim 300 \text{ MHz}$ , even though the model is able to describe the nanoshot time scales

and frequency structure.

If we assume that in fact both phenomena are present within the magnetosphere, then the relative dominance of the processes would depend on, for example, the driving beam densities and ambient plasma characteristics. Typically, one can assume that the charged particles streaming from the pulsar are accelerated along the electric fields as they move away from the neutron star surface. In most models,  $\gamma_s > 100$  and  $\gamma_b^2 \sim 10\text{--}100$  are required in order to match the observed nanoshot frequency-time product (Eilek & Hankins, 2016). In this way, one could imagine strong plasma turbulence begins to dominate in the region where the low radio frequency emission is produced in the upper magnetosphere, where particles are further away from the star and therefore travelling faster.

Without further exploration of these models (and others), in terms of observational emission characteristics, it is difficult to say more. How the nanoscale attributes translate to millisecond time scales, and predictions for the flux density frequency scaling, are critical for meaningful comparison to observation. At low frequencies, there is the additional complication of pulse broadening which distorts the intrinsic emission.

### 3.6.3 FRBs as extragalactic super-giant pulses

Wide band observations are able to provide limits of FRB spectral index distributions (e.g. Burke-Spolaor et al., 2016b). Typically, the measured spectral indices of FRBs are poorly constrained. For example, the measured spectral index (1.214–1.537 GHz) of FRB 121102 ranges between  $-10$  and  $+14$  (Spitler et al., 2016), and for other FRBs the range is approximately  $-8$  to  $+6$  (e.g. Lorimer et al., 2007; Keane et al., 2012; Ravi et al., 2015; Burke-Spolaor et al., 2016b). These values are consistent with the large spread in spectral indices measured for Crab giant pulses, including those calculated herein. If some FRBs are “super-giant” pulses from extragalactic pulsars, and assuming our low-frequency spectral index ( $\alpha = -0.7 \pm 1.4$ ) is representative, it is possible to estimate the number of

expected FRB detections at MWA frequencies. Based on the calculations of Trott et al. (2013), we would expect to see somewhere between  $\sim 0.1$ – $100$  FRBs per 10-hours of observing with the MWA, above a signal-to-noise ratio of 7, depending on scattering effects and the data processing.

Given that no low-frequency instrument has claimed an FRB detection to date (e.g. Coenen et al., 2014b; Tingay et al., 2015; Karastergiou et al., 2015a; Rowlinson et al., 2016), there are two obvious constraints we can make. If FRBs are close enough to be detectable ( $\lesssim$  few hundred Mpc), then the non-detections thus far would suggest that the spectrum has turned over or flattened sufficiently for the giant pulses to become undetectable. From our results, this seems at least plausible assuming that the emission originates from a Crab-like pulsar. However, if the spectrum has not inverted then the non-detections perhaps suggest that these objects are much further away than assumed in the giant pulse FRB models. The latter is supported by the localisation of FRB 121102 (Chatterjee et al., 2017) at  $\sim 1$  Gpc and the stable DM that FRB 121102 exhibits (see e.g. Lyutikov, 2017). With these results in mind, a “super-giant” pulse origin for FRBs seems less likely.

### 3.7 Conclusions

Our observations sampled from 120 to 3100 MHz (a factor of  $\sim 30$  in frequency), and thus simultaneously span low-, mid- and high-frequencies, which provides a unique view of the giant pulse spectrum. Giant pulses were detected in all bands, ranging from 90 at 120 MHz to 6344 at 732 MHz. Seven giant pulses (6 main pulses and 1 interpulse) were detected simultaneously in five of the observing bands (excluding 184.96 MHz due to no time overlap with the 120.96, 165.76, and 210.56 MHz bands). The correlation of detected pulses between bands varies, ranging from  $\sim 40\%$  (184.96 to 732 MHz, relative to 184.96 MHz detections) to  $\sim 87\%$  (120.96 to 165.76 MHz, relative to 120.96 MHz detections).

The mean spectral index for the sample of simultaneous giant pulses tends to flatten at low frequencies, from  $\alpha = -2.6 \pm 0.5$  (732–3100 MHz) to  $-0.7 \pm 1.4$

(120.96–165.76 MHz). By creating a synthetic spectrum based on the distributions of spectral indices, we also see the evolution in spectral shape is not well characterised by a single power-law. This observed spectral flattening is unlikely to be caused by propagation effects within the nebula.

The emission mechanism required to explain this phenomenon is currently not well understood. Further work is required to extend current giant pulse emission models in order to determine how the flux density spectrum changes and how the intrinsic nanoshot characteristics translate to observing their superposition.

We also comment on the plausibility of a giant pulse origin of some FRBs. Considering the localisation of FRB 121102, and the flattening spectrum that we observe, it appears that a giant pulse emission origin for FRBs (assuming the Crab is typical) is less likely. This is supported by the non-detections of FRBs from any low frequency telescope to date.

Investigations of giant pulse spectra over wide frequency ranges, especially extending down below  $\sim 100$  MHz, have not been attempted for other giant-pulse emitting pulsars. Such studies are particularly important to check whether the Crab is a special case or typical in terms of giant pulse emission. We also emphasise the important role of simultaneous observations in this endeavour.

## Acknowledgements

The authors would like to thank the anonymous referee for their valuable input and suggestions, which have significantly improved the paper. B. W. M. would like to thank A. Sutinjo, D. Ung and M. Xue for useful discussions regarding array factor calculations, array efficiencies and flux density calibration. N. D. R. B. acknowledges the support from a Curtin Research Fellowship (CRF12228). F. K. acknowledges funding through the Australian Research Council grant DP140104114. The authors acknowledge the contribution of an Australian Government Research Training Program Scholarship in supporting this research.

This scientific work makes use of the Murchison Radio-astronomy Observa-

tory, operated by CSIRO. We acknowledge the Wajarri Yamatji people as the traditional owners of the Observatory site. Support for the operation of the MWA is provided by the Australian Government (NCRIS), under a contract to Curtin University administered by Astronomy Australia Limited. We acknowledge the Pawsey Supercomputing Centre which is supported by the Western Australian and Australian Governments. The Parkes Radio Telescope is part of the Australia Telescope National Facility, which is funded by the Commonwealth of Australia for operation as a National Facility managed by CSIRO. Parts of this research were conducted by the Australian Research Council Centre of Excellence for All-sky Astrophysics (CAASTRO), through project number CE110001020. Some of the results in this paper have been derived using the HEALPix (K. M. Górski et al., 2005, ApJ, 622, p759) package.



# Chapter 4

## Hunting for Radio Emission from the Intermittent Pulsar **J1107–5907 at Low Frequencies**

This work was published by:

Meyers, B. W., Tremblay, S. E., Bhat, N. D. R., Flynn, C., Gupta, V. Shannon, R. M., Murray, S. G., Sobey, C., Ord, S. M., Osłowski, S., Crosse, B., Williams, A., Jankowski, F., Farah, W., Venkatrama Krishnan, S., Bateman, T., Bailes, M., Beardsley, A., Emrich, D., Franzen, T. M. O., Gaenslar, B. M., Horsley, L., Johnston-Hollitt, M., Kaplan, D. L., Kenney, D., Morales, M. F., Pallot, D., Steele, K., Tingay, S. J., Trott, C. M., Walker, M., Wayth, R. B. and Wu, C., “Hunting for radio emission from the intermittent pulsar J1107–5907 at low frequencies”, 2018, *The Astrophysical Journal*, 869, 2

### 4.1 Summary

In this paper, we examine simultaneous observations of the active emission state of the intermittent pulsar J1107–5907 made with the MWA and UTMOST, covering a frequency range from 140–850 MHz. This represents the first low-frequency

( $< 300$  MHz) detection of an intermittent pulsar. We found that, generally, the single-pulse spectral index and fluence distributions were typical of the normal pulsar population, with one of the profile components having a slightly steeper-than-average (mean) spectral index. This result indicates that the emission from this pulsar is similar to that of normal pulsars. We also explored:

- the shape of the fluence distribution for the two detected profile components, showing that a log-normal distribution fits well, contrary to the previously claimed power law model (though it should be noted that distinguishing between the two is difficult with the total number of pulses that we detected);
- the rotation measure of the pulsar (since low frequencies provide far greater precision due to the  $\lambda^2$  scaling of the Faraday rotation), which we measured with an order of magnitude better precision; and
- the nulling characteristics and pulse rates, identifying that the bright single pulses from the active state began earlier at higher frequencies and finished later, noting that while the overall emission is broadband, the subtleties are important when you are able to examine the emission at the single-pulse level.

We comment on the detectability of this class of pulsars in the context of the next-generation of radio telescopes, specifically the SKA-Low. PSR J1107–5907 is an opportune target given its moderate DM, bright emission and a relatively short “interburst” time scale, and it serves as an interesting potential link between nulling pulsars, RRATs and intermittent pulsars. During the observations we also detected an extremely bright single pulse with a peak flux density of  $\sim 2.5$  kJy, which indicates that, if other similar pulsars exist, they should be detectable with conventional single-pulse and transient search pipelines. This is especially true when considering the the enormous field of view and on-sky time possible with future telescopes, such as the SKA-Low.

As in Chapter 3, minor alterations have been made to the published work in the following sections in order to enforce consistent formatting. The introductory material and observation details sections have already been discussed at length in Chapter 2, thus the respective text has been removed or reduced significantly. Some additional text has been added to clarify certain points at the request of the thesis reviewers, though this has not changed the science or outcomes presented. The conclusions have also been shortened and edited to enhance the thesis flow between chapters, and citations have been updated where necessary to reflect their current status.

## 4.2 Introduction

Pulsars that only emit occasionally are not only difficult to detect, but pose a fundamental challenge to understanding pulsar emission physics. The duty cycle and timescales vary drastically for the pulsar population subclasses and individual pulsars within them, from seconds to minutes (i.e. nulling, Backer 1970b), hours to days (i.e. Rotating Radio Transients, RRATs, McLaughlin et al. 2006), and in the most extreme cases, months or years (i.e. intermittent pulsars, Kramer et al. 2006). How the pulsar magnetospheric configuration changes so severely as to halt emission on short timescales (suddenly within a few rotations of the neutron star) is unclear, even when excluding the added complexity of the wide variety of timescales on which these state-switching phenomena occur.

The geometry of a pulsar is thought to play a significant role in governing the salient properties of its radio emission. It has been shown, for example, that there is a strong correlation between the “intermittency” of a pulsar and the alignment of the magnetic and spin axes (Cordes & Shannon, 2008). There are myriad models for sporadic radio emission from pulsars to explain phenomena such as nulling or RRATs, including: magnetospheric plasma properties, particle supply, and acceleration region evolution (e.g. Timokhin, 2010; Li et al., 2012a; Melrose & Yuen, 2014; Szary et al., 2015), interstellar dust interactions with currents

within the magnetosphere (Cheng, 1985), and mechanisms such as circumpulsar plasma disks (Michel & Dessler, 1981) or asteroidal debris (Cordes & Shannon, 2008; Mottez et al., 2013). Others suggest that, in some systems, the intermittency is related to free precession (Akgün et al., 2006; Jones, 2012), or is a chaotic process (e.g. Seymour & Lorimer, 2013). Notably, sporadic emission from pulsars is also thought to be a broadband phenomenon based on contemporaneous high-energy and radio observations. An example of this broadband nature is the observed mode changing (i.e. where the profile and pulsar spin properties change significantly and abruptly, Lyne et al. 2010) of PSRs B0943+10 (Hermsen et al., 2013; Mereghetti et al., 2016) and B0823+26 (Hermsen et al., 2018) in contemporaneous radio and X-ray data. There is no consensus regarding which model is favored, and testing these hypotheses is notoriously difficult—only now becoming possible with the next generation of space and ground-based telescopes.

There are five<sup>1</sup> confirmed examples of intermittent pulsars in the literature: PSRs J1107–5907 (Lorimer et al., 2006; O’Brien et al., 2006; Young et al., 2014; Hobbs et al., 2016), J1717–4054 (B1713–40, Johnston et al., 1992; Kerr et al., 2014), J1832+0029 (Lorimer et al., 2006, 2012), J1841–0500 (Camilo et al., 2012), and J1933+2421 (B1931+24, Stokes et al. 1985a; Kramer et al. 2006; Rea et al. 2008; Young et al. 2013). Intermittent pulsars have been recognized as a population relatively recently, and thus are not particularly well-studied, other than perhaps the prototypical example of J1933+2421. In all cases, the frequency coverage over which intermittent pulsars have been observed is relatively small and does not include any low-frequency information (i.e.  $\lesssim 300$  MHz). Low frequencies are thought to probe substantially different regions of the pulsar magnetosphere, provide improved constraints on the shape of the pulsar emission spectrum<sup>2</sup>, and allow us to sample frequency dependent intermittency rates (e.g. McLaughlin & Cordes, 2003; Deneva et al., 2009), particularly if observed regularly and simul-

---

<sup>1</sup>In fact there are at least seven, where the additional two confirmed examples were discovered by Lyne et al. (2017).

<sup>2</sup>Throughout, we define the spectral index  $\alpha$  as  $S_\nu \propto \nu^\alpha$ ,  $S_\nu$  as the flux density at frequency  $\nu$ , and  $F_\nu = \int S_\nu dt$  as the fluence at frequency  $\nu$ , which acts as a proxy to the pulse energy.

taneously over a wide frequency range.

PSR J1107–5907 is a relatively old ( $\approx 440$  Myr) and isolated pulsar discovered in the Parkes Multibeam Pulsar Survey (PMPS; Manchester et al., 2001; Lorimer et al., 2006), with a period of  $P \approx 0.253$  s and a moderate cataloged dispersion measure of  $40.2 \pm 1.1$  pc cm $^{-3}$ . It is the brightest and one of the most active (in terms of its “off” timescale being relatively small for frequencies  $\geq 700$  MHz) of the intermittent pulsar population (see, e.g., Figure 10 of Hobbs et al. 2016). The pulsar was investigated after its discovery by O’Brien et al. (2006), who identified three distinct emission states: a bright state with a wide profile, a weak state with a narrow profile, and an “off” state. Young et al. (2014) used Parkes monitoring data collected over a decade to further explore the properties of each of the emission states, finding that the bright state has a complex temporal structure, with a relatively wide main pulse and lower-level emission across a large fraction of the pulsar rotation. The weak state exhibited almost exclusively single-pulse events (though these were analyzed by creating subintegrations) without any particular phase localization and showed an extreme level of nulling. The “off” state consists of no observable emission, though this can be difficult to disentangle from the weak emission state. Polarization analysis of the Parkes data also revealed that PSR J1107–5907 is consistent with being a nearly aligned rotator, which is reinforced by both its broad emission profile and large characteristic age (Rankin, 1990; Tauris & Manchester, 1998; Weltevrede & Johnston, 2008; Young et al., 2010).

Typically, PSR J1107–5907 switches between bright and weak (or “off”) states on a timescale of hours that is atypical for what would be considered normal nulling behavior, which typically occurs on timescales of  $\lesssim 100P$  (Wang et al., 2007). Analysis from both Young et al. (2014) and Hobbs et al. (2016) show that, in general, the duration of a typical bright state is 1–45 minutes, while the fraction of time during which PSR J1107–5907 is actually detected in the bright state versus the observing duration (i.e. its “bright-state duty cycle”) is

$\delta \sim 5\text{--}8\%$ . Compared to the other intermittent pulsars, which exhibit “off” times scales between  $\sim 1\text{--}10^4$  hr, PSR J1107–5907 is the second-most active intermittent pulsar (after PSR J1717–4054), but still poses a significant observational challenge.

## 4.3 Observations and Data Processing

In 2017 April, we began an observing campaign with the MWA and UTMOST to simultaneously observe PSR J1107–5907. This amounted to 10 contemporaneous observations over a period of six months, during which not only did the MWA change configurations, but UTMOST also converted into a transit instrument. These observations were facilitated by the real-time processing capabilities of UTMOST and the triggering capability (newly developed in the case of the MWA, see Section 4.3.2.1) of both instruments. For all but one observation, personnel at both instruments were required to monitor the telescopes for the duration of the observing runs (typically  $\sim 30\text{--}40$  minutes), and in the case of the MWA, trigger data recording to mitigate storage concerns (see Section 4.3.2). The initial observing runs were before UTMOST was converted into a transiting telescope; thus on 2017 April 26 (MJD 57869), we observed PSR J1107–5907 for  $\sim 5$  minutes every 30 minutes for a total of 8 times with UTMOST. Monitoring was not possible on 2017 September 3 (MJD 57999), so a standard pulsar observation was scheduled on the MWA to coincide with when the pulsar would be transiting UTMOST. The final observation of the campaign was conducted on 2017 December 2. An overview of the observations can be found in Table 4.1.

On 2017 September 3, the MWA VCS recorded  $\approx 1.4$  hr of data at a central frequency 154.24 MHz with a bandwidth of 30.72 MHz, and UTMOST recorded  $\approx 0.5$  hr of data at a central frequency 835.59 MHz with 31.25 MHz bandwidth as the target transited. This observation is the primary focus of this work. Observation details of the bright state detection are summarized in Table 4.2.

Table 4.1: Simultaneous observation attempts.

MJD	UTC	Duration (min)	Bright state detected	Single pulse(s) detected	Coincident?
57865 <sup>a</sup>	2017 Apr 22	5	Yes	–	No
57869	2017 Apr 26	8 × 5	No	No	–
57970	2017 Aug 5	30	No	Yes (2)	Yes (1)
57977	2017 Aug 12	30	No	No	–
57984	2017 Aug 19	30	No	No	–
57995	2017 Aug 30	30	No	Yes (1)	No
57997	2017 Sep 1	30	No	Yes (2)	No
57998	2017 Sep 2	30	No	No	–
57999	2017 Sep 3	30	Yes	Yes	Yes
58089	2017 Dec 2	30	No	No	–

NOTE—The numbers in parenthesis in the last two columns indicate the number of events for that observation. The pulsar was detected in its bright state on MJD 57999, hence the number of single-pulse events are not recorded here.

<sup>a</sup>The MWA was unable to point correctly for this attempt. UTMOST has a marginal bright state detection lasting ∼5 minutes. Single-pulse data were not available for this observation, thus we cannot comment on whether single pulses were detected.

Table 4.2: Observation parameters on 2017 September 3.

Parameter	MWA	UTMOST
Center frequency (MHz)	154.24	835.59
Bandwidth (MHz)	30.72	31.25
System temperature (K)	473	278 <sup>a</sup>
Gain (K Jy <sup>-1</sup> )	0.24	2.3
FWHM (arcmin)	$\approx 2.8$	$0.77 \times 168$
Time resolution ( $\mu$ s)	100	655.36
Frequency resolution (MHz)	0.01	0.78125
UTC start time	02:05:09	02:05:56
Observations duration (s)	5154	1799
Dispersion smearing in lowest channel (ms) <sup>b</sup>	1.26	0.48
Dispersion delay across bandwidth (ms) <sup>b</sup>	2887.81	18.12
Dispersion delay between observed bands (ms) <sup>b,c</sup>	8532.06	

<sup>a</sup>See Section ?? for details regarding the flux density calibration of UTMOST.

<sup>b</sup>Assuming a dispersion measure of 40.75 pc cm<sup>-3</sup> – see Section 4.4.2 for details.

<sup>c</sup>Delay between the top of UTMOST band and the bottom of the MWA band.

### 4.3.1 UTMOST

PSR J1107–5907 was typically observed for approximately 30 minutes around the meridian transit of the source. At its declination, the source transits the  $\sim 4^\circ$  primary beamwidth in 31 minutes. The UTMOST real-time pulse detection system, which runs HEIMDALL<sup>3</sup>, reports pulse candidates with a signal-to-noise ratio  $S/N > 10$  while operating. Additionally, UTMOST is able to produce coherently de-dispersed pulses from voltages and fold the pulsar time series in real time, allowing alerts to be transmitted within 60 s regarding whether the source is active or if there have been single-pulse events.

The UTMOST backend writes SIGPROC<sup>4</sup> filterbank format files to disk with  $327\,\mu\text{s}$  time resolution resolution for 320 frequency channels at a frequency resolution of 98 kHz. In normal operations, these are decimated to  $655\,\mu\text{s}$  and  $40 \times 0.78\,\text{MHz}$  channels before being archived, but the decimation process was interrupted for the majority of observations and the high-resolution data were recorded. After the bright-state detection in September, the pre-decimation data were not retrieved, so we instead used the coarser-resolution data. For all observations of PSR J1107–5907 (excluding 2017 April 22), the data were incoherently de-dispersed and subdivided into single-pulse data files (“archives”) using the DSPPSR pulsar data processing software (van Straten & Bailes, 2011). At the time of the primary bright state detection of PSR J1107–5907 in this paper (2017 September), the SEFD of UTMOST is estimated to be  $\sim 120\,\text{Jy}$  with an uncertainty of  $\sim 50\%$ .

### 4.3.2 MWA

All data examined in this campaign were collected in Phase II of the MWA using the VCS, in both the compact and extended configurations (see Section 2.1). For all of our observations, we observed with a contiguous 30.72 MHz bandwidth (i.e.

---

<sup>3</sup><https://sourceforge.net/projects/heimdall-astro/>

<sup>4</sup><http://sigproc.sourceforge.net/>

all 24 coarse channels are adjacent) at a center frequency of 154.24 MHz.

#### 4.3.2.1 Buffered VCS recording

One of the difficult aspects of observing this pulsar with the MWA-VCS is the inherent limitation to the amount of data we can record at any time (storage capacity is reached after  $\approx 100$  minutes). To mitigate this, we observed the pulsar with the VCS in a bespoke buffer mode (P. Hancock et al. in prep.), where rather than writing data to disk, the voltages are kept in memory for as long as possible. When we receive a trigger from UTMOST that the pulsar was either in its bright state or emitting single pulses, we dump those voltages in memory onto the disks while continuing to record new data. This effectively gives the VCS the ability to record voltages from approximately three minutes prior to the actual trigger time. The buffered VCS mode is still under development, but we were able to use an early version of this recording mode between 2017 April–December, albeit with significant human interaction (triggers from UTMOST were sent manually and the VCS recording also needed to be started and stopped manually). Using this prototype stage of buffered recording, we triggered voltage capture in three instances (out of 10 observations) when UTMOST detected single pulses from PSR J1107–5907 (see Table 4.1).

For the observation on 2017 September 3, when the pulsar was in its bright state, we were not operating in this buffer mode and had scheduled a “normal” VCS observation (1.5 hr) to begin recording  $\sim 1$  minute before the target entered the UTMOST beam. Regardless of the VCS recording mode, the captured voltages are in the same format and thus need to be post-processed and calibrated using the standard pipeline.

#### 4.3.2.2 Tied-array beamforming

The tied-array beamformed data were procedure using the same procedures as laid out in Sections 2.1.2.2 and 3.4.2.1. In the case of the bright-state detections,

the calibration model was produced from an observation of Pictor A (PKS 0518–45), approximately 4 hr before the start of the observation. After the recent reconfiguration of the MWA, data from 38 of the 128 tiles were excised due to poor calibration solution quality and/or unreliable dipole elements. The recorded voltages were de-dispersed and subdivided into single-pulse archives using DSPSR.

#### 4.3.2.3 Flux density calibration

Flux density calibration was realized using the method described by Meyers et al. (2017), which we briefly summarize below. The flux density estimation is carried out by simulating the tied-array beam pattern and combining it with the tile beam model (Sutinjo et al., 2015; Sokolowski et al., 2017), thereby allowing the gain ( $G$ ) and system temperature ( $T_{\text{sys}}$ ) to be calculated. This involves integrating over the tied-array beam pattern (to determine the gain) and then over the product of the tied-array and tile beam patterns with a given sky temperature map (to determine the sky temperature). We elected to use the Global Sky Model of de Oliveira-Costa et al. (2008), evaluated at 154.24 MHz, as our sky temperature map. The simulations assume that the tied-array beamforming process is ideal and that we should see an increase in S/N by a factor of  $\sqrt{N_{\text{tiles}}}$ , as previously explained. However, in general, the theoretical improvement is not achieved due to a combination of factors including calibration quality, the beam-forming process, and the beam models employed. At the time of the bright-state detection with UTMOST, we achieved  $\approx 60\%$  of the theoretical improvement. Using the estimated gain and system temperature, and taking into account the above considerations (see equation 2 of Meyers et al., 2017), the SEFD during the bright state observation was  $\sim 3300$  Jy.

## 4.4 Results and Discussion

Throughout this Section, we focus on the simultaneous bright-state detection on MJD 57999 (2017 September 3), unless otherwise noted in the text.

### 4.4.1 Pulse finding and cross-matching

We used the PSRCHIVE (Hotan et al., 2004; van Straten et al., 2012) software suite to process the single-pulse archives produced by DSPSR. Radio-frequency interference (RFI) was mitigated using the PAZ routine by utilizing the built-in median-smoothed difference algorithm. For the MWA, we also excised the edge channels of each of the 24 coarse channels to mitigate the effects of aliasing introduced by the channelization process. We then summed the archives for every pulsar rotation in polarization and frequency to create a time series of each rotation, ensuring they were re-binned to the same time resolution (256 bins, or  $\Delta t \approx 987 \mu\text{s}$ ). To find individual pulses in these time series, we used the PSRSPA routine with a detection threshold of  $6\sigma$  on the overlapping time when the pulsar was active for both telescopes, which corresponds to  $\sim 1344$  s. The signal-to-noise ratio thresholds were then converted into flux density limits using the radiometer equation,

$$\sigma_\nu = \frac{\text{SEFD}}{\sqrt{n_p t_{\text{int}} \Delta\nu}}, \quad (4.1)$$

where  $\sigma_\nu$  is the  $1\sigma$  noise measured in Jy at frequency  $\nu$ ,  $n_p$  is the number of polarizations sampled,  $t_{\text{int}}$  is the integration time (in this case, because we are applying this to the measured S/N of each time sample in the time series,  $t_{\text{int}} = \Delta t \approx 987 \mu\text{s}$ ), and  $\Delta\nu$  is the bandwidth.

A special consideration needs to be made for UTMOST, given that it only samples a single polarization ( $n_p = 1$ ). For polarized sources, depending on the degree of polarization, this means that the measured flux densities can be significantly inflated or reduced. PSR J1107–5907 is a moderately polarized pulsar, and from archival Parkes data at 3.1 GHz (a subset of that used by Young

et al., 2014) the bright-state emission circular polarization fraction is  $V/I \approx -0.1$ . This means that UTMOST flux densities need to be scaled<sup>5</sup> by a factor of 0.9 for the analysis herein (see Appendix C for details on computing the scaling factor). Additionally, due to the bandpass shape and RFI excision at UTMOST, the estimated S/N for pulses is underestimated by  $\sim 25\%$ , thus we apply another scaling factor of 1.25 to correct for this when converting to flux density units. Bandwidth considerations need to also be made for the MWA data, given that 10 of the 128 fine channels (each 10 kHz wide) are zero-weighted on each side of all coarse channels to avoid aliasing effects. This culminates in reducing our effective bandwidth to  $\sim 70\%$  of the full 30.72 MHz, ergo the MWA flux densities are scaled by a factor of  $(0.7)^{-1/2} \approx 1.2$  to correct for this.

Taking into account the above considerations, the nominal flux density limits are then  $6\sigma_{154} \approx 97$  Jy and  $6\sigma_{835} \approx 4.6$  Jy for the MWA and UTMOST, respectively.

After the automated pulse finding (using data that had been processed with an updated ephemeris; see Section 4.4.2), each candidate pulse was visually inspected to ensure the validity of the detection, resulting in the identification and subsequent removal of 1 MWA and 17 UTMOST spurious events that were narrowband and likely RFI. In total, 86 pulses were detected at the MWA, and 283 with UTMOST above the  $6\sigma$  level<sup>6</sup>. We created a catalog of these detections for each telescope and cross-matched them based on their assigned “pulse number” using the STILTS software package (Taylor, 2006). The pulse number is computed as the number of rotations since some arbitrary time (for us, MJD 53089.00000), which is defined in the pulsar ephemeris. Thus, the same rotation of the pulsar can be compared at each telescope. After accounting for the disper-

---

<sup>5</sup>Assuming that a similar level of circular polarization is present at 835 MHz. Generally speaking, the frequency dependence of circular polarization is an open question, and thus the scaling factor could be in error. However, we stress that the error introduced by incorrectly estimating the circular polarization fraction is far outweighed by the intrinsic uncertainty in the UTMOST SEFD, which is  $\sim 50\%$ .

<sup>6</sup>We note that, for UTMOST, there are 20/283 pulses with peak flux densities between 3.3–4.3 Jy, which is slightly less than the nominal limit (i.e.  $\geq 4.3\sigma$ ).

sive delay between the telescopes, 51 pulses were simultaneously detected with the MWA and UTMOST, i.e. a match rate (based on the MWA population) of 60%.

The same processing steps were applied to the other three simultaneous observations (MJD 57970, 57995, and 57997 in Table 4.1) when UTMOST detected single pulses from PSR J1107–5907 while it was in its weak state. In total, five single pulses were detected over those three separate observations. For one of the two single pulses detected at UTMOST on MJD 57970 (2017 August 5), there was a marginal simultaneous single-pulse detection from the MWA. This single-pulse was detected in the UTMOST observation with  $S/N \sim 14$ , and was consequently detected (with a  $S/N \lesssim 5$ ) by eye when looking at the corresponding pulsar rotation number in the MWA data. There were no other coincident detections of weak state single pulses with the MWA.

#### 4.4.2 Dispersion measure

Propagation effects imposed on pulsar signals by the interstellar medium (ISM) are much stronger at low radio frequencies (e.g. dispersive delays scale as  $\nu^{-2}$ ). To that end, measurements of the dispersion measure (DM) of a pulsar from even a single observation at low frequency can often be equally, if not more, precise compared to that obtainable using months of timing data at higher frequencies from larger telescopes. These refinements are important for understanding the ISM along the line of sight to the pulsar and for pulsar timing experiments at higher frequencies (e.g. Pennucci et al., 2014; Lam et al., 2015; Lentati et al., 2017), where any errors in the DM, due to the frequency lever-arm or time variability, are not obvious from single observations.

We averaged together single pulses above a detection significance of  $6\sigma$ , using the cataloged dispersion measure ( $40.2 \pm 1.1 \text{ pc cm}^{-3}$ ; Young et al., 2014). There was significant residual frequency-dependent delay of the arrival of pulses in the MWA data, corresponding to an excess time delay across the observed 30.72 MHz

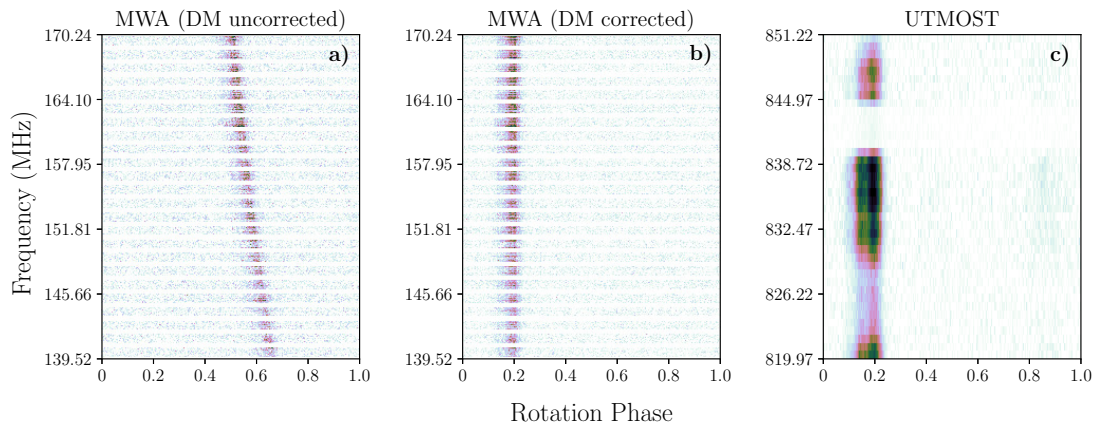


Figure 4.1: Frequency vs. phase waterfall plot of the signal arriving at both telescopes. The panels are as follows: (a) the addition of all pulses detected with a signal-to-noise above 6, de-dispersed to the nominal cataloged dispersion measure ( $40.2 \text{ pc cm}^{-3}$ ); (b) the MWA data again, de-dispersed with the optimal DM output by a PDMP search ( $40.75 \text{ pc cm}^{-3}$ ), and; (c) the UTMOST data de-dispersed with a DM of  $40.75 \text{ pc cm}^{-3}$ . The horizontal stripes in the MWA images are where edge channels have been flagged for each of the 24 coarse channels. For the UTMOST plot, a fraction of the bandwidth around 841 MHz was removed due to RFI caused by mobile phone networks, and the reduced signal around 826 MHz is due to the instrument bandpass.

bandwidth of  $\approx 39$  ms, which is  $\sim 15\%$  of the pulse period (see Figure 4.1a). The delay in the MWA band is dispersive, exhibiting the classical quadratic sweep, which is expected for an offset from the true DM.

To determine a more precise DM, we made use of the PSRCHIVE routine PDMP on the MWA data, which calculated the optimal DM to be  $40.75 \pm 0.02$  pc cm $^{-3}$ . While this is within the uncertainty associated with the original and cataloged value,  $DM_{\text{cat}} = 40.2 \pm 1.1$  pc cm $^{-3}$ , a correction of  $\delta DM = 0.55$  pc cm $^{-3}$  is indeed significant, as is the factor of  $\sim 50$  improvement in precision. This DM offset introduces a delay across the UTMOST bandwidth of  $\sim 1/4$  of a time sample ( $\sim 0.25$  ms), and hence it was not discernible from the UTMOST data (see Figure 4.1). The revised DM results in a delay between the top of the UTMOST band and bottom of the MWA band of approximately 8532 ms (see Table 4.2).

We note that, while this level of precision in DM is impressive from a single observation, we are only using the brightest pulses from the  $\sim 20$  minutes of data containing the bright state and do not account for any potential profile evolution, nor the possibility of a frequency-dependent (chromatic) DM (Cordes et al., 2016; Shannon & Cordes, 2017). Nonetheless, for our purposes, the updated DM produces higher signal-to-noise ratios for both the profiles and single pulses, and aligns the profiles in phase without any other alteration to the ephemeris used.

#### 4.4.3 Pulse profile

After determining the DM offset, we applied the correction and re-processed the bright-state data, again conducting a single-pulse search as described in Section 4.4.1. Combining only those pulses with a detection significance  $\geq 6\sigma$ , as defined by the PSRSPA single-pulse finding algorithm from PSRCHIVE (86 pulses for the MWA, 283 pulses for UTMOST), we form a “pseudo-integrated” profile<sup>7</sup>

---

<sup>7</sup>We note that this includes those UTMOST pulses that are nominally less than the  $6\sigma$  flux density limit, which is ultimately due to the different ways in which the noise was estimated during single-pulse detections (automated off-pulse estimation) versus flux calibration (sigma-

(see Figure 4.2). This highlights the emission across a large portion of pulse longitude, hence Figure 4.2 is split into three phase regions, where we label these regions (left to right) with their corresponding profile component from Young et al. (2014): the “main pulse” (MP), “postcursor” (PC), and “precursor” (PR).

Even with the caveat that only a limited number of pulses contributed to these profiles, it is clear that there are some differences between the two frequencies. In particular, the PR component appears brighter, wider, and shifted at 154 MHz with respect to the 835 MHz profile. At MWA frequencies, the PR component appears as a gradual rise from a phase of  $\sim 0.6$  with a sudden cutoff around 0.9, whereas the equivalent UTMOST component only appears between  $\sim 0.8\text{--}1$  in phase and is smoother overall. Single pulses in the PC phase regions are recorded at both telescopes, but there was one exceptionally bright pulse in the MWA data ( $S/N \sim 150$ ) that dominates in this case, whereas the PC single pulses from UTMOST were typically quite weak (see Figure 4.3). This bright pulse acts as an alignment anchor, indicating that the profile alignment is real and thus the differences in the profile features must be due to the emission mechanism(s) and/or magnetospheric propagation effects at play.

#### 4.4.4 Spectral index

From the individually matched pulses (51 in total), we calculated the spectral index distributions for the MP and PR components using their measured fluences. For the MP component, the mean spectral index is relatively typical of the normal pulsar population, with  $\alpha_{\text{MP}} = -1.85 \pm 0.08$  and a standard deviation of 0.50. The mean spectral index of the PR component is steeper than typical with  $\alpha_{\text{PR}} = -2.21 \pm 0.10$  and has a narrower distribution with a standard deviation of 0.35 (see Figure 4.4). The only pulse in the PC phase region with a counterpart (see Figure 4.3) has an extreme spectral index of  $\alpha_{\text{PC}} \approx -3.5$ . We note that, given our definition of fluence, we are often summing over multiple components within

---

clipping).

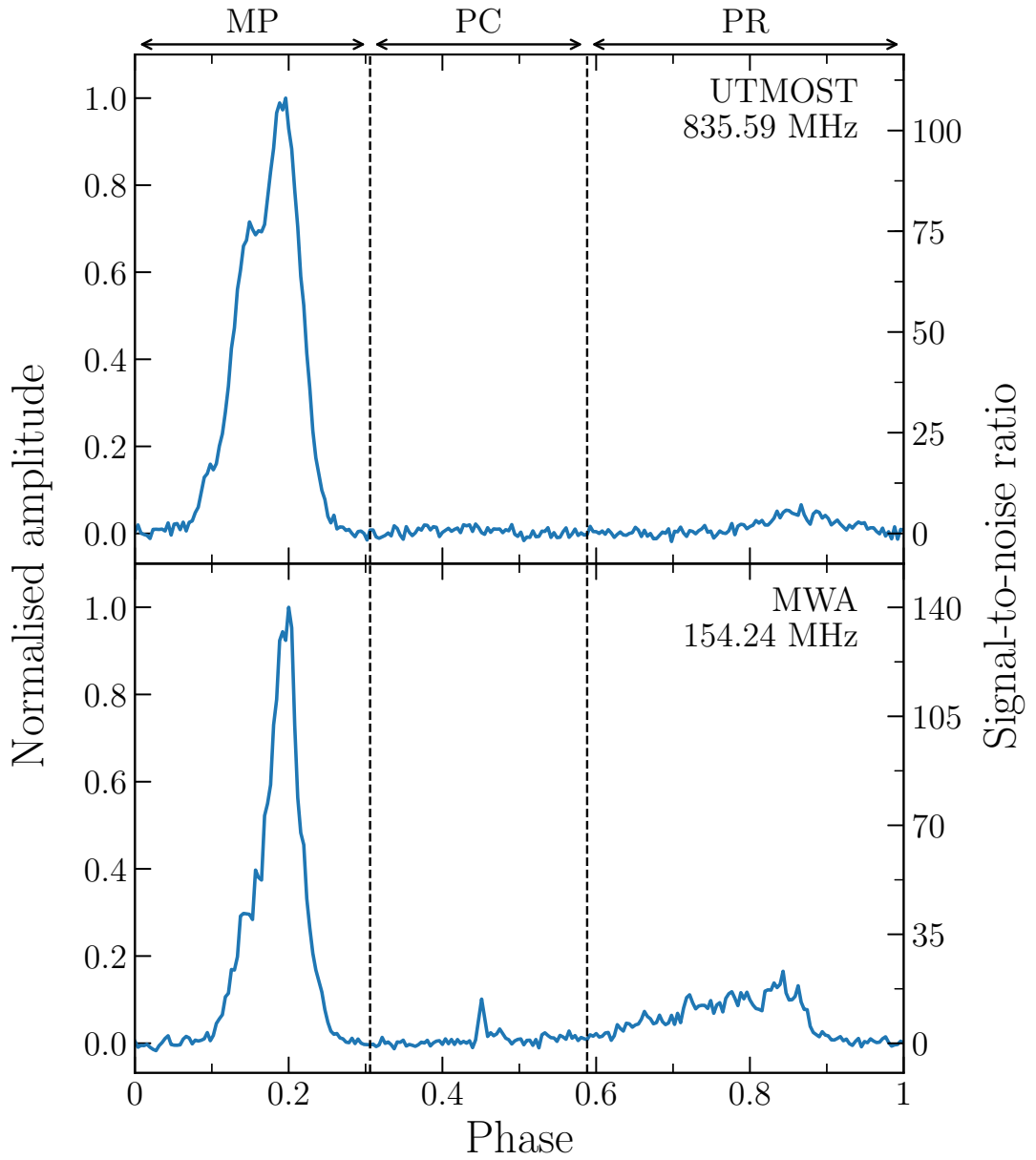


Figure 4.2: A pseudo-integrated profile created by averaging all pulses with  $S/N > 6$  of J1107–5907 from each telescope from the 2017 September 3 detections (86 from the MWA, 283 from UTMOST). The profile is split into three regions, corresponding to the components within, which have been labelled based on the classifications made by Young et al. (2014). It appears that the postcursor (PC) and precursor (PR) components are more prominent at lower frequencies. The PR emission is also shifted and has a significant rise time at low frequencies.

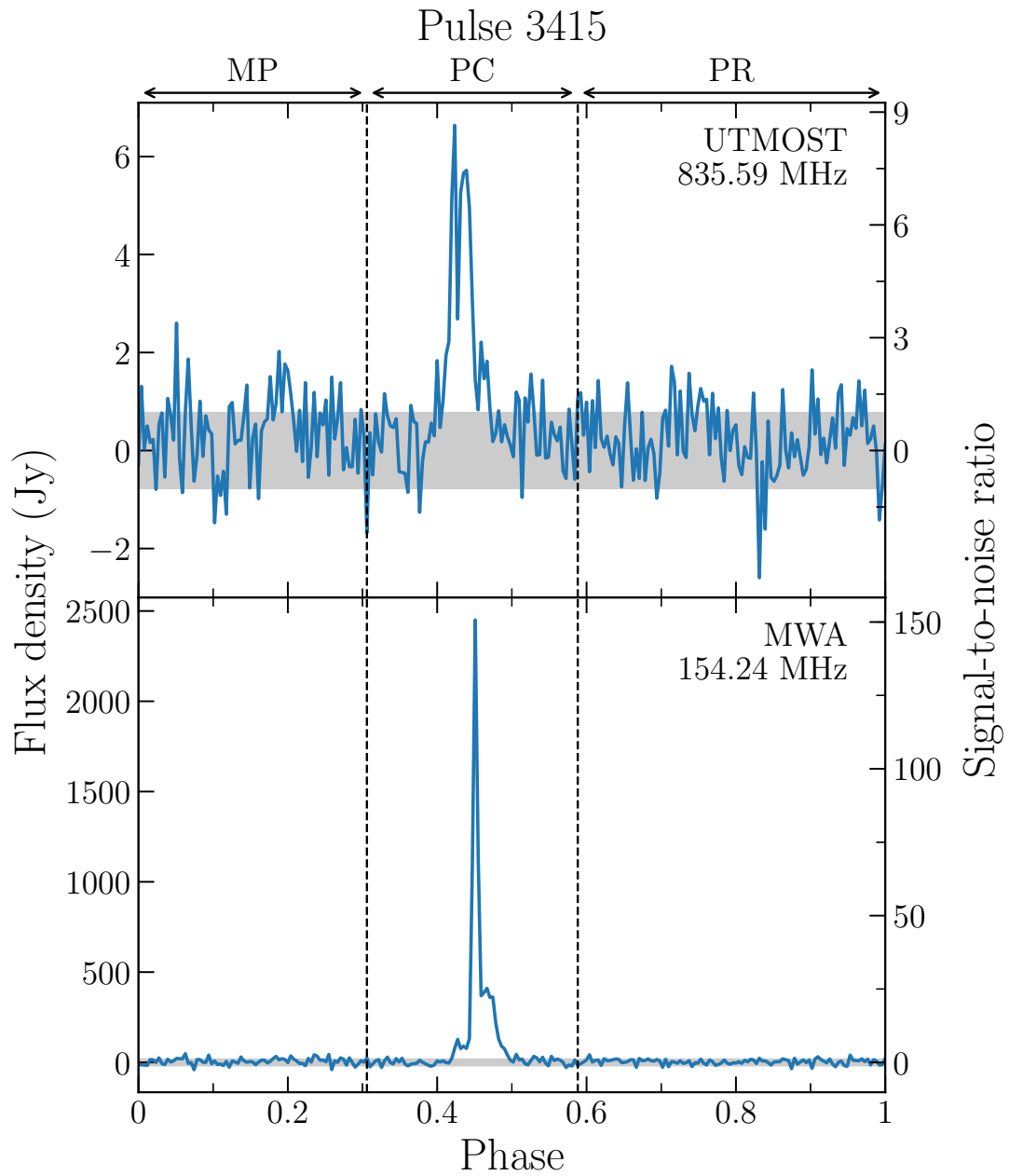


Figure 4.3: A relatively weak PC-component pulse detected by UTMOST (top) with a peak flux density of  $\approx 7$  Jy, which is exceptionally bright at MWA frequencies (bottom), with a peak flux density of  $\approx 2.5$  kJy. The grey-shaded region indicates the  $\pm 1\sigma$  noise level. This pulse occurred 3415 rotations after the first simultaneously observed pulsar rotation.

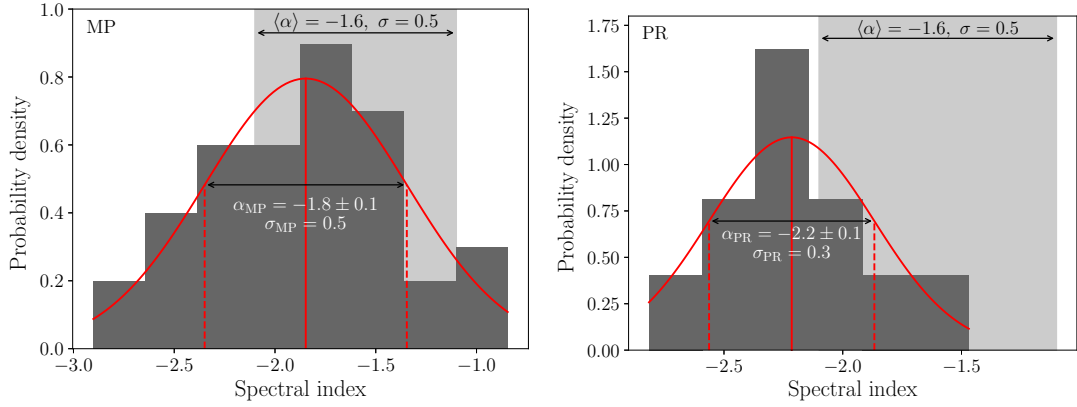


Figure 4.4: Spectral indices between the MWA (154.24 MHz) and UTMOST (835.59 MHz) for cross-matched pulses, separated by component. The typical spectral index range (i.e. a mean of  $\alpha = -1.6$  and standard deviation of  $\sigma = 0.5$ ) for pulsars, as determined by Jankowski et al. (2018b), is shaded in the background to provide context. The Gaussian fits are only indicative, given the small number of pulses contributing to each of the distributions (39 and 11 for the MP and PR components, respectively), but identify the mean spectral indices to be  $\alpha_{\text{MP}} = -1.85 \pm 0.08$  and  $\alpha_{\text{PR}} = -2.21 \pm 0.10$  for the MP and PR components, respectively.

the specified MP and/or PR windows (e.g. pulse 3773 in Figure 4.6), which can act to bias the measured spectral index.

The spectral index distribution for the MP component is generally within the normal pulsar population spectral index distribution, which has a mean of  $\langle \alpha \rangle = -1.6 \pm 0.03$  and a standard deviation of  $\sigma = 0.5$  (Jankowski et al., 2018b; see also Maron et al., 2000a; Bates et al., 2013), as indicated by the shaded regions in Figure 4.4. The steepness of the PR component spectral index could explain the disparity between the number of pulses detected in each phase range (see Section 4.4.6), where the PR component will become brighter at lower frequencies faster than the MP component, thus somewhat equalizing our MP-to-PR ratio measured with the MWA. However, scaling the detected MWA pulses in the PR phase range with the measured spectral index to the expected flux density at 835.59 MHz, we find that only eight of the 43 pulses fall below the nominal UTMOST flux density limit. Thus, there must be some other contributing factor as to why some of these pulses are detected at the lower, but not the higher,

frequencies.

Based on a radius-to-frequency mapping argument, it is possible that, at low frequencies, the magnetospheric region producing the PR emission is actually distinct from, and possibly more active than, the higher frequency emission region. The separate emission regions would therefore also experience different propagation paths through the magnetosphere along the line of sight, which could also act to suppress the higher-frequency emission in this region.

#### 4.4.5 Pulse energy distributions

Characterizing the pulse energy or amplitude distribution of a pulsar is useful in understanding the pulse emission process. The pulse energy distributions of individual pulsars vary substantially, but are typically seen to be a log-normal (LN) or exponential distribution (e.g. Burke-Spoloar et al., 2012), or a power law (PL) in the case of giant pulses (e.g. Bhat et al., 2008; Mickaliger et al., 2012; Meyers et al., 2017). Few studies of this kind have been done for intermittent pulsars in general (e.g. Sobey et al., 2015). Here, we attempt to characterize the pulse energy distributions of the MP and PR components (see Figure 4.2) from the MWA and UTMOST.

The pulse energy distribution of PSR J1107–5907 is hard to assess, given its intermittent nature, but there are a handful of examples where estimates have been made. Burke-Spoloar et al. (2012) attempted to estimate the Gaussian and LN distribution parameters for a weak state detection of one pulse, so the results are not statistically significant. Young et al. (2014), who have the largest sample of pulses from PSR J1107–5907 in all emission states in the literature, report that a PL distribution is the most appropriate fit during the bright state, while the weak state is better parametrized by a LN distribution. However, the authors use the term “pulse energy” interchangeably with pulse intensity (i.e. flux density or amplitude), thus it is unclear whether we can directly compare distribution parameters. In any case, a LN model was not fit to the data, so we

cannot compare those distribution parameters. Mickaliger et al. (2018a), through reprocessing of PMPS archival data, also re-detect PSR J1107–5907 in a single-pulse search in the weak state. The data did not provide sufficient statistical power to discriminate between the trial distributions (PL, LN and exponentially truncated power law (TPL)), which is to be expected given the small number of detections (18 out of 8300 rotations).

We define the pulse energy (or “fluence”) as the integrated flux density over the emission component window above the baseline fluctuations. During the integration, the baseline noise was estimated independently for each pulsar rotation using the sigma-clipping method. In our case, we integrate over each of the three phase regions defined previously for every pulsar rotation, regardless of whether there was a pulse detected, and take that as an estimate of the component fluence for that rotation. We normalize our pulse energies by dividing each measurement by the average energy,  $\langle F \rangle$ , for each of the pulse components over the  $\sim 5300$  rotations (see top row of Figure 4.5). The Python POWERLAW<sup>8</sup> module (Alstott et al., 2014) was used to fit distributions typically tested in the literature: a PL, LN, and TPL. We also limited ourselves to only fit pulses with a normalized fluence  $F \geq 4 \langle F \rangle$ , which we note is a somewhat arbitrary choice. In general, the POWERLAW package can compute the appropriate cutoff by minimizing the Kolmogorov-Smirnov distance, but in this case, because we are so heavily dominated by the “noise,” the automatic estimation fails—so we elected to ensure that only real pulses are being included by setting a relatively conservative limit. The respective non-normalized probability density forms of these distributions

---

<sup>8</sup><https://github.com/jeffalstott/powerlaw>

are given in equations (4.2), (4.3), and (4.4) below:

$$P_{\text{PL}}(x) \propto x^{-\beta} \quad (4.2)$$

$$P_{\text{LN}}(x) \propto \frac{1}{\sigma x} \exp \left[ -\frac{(\ln x - \mu)^2}{2\sigma^2} \right] \quad (4.3)$$

$$P_{\text{TPL}}(x) \propto x^{-\Gamma} \exp(-\lambda x) \quad (4.4)$$

To determine which of the distributions best parametrizes our data, we compare the log-likelihood ratios ( $R$ ), initially with respect to a PL, and the corresponding significance ( $p$ -values), which are calculated as part of the fitting procedure. In this case, negative values of  $R$  favor the opposing model (i.e. not the PL). Parameters for the best-fitting distributions of each kind are given in Table 4.3, along with their associated  $R$  and  $p$ -values with respect to a PL. The best fits are shown in the middle and bottom rows of Figure 4.5.

For the MP component, a LN distribution is favored for the UTMOST data ( $R = -13.3$ ), while either a LN or TPL are statistically plausible for the MWA data. To better determine which distribution is favored for the MWA overall, we compared the  $R$  and  $p$ -values of a TPL with respect to a LN distribution, which indicated that the LN distribution may be a better fit ( $R = 0.1$ ), but the significance ( $p = 0.9$ ) is inconclusive.

We conducted the same fitting procedures for the PR component data and found that we cannot significantly discern which trialled model provides the best fit for either telescopes. The fits to the MWA data slightly favor a LN or TPL distribution based on their  $R$  values, however, we cannot statistically reject the PL based on the respective  $p$ -values. As found for the MP component, a LN model is favored over a TPL ( $R = 0.02$ ), however the  $p$ -value here is also inconclusive ( $p = 0.6$ ). For the UTMOST data, given there are only six data points, caution must be taken when interpreting the results, but the log-likelihood ratios tend to favor a LN distribution in all cases, including when compared to a TPL.

From a global perspective, it appears that a simple PL distribution is not

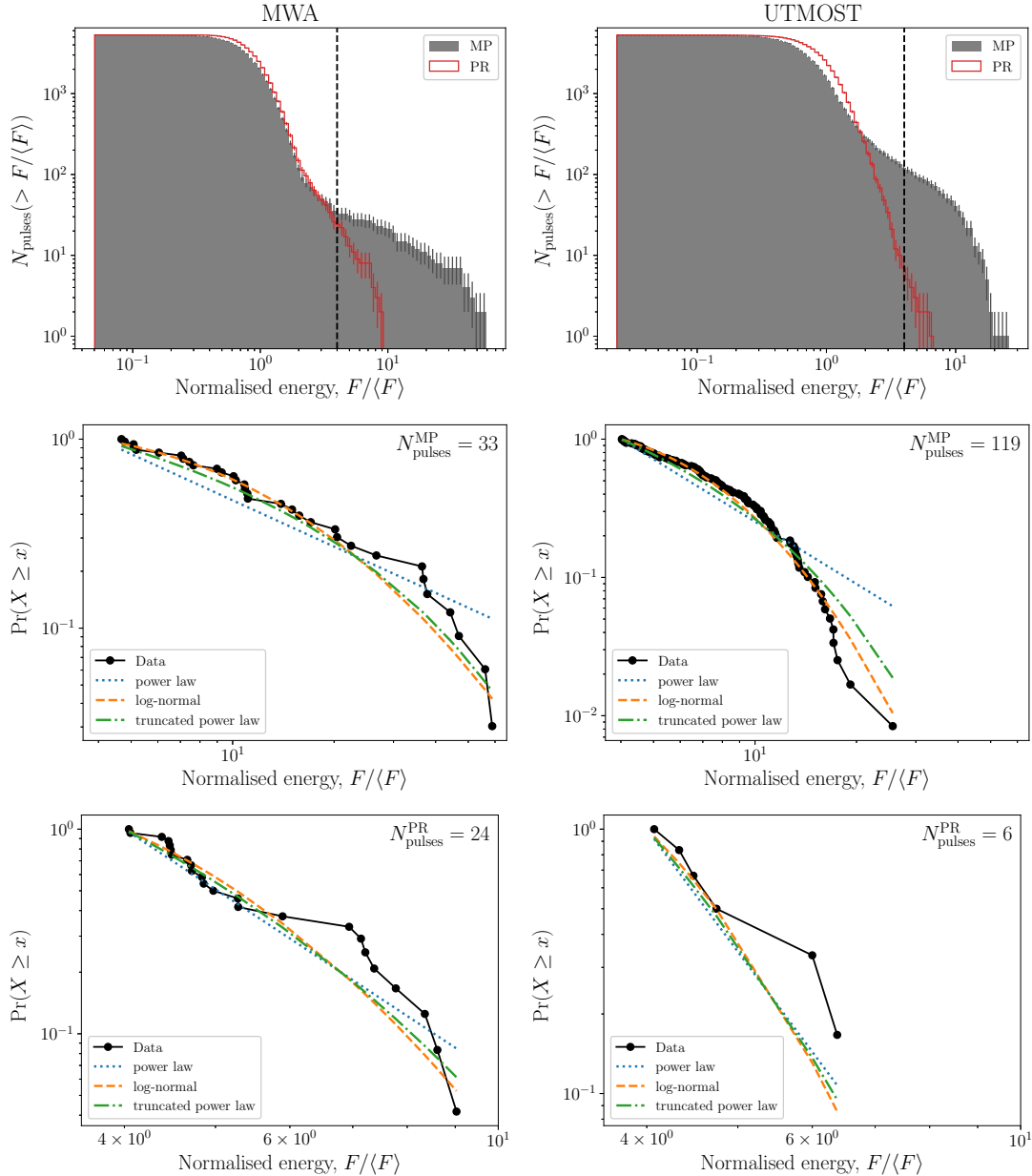


Figure 4.5: Normalized fluence cumulative distributions for the MP and PR components from the MWA (left) and UTMOST (right). The top row shows the number of pulses above a given normalized energy. The middle and bottom rows show the distribution for those pulses in the MP and PR phase regions, respectively, with normalized fluences  $F \geq 4\langle F \rangle$  (indicated by the vertical dashed line in the top row). The best-fit models are also drawn (see Table 4.3), though the PR component from UTMOST is not well constrained given only six data points. For the middle and bottom rows, the ordinate is scaled to represent the fraction of pulses above a given normalized energy, i.e. the survival function,  $\Pr(X \geq x)$ .

appropriate for our data, with the caveat that we are limited by small number statistics. Assuming that the pulse energy distribution does not change “type” as a function of frequency or component, we tend to favor a LN distribution for the MP and PR pulse energies. In this respect, PSR J1107–5907 is like most normal pulsars (e.g. Burke-Spolaor et al., 2012).

#### 4.4.6 Single pulses and nulls

As with most long-period pulsars, there is wide variation in the pulse-to-pulse structure and intensities from PSR J1107–5907 (see Figure 4.6). This behavior is present at both frequencies. Specifically, counterparts are not always seen for all bright pulses, even to the level of individual pulse components. There are examples of emission within both the MP and PR locations at one frequency but not necessarily at the other (e.g. the first column in Figure 4.6).

Within each of the emission regions, the number of pulses detected are also different. The MWA detected 40 pulses in the MP phase region and 43 pulses in the PR region (a 1:1 ratio), whereas UTMOST detected 241 and 38 in the MP and PR regions, respectively (a 6:1 ratio). With additional detections, it would be possible to (statistically) probe this aspect of the pulse-to-pulse variation and intermittency.

The median number of rotations between detected pulses is  $31 \pm 6$  and  $9 \pm 1$  pulsar rotations for the MWA and UTMOST, respectively. These could be considered apparent nulls, though in this case a null is simply defined as a  $\lesssim 6\sigma$  single pulse event. In reality, there are weaker pulses visible in the time series of both telescopes, so the numbers we present here should be considered only as upper limits.

In addition to the above, it appears that the pulsar enters its bright state earlier at UTMOST frequencies, and also finishes later than emission at MWA frequencies. There are four MP pulses, one PC pulse, and one PR pulse detected by UTMOST before the first MWA pulse in the respective phase regions. The

Table 4.3: Best-fitting parameters for the normalized fluence distributions.

Component	$N_{\text{pulses}}$	Power law (PL)	Log-normal (LN)		Truncated power law (TPL)		
Main pulse (MP)							
MWA	33	$1.81 \pm 0.14$	$2.3 \pm 0.5$	$1.0 \pm 0.2$	$-4.8/0.03$	$1.0 \pm 0.1$	$0.03 \pm 0.01$
UTMOST	119	$2.49 \pm 0.13$	$1.8 \pm 0.1$	$0.6 \pm 0.1$	$-13.3/0.002$	$1.0 \pm 10^{-5}$	$0.12 \pm 0.01$
Precursor (PR)							
MWA	24	$4.0 \pm 0.6$	$1.3 \pm 0.4$	$0.4 \pm 0.3$	$-0.98/0.3$	$1.0 \pm 0.7$	$0.4 \pm 0.1$
UTMOST	6	$5.8 \pm 1.9$	$1.2 \pm 0.4$	$0.3 \pm 0.7$	$-0.17/0.68$	$1 \pm 2$	$0.8 \pm 0.7$
NOTE—Uncertainties are the standard deviation of results after bootstrapping 100 times. The nominal power law index from Young et al. (2014) is $\beta = 1.29$ .							

<sup>a</sup>The log-likelihood ratio,  $R$ , and corresponding  $p$ -values with respect to a power law. A negative  $R$  corresponds to favoring the opposing model.

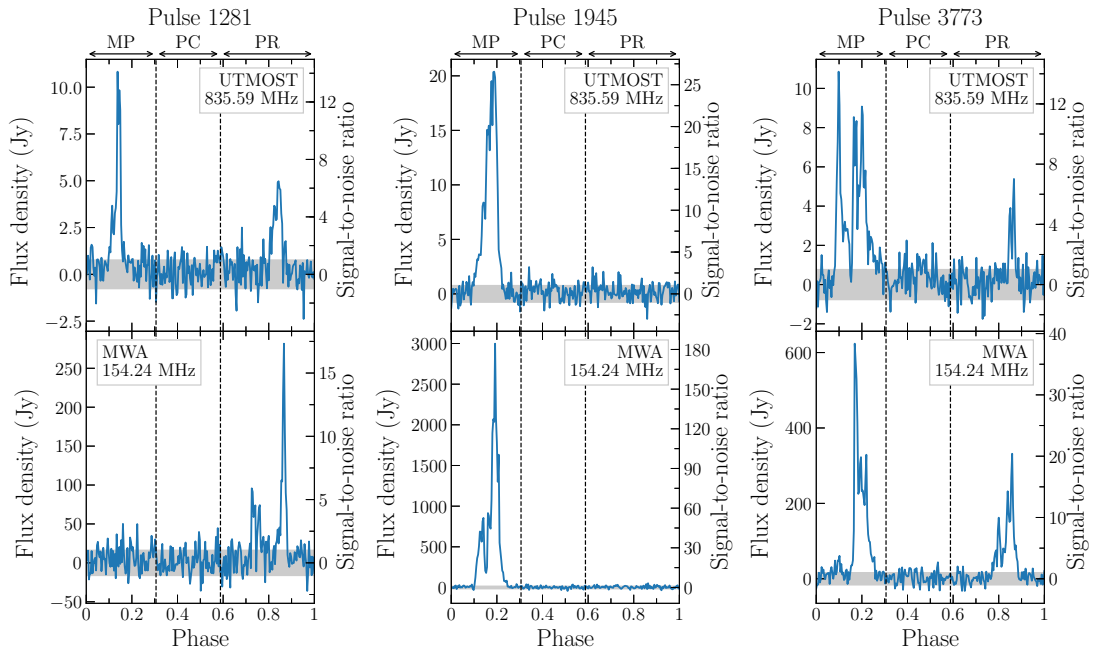


Figure 4.6: Examples of coincident single pulses between UTMOST (top) and the MWA (bottom). There is a wide variety of pulse shapes and intensities, including instances where entire components are apparently missing at one frequency (e.g. the right-most column of pulses shown here). These examples also imply that the spectral index is varying from pulse-to-pulse and between components substantially, which is not unexpected. The gray-shaded region indicates the  $\pm 1\sigma$  noise level. Each pulse is titled with its pulse number, corresponding to the number of rotations since the first simultaneous MWA and UTMOST rotation.

Table 4.4: Pulse rates for each component of PSR J1107–5907 above the given minimum peak flux density detected,  $\min\{S_\nu\}$ .

Telescope	$\min\{S_\nu\}$ (Jy)	Total (hr $^{-1}$ )	MP (hr $^{-1}$ )	PC (hr $^{-1}$ )	PR (hr $^{-1}$ )
MWA	136	230	107	8	115
UTMOST	3.3	760	645	13	101

first MWA pulse in any phase window arrives 14 pulsar rotations ( $\sim 3.5$  s) after the first UTMOST pulse. Additionally, there are three MP pulses and two PR pulses detected by UTMOST after the last MWA pulse in the respective phase windows. The last UTMOST pulse from any phase window arrives 53 pulsar rotations ( $\sim 13.4$  s) after the final MWA pulse.

Scaling the peak flux densities of these UTMOST pulses to MWA frequencies, with their corresponding component spectral index (see Section 4.4.4), and comparing to the nominal flux density threshold placed on the MWA single pulse detection process, we expected to see at least five of the 11 UTMOST single pulses (the weaker pulses could feasibly have fallen below the MWA’s flux density threshold). This then suggests that, while the intermittency properties are roughly broadband, the details of the sporadic emission are different at widely spaced frequencies, where in this case we observed a handful of bright single pulses before and after that nominal bright state has begun/ended at the other frequency.

#### 4.4.7 Pulse rates and intermittency

In 5319 rotations of the pulsar, we detected 86 and 283 pulses from the MWA and UTMOST, respectively, corresponding to overall pulse rates of  $0.06\text{ s}^{-1}$  and  $0.21\text{ s}^{-1}$ . In general, we see that the number of PC and PR components detected at each telescope is similar, but the number of pulses arriving in the MP window are far fewer at MWA frequencies, regardless of the steep measured spectral index. For a component-wise split and summary, see Table 4.4.

We conducted nine simultaneous observations over the course of six months (excluding MJD 57865) using the MWA in conjunction with UTMOST and detected PSR J1107–5907 in the bright state only once. While we are limited by small number statistics (in terms of both attempts and detections), this indicates that at MWA frequencies, the duty cycle of bright-state emission from PSR J1107–5907 is  $\delta \sim 11\%$ . Additional observations (and detections) will be required to further constrain this number, but in general it seems to roughly agree with the few estimates available in the literature, i.e.  $\delta \sim 5\text{--}8\%$  (Young et al., 2014; Hobbs et al., 2016).

In addition to the contemporaneous observations with the MWA, we examined archival UTMOST data taken since mid-2015 for examples of both bright-state and single pulse detections (the “weak” state). Of 148 observations (including those simultaneous with the MWA), ranging in length from  $\sim 100\text{--}3600$  s and spanning  $\sim 1200$  days (see Figure 4.7), there were only five bright-state detections. The sensitivity of UTMOST has varied drastically in time due to hardware maintenance and upgrades, as well as the reconfiguration into a transit-only telescope (starting around 2017 May, lasting  $\sim 2$  months). Thus, the SEFD of the instrument is also included in Figure 4.7 as a sensitivity indicator. The bright-state duty cycle from UTMOST detections is  $\delta \sim 3.4\%$ , which is slightly lower than previously reported.

We can also calculate a duty cycle based on the duration of time PSR J1107–5907 for which was detected in the bright state with respect to the total observing time (e.g. Young et al., 2012, 2014)<sup>9</sup>. The bright state duty cycle evaluated in this way is  $\delta \sim 2.2\%$ , again lower than previous estimates. This estimate comes with the caveat that, for three of the five detections, the bright-state pulse train was not fully sampled (i.e. observations started after the bright state had already begun, or finished before it ended), so there is a bias toward a smaller duty cycle.

In the remaining observations, there were a total of 19 possible single-pulse

---

<sup>9</sup>The methods described by these authors are not applicable in our case, given the low number of detections, the irregularity in observing times and durations, and telescope sensitivity.

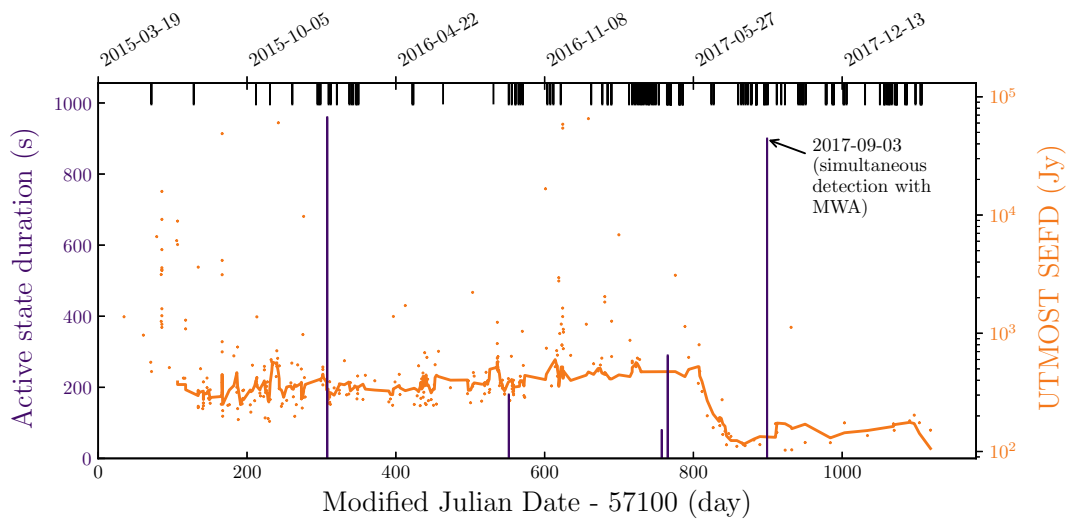


Figure 4.7: UTMOST observations, detections and sensitivity over time. Observations made without a bright state detection are shown as black lines at the top of the figure. Detections and the respective bright state duration are drawn in dark purple (left ordinate). Only for the first and last bright state detections was the full pulse train observed (i.e. beginning and end of the bright state was captured). The orange points are the estimated system equivalent flux density (SEFD) for UTMOST over time (right ordinate), calculated by calibrating the system to a standard bright pulsar (PSR J1644–4559). A 20-point running average, excluding the extreme outliers, is also drawn (solid orange line) to give a more representative measure of the sensitivity over time.

detections, but only five of these proved to be significant (one of which is the single pulse we simultaneously detected on 2017 August 5). The pulsar emits in the weak state much more frequently than the bright state, so we believe that we are sensitivity-limited for both telescopes, and only capture the brightest pulses of the weak-state emission.

#### 4.4.8 Rotation measure

The degree of Faraday rotation the radio emission from a source experiences when traversing the ISM is quantified by the rotation measure (RM). Typically, the RM is estimated by measuring the change in the polarization position angle across the observed bandwidth (e.g. Noutsos et al., 2008; Han et al., 2018) and thus requires the detector to measure the radiation polarization properties. While the UTMOST detects only right-hand circular polarization, the MWA is capable of producing fully polarimetric (Stokes  $I$ ,  $Q$ ,  $U$  and  $V$ ) data (S. Ord et al. submitted). Currently, the polarization response is undergoing self-consistency tests (M. Xue et al. submitted) and cross-validation (S. Tremblay et al. in prep.) that will be described in forthcoming publications, hence we do not provide a polarization profile. However, because RM estimates do not rely on absolute polarimetric calibration, we do provide an estimate of the RM for PSR J1107–5907 from the MWA data. Performing RM synthesis (Brentjens & de Bruyn, 2005) on the  $6\sigma$  pseudo-integrated profile (Figure 4.2) produces  $\text{RM}_{\text{obs}} = 23.85 \pm 0.08 \text{ rad m}^{-2}$ . The ionospheric RM contribution was calculated to be  $\text{RM}_{\text{ion}} \approx -2.1 \pm 0.2 \text{ rad m}^{-2}$  using an updated version of `IONFR`<sup>10</sup> (Sotomayor-Beltran et al., 2013), so that the latest version of the International Geomagnetic Reference Field (IGRF12; Thébault et al., 2015) could be used as an input, along with International GNSS Service vertical total electron content maps (e.g. Hernández-Pajares et al., 2009). Thus, the ISM contribution is  $\text{RM}_{\text{ISM}} = \text{RM}_{\text{obs}} - \text{RM}_{\text{ion}} = 25.95 \pm 0.28 \text{ rad m}^{-2}$ . This is consistent with the previously published value of  $23 \pm 3 \text{ rad m}^{-2}$  (Young

---

<sup>10</sup><http://ascl.net/1303.022>

et al., 2014), which does not account for ionospheric contributions. In order to comment further, we would require additional observations of PSR J1107–5907 in the bright state in order to obtain a better integrated profile and average over ionospheric effects in order to minimize their contribution to the uncertainties.

## 4.5 Low-frequency detection prospects

With the next generation of radio telescopes on the horizon, there will soon be new opportunities for pulsar searches. In particular, precursor instruments such as the MWA can be used to gain valuable insights into what can be expected in terms of survey yields (e.g. Xue et al., 2017). Furthermore, studying the frequency evolution of pulsar profiles down to the single pulse level is imperative to correctly measuring the pulse-to-pulse energetics, such as the spectral index.

The intermittency of PSR J1107–5907 is broadband, in that the pulsar switches between bright and weak states contemporaneously (see also Section 4.4.6), over frequencies separated by at least a factor of five. The bright-state duty cycle is comparable across frequencies, with  $\delta \sim 2\text{--}11\%$  corresponding to approximate interburst (or “off”) timescales of a few hours, and the bright-state duration is between one and 45 minutes. PSR J1107–5907 exhibits a relatively rare combination of bright emission, a moderate DM, and relatively active state-switching. Therefore, this pulsar serves as an interesting link between nulling, RRATs, and state-switching (intermittent) pulsars. For instance, its interburst timescale is similar to some RRAT burst-rates<sup>11</sup>; moreover, it also nulls during its bright emission state. Young et al. (2014) showed that, if the pulsar were a factor of  $\sim 4$  farther from Earth, it could be detected as a RRAT when in its weak mode, while the bright state could always be detected in both single-pulses and the average profiles (at 20 cm). We cannot comment on the weak-mode emission; however, if we increased the noise in the MWA data by a factor of  $\sim 16$ , which artificially replicates moving the pulsar to be  $\sim 4$  times as distant, then our combined pulse

---

<sup>11</sup>See <http://astro.phys.wvu.edu/rratalog/> for published RRAT data

rate drops to  $\sim 19 \text{ hr}^{-1}$ , similar to many RRATs. Furthermore, the steep spectral index and the extent of emission in longitude ( $\gtrsim 180^\circ$  based on Figure 4.2) argues in favor of the low-frequency detectability of pulsars similar to PSR J1107–5907.

In particular, planned pulsar and fast-transient searches using instruments such as the MWA and SKA-Low are in an advantageous position to find more such sources. The large field of view and the ability to regularly return to observing fields offer better prospects in detecting (and monitoring) objects like this. As an example, detection of super-bright bursts, like that observed with the MWA in this work (Figure 4.3) with a peak flux density of  $\sim 2.5 \text{ kJy}$ , imply that conventional single-pulse search and transient search pipelines would be capable of detecting these objects. While more sensitive telescopes at higher frequencies (e.g. Parkes, MeerKAT) may reveal the subtler features in the underlying emission, particularly in the apparent “off” emission states, the initial discoveries and identification of spectrally steep components will likely be made by these low-frequency wide field telescopes (e.g. Sobey et al., 2015).

## 4.6 Summary and Conclusions

The simultaneous detection of PSR J1107–5907 in its bright emission state with the MWA (154.25 MHz) and UTMOST (835.59 MHz) on 2017 September 3 marks the first low-frequency detection of this object. Our detections allowed a measurement of the spectral index, which for the main pulse component is relatively typical of the average pulsar population, where  $\alpha_{\text{MP}} = -1.85 \pm 0.08$ , whilst the so-called precursor component is steeper than average, with  $\alpha_{\text{PR}} = -2.21 \pm 0.10$ . We also characterized the fluence distributions of two prominent profile components (MP and PR), and contrary to previous results (which indicated a power law distribution), find that a log-normal distribution is the most appropriate fit for both the MWA and UTMOST data.

In addition to properties relating to the emission physics, the MWA also provides an excellent opportunity to study the effects of the ISM. We measured the

DM of PSR J1107–5907 and found that it required a correction to the cataloged DM ( $40.2 \pm 1.1 \text{ pc cm}^{-3}$ ; Lorimer et al., 2006) of  $\delta\text{DM} = 0.55 \text{ pc cm}^{-3}$ . Our improved value (DM =  $40.75 \pm 0.02 \text{ pc cm}^{-3}$ ) is consistent with the previous estimate within uncertainties, but is  $\sim 50\times$  more precise. We also used the MWA data to estimate the RM of this pulsar, measuring  $\text{RM}_{\text{ISM}} = 25.95 \pm 0.28 \text{ rad m}^{-2}$  (after subtracting the ionospheric contribution), which is also consistent with—and about an order of magnitude more precise than—the previously published value ( $23 \pm 3 \text{ rad m}^{-2}$ ; Young et al., 2014). Further observations of this pulsar, particularly with the MWA, will help to better constrain the DM and RM, in addition to the pulse profiles.

The next generation of wide-field, wide-bandwidth radio telescopes and their pulsar search surveys are on the horizon. Detection and characterization of objects like PSR J1107–5907 over a wide frequency range is fundamentally important to developing a comprehensive understanding of the Galactic pulsar population, and more broadly the Galactic neutron star population.

#### 4.6.1 Acknowledgements

B.W.M. and V.G. would like to thank Willem van Straten for valuable discussion of the single-polarization correction applied to UTMOST flux densities. The authors acknowledge the contribution of an Australian Government Research Training Program Scholarship in supporting this research. This scientific work makes use of the Murchison Radio-astronomy Observatory, operated by CSIRO. We acknowledge the Wajarri Yamatji people as the traditional owners of the Observatory site. Support for the operation of the MWA is provided by the Australian Government (NCRIS), under a contract to Curtin University administered by Astronomy Australia Limited. We acknowledge the Pawsey Supercomputing Centre, which is supported by the Western Australian and Australian Governments. We acknowledge the Australian Research Council grants CE110001020 (CAASTRO) and the Laureate Fellowship FL150100148. Part of this research was supported

by the Australian Research Council Centre of Excellence for All Sky Astrophysics in 3 Dimensions (ASTRO 3D), through project number CE170100013. This paper made use of archived data obtained through the Australia Telescope Online Archive and the CSIRO Data Access Portal (<http://data.csiro.au>).

**Facilities:** MWA, Molonglo Observatory

**Software:** Astropy (The Astropy Collaboration et al., 2013, 2018; v2.0.2), DSPSR (van Straten & Bailes, 2011), ionFR (Sotomayor-Beltran et al., 2013), Matplotlib (Hunter, 2007a; v2.0.2), powerlaw (Alstott et al., 2014; v1.4.1), PSRCHIVE (Hotan et al., 2004; van Straten et al., 2012), STILTS (Taylor, 2006)



# **Chapter 5**

## **The emission and scintillation properties of RRAT J2325–0530 at 154 MHz and 1.4 GHz**

This work has been accepted for publication in the Publications of the Astronomical Society of Australia (PASA). The final published version will likely include minor additions and/or alterations to the text provided here. The citation will nominally read:

Meyers, B. W., Tremblay, S. E., Bhat, N. D. R., Shannon, R. M., Ord, S. M., Sobey, C., Johnston-Hollitt, M., Walker, M. and Wayth, R., “The emission and scintillation properties of RRAT J2325–0530 at 154 MHz and 1.4 GHz”, 2019, *Publications of the Astronomical Society of Australia*

As in Chapters 3 and 4, minor alterations have been made to the submitted work in the following sections in order to enforce consistent formatting. The introductory material and observation details sections have already been discussed at length in Chapter 2, thus the respective text has been removed or reduced significantly. The conclusions have also been shortened and edited to enhance the thesis flow between chapters, and citations have been updated where necessary to reflect their current status.

## 5.1 Introduction

RRATs are almost certainly Galactic neutron stars with extreme emission variability (e.g. McLaughlin et al., 2006, 2009; Keane et al., 2011; Keane, 2016; Bhattacharyya et al., 2018). Based on objects with adequate observations, we expect single pulse rates in the range of a few pulses to a few hundred pulses per hour. RRATs are therefore more easily detected through single-pulse searches as opposed to the standard Fourier domain search or traditional folding techniques. Even though there are 111 known RRATs<sup>1</sup>, the inherent difficulty in their detection has meant that the physics responsible for the sporadic nature of the emission remains unclear.

The pulsar and magnetosphere system geometries are thought to play a vital role in the characteristics of pulsar emission, and can be constrained through polarisation measurements (e.g. Gould & Lyne, 1998; Manchester et al., 1998; Weisberg et al., 1999; Everett & Weisberg, 2001; Mitra et al., 2016; Johnston & Kerr, 2018). For RRATs this can pose a challenge given that, in general, the folded profiles are not particularly well defined by virtue of their sporadic emission. Nevertheless, when the polarisation properties have been analysed, even based on a small sample of single pulses, they provide remarkable insight into the nature of the emission (e.g. RRAT J1819–1458, Karastergiou et al., 2009). Generally speaking, very little is known about whether the RRAT population exhibits polarisation characteristics similar to the normal pulsar population. This is, in part, due to a lack of single-pulse analysis of normal pulsars in the literature, combined with the difficulty of creating high quality polarimetric profiles of RRATs.

Several models have been proposed to explain the sporadic emission, most of which are also linked to intermittent pulsars and the nulling phenomenon (see Section 4.2). Studying the pulse-energy distributions (e.g. Shapiro-Albert et al., 2018; Mickaliger et al., 2018b), timing periodicities and pulse clustering (e.g.

---

<sup>1</sup>Retrieved from <http://astro.phys.wvu.edu/rratalog>

Palliyaguru et al., 2011), and flux density or pulse energy correlations with single-pulse detection statistics (e.g. Cui et al., 2017) of RRATs is vital in understanding their emission and how they connect to the canonical pulsar population.

To further uncover connections between RRATs and normal pulsars it is also important to understand their kinematic properties, such as space velocities and proper motions. Techniques used to do this for normal pulsars include Very Long Baseline Interferometry (VLBI) (e.g. Deller et al., 2018), multi-wavelength analysis of binary systems (e.g. Jennings et al., 2018), long-term precision timing experiments (e.g. Janssen et al., 2010; Gonzalez et al., 2011), and scintillation analysis (e.g. Cordes et al., 1986; Johnston et al., 1998; Bhat et al., 2018). None of these techniques have been applied to RRATs in order to extract the pulsar velocities, specifically. In particular cases, scintillation studies of RRATs would nominally be able to not only provide estimates of the space velocities (e.g. Gupta et al., 1994), but also allow direct measurement of the turbulence and characteristic scales of the interstellar medium (ISM) along the respective sight-lines, thus allowing them to be used as additional probes of the structure and composition of the ISM.

RRAT J2325–0530 was originally discovered as part of the Robert C. Byrd Green Bank Telescope (GBT) 350 MHz Drift-scan pulsar survey (Boyles et al., 2013; Lynch et al., 2013). The pulsar has a pulse period of  $P = 0.868$  s, a moderate dispersion measure,  $\text{DM} = 14.966 \pm 0.007 \text{ pc cm}^{-3}$  and a nominal pulse rate of  $\sim 50 \text{ hr}^{-1}$ . Karako-Argaman et al. (2015b) conducted follow-up observations of a subset of those RRATs detected in the survey, including RRAT J2325–0530, using the GBT at 350 MHz (though with a larger bandwidth and upgraded digital backend) and the Low Frequency Array (LOFAR; van Haarlem et al., 2013; Stappers et al., 2011) core stations at 150 MHz. This pulsar has also been observed with the first station of the Long Wavelength Array (LWA1; Taylor et al., 2012) over a frequency range of 30–80 MHz (Taylor et al., 2016), allowing the measurement of a relatively shallow spectral index<sup>2</sup> ( $\alpha_{30}^{80} \approx -0.7$ ).

---

<sup>2</sup>Throughout, we define the spectral index,  $\alpha$ , by  $S_\nu \propto \nu^\alpha$ , where  $S_\nu$  is the flux density

Table 5.1: Observing details for MWA and Parkes on 2017 June 27.

Parameter	MWA	Parkes
Centre frequency (MHz)	154.24	1396
Bandwidth (MHz)	30.72	256
Time resolution (ms)	0.1	0.256
Channel bandwidth (MHz)	0.01	0.5
UTC start time	20:30:05	20:30:22
Observation duration (s)	4399	5867
Dispersion smearing in lowest channel (ms)	0.46	0.03
Dispersion delay across bandwidth (ms)	1060.58	11.88
Dispersion delay between observed bands <sup>a</sup> (ms)	3192.48	

<sup>a</sup>Delay between the highest Parkes band and the lowest MWA band.

## 5.2 Observations and Calibration

RRAT J2325–0530 was simultaneously observed with the MWA and Parkes radio telescope on 2017-06-27. The MWA observed with a 30.72 MHz band centred on 154.24 MHz for 1.4 hours, while Parkes observed at a centre frequency of 1396 MHz with 256 MHz bandwidth for 1.6 hours. Observing details are summarised in Table 5.1.

### 5.2.1 MWA

Observations of RRAT J2325–0530 were taken with the MWA-VCS in the Phase II compact configuration. For this observation, we recorded data at a centre frequency of 154.24 MHz with a bandwidth of 30.72 MHz for 5153 seconds.

#### 5.2.1.1 Tied-array beamforming

For this observation, calibration solutions were created from an observation of PKS 2356–61, approximately 2 hours after the observation of RRAT J2325–0530. The voltage data were then processed and a tied-array beam was formed using the procedures detailed in Section 2.1.2.2. The output from the tied-array beamforming software is full Stokes search-mode PSRFITS data, with the native VCS

---

measured at frequency  $\nu$ .

time and frequency resolution.

### 5.2.1.2 Flux density calibration

To determine the system temperature and gain for the tied-array beam, we followed the procedure developed by Meyers et al. (2017) (Chapter 3, and summarised in Section 2.1.3). For this observation we estimate  $T_{\text{sys}} = 274 \text{ K}$  and  $G = 0.33 \text{ K Jy}^{-1}$ . Incorporating the coherency correction factor (Section 2.1.3.1, eq. 2.12), the SEFD of the MWA tied-array beam was effectively 1708 Jy

## 5.2.2 Parkes

We observed RRAT J2325–0530 with the central beam of the 20-cm multibeam receiver on the 64-m Parkes radio telescope, recording at a centre frequency of 1396 MHz with 256 MHz bandwidth. The observation started on 2017 June 27 20:30:22 and lasted for 5867 seconds. Data were collected with the Parkes digital filter bank mark-4 (PDFB4) backend, producing  $512 \times 0.5 \text{ MHz}$  frequency channels across the band. The data were recorded in polarimetric search-mode, where the receiver coherency products were detected and averaged to a time resolution of  $256 \mu\text{s}$  and written to disk.

### 5.2.2.1 Flux density and polarisation calibration

Flux density and polarisation calibration was achieved through the standard procedures, as described in Section 2.2.1. We also corrected the cross-coupling and ellipticity of the multibeam feed receptors using a model of the full instrumental response (e.g. Ord et al., 2004). These calibration solutions were derived and applied using standard PSRCHIVE tools (Hotan et al., 2004; van Straten et al., 2012). The nominal SEFD throughout the observation was  $\approx 36 \text{ Jy}$ .

## 5.3 Analysis and Results

### 5.3.1 Single pulse detection

Both the MWA and Parkes data sets were processed using the DSPPSR software package (van Straten et al., 2010), which subdivided the data into single-pulse time series, with 2048 bins across the pulse period, and were incoherently dedispersed using the catalogued dispersion measure ( $14.966 \text{ pc cm}^{-3}$ ). The data were then processed with the PSRCHIVE routine PAZ using the median-difference filter to remove the vast majority of radio frequency interference (RFI). Additionally, we excised five per cent of each band edge from the Parkes data, and 10 fine channels (each 10 kHz) for each edge of the MWA 1.28 MHz coarse channels, where aliasing caused by the polyphase filter bank overlap degrades the data.

To find pulses we used the PSRCHIVE single-pulse finding routine, PSRSPA, looking for pulses above a signal-to-noise ratio (S/N) threshold of six<sup>3</sup>. This produced a list of 162 candidates for Parkes and 188 candidates for the MWA. A significant fraction of these candidates were detections within the same pulsar rotation (i.e. peaks above the respective telescope's detection threshold), thus, after filtering for unique pulses, there were 102 detected with Parkes and 89 detected with the MWA. The time and frequency characteristics of the remaining candidates were visually inspected, which resulted in the removal of a further 32 candidate pulses from the Parkes data. These final excisions were due to RFI that was not automatically removed in the earlier processing steps.

The final catalogue of pulses contained 89 and 70 pulses for the MWA and Parkes, respectively. At this stage, the corresponding flux density scales (see Sections 5.2.1.2 and 5.2.2.1) were applied to each single-pulse time series. For Parkes this was achieved using the standard PSRCHIVE tools and calibration procedures (see e.g. van Straten et al., 2012). Briefly, this required us to construct polarisation and flux density calibration solutions, and then apply these to the

---

<sup>3</sup>Specifically using the peak finding algorithm `above:threshold=6`

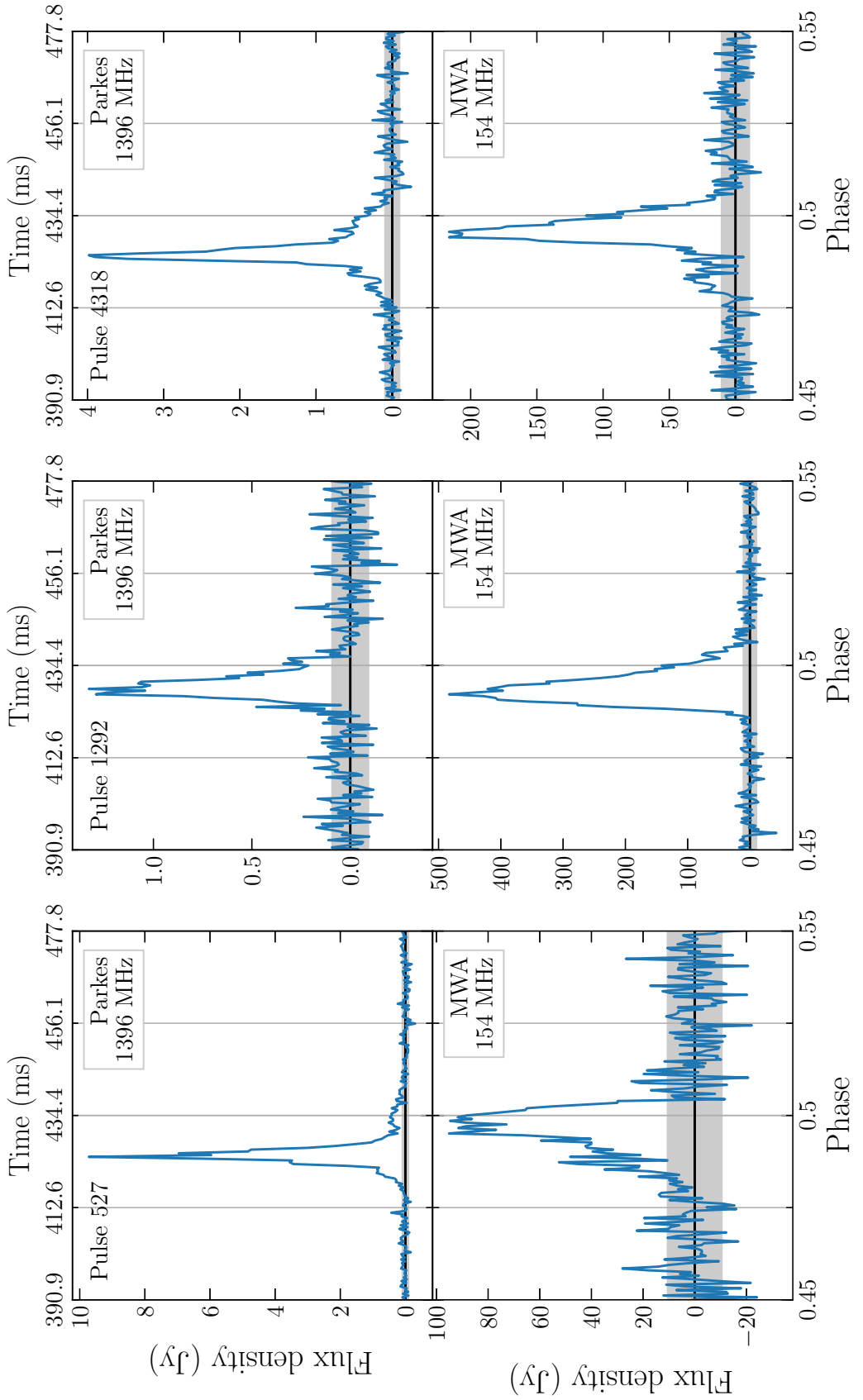


Figure 5.1: Examples of coincident single pulses from RRAT J2325–0530 at 1.4 GHz (Parkes; top row) and 154 MHz (MWA; bottom row). The pulses have been absolutely aligned, in that the same ephemeris was used to reduce the data sets. The number of rotations since the first simultaneously observed rotation of the pulsar are also given for each pair. Pulse 527 is the brightest pulse in the Parkes band of the coincident pulses, while pulse 1292 is the brightest in the MWA band. Pulse 4318 is a relatively average example of a simultaneous pulse.

individual single pulse archives using the PAC tool. For the MWA VCS data we evaluated the noise baseline on a per-pulse basis and applied the standard radiometer equation, incorporating the simulated system temperature and gain. Three examples of simultaneously detected pulses are shown in Figure 5.1. The fluence (pulse energy) is estimated by integrating over the pre-determined on-pulse phase window ( $\approx$  167–193 degrees in pulse longitude, or 400–466 ms) for every detection.

### 5.3.2 Profiles and polarisation

We combined the detected pulses into pseudo-integrated profiles which are shown in Figure 5.2. The profiles have been rotated by 0.5 turns for ease of comparison. No time alignment procedures have been applied to the profiles, thus the profiles are absolutely aligned based on the ephemeris alone. The “knee”-like feature in the Parkes profile and the notch at the nominal profile peak are particularly interesting, given that the MWA profile is relatively smooth in comparison<sup>4</sup>. The residual dispersion smearing within the 10 kHz channels of the MWA data is (at worst)  $\sim$  0.5 ms, which is similar in scale to the Parkes notch feature ( $\sim$  1 ms), thus the smoothness of the MWA profile is possibly an artefact of incoherent dedispersion. The knee feature in the Parkes profile, and the relatively extended rising edge of the MWA profile are also intriguing. These profile features would require coherently de-dispersed, high signal-to-noise ratio profiles constructed from many hundreds or thousands of pulses, to examine in detail and to ensure their authenticity.

The polarisation response of the MWA tied-array beam is currently undergoing self-consistency and cross-validation tests (e.g. Ord et al., 2019; Xue et al., 2019). Nonetheless, we present here the first polarisation profile of RRAT J2325–0530 at 154 MHz and 1.4 GHz. The profiles have been corrected for Faraday rotation,

---

<sup>4</sup>However, we note that these pseudo-profiles are constructed from less than 100 pulses, whereas pulse profiles typically stabilise only after  $\sim$  1000 pulses are averaged (e.g. Liu et al., 2012).

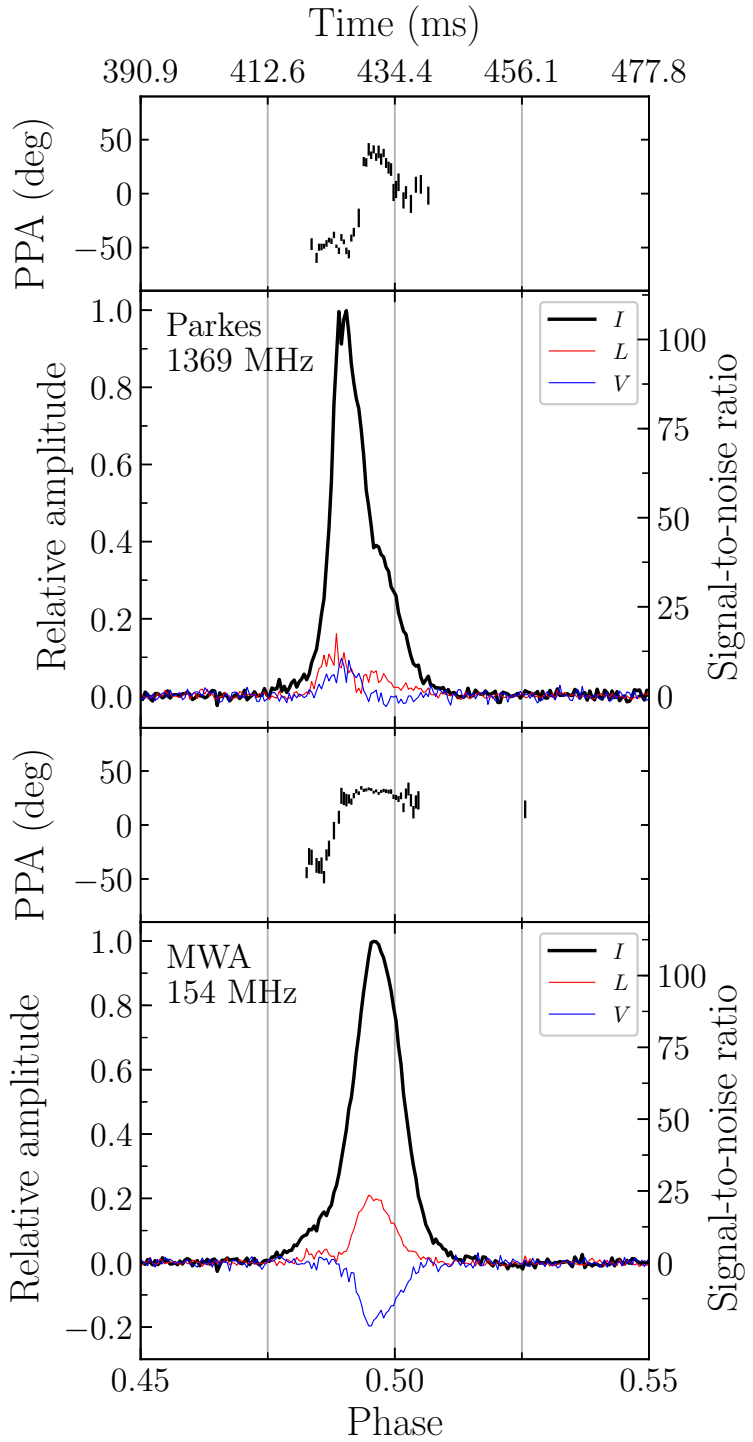


Figure 5.2: A pseudo-integrated profile, combining all single pulses with a  $S/N \geq 6$ . The profiles were produced using the same ephemeris and then rotated by 0.5 phase turns. Total intensity (Stokes  $I$ ) is drawn in black, with linear ( $L = \sqrt{Q^2 + U^2}$ ) and circular ( $V$ ) polarisation in red and blue, respectively. Above each profile is the linear polarisation position angle in degrees. Both profiles have been corrected for rotation measure (see Section 5.3.7).

removing the effects induced by the interstellar medium and ionosphere (see Section 5.3.7). There is clearly substantial polarisation evolution with frequency in this case (see also Xue et al., 2019). Even though the polarisation positional angle (PPA) has not been absolutely calibrated for the MWA, it is reassuring that the general shapes are similar. For both profiles, we were unable to fit the standard rotating vector model (RVM). In the case of the MWA profile, one possible reason for this is that scattering induced by the ISM can cause significant deviations from the normally expected RVM (S-like swing) shape (e.g. Karastergiou et al., 2009).

### 5.3.3 Scintillation

After combining the single pulses as in Section 5.3.2, it was clear that RRAT J2325–0530 is affected by diffractive scintillation in the Parkes band. This was confirmed by examining the dynamic spectrum (see Figure 5.3). Due to the nature of RRAT emission, the diffractive scintillation pattern is sampled sparsely and irregularly in time, thus performing the standard autocorrelation analysis (e.g. Gupta et al., 1994; Bhat et al., 1999, 2018) is non-trivial. Furthermore, it is difficult to robustly constrain the scintillation parameters given that we only partially sample scintles in time or frequency at 1.4 GHz (which leads to large statistical uncertainties). At 154 MHz it is not immediately clear if there is any scintillation structure present, which suggests that the fine-channel width (10 kHz) is inadequate to capture the frequency structure. The results are summarised in Table 5.2. Given these complications, the diffractive scintillation parameters presented here should be considered with caution.

#### 5.3.3.1 Scintillation bandwidth

To estimate the scintillation bandwidth, we measured the mean flux density per frequency channel,  $I(t, \nu)$ , for every pulse (i.e. the spectrum). Following Cordes

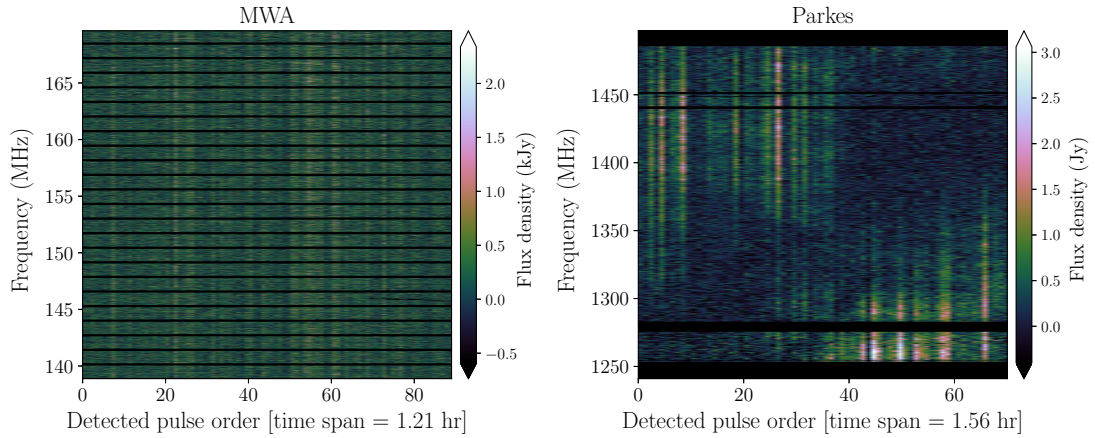


Figure 5.3: A dynamic spectrum of the brightest single pulses from RRAT J2325–0530 at 154 MHz (MWA; left) and 1.4 GHz (Parkes; right). The colour scale units are different for each dynamic spectrum (kJy for the MWA data, Jy for the Parkes data), and the  $x$ -axis represents the order in which the pulses were detected, with the total time spanned by these pulses given for context in the label. Note that this means the time axis is not continuous (i.e. each column of pixels, corresponding to a single pulse, is not necessarily contiguous with the previous column), unlike standard dynamic spectra. Nevertheless, it is clear that there is frequency and time structure indicative of diffractive scintillation in the Parkes data, though this is not the case for the MWA data. The black masked regions are those time and frequency samples excised by the RFI mitigation steps taken during post-processing of the single-pulse data, including coarse channel edges for the MWA, and the colour scale is linear.

Table 5.2: Scintillation properties of RRAT J2325–0530.

Frequency (MHz)	$\nu_{\text{diss}}$ (MHz)	$\tau_{\text{diss}}$ (s)	$V_{\text{iss}}$ [ $D = 0.7 \text{ kpc}$ ] ( $\text{km s}^{-1}$ )	$V_{\text{iss}}$ [ $D = 1.49 \text{ kpc}$ ] ( $\text{km s}^{-1}$ )	$\overline{C}_{\text{n}}^2$ ( $\text{m}^{-20/3}$ )
154	$\lesssim 0.01$	$34 \pm 18$	—	—	—
1369	$102 \pm 72$	$3478 \pm 2550$	$44 \pm 36$	$64 \pm 52$	$\lesssim 2.8 \times 10^{-4}$

et al. (2004), we then computed the intensity autocorrelation function (ACF),

$$A(\delta\nu) = \langle I(t, \nu) I(t, \nu + \delta\nu) \rangle \quad (5.1)$$

for each pulse, where  $\delta\nu$  is the frequency lag representing a shift of one channel. For each  $A(\delta\nu)$  we fit a Gaussian to measure the standard deviation,  $\sigma$ , and calculate the scintillation bandwidth as  $\nu_{\text{diss}} = (2 \ln 2)^{1/2} \sigma$  (which corresponds to the half-width at half-maximum of the Gaussian, e.g. Cordes et al., 1986). The ACFs and models are normalised by the correlation value corresponding to zero frequency lag, which is calculated as the mean of the correlation value in the adjacent six frequency lag bins (three positive and three negative). In Figure 5.4 we show the ACFs and best-fit Gaussian models for the subset of pulses used to estimate the scintillation bandwidth.

Using the above method, we measure an average  $\nu_{\text{diss}} = 102 \pm 12$  MHz at 1.4 GHz (i.e. at Parkes) based on the subset of single pulses with  $S/N > 40$  (12/70 pulses). This is nominally a lower limit given that over the observed bandwidth, we do not fully sample even one scintle. To calculate the expected characteristic scintillation bandwidth at MWA frequencies (154 MHz), we assume a frequency scaling index of  $\gamma = -3.9 \pm 0.2$  (e.g. Bhat et al., 2004), where  $\nu_{\text{diss}} \propto \nu^\gamma$ . We find that the expected scintillation bandwidth is  $\nu_{\text{diss}} \approx 15$  kHz.

Processing the single pulses with  $S/N > 20$  (15/89 pulses) from the MWA in the same way, we find that in all cases the ACF drops to zero by the first frequency lag bin, indicating that the scintillation bandwidth at 154 MHz is less than our channel width (i.e.  $\nu_{\text{diss}} \lesssim 10$  kHz). This indicates that the frequency scaling is steeper than  $\gamma = -3.9$ . If we take the nominal measured values of  $\nu_{\text{diss}}$  at each frequency, and again use the previous defined scaling relation, we find that  $\gamma \approx -4.2$ , which is steeper than the empirically derived global scaling index (Bhat et al., 2004). We note that nearby pulsars tend to show a steeper scaling index, approaching the extremum (Kolmogorov turbulence) scaling of  $\gamma = -4.4$ , due to the decreased probability of intervening structures in the ISM that would

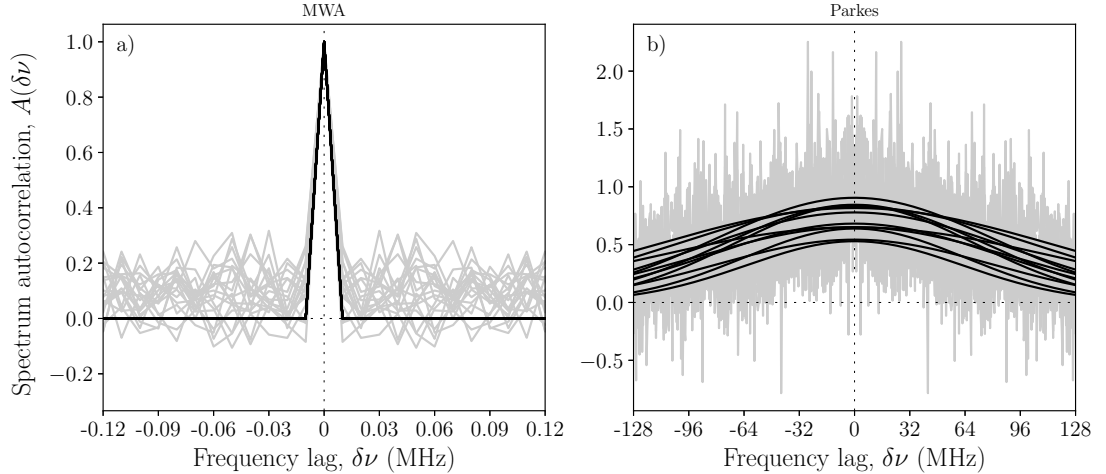


Figure 5.4: The set of ACFs (grey) for the brightest pulses, and their best-fitting Gaussian model (black), from: a) the MWA (15 pulses), and b) Parkes (12 pulses). The MWA autocorrelations drop to zero by the first frequency lag bin and thus we are not able to even partially resolve the frequency structure. From the Parkes data we see structure, though the fact that the autocorrelations do not drop to zero before the last meaningful frequency lag bins indicates that we are not fully sampling a scintle, which is corroborated by the dynamic spectrum in Figure 5.3.

serve to shallow the scaling index.

Finally, the scintillation characteristics are statistical quantities, thus the sample variance must be included in all quantities derived from the scintillation properties, especially when a small number of scintles are observed. This uncertainty is given by  $\sigma_{\text{stat}} \approx N_{\text{scint}}^{-1/2}$ , where the number of scintles observed,  $N_{\text{scint}}$ , in the total observing time,  $t_{\text{obs}}$ , over a bandwidth,  $B_{\text{obs}}$ , is given by

$$N_{\text{scint}} = \left( \frac{B_{\text{obs}} t_{\text{obs}}}{\nu_{\text{diss}} \tau_{\text{diss}}} \right) f_d, \quad (5.2)$$

where  $f_d$  is a filling fraction that describes how much of the observed frequency-time phase space contains signal (e.g. Bhat et al., 1999), which we assume to be  $f_d \approx 0.5$  based on the Parkes dynamic spectrum in Figure 5.3. For the MWA, where the scintles are on the order of 10 kHz wide, this factor is negligible ( $N_{\text{scint}} \approx 2 \times 10^5$  and  $\sigma_{\text{stat}} \sim 0.2\%$ , or 20 Hz). However, in the case of Parkes, we clearly sample far fewer scintles ( $N_{\text{scint}} \approx 2$ ), ergo the sampling error is  $\sigma_{\text{stat}} \approx 70\%$ .

and  $\nu_{\text{diss}} = 102 \pm 72$  MHz (where the final error is the quadrature sum of the fitting error and statistical error).

### 5.3.3.2 Scintillation time scale

The RRAT emission irregularly samples the scintillation pattern which makes estimating the scintillation time scale,  $\tau_{\text{diss}}$ , difficult. Nevertheless, we calculate the intensity cross-correlation,

$$\rho(\tau, \delta\nu = 0) = \langle \Delta I(t, \nu) \Delta I(t + \tau, \nu + \delta\nu) \rangle \quad (5.3)$$

between every mean-subtracted single-pulse spectra,  $\Delta I(t, \nu)$ , and subsequent pulses, while recording the corresponding time lag,  $\tau$ , as the number of pulsar rotations between the correlated pulse spectra<sup>5</sup>. We average the correlation coefficients for each time lag and then re-bin the results such that there is one  $\rho(\tau, 0)$  per 150 seconds for the Parkes data. In Figure 5.5 we plot these correlation coefficients against time lag.

The scintillation time scale is the  $1/e$ -half-width of the fitted Gaussian ( $\tau_{\text{diss}} = \sqrt{2}\sigma$ ), where the mean is forced to zero, which we measure to be  $\tau_{\text{diss}} = 3478 \pm 761$  s at 1.4 GHz. Including the relative sampling error of  $\sim 70\%$ , we find that  $\tau_{\text{diss}} = 3478 \pm 2550$  s. Additionally, we can estimate the expected refractive interstellar scintillation (RISS) time scale (e.g. Rickett, 1990) at 1.4 GHz, where  $\tau_{\text{riss}} = \tau_{\text{diss}} (\nu / \nu_{\text{diss}}) \approx 13$  hours. These values should be considered with caution given that, as for the scintillation bandwidth, we do not actually sample a full scintle over the 1.5 hour observation.

Scaling the decorrelation time from 1.4 GHz, assuming  $\tau_{\text{diss}} \propto \nu^{1.2}$ , implies  $\tau_{\text{diss}} \approx 250 \pm 185$  s at 154 MHz. Using the same technique as above on the MWA data, except re-binning to one  $\rho(\tau, 0)$  per 10 seconds (given the expected  $\tau_{\text{diss}}$ ), we find that we are severely limited by the signal-to-noise ratio of our detected

---

<sup>5</sup>The actual correlation is implemented using the NumPy function `numpy.correlate` with `mode='same'`.

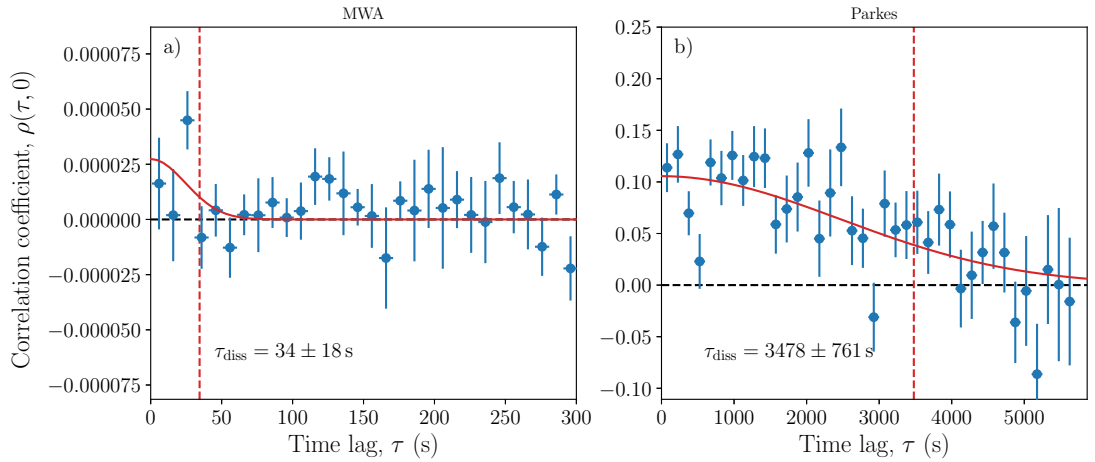


Figure 5.5: Mean correlation coefficients of individual pulse spectra, binned into: a) 10-second intervals for MWA data, and b) 150-second intervals for Parkes data. The Gaussian fit to the data (red, solid line) is weighted based on the standard error of each of the points, where the  $1/e$ -half-width of the Gaussian corresponds to the scintillation time scale. We measure a scintillation time scale  $\tau_{\text{diss}} = 3478 \pm 2550$  s at 1.4 GHz, and  $\tau_{\text{diss}} = 34 \pm 18$  s at 154 MHz, marked by the vertical dashed red lines.

pulses. This is due to the scintillation bandwidth being on the order of, or less than, the channel width. The estimated scintillation time scale is a factor of 7 less than expected, where  $\tau_{\text{diss}} = 34 \pm 18$  s. Visually inspecting Figure 5.5 one can see that the correlation coefficients, even after averaging in time, are consistent with noise except for one outlier. Furthermore, the quality of the Gaussian fit changes drastically depending on how the correlation coefficients are averaged, and generally results in an unconstrained estimate of  $\tau_{\text{diss}}$  (i.e. undefined uncertainty or failing to find an adequate fit altogether). For these reasons we caution against interpretation of the measured scintillation parameters at 154 MHz alone.

### 5.3.3.3 Scintillation velocity and turbulence strength

We can calculate the scintillation velocity—as a proxy to the RRAT space velocity—under the caveats that: both  $\nu_{\text{diss}}$  and  $\tau_{\text{diss}}$  are nominally lower limits; that we do not know the relative distance of the scattering screen to the pulsar, and; that

there is a factor of 2 discrepancy in distance estimates, where  $D = 0.7$  kpc and  $D = 1.49$  kpc, from NE2001 (Cordes & Lazio, 2002, 2003) and YMW2016 (Yao et al., 2017) models, respectively. We assign a 25% uncertainty to each distance estimate. The scintillation velocity is given by

$$V_{\text{iss}} = A_{\text{iss}} \frac{(Dx\nu_{\text{diss}})^{1/2}}{\nu\tau_{\text{diss}}}, \quad (5.4)$$

where  $D = D_{\text{os}} + D_{\text{ps}}$  is the total distance to the pulsar in kpc;  $D_{\text{os}}$  and  $D_{\text{ps}}$  are the distances from the screen to the observer and pulsar respectively in kpc;  $x = D_{\text{os}}/D_{\text{ps}}$  (in this case we assume  $x = 1$ , i.e. the screen is located exactly half way between the observer and the pulsar);  $\nu$  is the observing frequency in GHz;  $\nu_{\text{diss}}$  is in MHz, and  $\tau_{\text{diss}}$  in seconds. The scaling constant  $A_{\text{iss}} = 2.53 \times 10^4 \text{ km s}^{-1}$  is derived for a homogeneously distributed ISM with a Kolmogorov turbulence spectrum (Cordes & Rickett, 1998), which appears to be a valid approximation for this pulsar given the scintillation frequency scaling index calculated in Section 5.3.3.1. For a distance  $D = 0.70 \pm 0.18$  kpc we find  $V_{\text{iss}} = 44 \pm 36 \text{ km s}^{-1}$ , while for  $D = 1.49 \pm 0.37$  kpc,  $V_{\text{iss}} = 64 \pm 52 \text{ km s}^{-1}$ . The uncertainties correspond to the quadrature sum of the scintillation bandwidth, scintillation time scale and distance errors, given by

$$\Delta V_{\text{iss}} = \left( \left[ \frac{\partial V_{\text{iss}}}{\partial \nu_{\text{diss}}} \Delta \nu_{\text{diss}} \right]^2 + \left[ \frac{\partial V_{\text{iss}}}{\partial \tau_{\text{diss}}} \Delta \tau_{\text{diss}} \right]^2 + \left[ \frac{\partial V_{\text{iss}}}{\partial D} \Delta D \right]^2 \right)^{1/2}, \quad (5.5)$$

where  $\Delta X$  represents the uncertainty in parameter  $X$ . We did not calculate the scintillation velocities from the MWA data since we do not have reliable estimates of  $\nu_{\text{diss}}$  and  $\tau_{\text{diss}}$  (see Table 5.2).

We can also place limits on the mean turbulence strength,  $\overline{C_n^2}$ , along the line-of-sight. Assuming Kolmogorov turbulence, the mean turbulence strength in units of  $\text{m}^{-20/3}$  is

$$\overline{C_n^2} \approx 0.002 \nu^{11/3} D^{-11/6} \nu_{\text{diss}}^{-5/6}, \quad (5.6)$$

(cf. eq. 9 of Cordes et al., 1990) where  $\nu$ ,  $D$  and  $\nu_{\text{diss}}$  are in the same units as for eq. (5.4). Given the range in distances, we find that the corresponding range in turbulence strength is  $\overline{C_n^2} \approx (7\text{--}28) \times 10^{-5} \text{ m}^{-20/3}$  at 1.4 GHz, and note that given the lower limit on  $\nu_{\text{diss}}$  from Parkes data we can only confidently say that  $\overline{C_n^2} \lesssim 2.8 \times 10^{-4} \text{ m}^{-20/3}$ .

### 5.3.4 Spectral index

A cross-matched list of single-pulses was created from the independent MWA and Parkes pulse data sets using the STILTS table manipulation software (Taylor, 2006). After the cross-matching stage, there were 45 pulses coincident in both bands. For each of these pulses we used their measured fluences to calculate a spectral index, the distribution of which is shown in Figure 5.6 along with an indicator of the normal pulsar population spectral index range in grey.

We measure a mean single pulse spectral index of  $\alpha_{154}^{1369} = -2.2 \pm 0.1$  which is relatively steep compared to mean spectral index observed in the typical pulsar population, where  $\langle \alpha \rangle \approx -1.6$  (see e.g. Maron et al., 2000a; Bates et al., 2013; Jankowski et al., 2018b). The range of single-pulse spectral indices we measure is  $-2.8 < \alpha_{154}^{1369} < -1.5$ . The steep spectral index we measure seems to agree empirically with the detections reported in the literature, given that RRAT J2325–0530 has been detected multiple times with low-frequency observations in the past from the GBT (350 MHz), LOFAR (150 MHz) and LWA1 (30–80 MHz).

### 5.3.5 Fluence distributions

From the detected pulses we constructed fluence (pulse energy) distributions for each band. To these distributions we fit three relatively common models using the Python LMFIT module<sup>6</sup>: a power law (PL), a truncated exponential (TE; functionally the same as eq. 3 of Mickaliger et al., 2018b), and a log-normal

---

<sup>6</sup><https://github.com/lmfit/lmfit-py> (v0.9.11, doi: 10.5281/zenodo.1301254)

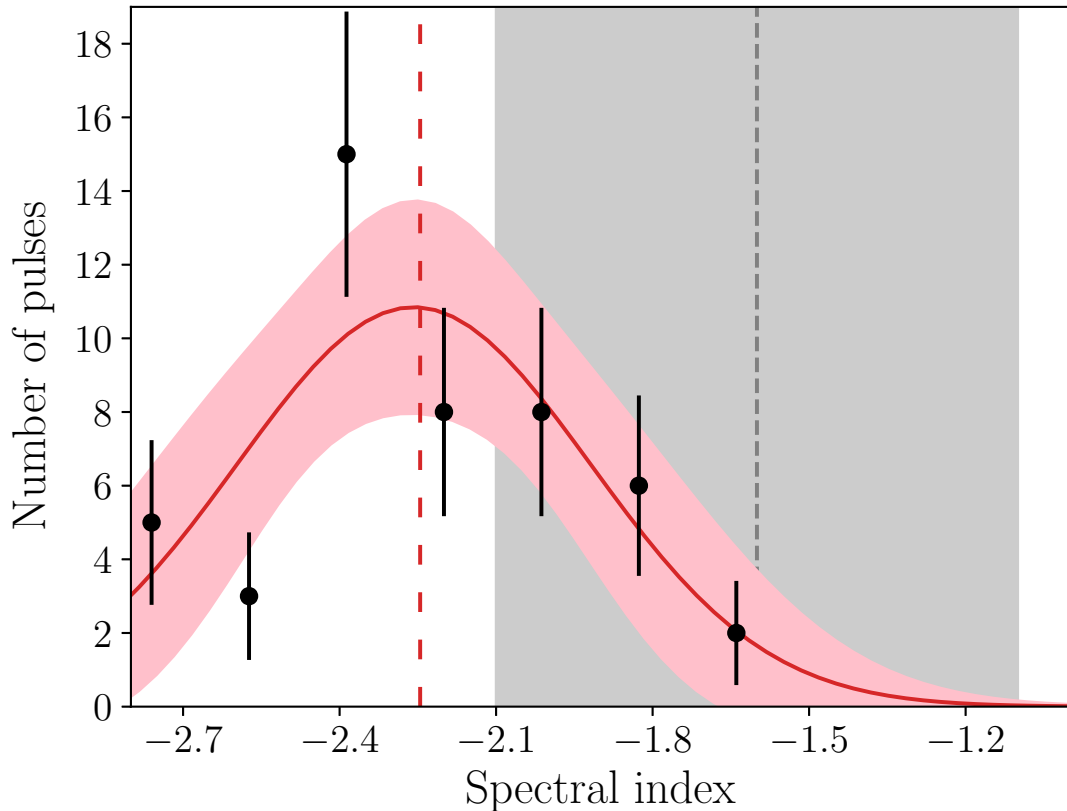


Figure 5.6: Spectral index distribution for detected simultaneous pulses between the MWA and Parkes. The red solid line is a Gaussian fit to the distribution, and the pink envelope represents the 1- $\sigma$  confidence interval of the model. Error bars on the points are Poisson uncertainties only. The mean spectral index is  $\alpha = -2.2 \pm 0.1$  with a standard deviation of  $\sigma = 0.4 \pm 0.1$ . The grey shaded region is the typical distribution of spectral indices, with a mean of  $\langle \alpha \rangle = -1.6$  and standard deviation of  $\sigma = 0.5$  (Jankowski et al., 2018b).

distribution (LN). The relevant functional forms are:

$$N_{\text{PL}}(x) = Ax^{-\beta}, \quad (5.7)$$

$$N_{\text{TE}}(x) = Bx^{-\zeta}e^{-\lambda x}, \quad (5.8)$$

$$N_{\text{LN}}(x) = \frac{C}{x\sigma} \exp \left[ -\frac{(\ln x - \mu)^2}{2\sigma^2} \right], \quad (5.9)$$

where  $N(x) dx$  is the number of pulses at fluence  $x$ ,  $A$ ,  $B$  and  $C$  are arbitrary scaling constants,  $\beta$  and  $\zeta$  are power law exponents,  $\lambda$  is a decay parameter, and  $\mu$  and  $\sigma$  are the location and scale parameters for the normally distributed logarithm (i.e.  $\ln x$ ). Note that in this case the power laws are fitted only to the pulses which have fluences greater than 0.8 and 0.006 Jy s for the MWA and Parkes, respectively. These cutoffs were chosen to coincide roughly with where the distributions peak. Without these restrictions, the power law model is a poor fit to the data. The data and fitted models are shown in Figure 5.7, and model parameters (with standard errors) are given in Table 5.3. In general it appears that a log-normal distribution is favoured, though see Section 5.4.3 for further discussion.

### 5.3.6 Pulse rates and clustering

We measured a total of 89 and 70 pulses with  $S/N \geq 6$  with the MWA and Parkes, respectively. These detections correspond to pulse rates of  $73 \pm 7 \text{ hr}^{-1}$  above a peak flux density of 65 Jy at 154 MHz, and  $43 \pm 5 \text{ hr}^{-1}$  above a peak flux density of 0.6 Jy at 1.4 GHz, where the uncertainties correspond to the Poisson counting error. The pulse rates we measure, as well as those in the literature are presented in Table 5.4. In the case of the minimum detectable flux density for the LOFAR results (Karako-Argaman et al., 2015b), we assign a gain for the core stations of  $0.68 \text{ K Jy}^{-1}$  (based on estimates of the collecting area of van Haarlem et al. (2013), modified by a projection factor of  $\cos^2(\pi/6) = 3/4$  assuming a best-case scenario where the source was observed at  $\sim 60$  deg elevation) and

Table 5.3: Best-fit parameters for trial fluence distribution models.

Frequency (MHz)	Power law*			Truncated exponential			Log-normal		
	$\beta$	$\chi^2_r$	$\zeta$	$\lambda$ (Jy $^{-1}$ s $^{-1}$ )	$\chi^2_r$	$\mu^a$ (Jys)	$\sigma^a$ (Jys)	$\chi^2_r$	
154	$1.6 \pm 0.2$	1.9	$-1.7 \pm 0.4$	$2.1 \pm 0.3$	1.5	$0.18 \pm 0.07$	$0.69 \pm 0.06$	1.7	
1369	$2.2 \pm 0.4$	1.8	$-3 \pm 0.7$	$488 \pm 97$	2.5	$-4.8 \pm 0.1$	$0.53 \pm 0.05$	2.2	

\*Restricted to fitting pulses with fluences greater than 0.8 and 0.06 Jys for the MWA and Parkes (see text).

<sup>a</sup>The location ( $\mu$ ) and scale ( $\sigma$ ) parameters, as defined by Python's `scipy.stats.lognorm`.

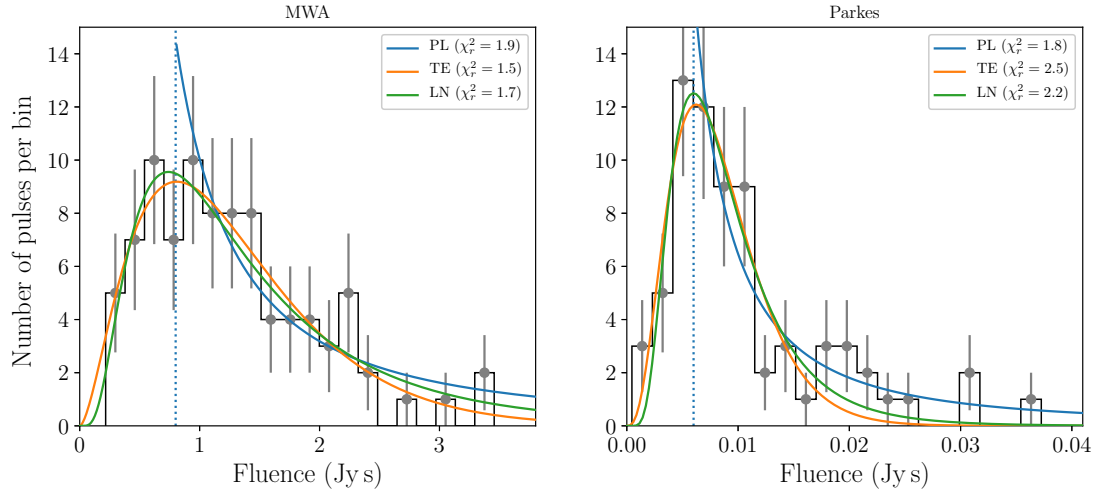


Figure 5.7: Pulse fluence (energy) distributions for single pulses detected with the MWA (left) and Parkes (right). We fitted a power law (blue), truncated exponential (orange) and log-normal (green) distribution model to the binned single-pulse fluences. The error bars represent statistical (Poisson) errors only. The reduced chi-squared values of the fits are given in the legend. The power law cut-off for each frequency is indicated by the blue vertical dotted lines.

add 250 K to the nominal 400 K receiver temperature in an attempt to include sky noise contributions. Using these values, we estimate a minimum detectable flux density of  $\sim 21$  Jy, assuming the same caveats of the original estimate (i.e.  $\text{SNR} \geq 5$  and 10 ms pulse width).

We also examine the distribution of the number of rotations between subsequent pulses (“wait times”) within our observation. These wait times are presented in Figure 5.8. In this case, we binned the wait times into 50 equally spaced intervals, ranging from one pulsar rotation to the maximum wait time, which corresponds to 596 rotations ( $\sim 517$  s) in the Parkes data. The median wait times for the MWA and Parkes pulses are 52 and 68 rotations, respectively. In both the MWA and Parkes data, the minimum wait time is one rotation. The maximum wait time in the MWA data is 184 rotations (i.e.  $\sim 159$  seconds), with 75 instances of wait times less than 100 rotations. For Parkes, the maximum wait time is substantially longer, at 596 rotations (i.e.  $\sim 520$  seconds), and there are 46 wait times less than 100 rotations. Given the different sensitivity thresholds of

Table 5.4: Pulse rates and nominal detection sensitivity for single-pulses from RRAT J2325–0530.

Telescope	Frequency (MHz)	Bandwidth (MHz)	Min. $S_\nu$ (Jy)	Min. fluence <sup>a</sup> (Jy s)	Observing time (hours)	Pulse rate (hr <sup>-1</sup> )	Ref.
IWA1	35.1, 49.8, 64.5, 79.2	$4 \times 15$	$\sim 60^b$	$\sim 0.3$	26 <sup>c</sup>	12–21	T+16
LOFAR	150	80	$\sim 21^d$	$\sim 0.11$	0.75	$52 \pm 8$	KA+15
MWA	154	30.72	$\sim 65$	0.19	1.4	$73 \pm 7$	<i>This work</i>
GBT	350	100	$\sim 0.4^d$	$\sim 0.002$	~0.5	$46 \pm 9$	KA+15
Parkes	1369	256	$\sim 0.6$	0.0005	1.6	$43 \pm 5$	<i>This work</i>

References — T+16: Taylor et al. (2016), KA+15: Karako-Argaman et al. (2015b).

<sup>a</sup>Fluence limits from other works were estimated by calculating the area under a tophat with amplitude equal to the corresponding sensitivity and a width of 5 ms (mean effective width of pulses measured in this work).

<sup>b</sup>Over the full observed bandwidth, which was at best 60 MHz. Individual subband sensitivities are therefore  $\sim 120$  Jy.

<sup>c</sup>Split into 2–3 hour blocks over 10 days spread throughout late-2013 and late-2014, see Taylor et al. (2016) for details.

<sup>d</sup>Calculated using eq. 1 and observing parameters from Table 1 (though see text regarding LOFAR parameters) of Karako-Argaman et al. (2015b), assuming a detection threshold of  $S/N \geq 5$ .

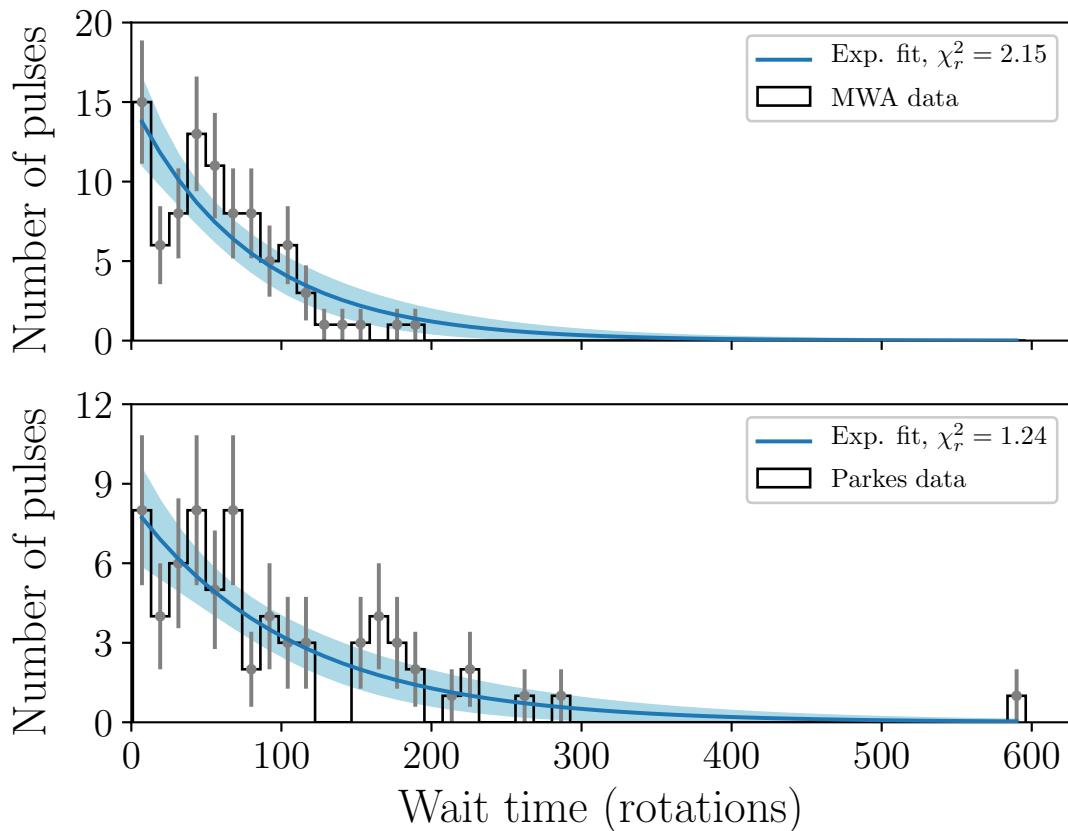


Figure 5.8: Histogram of the number of rotations between subsequent pulses (i.e. wait times) for the MWA pulses (top) and Parkes pulses (bottom). The blue solid lines are a fit to an exponential distribution, and the light blue shaded regions represent the 99% confidence interval based on the fitting uncertainties. Wait times were binned into 50 equally spaced bins ranging from 1 rotation to 596 rotations (i.e. 517 seconds, the maximum wait time in either frequency band). The reduced chi-square statistic,  $\chi^2_r$ , for each fit is 2.15 and 1.24 for the MWA and Parkes, respectively.

each telescope, it is difficult to quantitatively compare these numbers, especially since scaling thresholds and selecting pulses from either sample only adds to the issue of small number statistics in this case.

If the single-pulse emission is produced by a Poisson (random) process, then we would expect that the time between events (i.e. the wait times) would be exponentially distributed ( $N(x) dx \propto e^{-\eta x}$ ). After fitting each sample independently, we find that the exponents are similar, where  $\eta_{\text{MWA}} = 0.013 \pm 0.001$  for the MWA, and  $\eta_{\text{PKS}} = 0.009 \pm 0.001$  for the Parkes data. From these data, it is unclear whether there is a significant excess beyond what would be expected of pulse events drawn from a Poisson distributed process (an exponential distribution has been fitted to the wait times, see Figure 5.8). In the context of the general pulsar population, similar work has been done for nulling pulsars, noting examples of clustering (e.g. Redman & Rankin, 2009), and of random processes (e.g. Gajjar et al., 2012). The latter is reasonably consistent with what we find for RRAT J2325–0530. Ultimately, we are limited in this case by the number of single-pulse detections, and note that the Parkes wait time distribution will be biased by the scintillation effects.

### 5.3.7 Rotation measure

The rotation measure (RM) quantifies the degree of Faraday rotation that the radio emission from a source experiences after traversing the ISM, and was traditionally measured by calculating the change in linear polarisation angle across the observing band (e.g. Noutsos et al., 2008; Han et al., 2018). We used the PSRCHIVE rotation measure fitting routine, RMFIT, which effectively implements the RM synthesis method (e.g. Brentjens & de Bruyn, 2005), to determine the nominal rotation measure of the Parkes and MWA data based on the polarisation properties of the pseudo-integrated pulse profiles (Figure 5.2).

The ionosphere can significantly contribute to the measured RM, thus we cal-

Table 5.5: Rotation measure estimate for RRAT J2325–0530.

Frequency (MHz)	$\text{RM}_{\text{obs}}$ (rad m $^{-2}$ )	$\text{RM}_{\text{ion}}$ (rad m $^{-2}$ )	$\text{RM}_{\text{ISM}}$ (rad m $^{-2}$ )
154	$3.38 \pm 0.03$	$-0.47 \pm 0.09$	$3.85 \pm 0.12$
1396	$2.41 \pm 2.74$	$-0.41 \pm 0.15$	$2.82 \pm 2.89$

culated the ionospheric contribution for both Parkes and the MWA using IONFR<sup>7</sup> (Sotomayor-Beltran et al., 2013), using the latest version of the International Geomagnetic Reference Field (IGRF12; Thébault et al., 2015) and the International Global Navigation Satellite System Service vertical total electron content maps (e.g. Hernández-Pajares et al., 2009). The RM contribution from the ISM is given by  $\text{RM}_{\text{ISM}} = \text{RM}_{\text{obs}} - \text{RM}_{\text{ion}}$ , the values for which are given in Table 5.5. The ionosphere was relatively quiet during the observations, but is still the dominant source of uncertainty in estimating the RM imparted by the ISM for the MWA measurements.

After ionospheric correction, the ISM contribution to the RM along this line-of-sight based on the MWA data, is  $\text{RM}_{\text{ISM}} = 3.85 \pm 0.12 \text{ rad m}^{-2}$ . While the Parkes data measurement is less constraining, it does agree within uncertainty. Given the RM and DM we can estimate the average line-of-sight magnetic field strength using the approximation

$$\langle B_{\parallel} \rangle \approx 1.23 \left( \frac{\text{RM}}{\text{DM}} \right) \mu\text{G}, \quad (5.10)$$

where we find that  $\langle B_{\parallel} \rangle \approx 0.32 \pm 0.01 \mu\text{G}$ , where the uncertainty is the quadrature sum of the relative error in the DM and RM measurements. While reasonably small, this magnetic field strength is well within the distribution of measured values for larger samples of pulsars over a wide range of Galactic latitudes (e.g. Mitra et al., 2003; Noutsos et al., 2008; Sobey et al., 2019).

---

<sup>7</sup><http://ascl.net/1303.022>

## 5.4 Discussion

### 5.4.1 Scintillation characteristics compared to normal pulsars

The analysis we present is the first direct example of detected scintillation from RRATs. Generally, parameterising the scintillation can characterise the turbulence in the ISM and estimate pulsar space velocities. While scintillation is expected for these objects, it is technically difficult given that the sporadic nature of RRAT emission will often hinder the robust characterisation of parameters. In particular, the irregular sampling of the intensity modulation in time makes estimating the scintillation time scale more difficult, while in our case we are also limited by the bandwidth (in the case of the 1.4 GHz data) and frequency resolution (in the case of the 154 MHz data). Nonetheless, we have attempted to constrain the scintillation bandwidth and time scale (and related quantities) for RRAT J2325–0530 based on our observations of  $\sim 100$  single pulses over  $\sim 5800$  s.

For RRAT J2325–0530, the full scintle size (in frequency) at 1.4 GHz is considerably larger than the 256 MHz observing bandwidth; thus, we interpret the measured scintillation bandwidth of  $\nu_{\text{diss}} = 102 \pm 72$  MHz as a lower limit. The predicted scintillation bandwidth from NE2001 along the line-of-sight to RRAT J2325–0530 is  $\nu_{\text{diss}}^{\text{NE2001}} = 27^{+20}_{-9}$  MHz which is a factor of  $\sim 4$  lower than what we measure. This is not necessarily alarming given that the NE2001 model attempts to model the turbulence within the ISM, largely based on Galactic plane measurements, thus a factor of a few discrepancy is expected for objects with large Galactic latitudes. Furthermore, it is known that the measured scintillation properties of nearby pulsars are modulated by factors of  $\sim 3$ – $5$  over time (Bhat et al., 1999; Levin et al., 2016).

The scattering strength,  $u = (\nu/\nu_{\text{diss}})^{1/2} \approx 4$ , suggests that, at 1.4 GHz, we are in the strong scintillation regime ( $u > 1$ ). It also implies that we are sampling

only a small range of turbulence scale sizes in the ISM. This is consistent with the calculated turbulence strength (Table 5.2) and with expectations based on the Galactic latitude of the pulsar ( $b = -60.2^\circ$ ). The turbulence towards RRAT J2325–0530 is typical of nearby pulsars, especially when comparing the turbulence strength we calculate,  $\overline{C_n^2} \lesssim 2.8 \times 10^{-4} \text{ m}^{-20/3}$ , to other pulsars with anomalously reduced turbulence. For example, the ISM along the line-of-sight to PSR J0437–4715 is, on average,  $\sim 30\%$  as turbulent as towards RRAT J2325–0530 ( $\overline{C_n^2} = 8 \times 10^{-5} \text{ m}^{-20/3}$ ; Bhat et al. 2018), and the ISM towards PSR J0953+0755 is only  $\sim 7\%$  as turbulent ( $\overline{C_n^2} \sim 2 \times 10^{-5} \text{ m}^{-20/3}$ ; Phillips & Clegg 1992). Overall, the scintillation properties<sup>8</sup> of RRAT J2325–0530 suggest that this is a relatively typical line-of-sight through the ISM.

The scintillation velocity for RRAT J2325–0530 is relatively small, though is within the measured range for normal pulsars (e.g. Lyne & Smith, 1982; Cordes et al., 1986; Johnston et al., 1998) with similarly low/moderate DMs. This further supports the idea that RRAT J2325–0530 and the ISM surrounding it is not particularly anomalous compared to normal pulsars or other sight-lines. We have shown that scintillation analysis is a feasible way of constraining the space velocities of RRATs, and placing them in context with the broader pulsar population. This kind of analysis could be particularly powerful when making use of both wideband receiver backends and long duration observations, especially with next generation instruments.

At 154 MHz the scintles are too small to robustly resolve, thus our estimates of  $\nu_{\text{diss}} \lesssim 10 \text{ kHz}$  and  $\tau_{\text{diss}} = 34 \pm 18 \text{ s}$  should be interpreted with caution. An intermediate frequency band, in the range of 300–700 MHz, would be ideal to further characterise the scintillation properties of this pulsar. At 500 MHz, assuming  $\nu_{\text{diss}} \propto \nu^{-4.2}$  and scaling from the Parkes values, one would expect that the scintillation bandwidth is  $\nu_{\text{diss}} \approx 1.4 \text{ MHz}$ , which should be resolvable with careful

---

<sup>8</sup>An important note regarding these estimates is that we are fundamentally biased, because even if over the observation more than one full scintle passes through the line-of-sight, we do not fully sample it given that we are only counting the  $S/N \geq 6$  pulses (i.e. if some pulses are scintillating down then we simply don't detect them in this collection).

selection of observing parameters. Furthermore, observing the pulsar over a very wide bandwidth (e.g. the newly commissioned ultra-wide bandwidth receiver at Parkes, which samples 0.7–4 GHz contiguously) would enable us to resolve  $> 1$  scintles and therefore more robustly estimate the scintillation parameters, even though the steep spectral index could impact the detections at higher frequencies.

### 5.4.2 Spectral index

The spectral index distribution of RRATs is poorly explored. Recently Shapiro-Albert et al. (2018) provided single-pulse based spectral index measurements (similar to those presented here) for three RRATs (J1819–1458, J1913+1313 and J1317–5759) and find that while the average spectral indices fall within the normal pulsar population distribution, they are typically flatter than normal pulsars, which is in contradiction to what we find for RRAT J2325–0530. That being said, given that the mean spectral index measurement is based only on simultaneously detected pulses, our analysis is subject to a selection effect, whereby not including shallower single-pulse spectral indices simply because they are not detected with the MWA could act to artificially steepen the measured value. Another caveat is that the matched pulses are not always aligned (see Section 5.4.5), which could act to bias the spectral index measurement for each pulse since we are not necessarily measuring the energy from the same components/emission regions. Shapiro-Albert et al. (2018) also note a wide range of single-pulse spectral indices ( $-7 < \alpha < +4$ ), which could be due to the intrinsic emission process or because the spectral indices were measured within the observed bandwidth (where the frequency lever-arm is relatively small). Spectral indices are known to widely vary from pulse-to-pulse, for normal pulsars (e.g. Kramer et al., 2003a), and giant pulses from the Crab pulsar (e.g. Karuppusamy et al., 2010a; Meyers et al., 2017); so, it is not necessarily surprising that this is also true for RRATs.

The steep spectral index we find for RRAT J2325–0530 indicates that at least some RRATs also exhibit a relatively large range of average spectral indices,

just like the normal pulsar population. We note though that the scintillation occurring at 1.4 GHz will bias the mean spectral index to be steeper than in reality (assuming no intrinsic time variability in the emission). Taylor et al. (2016) measure a spectral index  $\alpha_{35}^{80} \approx -0.7$  across the observing band of LWA1 (35–80 MHz), which is substantially shallower than what we measure (though consistent with the trend observed by Stovall et al., 2015) and indicates that a spectral flattening may occur at frequencies  $\lesssim 150$  MHz. From a detection and characterisation perspective, this means that the next generation of radio telescopes (e.g. the SKA and ngVLA) and their pulsar/fast-transient search experiments will be in a position to compliment each other, where the low and high-frequency observations will together sample a wider range of (and possibly different) objects in the pulsar population.

### 5.4.3 Fluence distributions

Our ability to robustly distinguish between pulse energy distribution models is somewhat diminished given the relatively small number of pulses available. As previously noted, the power law models should be interpreted carefully as they only provide reasonable fits to pulses above an arbitrary fluence cut-off. This is an unfortunate, and often ignored, bias that is difficult to correct even when using more complicated fitting methods and larger data sets. Given that the data being used are only real pulse detections, any model should nominally be able to account for the high and low-energy pulses simultaneously, and the power law cannot do this. Nevertheless, comparing the relative reduced chi-squared statistics, it seems that the truncated exponential and log-normal distributions are similarly good fits to the data, while the power law is nominally a better match if we ignore the caveat of arbitrary fluence cut-offs.

Given that the normal pulsar population is seen to exhibit mostly log-normal pulse energy distributions (e.g. Burke-Spolaor et al., 2012) and that there has been recent work showing similar results for RRATs and intermittent pulsars (e.g. Cui

et al., 2017; Mickaliger et al., 2018b; Shapiro-Albert et al., 2018; Meyers et al., 2018), it appears that RRAT J2325–0530 follows the trend. An important caveat is that comparing amplitude (i.e. peak flux density) distributions to fluence (i.e. pulse energy) distributions can be confusing given that the distribution types and parameters do not necessarily map one-to-one. In our case though, we are unable to unequivocally state that a log-normal model is the best fit without further observations and a larger sample of single pulses. Furthermore, a log-normal distribution does seem to align with the evidence in the literature. Ignoring the fact that an arbitrary fluence cut-off was employed, the power law indices measured, at least for the Parkes data, are similar to those seen for Crab giant pulses (e.g. Bhat et al., 2008; Mickaliger et al., 2012), though it is difficult to confidently determine whether there is actually a steep power law tail, given our small number of detections. We do not see evidence of multiple overlapping distributions for RRAT J2325–0530 pulse energies, though, again, a larger sample of pulses is required to robustly test this.

#### 5.4.4 Pulse rates and clustering

The majority of RRATs do not have published pulse rates making it difficult to compare our measured rates for RRAT J2325–0530 to the overall population. For J2325–0530, the previously published pulse rates are:  $46 \pm 9 \text{ hr}^{-1}$  with the GBT at 350 MHz,  $52 \pm 8 \text{ hr}^{-1}$  with LOFAR at 150 MHz (Karako-Argaman et al., 2015b), and  $12\text{--}21 \text{ hr}^{-1}$  with the LWA1 between 35–79 MHz (Taylor et al., 2016). Our measured pulse rate from the Parkes data ( $43 \pm 5 \text{ hr}^{-1}$ ) is in relative agreement with these values, though we again note the importance of considering the effects of scintillation, and a different sensitivity threshold per instrument, on the detection statistics. From the perspective of the MWA, we find that the pulse rate is somewhat higher ( $73 \pm 7 \text{ hr}^{-1}$ ), despite LOFAR nominally having substantially better sensitivity. The RFI environment has the potential to adversely impact single-pulse statistics, and could be a reason why the LOFAR pulse rate

is smaller than expected from the MWA measurements. Nominally, the MWA is substantially less affected by RFI than LOFAR in certain frequency bands, particularly around 150 MHz (e.g. Offringa et al., 2013, 2015).

A caveat to this discussion is that comparing pulse rates between different observing epochs intrinsically assumes that the pulses are produced by a Poisson process, where pulses occur independently and at a constant average rate. It is unclear whether this is the case for RRAT emission in general. Shapiro-Albert et al. (2018) find that there is evidence for pulse clustering on relatively short time scales (tens of rotations) beyond what can be attributed to a random emission process, whereas Palliyaguru et al. (2011) did not find such an effect occurring on longer time scales. From our analysis, we do not find evidence that single pulse emission from RRAT J2325–0530 is anything other than randomly distributed.

#### 5.4.5 Pulse peak misalignment

In many instances when comparing our coincident pulses, there is an offset between the peak emission locations. For example, in Figure 5.1, we see that the peaks at 154 MHz and 1.4 GHz align reasonably well for pulse 1292 (middle), but do not in pulses 527 (left) and 4318 (right). Initially, one might assume a clock offset between the two telescopes that has not been taken into account, although this would nominally appear as a constant offset between the peaks of coincident pulses. Upon careful inspection of matched single pulses, it is interesting to note that while the peaks do not align, there is generally complete overlap in the total emission envelope at each frequency (which is also true for pulses 527 and 4318). This points towards a phase-dependent spectral index such as those seen for some millisecond pulsars (e.g. Dai et al., 2015). Another possibility, assuming that the emission frequency is proportional to the emission location (e.g. altitude), is that there are multiple discrete emission zones firing at slightly different times. Given that characterising the pulse-to-pulse variability of even well-studied pulsars is challenging (e.g. jitter noise, Liu et al., 2012; Shannon et al., 2014), it is difficult

to confidently determine why single pulses from a RRAT would exhibit emission peak phase offsets. Determining the geometry of the system through additional wideband single-pulse polarisation measurements and analysis (e.g. Caleb et al., 2019) would provide stronger evidence as to the nature of the single-pulse misalignment and why it changes from pulse to pulse.

## 5.5 Concluding remarks

We present the first detection of RRAT J2325–0530 made simultaneously over a wide range in frequency (154–1400 MHz) with the MWA and Parkes radio telescopes. Over the respective observations we detected 89 and 70 pulses with the MWA and Parkes, implying pulse rates of  $73 \pm 7$  and  $43 \pm 5$  pulses per hour. The single-pulse spectral index distribution of RRAT J2325–0530 with a mean of  $\alpha_{154}^{1369} = -2.2 \pm 0.1$  is relatively steep compared to the normal pulsar population, though scintillation bias makes it difficult to robustly estimate from a single observation. The pulse energy distribution of RRAT J2325–0530 is best described by either a log-normal or truncated exponential model, in general agreement with previous RRAT studies, and with the typical pulsar population. We also provide the first polarimetric profiles and RM estimate for this pulsar, with  $\text{RM}_{\text{ISM}} = 3.8 \pm 0.1 \text{ rad m}^{-2}$ , where the ionospheric correction is the dominant source of uncertainty for the low-frequency MWA measurement.

This is the first time scintillation properties have been measured for a RRAT, using a necessarily modified version of the standard autocorrelation analysis employed. Even with the inherently irregular single-pulse emission, we clearly see scintillation at 1.4 GHz, with a characteristic bandwidth of  $\nu_{\text{diss}} = 102 \pm 72 \text{ MHz}$  and time scale of  $\tau_{\text{diss}} = 3478 \pm 2550 \text{ s}$ . Notwithstanding the limitation of the number of scintles observed at 1.4 GHz, and the inadequate frequency resolution at 154 MHz, we place constraints on the scintillation velocity and turbulence within the ISM along the line-of-sight to RRAT J2325–0530. We also measure a scintillation frequency scaling index of  $\gamma = -4.2$ , which is close to the theo-

retically steepest value,  $\gamma = -4.4$ , of Kolmogorov turbulence. The line-of-sight for this RRAT is relatively typical of near-Earth pulsars based on the estimated scaling index, and on the turbulence strength ( $\overline{C_n^2} \lesssim 2.8 \times 10^{-4} \text{ m}^{-20/3}$ ), as might be expected given its large Galactic latitude ( $b = -60.2^\circ$ ). In future scintillation analysis of RRAT J2325–0530, it will be important to study the emission at an intermediate frequency band, nominally in the 300–700 MHz range, where the scintillation properties are expected to be better suited to characterisation.

It is important to make use of multi-telescope, multi-frequency studies of these objects in order to place their emission properties in the context of the normal pulsar population, given that many emission characteristics of RRATs remain a mystery. The steep spectrum of the emission and the relatively large pulse rates indicate that future and on-going surveys, such as those using LOFAR, the MWA and those planned with the SKA, will be in a good position to find new examples of these objects.

### 5.5.1 Acknowledgements

*People and funding:* B.W.M. thanks C. Karako-Argamann and P. Chawla for valuable discussion regarding the pulse rates of J2325–0530 and the comparison thereof. The authors acknowledge the contribution of an Australian Government Research Training Program Scholarship in supporting this research. R.M.S also acknowledges support through ARC grant CE170100004. Part of this research was supported by the Australian Research Council Centre of Excellence for All-sky Astrophysics (CAASTRO), through project number CE110001020.

*Software:* This work made use of the following software packages: PSRCHIVE (Hotan et al., 2004; van Straten et al., 2012), DSPSR (van Straten & Bailes, 2011) and STILTS (Taylor, 2006). The following Python modules we also used as part of this work: AstroPy (The Astropy Collaboration et al., 2013, 2018), NumPy (van der Walt et al., 2011), SciPy (Jones et al., 2001), LMFIT (Newville et al., 2014), and Matplotlib (Hunter, 2007b).

*Facilities:* This scientific work makes use of the Murchison Radio-astronomy Observatory, operated by CSIRO. We acknowledge the Wajarri Yamatji people as the traditional owners of the Observatory site. Support for the operation of the MWA is provided by the Australian Government (NCRIS), under a contract to Curtin University administered by Astronomy Australia Limited. The Parkes radio telescope is part of the Australia Telescope National Facility, which is funded by the Commonwealth of Australia for operation as a National Facility managed by CSIRO. We acknowledge the Pawsey Supercomputing Centre which is supported by the Western Australian and Australian Governments.

# Chapter 6

## Linking the sub-populations of intermittent and sporadically emitting pulsars

There are numerous pulsar populations, and these populations are almost exclusively determined by the physical properties of the pulsars (see e.g. Kaspi & Kramer, 2016). For example, there are the canonical pulsars which make up the vast majority of the  $P-\dot{P}$  diagram; the millisecond pulsars which exist in their own island; and the magnetars which form a small but distinct region at the top of the  $P-\dot{P}$  phase space. These populations are based on the pulsar physical properties (i.e. spin rate, magnetic field strength, energy loss rate, etc.). On the other hand, one can construct sub-populations from the observed emission properties. From this perspective, one finds the populations of nulling pulsars, RRATs, intermittent pulsars, and giant pulse emitters. These pulsars generally do not appear to form their own regions in the  $P-\dot{P}$  diagram (with the notable exception of giant pulses which all appear to have high magnetic field at the light cylinder and large  $\dot{E}$ ), made clear in Figure 1.4.

Within the literature, these different sub-populations of pulsars are often treated as separate distinct objects or phenomena. In reality these objects all

share many common characteristics (as they are all still neutron stars), and it is not clear whether they are as distinct as previously thought. These different kinds of pulsar could well be linked, and do not necessarily need individual bespoke explanations, but could be on a continuous spectrum of emission behaviour. This notion is not necessarily new (e.g. Redman & Rankin, 2009; Burke-Spolaor & Bailes, 2010; Esamdin et al., 2012), but as more examples of sporadic and intermittent pulsar emission are discovered (or examined more closely), there is mounting evidence that this is the case.

In this thesis, examples of three different kinds of pulsar emission have been examined in detail: giant pulses (PSR J0534+2200; Chapter 3), intermittent and/or state-switching emission (PSR J1107–5907; Chapter 4), and sporadic single burst events (RRAT J2325–0530; Chapter 5). This approach made three case studies, providing a detailed analysis of the broadband emission of these pulsars, particularly focussing on their single pulse properties. The analysis leveraged low frequencies from the MWA in conjunction with other telescopes at higher frequencies (i.e. the UTMOST and Parkes telescope) to facilitate the broadband, simultaneous single-pulse approach. The novelty of this approach was to consistently adopt a single-pulse, multi-frequency, simultaneous observing strategy in order to extract as much information as possible about the dynamics of the pulsar emission mechanism across different classes of pulsar, from short duration data sets. Additionally, the use of the MWA provides a new parameter space for these pulsars in the southern hemisphere.

The motivation for this thesis is to explore the possible relationships between different pulsar sub-populations that display intermittent or sporadic emission phenomenon. To do this, we first outline the differences as well as common attributes observed to date, before delving into the specifics and outlining future directions.

## 6.1 Distinguishing properties

The objects studied in this thesis are similar; they are pulsars that emit bright, coherent radio emission over a broad frequency range ( $\sim 100$  MHz to several GHz). At first glance, giant pulse emitters, intermittent pulsars and RRATs each present a different kind of emission phenomenology. In terms of the maturity of understanding of each sub-population, giant pulses have been studied for several decades, whereas intermittent pulsars and RRATs were only discovered just over a decade ago. Furthermore, the sub-population sizes are small, with only a handful of giant pulse emitters and intermittent pulsars, and just over one hundred RRATs (the majority of which have only been detected once). Nevertheless, it is important to consider some of the major differences explicitly in order to compare them meaningfully.

It is well established that giant pulses are orders of magnitude brighter and exhibit different emission characteristics (e.g. pulse energy distributions, intrinsic time scales, spectral index) than regular pulses from the same pulsar. The occurrence of giant pulses appears to be random, at least in the case of the Crab pulsar. More generally, giant pulses typically occur on time scales of seconds, though this can range anywhere from  $\sim 100$  ms–10 min depending strongly on the individual pulsar and observing configuration (e.g. Soglasnov et al., 2004; Knight et al., 2006; Meyers et al., 2017). Intermittent pulsars and RRATs are harder to distinguish from each other, though have some salient emission characteristics that help to define the different populations. RRATs typically produce single pulses, or small clusters of bursting emission, on time scales of minutes to hours. Intermittent pulsars exhibit more of a state-switching behaviour, wherein they abruptly switch between two or more emission states. One of those states is such that the pulsar appears “off”, and often lasts anywhere from hours to months. Naturally, the characteristic properties of sporadic emission depend on observing configuration and instrument sensitivity; e.g. an intermittent pulsar could mimic RRAT-like emission if placed far enough away or observed with a less sensitive

instrument (see e.g. Section 4 of Chapter 4 , where we show that pulses from the intermittent pulsar J1107–5907 could replicate RRAT-like emission properties if it were twice as far away). PSR J1717–4054 exhibits intermittency on time scales similar to PSR J1107–5907 (Kerr et al., 2014) and shows distinctly different behaviour to other high nulling fraction pulsars (e.g. Gajjar et al., 2014b). While the single pulse energy distribution of PSR J1717–4054 appears to have a relatively extended tail, there are no clear examples of exceptionally bright single pulses. This is generally true for the majority of intermittent pulsars in the literature, although it is difficult to currently say whether this is a significant difference (i.e. PSR J1107–5907 happens to be a special case), since the majority of analysis is focused on the timing and intermittency time scale aspects, rather than comparing individual pulses.

If we incorporate nulling pulsars into the picture, the division between distinct groups (based on time scales alone) becomes substantially less clear, as depicted in Figure 6.1. It is important to reiterate that these different sub-populations of pulsars do not form particularly distinct populations on the  $P$ – $\dot{P}$  diagram (Figure 1.4), other than the giant pulse emitters and perhaps some fraction of the RRATs — although the spread is very large and only 29 out of 112 have a timing solution (i.e.  $\dot{P}$ ). While phenomenological differences exist (i.e. how RRAT emission consists of single-pulse events, whereas intermittent pulsars enter “on” states for longer durations in terms of the time scale parameter space), these overlaps between populations make it difficult to claim they are characterised by fundamentally different mechanisms. Furthermore, we do not currently know of a physical mechanism that can predict multiple emission time scales, especially in the same pulsar. Adding to the complexity it is unclear how much of the difference seen in the observed emission time scales is a consequence of selection effects.

Finally, in comparing giant pulse emission to the emission from RRATs or intermittent pulsars, it is clear that the emission characteristics are different.

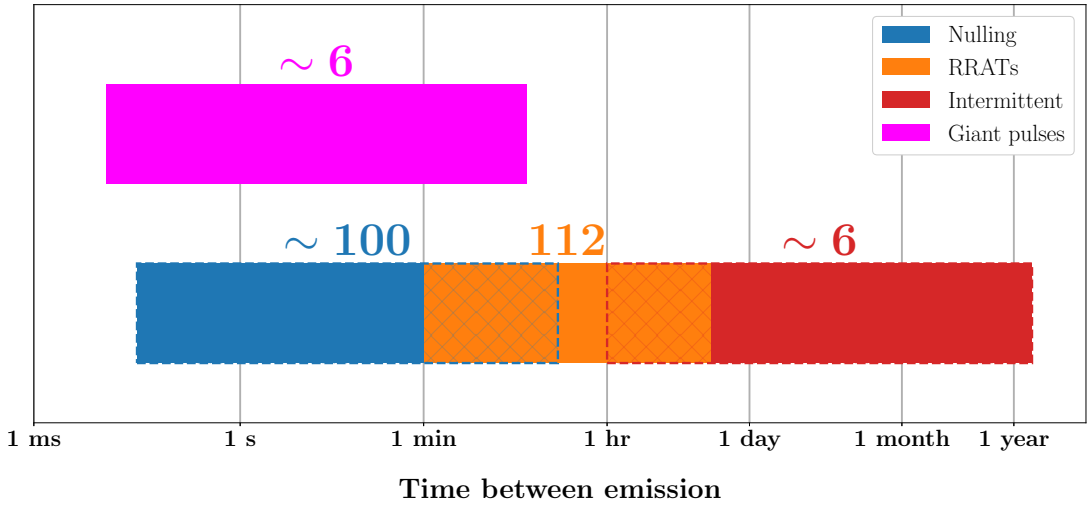


Figure 6.1: Approximate time scales on which emission occurs in different classes of pulsar. It is clear for nulling, RRATs and intermittent pulsars that there is significant overlap, as indicated (approximately) by the hatched regions. Giant pulses are separated because their emission time scale refers to the time between subsequent giant pulses (i.e. emission well above the norm), whereas for the other classes the time scale refers to the time between subsequent emission above quiescence.

Primarily, we see that giant pulses from the Crab pulsar have significantly different pulse energy and spectral index distributions when compared to the single pulses from the other two pulsars analysed. In this way, it is difficult to then claim that giant pulses could be responsible for the emission we see from these sporadically emitting pulsars, although it is also worth noting that giant pulse emitters also show normal radio emission. It is interesting to note that giant pulses have (currently) only been detected from young energetic pulsars or MSPs (e.g. Johnston & Romani, 2004), whereas emission intermittency is largely seen in older and/or solitary pulsars (e.g. the characteristic age of PSR J1107–5907 is  $\sim 440$  Myr) with a tentative overlap between the long-period pulsars and magnetar populations in the case of RRATs.

## 6.2 Similarities between populations

There is wide distribution of emission phenomenology and characteristics observed from canonical pulsars. This also appears to be true for sporadically emitting pulsars, with the added characteristic of emission intermittency. These intrinsic emission characteristics are the means by which we can determine whether the underlying emission mechanism(s) are common or qualitatively different between the different pulsar sub-populations. The three examples studied here indicate that at least RRATs and intermittent pulsars could share a common emission mechanism, while giant pulses (from the Crab pulsar) are certainly a distinct class of emission.

### 6.2.1 Broadband emission

One of the most basic observational qualities of pulsars, including those studied here, is that the radio emission is broadband, over at least an order of magnitude in frequency ( $\sim 0.1\text{--}1\,\text{GHz}$  for PSR J1107–5907 and RRAT J2325–0530,  $\sim 0.1\text{--}3\,\text{GHz}$  in the case of the Crab). While not a new insight, addressing this question from a single-pulse perspective for three different kinds of sporadic pulsar emission is rarely done and naturally provides more information about the emission mechanism than disparate observations over different epochs. This is an important aspect of pulsar emission to understand since most emission mechanism models predict emission within some finite bandwidth, and the broadband emission observed can be used to guide theoretical work towards a model (or set of models) that can produce emission across an extremely wide frequency range simultaneously. The work presented in Chapters 4 and 5 represents the first time this kind of broadband study, including low-frequency observations, has been accomplished for RRATs and intermittent pulsars. Multi-frequency studies of normal and millisecond pulsars are also conducted (and are becoming more tractable with the advancement of observing and processing technologies) and often produce a wide range of scientific outcomes beyond the original project scope.

From the perspective of investigating pulsar phenomenology (e.g. nulling in PSR J1136+1551, or subpulse drifting from PSRs J0034–0721 and J0814+7429), there have been efforts in the past using multi-frequency, multi-telescope observations (e.g. Backer et al., 1975; Bartel & Sieber, 1978; Biggs, 1992; Smits et al., 2006; Bhat et al., 2007a; Gajjar et al., 2014a; Naidu et al., 2017). In most cases, these studies were hindered by incomplete samples of single pulses due to sensitivity limitations. Additionally, low-frequency observations of the vast majority of pulsars in the southern hemisphere are lacking or non-existent, thus exploiting the capabilities of the current generation of low-frequency telescopes acts to break new ground and lay a path forward for the next generation of radio telescopes (i.e. the SKA). Ultimately, comparing the observed emission properties of these objects to those from the normal pulsar population allows us to meaningfully comment on how these pulsars emit, and to identify similarities.

### 6.2.2 Spectral index

The spectral index of radio emission from pulsars has been studied for decades (e.g. Sieber, 1973a; Lorimer et al., 1995; Maron et al., 2000a; Bates et al., 2013; Bilous et al., 2016; Jankowski et al., 2018b) and is known to vary widely between pulsars, but is generally quite steep, with  $-1.8 \lesssim \langle \alpha \rangle \lesssim -1.4$ . These measurements are predominately made at frequencies well above 300 MHz, where it is expected that the spectrum is described by a power law model,  $S \propto \nu^\alpha$ , at least in the radio regime. At low radio frequencies (i.e.  $\lesssim 300$  MHz) the expected behaviour of the pulsar spectral index is not well constrained, yet this is precisely where interesting spectrum shape features (i.e. a flattening, break(s), or a complete turn over) are expected to appear. This is exacerbated by the lack of examples in the literature where flux densities and spectral indices are calculated and compared at these frequencies. Furthermore, spectral indices are typically measured by comparing the mean profiles of pulsars, which misses the potentially critical information that can be extracted when measuring the spectral index on

a single-pulse level. The limiting factor in the case of the pulsars studied here is that, while broadband, they are not steady emitters, thus single-pulse spectral index measurements are the only reasonable approach. Thus, single-pulse spectral index measurements that include low-frequency information (which are poorly represented in the literature) provide a novel way to probe the underlying emission mechanism.

For the Crab, we found evidence that the spectral index flattens substantially at low radio frequencies ( $\alpha \approx -0.7$ ), compared to the normally very steep value observed above  $\sim 300$  MHz ( $\alpha \approx -2.6$ ; see Sections 4.5 and 5.1 of Chapter 3). This is the first time that such a drastic change in the flux density spectrum has been directly shown for Crab giant pulses, and raises some interesting questions about FRB emission detectability at low frequencies. Primarily, this does not support the idea that Crab-like giant pulses can be used to explain FRBs, since the objects are either close enough but have poorly matched spectral properties for low-frequency radio detection; or the FRB progenitors are at distances  $\gtrsim$  few hundred Mpc which puts them beyond the nominal distance limits of current giant pulse emission models (for details see Sections 5.2 and 5.3 of Chapter 3). Additionally, incorporating other observations over decades in time and frequency further reinforces the claim, and is summarised in Figure 11 of Chapter 3. The broadband, simultaneous single-pulse analysis was critical in this case, as it highlighted that individual giant pulses had widely varying spectral indices, but that on average they combined to produce the flattening observed. It can also partially explain why some giant pulses are not necessarily observed at other simultaneously observed frequencies.

In the cases of PSR J1107–5907 and RRAT J2325–0530, the single-pulse spectral index distributions appear slightly steeper ( $\alpha \approx -1.8$  and  $\alpha \approx -2.2$ , respectively), but within the scatter of the normal pulsar mean spectral index measured at higher frequencies ( $\langle \alpha \rangle = -1.6$ ; Jankowski et al., 2018b). For RRAT J2325–0530 in particular it is difficult to comment on the true spectral index

distribution statistics as the pulsar is scintillating (diffractive) strongly, which introduces a substantial bias to the measured flux densities as a function of time and frequency. In order to overcome this, regular wideband observations over a time scale of several months would be required such that several refractive scintillation cycles are sampled and that there are a significant number of individual scintles sampled so, at least on average, the effects of diffractive and refractive scintillation bias is reduced. A benefit to using single pulses in this case is that their intrinsic emission properties generally change on time scales much faster than the changes induced by the ISM, and thus give a less obfuscated view of the intrinsic emission mechanism.

PSR J1107–5907 is also interesting in this context as it has multiple profile components, each of which appear to have a different spectral index distribution (see Figure 4 of Chapter 4). The so-called “MP” component (brightest) has a mean single-pulse spectral index that is consistent with the normal pulsar population and a relatively wide distribution, whereas the “PR” component has a much steeper spectral index and a slightly more compact distribution. Furthermore, individual components appear to have a phase-dependent spectral index (also see in MSPs), though the caveat of acquiring enough individual pulses to stabilise the integrated profile applies here, too.

Importantly, while spectral index was not considered in selecting the pulsars studied here, the examples we present exhibit relatively steep spectral indices<sup>1</sup>. Even if this characteristic holds true for only some objects (which seems to be the case, at least for RRATs), it implies that the next generation of low-frequency telescopes will be in an excellent position to both study these known objects in greater detail, and find new objects that are beyond the capabilities and/or sensitivity range of current radio telescopes.

The work presented here, particularly in the case of Crab giant pulses, also solidifies the notion that the classical two-point spectral index measurements

---

<sup>1</sup>It is also important to recognise that we are likely subject to observational selection bias, given that low-frequency observations are more sensitive to steep-spectrum source.

are often inappropriate measures of the emission from pulsars, especially at low radio frequencies. It is often the case that only two frequencies are available on a pulsar SED (for single-epoch pulsar studies), given the difficulty in even organising simultaneous observations with two telescopes, let alone three or more. However, with wide-band instruments/backends coming online (e.g. the Ultra-Wide-Band receiver at Parkes, and a similar receiver planned for the GBT), and instruments with the capability to dynamically split their bandwidth across a wide frequency range (like the MWA), this issue is being alleviated.

The spectral index of the emission is a critical piece of information that will help to better understand pulsar emission. Few theories are developed enough to make predictions about the shapes and/or statistical parameters that define the radio frequency spectral index distribution of a pulsar (whether it is an intrinsic emission aspect, or an imprinted propagation effect). For example, Machabeli & Chkheidze (2014) model Crab giant pulse flux density spectra based on high-frequency radio and very high energy (X-ray and Gamma-ray) observations and therefore cannot reproduce the spectral behaviour we find. In the case of general pulsar emission the outlook is even less clear, with few models consistent with rich phenomenology of observed pulsar emission behaviour, discussed in detail by Melrose & Yuen (2016), Melrose (2017), and references therein. Having single-pulse spectral index distributions for a large sample of pulsars, both sporadically emitting and otherwise, will be key to both develop and then test theories of pulsar emission.

### 6.2.3 Pulse energy distributions

The mechanism responsible for the coherent radio emission from pulsars produces a (sometimes very wide) range of emission intensities that directly relate to the amount of energy injected or released. Measuring the form and characterising the shape of these pulse energy distributions (and, historically, the amplitude distributions) is another important avenue with which we can better constrain

emission mechanisms. The fluence (which is the integrated emission over a given time scale) in the single-pulse sense corresponds to an estimate of the total energy emitted by the pulsar and is therefore more closely linked to the emission mechanism than the peak flux density alone. While often not necessarily physically motivated by predictions from emission models, parametrising the distribution of single-pulse energies is important to statistically evaluate similarities between different pulsars and types of emission (e.g. Burke-Spolaor et al., 2011, 2012). For this reason, in all three cases presented here, we attempted to produce detail characterisation of the single pulse energetics, specifically examining the distribution shape and comparing to previous works of both other sporadically emitting pulsars and the canonical pulsar population.

A clear example of this is the distinction between giant pulse emission and the emission we have observed from both the intermittent pulsar and RRAT studied in this thesis. The giant pulse emission is drawn from a steep power law distribution which appears as a tail to the “normal” emission, which is either a log-normal or exponential distribution. This is complicated by the fact that the noise level of the detector often imprints its noise signature on top of the intrinsic emission distribution. Low-frequency observations are sky-noise dominated, thus it is extremely difficult to capture the true shape of the pulse energy distributions without contamination from system noise. Even the steep spectral index of most pulsar emission ( $S_{\text{psr}} \propto \nu^{-1.6}$ ) is ultimately dominated by the sky-temperature frequency scaling, where  $S_{\text{sky}} \propto \nu^{-2.5}$ . The benefit of studying individual pulses, though, is that not every pulse necessarily exhibits the same spectral index, as discussed in the previous section, thus we often find single pulses with exceptionally steep spectral indices (e.g. the extremely bright pulses from J1107–5907, in Figure 3 of Chapter 4), from pulsars that otherwise appear to fit with “normal” population statistics. This implies that to some level, the low frequency observations are sampling a slightly different population of pulses than the corresponding simultaneous observations at higher frequencies, and therefore (presumably) dif-

ferent emission regions and/or regimes within the magnetosphere of the pulsar. Continued efforts in this regard, especially with more sensitive instruments such as the uGMRT and LOFAR, is necessary if we are to further test this idea for a large sample of pulsars, including those that emit sporadically.

For the intermittent pulsars and RRATs, we see a more “standard” picture, in that their pulse energy distributions very much resemble those seen in the normal (long-period) pulsar population. This hints that the underlying physics responsible for normal pulsar radio emission is the same physics creating the bursting, sporadic emission we see in these other sub-populations. This is perhaps not surprising in a general sense, given that from the intermittent pulsar perspective, when these pulsars are in their “on” states, the emission properties (including the nulling phenomenon) are similar to normal pulsars. A testament to this is that most intermittent pulsars were not initially discovered to be switching between states, but were originally considered normal periodic emitters. In the case of RRATs, while their emission is only detected through bursts of pulses, we still see that the pulse energy distributions are similar in shape to those of normal pulsars.

From a technological and strategic perspective, the advent of the MWA has expanded the parameter space for single-pulse emission studies of pulsars in the southern hemisphere. The uGMRT and LOFAR telescopes have also made significant contributions to this effect in the northern hemisphere and mid-latitude regions (e.g. Coenen et al., 2014a; Bhattacharyya et al., 2016). As a SKA-Low pathfinder instrument, these results also provide a way of predicting, at least qualitatively, the impact that a survey of intermittent and sporadic pulsars will have in terms of constraining the emission mechanism at radio frequencies that are often under sampled.

## 6.3 Detection and characterisation in the future

The detectability of these types of pulsars increases with both the field-of-view and on-sky time. With the next generation of radio telescopes now entering design and/or construction, this work is timely and deserves consideration in the context of pulsar searches on these instruments. These telescopes will provide flexible (and possibly commensal) observing modes, which will allow us to exploit different pulsar finding strategies. One viable example would be to use the large field-of-view and regular monitoring cadence of the planned transient surveys to find pulsar candidates and then conduct follow-up observations of these objects with high-time resolution observations. Strategies like these, employed on next generation telescopes, will provide the best possible chances of detecting new examples of intermittent and sporadic pulsar emission, but will also allow for regular monitoring of known sources.

The regular re-observation of known sources is imperative in determining source properties and in constraining our understanding of the pulsar population. While currently there are very few population synthesis studies of RRATs (e.g. Patel et al., 2018) or intermittent pulsars<sup>2</sup>, these are clearly an important fraction of the total Galactic pulsar population. In particular, there is a clear dearth in low-frequency detections of these objects (which is gradually changing with surveys from LOFAR, the MWA and eventually the SKA) which imparts a significant bias onto the population modelling since it is not at all clear whether pulse emission below 300 MHz mimics that at  $\sim 1$  GHz. The low frequency characteristics of Crab giant pulses (Chapter 3) indicate this is not true. Observational data is required to inform these population synthesis studies, which is exactly where next generation telescopes can excel. The predicted number of pulsar detections for the SKA-Low Phase 1, even with relatively conservative assumptions, as informed directly by the MWA pulsar census (Xue et al., 2017) is  $\sim 9400$ . It is difficult to extrapolate what this, or any other population prediction, means for RRATs

---

<sup>2</sup>In many pulsar population studies, these objects are often completely ignored.

and intermittent pulsars as we do not have a good handle on how complete the samples are (i.e. how many are detectable versus how many have we detected). Again, this calls for more comprehensive (preliminary) population synthesis studies such that we may begin to better understand and predict the prevalence of sporadically emitting pulsars in our Galaxy.

Yet another area where the SKA-Low can potentially excel is the systematic searches for giant pulse emission from known pulsars. Blind, all-sky single pulse searches have been conducted, however, a small fraction of pulsars have been searched for giant pulses. Fresh examples of giant pulse emitters will provide new probes into the pulsar emission mechanism responsible, while also giving valuable insights into the properties of giant-pulse emitting pulsars (which are difficult to extract for a population based on only a handful of examples). Historically, this has not been done because not only is it difficult to record the required amount of data, with single pulse sensitivity, but the processing resources and time required to conduct such investigations can be intractable, especially if the processing needs to be done in semi-real-time or even on-the-fly. Nevertheless, contemporary single-pulse studies have shown that there is an enormous amount of information available about individual pulsars, and the general pulsar population (e.g. Burke-Spoliar et al., 2011, 2012; Mickaliger et al., 2018a). The ability to do this in real-time (e.g. as in the cases of Parkes and Arecibo), all of the time is an exciting prospect for this kind of science when also considering the all-sky observing nature of the next generation telescopes. With significant progress in simulation of pulsar emission, there is also significant theoretical traction for this kind of giant pulse search. For instance, using particle-in-cell simulations, Philippov et al. (2019) show that magnetic reconnection events in the outer magnetosphere are able to produce the nanoshot emission observed in giant pulses from the Crab pulsar. Furthermore, this model also predicts that pulsars with lower magnetic field strengths at the light-cylinder could still occasionally emit giant pulses with similar energetics that would only be detected at low radio frequencies.

The discovery and characterisation of further examples of intermittent and sporadically emitting pulsars will provide new insights into the radio emission mechanism of pulsars. A testament to this is that the distinctions between RRATs, intermittent pulsars and nulling have become blurred. Increasing the number of sources available to contrast will provide the key insights into whether these pulsars are operating with the same physical mechanisms, and to the plausibility of such a mechanism producing a wide range in emission time scales. Work in this area, using precursor instruments like the MWA and LOFAR, is an effective way of demonstrating the impact that the SKA-Low will have on pulsar science. Indeed, deeper insights are gleaned by combining efforts with other major telescope facilities in order to simultaneously observe over very wide frequency ranges. Sustained efforts in this regard, particularly employing the next generation of radio telescopes, will also enable us to construct a comprehensive understanding of the Galactic pulsar population, besides the potential of revealing the physics driving the radio emission mechanism.



# Appendices



# Appendix A

## Co-author agreements

Below are the responses from co-authors, addressing the statement made in Section 1.12 (also repeated here).

### A.1 Statement of Originality

This section is to comply with the requirement that all co-authors of work included in this thesis outline their contributions. In communicating this statement to the co-authors, they were also informed that the lack of a response would be taken as unconditional tacit approval. Otherwise, all co-authors have read and agreed to the following statement, and their responses can be found in Appendix A.

In Chapter 3, we investigated giant pulses from the Crab pulsar (PSR J0534+2200) with the MWA using the then newly implemented “coherent beamforming” pipeline. The MWA data for this project were reduced by F. Kirsten, and the analysis was carried out by myself under the supervision of S. Tremblay, R. Bhat and R. Shannon. The flux density calibration technique and application detailed in this work (which is also used in subsequent chapters) was also developed by myself with significant input from A. Sutinjo and D. Ung regarding the theoretical aspects of the design, and from M. Sokolowski regarding the practical application of the

simulation results to the data. R. Shannon provided the nominal Parkes observing and data processing procedure description included in the published article (which I edited to fit into the paper), and I wrote the other sections of the paper. S. Tremblay, R. Bhat and R. Shannon aided in the article writing process by providing guidance in terms of the structure and contextual discussion, both before and after referee comments were received. Additional co-authors for this paper provided comments on the paper drafts and contributed to the planning and execution of the experiment prior to the beginning of my PhD.

I led the proposal and organisational aspect of simultaneous MWA and UTMOST observations of the intermittent pulsar PSR J1107–5907 in 2017 (Chapter 4). The development of the MWA buffered triggering system was led by B. Crosse and A. Williams with input from myself and S. Tremblay in terms of testing and configuration. The corresponding observations with UTMOST were facilitated by C. Flynn, W. Farah and V. Gupta. Archival UTMOST data were retrieved and provided by C. Flynn and V. Gupta, as well as the relevant information required for the UTMOST flux density calculation. I conducted the processing and analysis of both data sets, and wrote the resulting paper, except for the text describing the UTMOST observations and technical details which was initially provided by C. Flynn and V. Gupta (and subsequently altered by me to fit into the paper). S. Tremblay, R. Bhat and R. Shannon provided detailed input on the scope and structure of the article, S. Murray provided input regarding the fluence distribution analysis and C. Sobey provided ionospheric rotation measure estimates used to correct the observed value. Other co-authors are members of the UTMOST or MWA telescope collaborations, and provided comments on the paper drafts and/or made contributions to the funding, development, management, and maintenance of their respective instrument.

Finally, in Chapter 5, we used the MWA and Parkes radio telescope to simultaneously observe the Rotating Radio Transient J2325–0530. Observations were provided through Director’s Time proposals submitted by myself to both

the MWA Director and Parkes time allocation/scheduling manager. I led the analysis of both data sets, and wrote the entirety of the article. Flux density and polarisation calibration advice for the Parkes data was provided by R. Shannon. C. Sobey provided ionospheric rotation measure estimates in order to correct both Parkes and MWA polarimetric profiles. S. Tremblay, R. Bhat, R. Shannon and S. Ord provided initial input into the scope of the analysis, with R. Bhat and R. Shannon providing particular input on the scintillation analysis. Additional co-authors provided comments and helped to shape the final published work, which has been submitted to the Publications of the Astronomical Society of Australia (PASA) journal.

## A.2 Co-author responses

**Matthew Bailes** <matthew.bailes@gmail.com>

I am happy with that.

Good luck!

**Charlotte Sobey** <Charlotte.Sobey@csiro.au>

Hi Bradley,

Thanks for your email.

That looks fine to me.

Good luck with the rest of your writing up. It sounds like you're on top of it, but feel free to ask if you need any help!

Many thanks and best wishes,

Charlotte

**Miguel Morales** <miguelfm@uw.edu>

I approve (congratulations in advance!)

-Miguel Morales

**Ryan Shannon** <rshannon@swin.edu.au>

Fine by me!

**Andrew Williams** <Andrew.Williams@curtin.edu.au>

Hi Bradley, fine with me - I'm not sure you need to mention Brian or I, because the buffered triggering is part of the MWA telescope, it wasn't developed just for that research project.

Andrew

**David Emrich** <D.Emrich@cutin.edu.au>

Hi Brad,

Looks fine to me.

Cheers,

Dave Emrich.

**Stephen Ord <Stephen.Ordinal@csiro.au>**

Hi Bradley,

I confirm that my contribution to the published works is consistent with the statement of originality as presented.

Best,

Stephen

**Franz Kirsten <franz.kirsten@chalmers.se>**

I, Franz Kirsten, hereby confirm that my contribution to the works published by Bradley Meyers is consistent with what is outlined in the Statement of Originality.

Cheers,

Franz

**Mia Walker <Mia.Walker@curtin.edu.au>**

To whom it may concern,

I confirm that I have read and agree to the statement of originality by Bradley Meyers regarding my contribution as a coauthor to the published works.

Kind regards,

Mia Walker

**Randall Wayth <R.Wayth@curtin.edu.au>**

I support the statement of originality.

Cheers,

Randall

**Thomas Franzen <franzen@astron.nl>**

Hi Bradley,

Thanks for your e-mail. I approve the statement in your thesis. I am a co-author on these papers because I am on the MWA Phase II Builders list.

Good luck with the thesis writing.

Cheers

Tom

**Samuel Oronsaye <oronsayes@gmail.com>**

Hi Bradley,

Congratulations. I agree strongly with your statement of originality.

Cheers,

Sam

**Fabian Jankowski <fjankowsk@gmail.com>**

Hi Bradley,

What is written in the attached Statement of Originality document sounds fine to me. I am happy to accept it as is. Good luck with your thesis submission and viva (if you have any)!

Cheers.

Fabian

**Steven Murray <smurra18@asu.edu>**

Hi Brad,

You have my approval, and good luck!

Cheers,

Steven

**Chris Flynn <cmlflynn@gmail.com>**

That's spot on Bradley – no worries!

**Marcin Sokolowski <marcin.sokolowski@curtin.edu.au>**

Dear Bradley,

Thank you for your e-mail.

To the best of my knowledge, hereby I confirm that the information in the provided statement is true and reflects Bradley Meyers' contributions to his papers and my small contribution to one of his publications.

Kind Regards,

Marcin Sokolowski

**David Kaplan <kaplan@uwm.edu>**

Looks good to me.

David

**Wael Farah <wael.a.farah@gmail.com>**

Hi Bradley,

Yes, I approve.

Cheers,

Wael

**Timothy Bateman <bateman.tim@gmail.com>**

Hi Bradley,

I'm not directly referenced with regards to the joint MWA/UTMOST observations and my contribution is completely covered where you mention other members and their contributions to their respective telescope collaborations. I require no further acknowledgement.

Thanks,

Tim Bateman

**Cathryn Trott <Cathryn.Trott@curtin.edu.au>**

Hi Bradley,

I see. In that case, I will agree with your statement as written, and add a bit more:

“Trott was involved in the design of Phase II of the MWA”

Cheers,

Cath

**Steven Tremblay <steven.tremblay@curtin.edu.au>**

Well... I was going to try and be different by going with the tacit approval approach, but since that seems to be such a popular option I guess I'll flip-flop and be explicit.

I'm happy with the statement of originality as written, and the description of my contributions within.

Steve Tremblay

**Ramesh Bhat** <ramesh.bhat@curtin.edu.au>

Hi Bradley,

Thanks for that. I had a look through this, and I can indeed confirm that my stated contribution to the published articles is consistent your statement of originality.

Regards,

Ramesh

**Chen Wu** <chen.wu@uwa.edu.au>

Hi Bradley,

I would like to give my consent as a co-author to the statement of originality.

Good luck with your thesis!

Regards,

Chen

**Steven Tingay** <s.tingay@curtin.edu.au>

I'm ok with it. You did say no response would be taken as tacit approval.

Steven

**Adam Beardsley** <adam.p.beardsley@gmail.com>

Hi Bradley

I can't really speak to the details, but I have no problem with it. So consider it approved from my end.

Thanks, and good luck submitting!

-Adam

**Vivek Venkatraman Krishnan** <vivekvenkris@gmail.com>

Looks good to me.

**Vivek Gupta** <vivek.gupta.app12@itbhu.ac.in>

Hi Bradley,

Just remembered to reply in time :)

Your outline looks perfectly fine to me.

All the best,

VG.



# Appendix B

## Simulating the MWA Tied-array Beam and Determining System Parameters

This Appendix is identical to the appendix of Meyers et al. (2017) (and the content of Chapter 3), with only minor alterations to aid with referencing of concepts and/or equations throughout the document.

For this thesis, given the importance of the described method and its use throughout the analysis presented in the document, it has been written as a stand-alone Appendix rather than included in the same appendix as the paper in which it was originally published.

### B.1 Array factor calculation

An antenna element in isolation has a complex voltage pattern given by some frequency-dependent function  $D(\theta, \phi)$ , where  $\theta$  is the zenith angle and  $\phi$  is the azimuth. The function  $D(\theta, \phi)$  is called the *element pattern* and gives the signal strength received by the element for any given direction, assuming it is positioned at the origin,  $\mathbf{r} = (0, 0, 0)$ . The coordinate system used here is such that the

azimuth ( $\phi$ ) is defined with  $0^\circ$  directly East and increases in an anticlockwise direction. The zenith angle ( $\theta$ ) is defined in the normal convention.

For an array of  $N$  elements, we define each element voltage pattern as  $D_n(\theta, \phi)$ . The tied-array beam pattern will be the sum of each element pattern in response to a wave,  $\psi_n$ , impinging on the array. Given that the source is in the far-field, this wave will be planar. It is practical to express the planar wave in terms of the coordinate system we have adopted, thus  $\psi_n$  can be written as

$$\psi_n = \exp(i\mathbf{k} \cdot \mathbf{r}_n) \equiv \exp\left[\frac{2\pi i}{\lambda}(x_n \sin \theta \cos \phi + y_n \sin \theta \sin \phi + z_n \cos \theta)\right], \quad (\text{B.1})$$

where  $\mathbf{k}$  is the three-dimensional wave vector,  $\mathbf{r}_n = (x_n, y_n, z_n)$  is the position of the  $n$ th element relative to the center of the array and  $\lambda$  is the observing wavelength.

We also apply weights,  $w_n$ , on a per element basis. For the MWA, when calculating the beam pattern for an individual tile (which consists of 16 dipole elements), these weights incorporate information about the cable losses and port currents required to accurately model the mutual coupling between dipoles and polarization characteristics (Sutinjo et al., 2015). On the tied-array scale, each element is now one MWA tile and the weights encode the phase delay information required to correctly point the array at a given sky position.

The tied-array voltage pattern is

$$D_{\text{array}}(\theta, \phi) = \frac{1}{N} \sum_{n=1}^N w_n D_n(\theta, \phi) \psi_n. \quad (\text{B.2})$$

If we assume the array elements are identical, then one can move the element factor out of the summation, and equation (B.2) becomes

$$D_{\text{array}}(\theta, \phi) = D(\theta, \phi) \frac{1}{N} \sum_{n=1}^N w_n \psi_n. \quad (\text{B.3})$$

Given we have two separable factors in equation (B.3), one of which is the element

pattern, we define the other as the *array factor*,

$$f(\theta, \phi) = \frac{1}{N} \sum_{n=1}^N w_n \psi_n(\theta, \phi). \quad (\text{B.4})$$

The array factor represents the response of an array of identical elements and encompasses the interference effects from the individual element patterns in response to the received radiation from the visible sky.

To point the tied-array radiation pattern, we adjust the complex weights  $w_n$ . In this case, we require the array factor to be unity at the desired pointing center, thus the weights are expressed as the complex conjugate of  $\psi_n$  evaluated only at the target position. Thus, the array factor pointed at some target zenith angle (za) and azimuth (az), is given by

$$f(\theta, \phi; \text{za}, \text{az}) = \frac{1}{N} \sum_{n=1}^N \psi_n(\text{za}, \text{az})^\dagger \psi_n(\theta, \phi) \quad (\text{B.5})$$

where  $\psi_n^\dagger$  denotes the complex conjugate of  $\psi_n$ . This ensures that the array factor power pattern,  $|f(\theta, \phi)|^2$ , will be unity only at the pointing center, and in the range [0, 1) elsewhere. The phased array power pattern is then

$$B_{\text{array}}(\theta, \phi) = |D_{\text{array}}(\theta, \phi)|^2 = |D(\theta, \phi)|^2 |f(\theta, \phi)|^2, \quad (\text{B.6})$$

which is evaluated over  $\theta = [0, \pi/2]$  and  $\phi = [0, 2\pi)$  to recover the array response to the sky visible to the elements. Both the element factor and array factor are also functions of frequency,  $\nu$ , therefore the tied-array beam pattern is a function of frequency and direction.

This process effectively recreates the naturally weighted synthesized beam for the array. The element pattern,  $D(\theta, \phi)$ , for the MWA has a grid-like morphology due to the MWA tiles being a regularly spaced grid of dipoles, thus we find that for some frequency and pointing combinations the tile pattern side lobes can have similar, or exceed the sensitivity of the main lobe. For a pseudo-random array, the

tied-array beam pattern grating lobes will be randomly distributed across the sky for each pointing and frequency, thus the element pattern dominates the sensitivity pattern on the sky. Contrary to our assumption, each tile is not necessarily identical, with some instances of individual dipoles failing which reduces the tile sensitivity by  $\sim 1/16$ . This effect is not accounted for in the beam simulations.

As an example, Figure B.1 shows a simulated MWA tile beam pattern and tied-array beam pattern at 210.56, 165.76 and 120.96 MHz. An important note here is that both the tile beam and tied-array beam models are theoretical, and in reality the true beam patterns will have features not described here.

## B.2 Antenna temperature

The antenna temperature  $T_{\text{ant}}(\nu, \theta, \phi)$  is calculated as the product of the antenna pattern  $B_{\text{array}}(\nu, \theta, \phi)$  and the sky temperature  $T_{\text{sky}}(\nu, \theta, \phi)$  via the convolution

$$T_{\text{ant}}(\nu, \theta, \phi) = \frac{\int_{4\pi} B_{\text{array}}(\nu, \theta, \phi) T_{\text{sky}}(\nu, \theta, \phi) d\Omega}{\int_{4\pi} B_{\text{array}}(\nu, \theta, \phi) d\Omega}. \quad (\text{B.7})$$

The tied-array beam pattern was output in the necessary format for software used by Sokolowski et al. (2015) to compute the above integral with the GSM, which is natively produced in HEALPix<sup>1</sup> format.

## B.3 Tied-array gain

To calculate the tied-array gain, we first determine the beam solid angle from the array factor power pattern in the standard way,

$$\Omega_A = \iint |f(\theta, \phi)|^2 \sin \theta d\theta d\phi. \quad (\text{B.8})$$

---

<sup>1</sup><http://healpix.sourceforge.net/>

The tied-array effective area is then

$$A_e = \eta \left( \frac{4\pi\lambda^2}{\Omega_A} \right), \quad (\text{B.9})$$

where  $\eta$  is a frequency and pointing dependent efficiency (see also eq. 1 of Chapter 3) and  $\lambda$  is the observing wavelength.

Here we note a divergence in the terminology used. The gain of an aperture array is defined as  $G = 4\pi A_e / \lambda^2 = 4\pi\eta/\Omega_A$  in standard antenna theory. We use a different definition (albeit common in radio astronomy), such that the gain is

$$G = \frac{A_e}{2k_B}, \quad (\text{B.10})$$

which relates directly to the system equivalent flux density of the array,  $\text{SEFD} = T_{\text{sys}}/G$ . In convenient radio astronomy units ( $\text{K Jy}^{-1}$ , where  $1 \text{ Jy} = 10^{-26} \text{ W m}^{-2} \text{ Hz}^{-1}$ ) this becomes simply

$$G = \frac{A_e}{2k_B} \times 10^{-26} \text{ W m}^{-2} \text{ Hz}^{-1}, \quad (\text{B.11})$$

where  $k_B$  is Boltzmann's constant and  $A_e$  is in units of  $\text{m}^2$ .

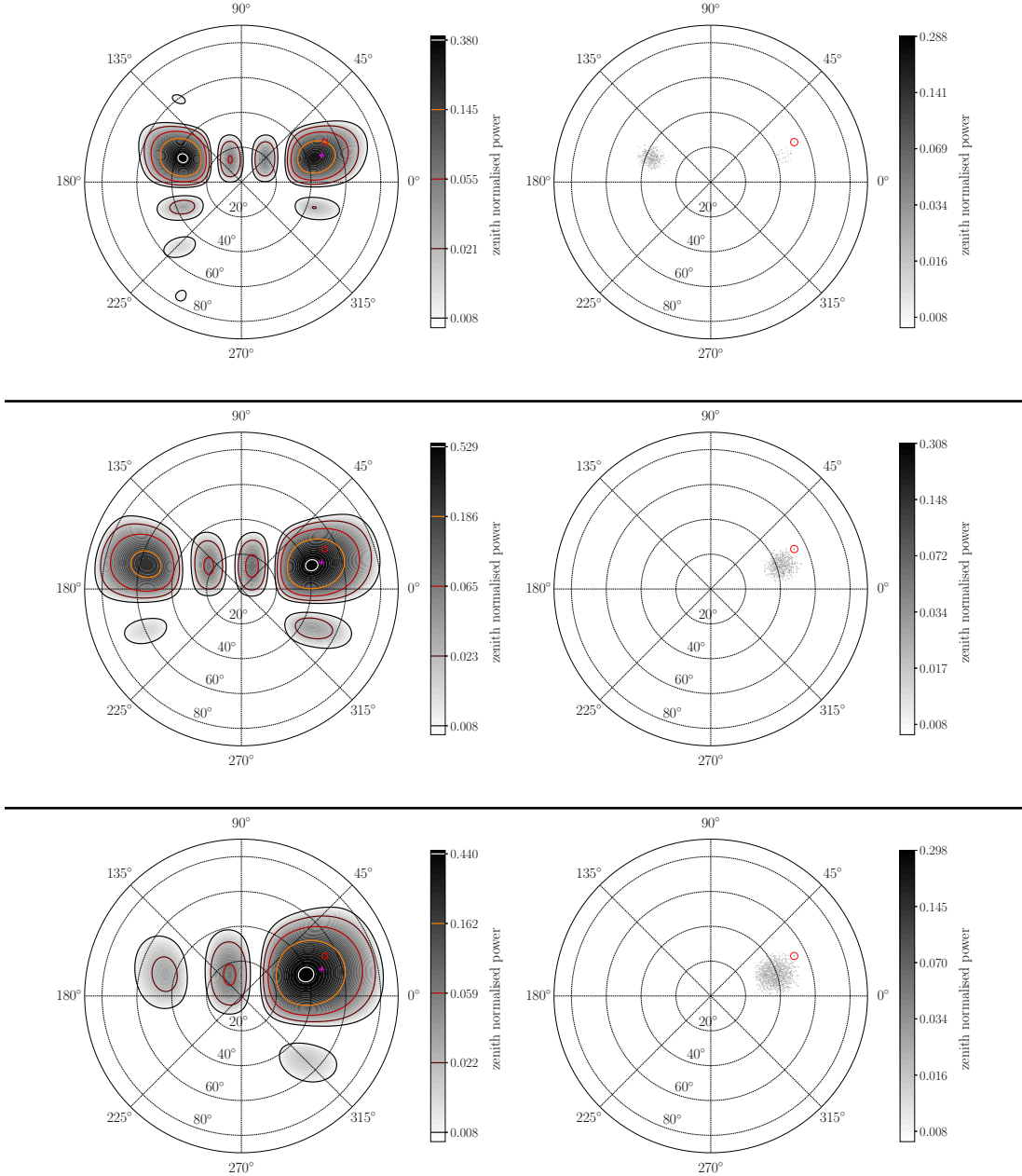


Figure B.1: The MWA tile pattern (left) and tied-array beam pattern (right) for each frequency: a) 210.56 MHz, b) 165.56 MHz, and c) 120.96 MHz. The gray-scale background gradient and the colored contours denote the zenith normalized power for the beam. The magenta cross marks the tile beam pointing center (azimuth =  $18.43^\circ$ , zenith angle =  $48.57^\circ$ ). In the case of the 210.56 MHz beam, the highest tile beam sensitivity region actually exists in the side-lobe. The red circles highlight the target position on each of the tied-array beam patterns.

## Appendix C

# Correcting UTMOST Flux Density Measurements of a Polarised Source

This Appendix is identical to the appendix of Meyers et al. (2018) (and the content of Chapter 4), with only minor alterations to aid with referencing of concepts and/or equations throughout the document.

For the complex electric field vector  $\varepsilon$ , the total intensity (Stokes  $I$ ) can be described as  $I = \varepsilon_L^2 + \varepsilon_R^2$ , where  $\varepsilon_L$  and  $\varepsilon_R$  are the left- and right-hand circularly polarised voltages induced in orthogonally polarised receptors. It is clear then that a detector sensitive to only one polarisation will detect 50 per cent of the total intensity from an unpolarised source (where  $\varepsilon_L$  and  $\varepsilon_R$  are equal but completely out of phase).

The measured SEFD for UTMOST is calibrated to nominally unpolarised pulsars, thus the quoted SEFD of 120 Jy implicitly corrects for the fact that the instrument only detects half of the total flux density. In the case where the target source is polarised, we must also correct for the polarised component of the total flux density. PSR J1107–5907 is slightly circularly polarised with  $V/I = -0.1$ ,

which indicates that  $\varepsilon_R^2 > \varepsilon_L^2$  (by the PSR/IEEE standard, Stokes  $V$  is positive for left-hand circularly polarised radiation, van Straten et al., 2010). UTMOST is therefore detecting 50 per cent of the unpolarised flux density (i.e. 45 percent of the total power) and 100 per cent of the polarised flux density (i.e. 10 per cent of the total power). Due to the SEFD implicitly correcting by a factor of 2 (i.e. accounting for the fact that only 50 per cent of the unpolarised flux density is detected), the measured UTMOST flux densities for PSR J1107–5907 will be over-estimated (i.e.  $2 \times (45\% + 10\%) = 110\%$  of the total flux density). We therefore must correct the UTMOST flux densities by a factor of  $\zeta = 1/1.1 \approx 0.9$ .

## **Appendix D**

### **Copyright Information**

#### **D.1 Chapter 3 & 4 copyright**

(Note: Chapters 3 and 4 were both published in the same journal, thus the following statement from the publisher applies to both pieces of work.)



Bradley Meyers <bradley.meyers1993@gmail.com>

---

## Request to re-publish article as a thesis chapter

2 messages

---

**Bradley Meyers** <bradley.meyers@postgrad.curtin.edu.au>  
To: "permissions@iop.org" <permissions@iop.org>  
Cc: "bradley.meyers1993@gmail.com" <bradley.meyers1993@gmail.com>

17 August 2018 at 09:52

Hello,

I'm writing to request the re-publication of my article "Spectral Flattening at Low Frequencies in Crab Giant Pulses" (doi: 10.3847/1538-4357/aa8bba) as a chapter in my Doctoral thesis.

From reading the AAS Copyright information, I understand that as first author I retain the right to reproduce the material how I see fit, however my University requires that I retrieve formal permission from the journal. Is it possible to get a letter or other official document allowing me to publish the material *unchanged* as part of my thesis?

Regards,  
Bradley Meyers  
16155145  
PhD Candidate  
Curtin University | Curtin Institute of Radio Astronomy  
International Centre for Radio Astronomy Research

---

**Permissions** <permissions@iop.org>  
To: Bradley Meyers <bradley.meyers@postgrad.curtin.edu.au>  
Cc: "bradley.meyers1993@gmail.com" <bradley.meyers1993@gmail.com>

17 August 2018 at 17:08

Dear Bradley Meyers,

Thank you for your email.

AAS authors may reuse their own work in a thesis without needing permission, providing it is not then being published commercially. You are also allowed to use figures from the article.

Therefore, please go ahead with the inclusion of this material in your new work – no permission is required from AAS.

This permission does not apply to any material/figure which is credited to another source in the AAS publication or has been obtained from a third party. Express permission for such materials/figures must be obtained from the copyright owner.

Kind regards,

Christina

**Copyright & Permissions Team**

Gemma Alaway – Senior Rights & Permissions Adviser  
Christina Colwell - Rights & Permissions Assistant

**Contact Details**

E-mail: [permissions@iop.org](mailto:permissions@iop.org)

For further information about copyright and how to request permission: <https://publishingsupport.iopscience.iop.org/copyright-journals/>

See also: <https://publishingsupport.iopscience.iop.org/>

Please see our Author Rights Policy <https://publishingsupport.iopscience.iop.org/author-rights-policies/>

**Please note:** We do not provide signed permission forms as a separate attachment. Please print this email and provide it to your publisher as proof of permission.

**Please note:** Any statements made by IOP Publishing to the effect that authors do not need to get permission to use any content where IOP Publishing is not the publisher is not intended to constitute any sort of legal advice. Authors must make their own decisions as to the suitability of the content they are using and whether they require permission for it to be published within their article.

---

**From:** Bradley Meyers <[bradley.meyers@postgrad.curtin.edu.au](mailto:bradley.meyers@postgrad.curtin.edu.au)>

**Sent:** 17 August 2018 02:52

**To:** Permissions

**Cc:** [bradley.meyers1993@gmail.com](mailto:bradley.meyers1993@gmail.com)

**Subject:** Request to re-publish article as a thesis chapter

[Quoted text hidden]

---

This email (and attachments) are confidential and intended for the addressee(s) only. If you are not the intended recipient please immediately notify the sender, permanently and securely delete any copies and do not take action with it or in reliance on it. Any views expressed are the author's and do not represent those of IOPP, except where specifically stated. IOPP takes reasonable precautions to protect against viruses but accepts no responsibility for loss or damage arising from virus infection. For the protection of IOPP's systems and staff, emails are scanned automatically.

**IOP Publishing Limited**

Registered in England under Registration No 00467514.  
Registered Office: Temple Circus, Bristol BS1 6HG England

Your privacy is important to us. For information about how IOPP uses your personal data, please see our [Privacy Policy](#)



# Bibliography

- A. A. Abdo, et al. (2010). ‘Fermi Large Area Telescope Observations of the Crab Pulsar And Nebula’. *The Astrophysical Journal* **708**:1254–1267.
- J. G. Ables, et al. (1970). ‘Pulse Broadening of PSR 0833-45 by Interstellar Scattering’. *Astrophysical Letters* **6**:147.
- T. Akgün, et al. (2006). ‘Precession of the isolated neutron star PSR B1828-11’. *Monthly Notices of the Royal Astronomical Society* **365**:653–672.
- J. Alstott, et al. (2014). ‘powerlaw: A Python Package for Analysis of Heavy-Tailed Distributions’. *PLoS ONE* **9**:e85777.
- M. Amiri, et al. (2017). ‘Limits on the Ultra-bright Fast Radio Burst Population from the CHIME Pathfinder’. *The Astrophysical Journal* **844**(2):161.
- B. C. Andersen & S. M. Ransom (2018). ‘A Fourier Domain ”Jerk” Search for Binary Pulsars’. *The Astrophysical Journal Letters* **863**:L13.
- K. M. V. Apparao (1973). ‘The Crab Nebula’. *Astrophysics and Space Science* **25**:3–116.
- P. N. Arendt, Jr. & J. A. Eilek (2002). ‘Pair Creation in the Pulsar Magnetosphere’. *The Astrophysical Journal* **581**:451–469.
- J. W. Armstrong, et al. (1995). ‘Electron density power spectrum in the local interstellar medium’. *The Astrophysical Journal* **443**:209–221.

- J. Arons & E. T. Scharlemann (1979). ‘Pair formation above pulsar polar caps - Structure of the low altitude acceleration zone’. *The Astrophysical Journal* **231**:854–879.
- W. Baade & F. Zwicky (1934). ‘Cosmic Rays from Super-novae’. *Contributions from the Mount Wilson Observatory, vol. 3, pp. 79-83* **3**:79–83.
- D. C. Backer (1970a). ‘Peculiar Pulse Burst in PSR 1237+25’. *Nature* **228**:1297–1298.
- D. C. Backer (1970b). ‘Pulsar Nulling Phenomena’. *Nature* **228**:42–43.
- D. C. Backer, et al. (1975). ‘Pulsar fluctuation spectra and the generalized drifting-subpulse phenomenon. II.’. *The Astrophysical Journal* **197**:481–487.
- M. Bailes, et al. (2017). ‘The UTMOST: A Hybrid Digital Signal Processor Transforms the Molonglo Observatory Synthesis Telescope’. *Publications of the Astronomical Society of Australia* **34**:e045.
- K. W. Bannister, et al. (2019). ‘A single fast radio burst localized to a massive galaxy at cosmological distance’. *arXiv e-prints* p. arXiv:1906.11476.
- N. Bartel & W. Sieber (1978). ‘Simultaneous single pulse observations of radio pulsars at two widely spaced frequencies.’. *Astronomy and Astrophysics* **70**:307–310.
- S. D. Bates, et al. (2013). ‘The pulsar spectral index distribution’. *Monthly Notices of the Royal Astronomical Society* **431**:1352–1358.
- G. Benford (1992). ‘Broadband microwave generation by beam-plasma turbulence’. *IEEE Transactions on Plasma Science* **20**:370–372.
- V. S. Beskin, et al. (1993). *Physics of the pulsar magnetosphere*. Cambridge University Press.

- N. D. R. Bhat, et al. (2004). ‘Multifrequency Observations of Radio Pulse Broadening and Constraints on Interstellar Electron Density Microstructure’. *The Astrophysical Journal* **605**:759–783.
- N. D. R. Bhat, et al. (2007a). ‘Simultaneous single-pulse observations of radio pulsars. V. On the broadband nature of the pulse nulling phenomenon in PSR B1133+16’. *Astronomy and Astrophysics* **462**:257–268.
- N. D. R. Bhat, et al. (2016). ‘Scintillation Arcs in Low-frequency Observations of the Timing-array Millisecond Pulsar PSR J0437-4715’. *The Astrophysical Journal* **818**:86.
- N. D. R. Bhat, et al. (1999). ‘Long-Term Scintillation Studies of Pulsars. I. Observations and Basic Results’. *The Astrophysical Journal Supplemental* **121**:483–513.
- N. D. R. Bhat, et al. (2008). ‘Bright Giant Pulses from the Crab Nebula Pulsar: Statistical Properties, Pulse Broadening, and Scattering Due to the Nebula’. *The Astrophysical Journal* **676**:1200–1209.
- N. D. R. Bhat, et al. (2018). ‘Observations of Low-frequency Radio Emission from Millisecond Pulsars and Multipath Propagation in the Interstellar Medium’. *The Astrophysical Journal Supplement Series* **238**:1.
- N. D. R. Bhat, et al. (2007b). ‘Detection of Crab Giant Pulses Using the Mileura Widefield Array Low Frequency Demonstrator Field Prototype System’. *The Astrophysical Journal* **665**:618–627.
- B. Bhattacharyya, et al. (2016). ‘The GMRT High Resolution Southern Sky Survey for Pulsars and Transients. I. Survey Description and Initial Discoveries’. *The Astrophysical Journal* **817**:130.
- B. Bhattacharyya, et al. (2018). ‘A long-term study of three rotating radio transients’. *Monthly Notices of the Royal Astronomical Society* **477**:4090–4103.

- M. F. Bietenholz, et al. (1997). ‘The Radio Spectral Index of the Crab Nebula’. *The Astrophysical Journal* **490**:291–301.
- J. D. Biggs (1992). ‘An analysis of radio pulsar nulling statistics’. *The Astrophysical Journal* **394**:574–580.
- A. V. Bilous, et al. (2016). ‘A LOFAR census of non-recycled pulsars: average profiles, dispersion measures, flux densities, and spectra’. *Astronomy and Astrophysics* **591**:A134.
- R. D. Blandford, et al. (1983). ‘Thermal origin of neutron star magnetic fields’. *Monthly Notices of the Royal Astronomical Society* **204**:1025–1048.
- D. C.-J. Bock, et al. (1999). ‘SUMSS: A Wide-Field Radio Imaging Survey of the Southern Sky. I. Science Goals, Survey Design, and Instrumentation’. *The Astronomical Journal* **117**:1578–1593.
- J. D. Bowman, et al. (2013). ‘Science with the Murchison Widefield Array’. *Publications of the Astronomical Society of Australia* **30**:31.
- J. Boyles, et al. (2013). ‘The Green Bank Telescope 350 MHz Drift-scan survey. I. Survey Observations and the Discovery of 13 Pulsars’. *The Astrophysical Journal* **763**:80.
- M. A. Brentjens & A. G. de Bruyn (2005). ‘Faraday rotation measure synthesis’. *Astronomy and Astrophysics* **441**:1217–1228.
- S. Burke-Spolaor & M. Bailes (2010). ‘The millisecond radio sky: transients from a blind single-pulse search’. *Monthly Notices of the Royal Astronomical Society* **402**:855–866.
- S. Burke-Spolaor, et al. (2011). ‘The High Time Resolution Universe Pulsar Survey - III. Single-pulse searches and preliminary analysis’. *Monthly Notices of the Royal Astronomical Society* **416**:2465–2476.

- S. Burke-Spolaor, et al. (2012). ‘The High Time Resolution Universe Pulsar Survey - V. Single-pulse energetics and modulation properties of 315 pulsars’. *Monthly Notices of the Royal Astronomical Society* **423**:1351–1367.
- S. Burke-Spolaor, et al. (2016a). ‘Limits on Fast Radio Bursts from Four Years of the V-FASTR Experiment’. *The Astrophysical Journal* **826**(2):223.
- S. Burke-Spolaor, et al. (2016b). ‘Limits on Fast Radio Bursts from Four Years of the V-FASTR Experiment’. *The Astrophysical Journal* **826**:223.
- M. Caleb, et al. (2017). ‘The first interferometric detections of fast radio bursts’. *Monthly Notices of the Royal Astronomical Society* **468**:3746–3756.
- M. Caleb, et al. (2016). ‘Fast Radio Transient searches with UTMOST at 843 MHz’. *Monthly Notices of the Royal Astronomical Society* **458**:718–725.
- M. Caleb, et al. (2019). ‘Polarization studies of Rotating Radio Transients’. *Monthly Notices of the Royal Astronomical Society* p. 1287.
- F. Camilo, et al. (2012). ‘PSR J1841-0500: A Radio Pulsar That Mostly is Not There’. *The Astrophysical Journal* **746**:63.
- S. Chatterjee, et al. (2017). ‘The direct localization of a fast radio burst and its host’. *Nature* **541**:58–61.
- P. Chawla, et al. (2017). ‘A Search for Fast Radio Bursts with the GBNCC Pulsar Survey’. *The Astrophysical Journal* **844**(2):140.
- A. F. Cheng (1985). ‘Interstellar grains and current flow in pulsar magnetospheres’. *The Astrophysical Journal* **299**:917–924.
- CHIME/FRB Collaboration, et al. (2019a). ‘A second source of repeating fast radio bursts’. *Nature* **566**(7743):235–238.
- CHIME/FRB Collaboration, et al. (2019b). ‘Observations of fast radio bursts at frequencies down to 400 megahertz’. *Nature* **566**:230–234.

- H.-Y. Chiu & E. E. Salpeter (1964). ‘Surface X-Ray Emission from Neutron Stars’. *Physical Review Letters* **12**:413–415.
- T. Coenen, et al. (2014a). ‘The LOFAR pilot surveys for pulsars and fast radio transients’. *Astronomy and Astrophysics* **570**:A60.
- T. Coenen, et al. (2014b). ‘The LOFAR pilot surveys for pulsars and fast radio transients’. *Astronomy and Astrophysics* **570**:A60.
- I. Cognard, et al. (1996). ‘Giant Radio Pulses from a Millisecond Pulsar’. *The Astrophysical Journal Letters* **457**:L81.
- J. M. Comella, et al. (1969). ‘Crab Nebula Pulsar NP 0532’. *Nature* **221**:453–454.
- L. Connor, et al. (2016). ‘Non-cosmological FRBs from young supernova remnant pulsars’. *Monthly Notices of the Royal Astronomical Society* **458**:L19–L23.
- J. M. Cordes (1978). ‘Observational limits on the location of pulsar emission regions’. *The Astrophysical Journal* **222**:1006–1011.
- J. M. Cordes, et al. (2004). ‘The Brightest Pulses in the Universe: Multifrequency Observations of the Crab Pulsar’s Giant Pulses’. *The Astrophysical Journal* **612**:375–388.
- J. M. Cordes & T. J. W. Lazio (2002). ‘NE2001.I. A New Model for the Galactic Distribution of Free Electrons and its Fluctuations’. *ArXiv e-prints*.
- J. M. Cordes & T. J. W. Lazio (2003). ‘NE2001. II. Using Radio Propagation Data to Construct a Model for the Galactic Distribution of Free Electrons’. *ArXiv e-prints*.
- J. M. Cordes, et al. (1986). ‘Refractive and diffractive scattering in the interstellar medium’. *The Astrophysical Journal* **310**:737–767.
- J. M. Cordes & B. J. Rickett (1998). ‘Diffractive Interstellar Scintillation Timescales and Velocities’. *The Astrophysical Journal* **507**:846–860.

- J. M. Cordes, et al. (2006). ‘Theory of Parabolic Arcs in Interstellar Scintillation Spectra’. *The Astrophysical Journal* **637**:346–365.
- J. M. Cordes & R. M. Shannon (2008). ‘Rocking the Lighthouse: Circumpulsar Asteroids and Radio Intermittency’. *The Astrophysical Journal* **682**:1152–1165.
- J. M. Cordes, et al. (2016). ‘Frequency-dependent Dispersion Measures and Implications for Pulsar Timing’. *The Astrophysical Journal* **817**:16.
- J. M. Cordes & I. Wasserman (2016). ‘Supergiant pulses from extragalactic neutron stars’. *Monthly Notices of the Royal Astronomical Society* **457**:232–257.
- J. M. Cordes, et al. (1985). ‘Small-scale electron density turbulence in the interstellar medium’. *The Astrophysical Journal* **288**:221–247.
- J. M. Cordes, et al. (1990). ‘Timing and Scintillations of the Millisecond Pulsar 1937+214’. *The Astrophysical Journal* **349**:245.
- B. Y. Cui, et al. (2017). ‘Timing Solution and Single-pulse Properties for Eight Rotating Radio Transients’. *The Astrophysical Journal* **840**:5.
- S. Dai, et al. (2015). ‘A study of multifrequency polarization pulse profiles of millisecond pulsars’. *Monthly Notices of the Royal Astronomical Society* **449**(3):3223–3262.
- K. Davidson & Y. Terzian (1969). ‘Dispersion Measures of Pulsars’. *The Astronomical Journal* **74**:849.
- A. de Oliveira-Costa, et al. (2008). ‘A model of diffuse Galactic radio emission from 10 MHz to 100 GHz’. *Monthly Notices of the Royal Astronomical Society* **388**:247–260.
- W. T. S. Deich, et al. (1986). ‘Null transition times, quantized drift modes, and no memory across nulls for PSR 1944 + 17’. *The Astrophysical Journal* **300**:540–550.

- A. T. Deller, et al. (2018). ‘A VLBI Distance and Transverse Velocity for PSR B1913+16’. *The Astrophysical Journal* **862**:139.
- P. B. Demorest (2011). ‘Cyclic spectral analysis of radio pulsars’. *Monthly Notices of the Royal Astronomical Society* **416**:2821–2826.
- J. S. Deneva, et al. (2009). ‘Arecibo Pulsar Survey Using ALFA: Probing Radio Pulsar Intermittency And Transients’. *The Astrophysical Journal* **703**:2259–2274.
- A. J. Deutsch (1955). ‘The electromagnetic field of an idealized star in rigid rotation in vacuo’. *Annales d’Astrophysique* **18**:1.
- J. Dowell, et al. (2017). ‘The LWA1 Low Frequency Sky Survey’. *Monthly Notices of the Royal Astronomical Society* **469**:4537–4550.
- T. Eftekhari, et al. (2016). ‘A Low frequency Survey of Giant Pulses from the Crab Pulsar’. *The Astrophysical Journal* **829**:62.
- J. A. Eilek, et al. (2002). ‘The Radio-Loud Plasma in Pulsars’. In W. Becker, H. Lesch, & J. Trümper (eds.), *Neutron Stars, Pulsars, and Supernova Remnants*, p. 249.
- J. A. Eilek & T. H. Hankins (2016). ‘Radio emission physics in the Crab pulsar’. *Journal of Plasma Physics* **82**(3):635820302.
- S. W. Ellingson, et al. (2013). ‘Observations of Crab Giant Pulses in 20-84 MHz using LWA1’. *The Astrophysical Journal* **768**:136.
- A. Esamdin, et al. (2012). ‘PSR B0826-34: Sometimes a Rotating Radio Transient’. *The Astrophysical Journal Letters* **759**:L3.
- A. Esamdin, et al. (2005). ‘Mode switching and subpulse drifting in PSR B0826-34’. *Monthly Notices of the Royal Astronomical Society* **356**:59–65.

- C. M. Espinoza, et al. (2011). ‘The Braking Index of PSR J1734-3333 and the Magnetar Population’. *The Astrophysical Journal Letters* **741**:L13.
- J. E. Everett & J. M. Weisberg (2001). ‘Emission Beam Geometry of Selected Pulsars Derived from Average Pulse Polarization Data’. *The Astrophysical Journal* **553**:341–357.
- W. Farah, et al. (2018). ‘FRB microstructure revealed by the real-time detection of FRB170827’. *Monthly Notices of the Royal Astronomical Society* **478**:1209–1217.
- C.-A. Faucher-Giguère & V. M. Kaspi (2006). ‘Birth and Evolution of Isolated Radio Pulsars’. *The Astrophysical Journal* **643**:332–355.
- V. Gajjar, et al. (2012). ‘A survey of nulling pulsars using the Giant Meterwave Radio Telescope’. *Monthly Notices of the Royal Astronomical Society* **424**:1197–1205.
- V. Gajjar, et al. (2014a). ‘Frequency Independent Quenching of Pulsed Emission’. *The Astrophysical Journal* **797**(1):18.
- V. Gajjar, et al. (2014b). ‘On the long nulls of PSRs J1738-2330 and J1752+2359’. *Monthly Notices of the Royal Astronomical Society* **439**(1):221–233.
- M. Geyer & A. Karastergiou (2016). ‘The frequency dependence of scattering imprints on pulsar observations’. *Monthly Notices of the Royal Astronomical Society* **462**:2587–2602.
- M. Geyer, et al. (2017). ‘Scattering analysis of LOFAR pulsar observations’. *Monthly Notices of the Royal Astronomical Society* **470**:2659–2679.
- N. K. Glendenning (1990). ‘Modulation of pulsar signals by deformation of the star’. *The Astrophysical Journal* **359**:186–191.
- T. Gold (1968). ‘Rotating Neutron Stars as the Origin of the Pulsating Radio Sources’. *Nature* **218**:731–732.

- P. Goldreich & W. H. Julian (1969). ‘Pulsar Electrodynamics’. *The Astrophysical Journal* **157**:869.
- M. E. Gonzalez, et al. (2011). ‘High-precision Timing of Five Millisecond Pulsars: Space Velocities, Binary Evolution, and Equivalence Principles’. *The Astrophysical Journal* **743**:102.
- D. M. Gould & A. G. Lyne (1998). ‘Multifrequency polarimetry of 300 radio pulsars’. *Monthly Notices of the Royal Astronomical Society* **301**:235–260.
- Y. Gupta (2000). ‘Pulsars and Interstellar Scintillations’. In M. Kramer, N. Wex, & R. Wielebinski (eds.), *IAU Colloq. 177: Pulsar Astronomy - 2000 and Beyond*, vol. 202 of *Astronomical Society of the Pacific Conference Series*, p. 539.
- Y. Gupta, et al. (1994). ‘Refractive Interstellar Scintillation in Pulsar Dynamic Spectra’. *Monthly Notices of the Royal Astronomical Society* **269**:1035.
- J. L. Han, et al. (2018). ‘Pulsar Rotation Measures and Large-scale Magnetic Field Reversals in the Galactic Disk’. *The Astrophysical Journal Supplement Series* **234**:11.
- T. H. Hankins (1971). ‘Microsecond Intensity Variations in the Radio Emissions from CP 0950’. *The Astrophysical Journal* **169**:487.
- T. H. Hankins & J. A. Eilek (2007). ‘Radio Emission Signatures in the Crab Pulsar’. *The Astrophysical Journal* **670**:693–701.
- T. H. Hankins, et al. (2016). ‘The Crab Pulsar at Centimeter Wavelengths. II. Single Pulses’. *The Astrophysical Journal* **833**:47.
- T. H. Hankins, et al. (2015). ‘The Crab Pulsar at Centimeter Wavelengths. I. Ensemble Characteristics’. *The Astrophysical Journal* **802**:130.
- T. H. Hankins, et al. (2003). ‘Nanosecond radio bursts from strong plasma turbulence in the Crab pulsar’. *Nature* **422**:141–143.

- T. H. Hankins & B. J. Rickett (1975). ‘Pulsar Signal Processing’. In B. Alder, S. Fernbach, & M. Rotenburg (eds.), *Radio Astronomy*, vol. 14 of *Methods in Computational Physics: Advances in Research and Applications*, pp. 55 – 129. New York: Academic Press.
- C. G. T. Haslam, et al. (1981). ‘A 408 MHz all-sky continuum survey. I - Observations at southern declinations and for the North Polar region’. *Astronomy and Astrophysics* **100**:209–219.
- C. G. T. Haslam, et al. (1982). ‘A 408 MHz all-sky continuum survey. II - The atlas of contour maps’. *Astronomy and Astrophysics Supplement Series* **47**:1.
- A. Heger, et al. (2004). ‘Presupernova Evolution of Rotating Massive Stars and the Rotation Rate of Pulsars (Invited Review)’. In A. Maeder & P. Eenens (eds.), *Stellar Rotation*, vol. 215 of *IAU Symposium*, p. 591.
- D. J. Helfand, et al. (1980). ‘Thermal X-ray emission from neutron stars’. *Nature* **283**:337–343.
- W. Hermsen, et al. (2013). ‘Synchronous X-ray and Radio Mode Switches: A Rapid Global Transformation of the Pulsar Magnetosphere’. *Science* **339**:436.
- W. Hermsen, et al. (2018). ‘Discovery of synchronous X-ray and radio moding of PSR B0823+26’. *Monthly Notices of the Royal Astronomical Society* **480**:3655–3670.
- M. Hernández-Pajares, et al. (2009). ‘The IGS VTEC maps: a reliable source of ionospheric information since 1998’. *Journal of Geodesy* **83**:263–275.
- A. Hewish, et al. (1968). ‘Observation of a Rapidly Pulsating Radio Source’. *Nature* **217**:709–713.
- A. S. Hill, et al. (2003). ‘Pulsar Scintillation Arcs. I. Frequency Dependence’. *The Astrophysical Journal* **599**:457–464.

- G. Hobbs, et al. (2012). ‘Development of a pulsar-based time-scale’. *Monthly Notices of the Royal Astronomical Society* **427**:2780–2787.
- G. Hobbs, et al. (2016). ‘A pilot ASKAP survey of radio transient events in the region around the intermittent pulsar PSR J1107-5907’. *Monthly Notices of the Royal Astronomical Society* **456**:3948–3960.
- G. Hobbs, et al. (2010). ‘An analysis of the timing irregularities for 366 pulsars’. *Monthly Notices of the Royal Astronomical Society* **402**:1027–1048.
- G. B. Hobbs, et al. (2006). ‘TEMPO2, a new pulsar-timing package - I. An overview’. *Monthly Notices of the Royal Astronomical Society* **369**:655–672.
- E. W. Hones, Jr. & J. E. Bergeson (1965). ‘Electric Field Generated by a Rotating Magnetized Sphere’. *Journal of Geophysical Research* **70**:4951–4958.
- A. W. Hotan, et al. (2004). ‘PSRCHIVE and PSRFITS: An Open Approach to Radio Pulsar Data Storage and Analysis’. *Publications of the Astronomical Society of Australia* **21**:302–309.
- J. D. Hunter (2007a). ‘Matplotlib: A 2D graphics environment’. *Computing In Science & Engineering* **9**(3):90–95.
- J. D. Hunter (2007b). ‘Matplotlib: A 2D graphics environment’. *Computing In Science & Engineering* **9**(3):90–95.
- V. A. Izvekova, et al. (1981). ‘Radio spectra of pulsars. I - Observations of flux densities at meter wavelengths and analysis of the spectra’. *Astrophysics and Space Science* **78**:45–72.
- F. Jankowski, et al. (2015). ‘Glitch event observed in the Vela pulsar (PSR J0835-4510)’. *The Astronomer’s Telegram* **6903**.
- F. Jankowski, et al. (2016). ‘Glitch event observed in the pulsar PSR J1740-3015’. *The Astronomer’s Telegram* **9054**.

- F. Jankowski, et al. (2017). ‘Large glitch event observed in PSR J1731-4744’. *The Astronomer’s Telegram* **10770**.
- F. Jankowski, et al. (2018a). ‘The UTMOST pulsar timing programme I: overview and first results’. *Monthly Notices of the Royal Astronomical Society* p. 3222.
- F. Jankowski, et al. (2018b). ‘Spectral properties of 441 radio pulsars’. *Monthly Notices of the Royal Astronomical Society* **473**:4436–4458.
- G. H. Janssen, et al. (2010). ‘Long-term timing of four millisecond pulsars’. *Astronomy and Astrophysics* **514**:A74.
- R. J. Jennings, et al. (2018). ‘Binary Pulsar Distances and Velocities from Gaia-Data Release 2’. *The Astrophysical Journal* **864**:26.
- S. Johnston & A. Karastergiou (2017). ‘Pulsar braking and the P- $\dot{P}$  diagram’. *Monthly Notices of the Royal Astronomical Society* **467**:3493–3499.
- S. Johnston, et al. (2008). ‘Multifrequency integrated profiles of pulsars’. *Monthly Notices of the Royal Astronomical Society* **388**:261–274.
- S. Johnston & M. Kerr (2018). ‘Polarimetry of 600 pulsars from observations at 1.4 GHz with the Parkes radio telescope’. *Monthly Notices of the Royal Astronomical Society* **474**:4629–4636.
- S. Johnston, et al. (1992). ‘A high-frequency survey of the southern Galactic plane for pulsars’. *Monthly Notices of the Royal Astronomical Society* **255**:401–411.
- S. Johnston, et al. (1998). ‘Scintillation parameters for 49 pulsars’. *Monthly Notices of the Royal Astronomical Society* **297**:108–116.
- S. Johnston & R. W. Romani (2004). ‘Giant Pulses - A Brief Review’. In F. Camilo & B. M. Gaensler (eds.), *Young Neutron Stars and Their Environments*, vol. 218 of *IAU Symposium*, p. 315.

- D. I. Jones (2012). ‘Pulsar state switching, timing noise and free precession’. *Monthly Notices of the Royal Astronomical Society* **420**:2325–2338.
- E. Jones, et al. (2001). ‘SciPy: Open source scientific tools for Python’.
- C. Kalapotharakos, et al. (2012). ‘Toward a Realistic Pulsar Magnetosphere’. *The Astrophysical Journal* **749**:2.
- C. Karako-Argaman & GBT Drift-Scan Collaboration (2013). ‘Discoveries of Rotating Radio Transients in the 350 MHz Green Bank Telescope Drift-scan Survey’. In J. van Leeuwen (ed.), *Neutron Stars and Pulsars: Challenges and Opportunities after 80 years*, vol. 291 of *IAU Symposium*, pp. 107–110.
- C. Karako-Argaman, et al. (2015a). ‘Discovery and Follow-up of Rotating Radio Transients with the Green Bank and LOFAR Telescopes’. *The Astrophysical Journal* **809**:67.
- C. Karako-Argaman, et al. (2015b). ‘Discovery and Follow-up of Rotating Radio Transients with the Green Bank and LOFAR Telescopes’. *The Astrophysical Journal* **809**:67.
- A. Karastergiou, et al. (2015a). ‘Limits on fast radio bursts at 145 MHz with ARTEMIS, a real-time software backend’. *Monthly Notices of the Royal Astronomical Society* **452**:1254–1262.
- A. Karastergiou, et al. (2009). ‘Radio polarization measurements from RRAT J1819-1458’. *Monthly Notices of the Royal Astronomical Society* **396**:L95–L99.
- A. Karastergiou & S. Johnston (2007). ‘An empirical model for the beams of radio pulsars’. *Monthly Notices of the Royal Astronomical Society* **380**:1678–1684.
- A. Karastergiou, et al. (2015b). ‘Understanding pulsar magnetospheres with the SKA’. *Advancing Astrophysics with the Square Kilometre Array (AASKA14)* p. 38.

- R. Karuppusamy, et al. (2012a). ‘Crab giant pulses at low frequencies’. *Astronomy and Astrophysics* **538**:A7.
- R. Karuppusamy, et al. (2012b). ‘Crab giant pulses at low frequencies’. *Astronomy and Astrophysics* **538**:A7.
- R. Karuppusamy, et al. (2010a). ‘Giant pulses from the Crab pulsar. A wide-band study’. *Astronomy and Astrophysics* **515**:A36.
- R. Karuppusamy, et al. (2010b). ‘Giant pulses from the Crab pulsar. A wide-band study’. *Astronomy and Astrophysics* **515**:A36.
- V. M. Kaspi & M. Kramer (2016). ‘Radio Pulsars: The Neutron Star Population & Fundamental Physics’. *arXiv e-prints* p. arXiv:1602.07738.
- D. Kaur, et al. (2019). ‘A high time resolution study of the millisecond pulsar J2241-5236 at frequencies below 300 MHz’. *arXiv e-prints* p. arXiv:1907.08916.
- E. F. Keane (2016). ‘Classifying RRATs and FRBs’. *Monthly Notices of the Royal Astronomical Society* **459**:1360–1362.
- E. F. Keane, et al. (2011). ‘Rotating Radio Transients: new discoveries, timing solutions and musings’. *Monthly Notices of the Royal Astronomical Society* **415**:3065–3080.
- E. F. Keane & M. A. McLaughlin (2011). ‘Rotating radio transients’. *Bulletin of the Astronomical Society of India* **39**:333–352.
- E. F. Keane, et al. (2012). ‘On the origin of a highly dispersed coherent radio burst’. *Monthly Notices of the Royal Astronomical Society* **425**:L71–L75.
- M. Kerr, et al. (2014). ‘The three discrete nulling time-scales of PSR J1717-4054’. *Monthly Notices of the Royal Astronomical Society* **445**:320–329.
- F. Kirsten, et al. (2019). ‘Probing Pulsar Scattering between 120 and 280 MHz with the MWA’. *The Astrophysical Journal* **874**(2):179.

- S. Kisaka, et al. (2016). ‘Electric Field Screening with Backflow at Pulsar Polar Cap’. *The Astrophysical Journal* **829**:12.
- H. S. Knight (2007). ‘A Parkes radio telescope study of giant pulses from PSR J1823-3021A’. *Monthly Notices of the Royal Astronomical Society* **378**:723–729.
- H. S. Knight, et al. (2006). ‘A Study of Giant Pulses from PSR J1824-2452A’. *The Astrophysical Journal* **653**:580–586.
- M. M. Komesaroff (1970). ‘Possible Mechanism for the Pulsar Radio Emission’. *Nature* **225**:612–614.
- M. Kramer, et al. (2003a). ‘Simultaneous single-pulse observations of radio pulsars. IV. Flux density spectra of individual pulses’. *Astronomy and Astrophysics* **407**:655–668.
- M. Kramer, et al. (2003b). ‘The Proper Motion, Age, and Initial Spin Period of PSR J0538+2817 in S147’. *The Astrophysical Journal Letters* **593**:L31–L34.
- M. Kramer, et al. (2006). ‘A Periodically Active Pulsar Giving Insight into Magnetospheric Physics’. *Science* **312**:549–551.
- M. T. Lam, et al. (2015). ‘Pulsar Timing Errors from Asynchronous Multi-frequency Sampling of Dispersion Measure Variations’. *The Astrophysical Journal* **801**:130.
- K. R. Lang (1971a). ‘Interstellar Scintillation of Pulsar Radiation’. *The Astrophysical Journal* **164**:249.
- K. R. Lang (1971b). ‘Pulse broadening due to angular scattering in the interstellar medium’. *Astrophysical Letters* **7**:175–178.
- M. I. Large, et al. (1968). ‘A Pulsar Supernova Association?’. *Nature* **220**:340–341.

- J. M. Lattimer (2012). ‘The Nuclear Equation of State and Neutron Star Masses’. *Annual Review of Nuclear and Particle Science* **62**:485–515.
- J. M. Lattimer & M. Prakash (2001). ‘Neutron Star Structure and the Equation of State’. *The Astrophysical Journal* **550**:426–442.
- J. M. Lattimer, et al. (1990). ‘Rapidly rotating pulsars and the equation of state’. *The Astrophysical Journal* **355**:241–254.
- L. C. Lee & J. R. Jokipii (1975). ‘Strong scintillations in astrophysics. II - A theory of temporal broadening of pulses’. *The Astrophysical Journal* **201**:532–543.
- L. Lentati, et al. (2017). ‘Wide-band profile domain pulsar timing analysis’. *Monthly Notices of the Royal Astronomical Society* **466**:3706–3727.
- L. Levin, et al. (2016). ‘The NANOGrav Nine-year Data Set: Monitoring Interstellar Scattering Delays’. *The Astrophysical Journal* **818**:166.
- W. Lewandowski, et al. (2013). ‘Pulse broadening analysis for several new pulsars and anomalous scattering’. *Monthly Notices of the Royal Astronomical Society* **434**:69–83.
- W. Lewandowski, et al. (2004). ‘Arecibo Timing and Single-Pulse Observations of Eighteen Pulsars’. *The Astrophysical Journal* **600**:905–913.
- J. Li, et al. (2012a). ‘On the Spin-down of Intermittent Pulsars’. *The Astrophysical Journal* **746**:L24.
- J. Li, et al. (2012b). ‘On the Spin-down of Intermittent Pulsars’. *The Astrophysical Journal* **746**:L24.
- J. Li, et al. (2012c). ‘Resistive Solutions for Pulsar Magnetospheres’. *The Astrophysical Journal* **746**:60.

- W. Li, et al. (2018). ‘Comparing Redundant and Sky-model-based Interferometric Calibration: A First Look with Phase II of the MWA’. *The Astrophysical Journal* **863**:170.
- A. Liu, et al. (2010). ‘Precision calibration of radio interferometers using redundant baselines’. *Monthly Notices of the Royal Astronomical Society* **408**:1029–1050.
- K. Liu, et al. (2012). ‘Profile-shape stability and phase-jitter analyses of millisecond pulsars’. *Monthly Notices of the Royal Astronomical Society* **420**:361–368.
- M. A. Livingstone, et al. (2007). ‘New phase-coherent measurements of pulsar braking indices’. *Astrophysics and Space Science* **308**:317–323.
- O. Löhmer, et al. (2001). ‘Anomalous Scattering of Highly Dispersed Pulsars’. *The Astrophysical Journal Letters* **562**:L157–L161.
- O. Löhmer, et al. (2004). ‘The frequency evolution of interstellar pulse broadening from radio pulsars’. *Astronomy and Astrophysics* **425**:569–575.
- D. R. Lorimer, et al. (2007). ‘A Bright Millisecond Radio Burst of Extragalactic Origin’. *Science* **318**:777.
- D. R. Lorimer, et al. (2006). ‘The Parkes Multibeam Pulsar Survey - VI. Discovery and timing of 142 pulsars and a Galactic population analysis’. *Monthly Notices of the Royal Astronomical Society* **372**:777–800.
- D. R. Lorimer & M. Kramer (2004). *Handbook of Pulsar Astronomy*. Cambridge University Press.
- D. R. Lorimer, et al. (2012). ‘Radio and X-Ray Observations of the Intermittent Pulsar J1832+0029’. *The Astrophysical Journal* **758**:141.
- D. R. Lorimer, et al. (1995). ‘Multifrequency flux density measurements of 280 pulsars’. *Monthly Notices of the Royal Astronomical Society* **273**:411–421.

- R. S. Lynch, et al. (2013). ‘The Green Bank Telescope 350 MHz Drift-scan Survey II: Data Analysis and the Timing of 10 New Pulsars, Including a Relativistic Binary’. *The Astrophysical Journal* **763**:81.
- A. Lyne, et al. (2010). ‘Switched Magnetospheric Regulation of Pulsar Spin-Down’. *Science* **329**:408.
- A. G. Lyne, et al. (2015). ‘45 years of rotation of the Crab pulsar’. *Monthly Notices of the Royal Astronomical Society* **446**:857–864.
- A. G. Lyne & R. N. Manchester (1988). ‘The shape of pulsar radio beams’. *Monthly Notices of the Royal Astronomical Society* **234**:477–508.
- A. G. Lyne, et al. (1993). ‘Twenty-Three Years of Crab Pulsar Rotational History’. *Monthly Notices of the Royal Astronomical Society* **265**:1003.
- A. G. Lyne, et al. (1996). ‘Very low braking index for the Vela pulsar’. *Nature* **381**:497–498.
- A. G. Lyne & B. J. Rickett (1968a). ‘Measurements of the Pulse Shape and Spectra of the Pulsating Radio Sources’. *Nature* **218**:326–330.
- A. G. Lyne & B. J. Rickett (1968b). ‘Radio Observations of Five Pulsars’. *Nature* **219**:1339–1342.
- A. G. Lyne & F. G. Smith (1982). ‘Interstellar scintillation and pulsar velocities’. *Nature* **298**:825–827.
- A. G. Lyne, et al. (2017). ‘Two Long-Term Intermittent Pulsars Discovered in the PALFA Survey’. *The Astrophysical Journal* **834**(1):72.
- M. Lyutikov (2017). ‘Fast Radio Bursts’ Emission Mechanism: Implication from Localization’. *The Astrophysical Journal Letters* **838**:L13.

- M. Lyutikov, et al. (2016). ‘Fast radio bursts as giant pulses from young rapidly rotating pulsars’. *Monthly Notices of the Royal Astronomical Society* **462**:941–950.
- G. Machabeli & N. Chkheidze (2014). ‘A possible mechanism for forming the radio emission spectrum of the Crab pulsar’. *Monthly Notices of the Royal Astronomical Society* **440**:3426–3429.
- J.-P. Macquart, et al. (2010). ‘The Commensal Real-Time ASKAP Fast-Transients (CRAFT) Survey’. *Publications of the Astronomical Society of Australia* **27**(3):272–282.
- V. M. Malofeev, et al. (2000). ‘Flux Densities of 235 Pulsars at 102.5 MHz’. *Astronomy Reports* **44**:436–445.
- R. N. Manchester, et al. (1998). ‘Polarization observations of 66 southern pulsars’. *Monthly Notices of the Royal Astronomical Society* **295**:280–298.
- R. N. Manchester, et al. (2013). ‘The Parkes Pulsar Timing Array Project’. *Publications of the Astronomical Society of Australia* **30**:e017.
- R. N. Manchester, et al. (2005). ‘The Australia Telescope National Facility Pulsar Catalogue’. *The Astronomical Journal* **129**:1993–2006.
- R. N. Manchester, et al. (2001). ‘The Parkes multi-beam pulsar survey: I. Observing and data analysis systems, discovery and timing of 100 pulsars’. *Monthly Notices of the Royal Astronomical Society* **328**:17–35.
- R. N. Manchester, et al. (1978). ‘The second Molonglo pulsar survey - discovery of 155 pulsars.’. *Monthly Notices of the Royal Astronomical Society* **185**:409–421.
- R. N. Manchester & J. H. Taylor (1972). ‘Parameters of 61 Pulsars’. *Astrophysical Letters* **10**:67.
- R. N. Manchester & J. H. Taylor (1977). *Pulsars*. W. H. Freeman & Co Ltd.

- O. Maron, et al. (2000a). ‘Pulsar spectra of radio emission’. *Astronomy and Astrophysics Supplement Series* **147**:195–203.
- O. Maron, et al. (2000b). ‘Pulsar spectra of radio emission’. *Astronomy and Astrophysics Supplement Series* **147**:195–203.
- T. Mauch, et al. (2003). ‘SUMSS: a wide-field radio imaging survey of the southern sky - II. The source catalogue’. *Monthly Notices of the Royal Astronomical Society* **342**:1117–1130.
- M. A. McLaughlin & J. M. Cordes (2003). ‘Searches for Giant Pulses from Extragalactic Pulsars’. *The Astrophysical Journal* **596**:982–996.
- M. A. McLaughlin, et al. (2009). ‘Timing observations of rotating radio transients’. *Monthly Notices of the Royal Astronomical Society* **400**:1431–1438.
- M. A. McLaughlin, et al. (2006). ‘Transient radio bursts from rotating neutron stars’. *Nature* **439**:817–820.
- W. H. McMaster (1954). ‘Polarization and the Stokes Parameters’. *American Journal of Physics* **22**:351–362.
- W. H. McMaster (1961). ‘Matrix Representation of Polarization’. *Reviews of Modern Physics* **33**:8–27.
- S. J. McSweeney, et al. (2017). ‘Low-frequency Observations of the Subpulse Drifter PSR J0034-0721 with the Murchison Widefield Array’. *The Astrophysical Journal* **836**:224.
- D. Melrose (2004). ‘Pulse Emission Mechanisms’. In F. Camilo & B. M. Gaensler (eds.), *Young Neutron Stars and Their Environments*, vol. 218 of *IAU Symposium*, p. 349.
- D. B. Melrose (1995). ‘The Models for Radio Emission from Pulsars - the Outstanding Issues’. *Journal of Astrophysics and Astronomy* **16**:137.

- D. B. Melrose (2017). ‘Coherent emission mechanisms in astrophysical plasmas’. *Reviews of Modern Plasma Physics* **1**.
- D. B. Melrose & R. Yuen (2014). ‘Non-corotating models for pulsar magnetospheres’. *Monthly Notices of the Royal Astronomical Society* **437**:262–272.
- D. B. Melrose & R. Yuen (2016). ‘Pulsar electrodynamics: an unsolved problem’. *Journal of Plasma Physics* **82**(2):635820202.
- S. Mereghetti, et al. (2016). ‘A Deep Campaign to Characterize the Synchronous Radio/X-Ray Mode Switching of PSR B0943+10’. *The Astrophysical Journal* **831**:21.
- B. W. Meyers, et al. (2018). ‘Hunting for Radio Emission from the Intermittent Pulsar J1107-5907 at Low Frequencies’. *The Astrophysical Journal* **869**:134.
- B. W. Meyers, et al. (2017). ‘Spectral Flattening at Low Frequencies in Crab Giant Pulses’. *The Astrophysical Journal* **851**:20.
- F. C. Michel & A. J. Dessler (1981). ‘Pulsar disk systems’. *The Astrophysical Journal* **251**:654–664.
- F. C. Michel & H. Li (1999). ‘Electrodynamics of neutron stars’. *Physics Reports* **318**:227–297.
- M. B. Mickaliger, et al. (2018a). ‘A study of single pulses in the Parkes Multibeam Pulsar Survey’. *Monthly Notices of the Royal Astronomical Society* **479**:5413–5422.
- M. B. Mickaliger, et al. (2018b). ‘A study of single pulses in the Parkes Multibeam Pulsar Survey’. *Monthly Notices of the Royal Astronomical Society* **479**:5413–5422.
- M. B. Mickaliger, et al. (2012). ‘A Giant Sample of Giant Pulses from the Crab Pulsar’. *The Astrophysical Journal* **760**:64.

- J. M. Migliazzo, et al. (2002). ‘Proper-Motion Measurements of Pulsar B1951+32 in the Supernova Remnant CTB 80’. *The Astrophysical Journal Letters* **567**:L141–L144.
- R. Mikami, et al. (2016). ‘Wide-band Spectra of Giant Radio Pulses from the Crab Pulsar’. *The Astrophysical Journal* **832**:212.
- J. Miller, et al. (2011). ‘Multiwavelength Studies of Rotating Radio Transients’. In M. Burgay, N. D’Amico, P. Esposito, A. Pellizzoni, & A. Possenti (eds.), *American Institute of Physics Conference Series*, vol. 1357 of *American Institute of Physics Conference Series*, pp. 161–164.
- D. A. Mitchell, et al. (2008). ‘Real-Time Calibration of the Murchison Widefield Array’. *IEEE Journal of Selected Topics in Signal Processing* **2**:707–717.
- D. Mitra, et al. (2016). ‘Meterwavelength Single-pulse Polarimetric Emission Survey’. *The Astrophysical Journal* **833**:28.
- D. Mitra, et al. (2003). ‘The effect of HII regions on rotation measure of pulsars’. *Astronomy and Astrophysics* **398**:993–1005.
- D. A. Moffett & T. H. Hankins (1999). ‘Polarimetric Properties of the Crab Pulsar between 1.4 and 8.4 GHZ’. *The Astrophysical Journal* **522**:1046–1052.
- F. Mottez, et al. (2013). ‘Towards a theory of extremely intermittent pulsars. II. Asteroids at a close distance’. *Astronomy and Astrophysics* **555**:A126.
- A. Naidu, et al. (2017). ‘Simultaneous multi-frequency single pulse observations of pulsars’. *Astronomy and Astrophysics* **604**:A45.
- R. Narayan (1992). ‘The Physics of Pulsar Scintillation’. *Philosophical Transactions of the Royal Society of London Series A* **341**:151–165.
- M. Newville, et al. (2014). ‘LMFIT: Non-Linear Least-Square Minimization and Curve-Fitting for Python’.

- A. Noutsos, et al. (2008). ‘New pulsar rotation measures and the Galactic magnetic field’. *Monthly Notices of the Royal Astronomical Society* **386**:1881–1896.
- J. T. O’Brien, et al. (2006). ‘Sometimes a Pulsar!’. *Chinese Journal of Astronomy and Astrophysics Supplement* **6**(2):4–7.
- A. R. Offringa, et al. (2013). ‘The LOFAR radio environment’. *Astronomy and Astrophysics* **549**:A11.
- A. R. Offringa, et al. (2015). ‘The Low-Frequency Environment of the Murchison Widefield Array: Radio-Frequency Interference Analysis and Mitigation’. *Publications of the Astronomical Society of Australia* **32**:e008.
- J. R. Oppenheimer & G. M. Volkoff (1939). ‘On Massive Neutron Cores’. *Physical Review* **55**:374–381.
- S. M. Ord, et al. (2015). ‘The Murchison Widefield Array Correlator’. *Publications of the Astronomical Society of Australia* **32**:e006.
- S. M. Ord, et al. (2019). ‘MWA Tied-Array Processing I: Calibration and Beam-formation’. *arXiv e-prints* p. arXiv:1905.01826.
- S. M. Ord, et al. (2004). ‘Polarimetric profiles of 27 millisecond pulsars’. *Monthly Notices of the Royal Astronomical Society* **352**:804–814.
- S. I. Oronsaye, et al. (2015). ‘Simultaneous Observations of Giant Pulses from the Crab Pulsar, with the Murchison Widefield Array and Parkes Radio Telescope: Implications for the Giant Pulse Emission Mechanism.’. *The Astrophysical Journal* **809**:51.
- F. Pacini (1968). ‘Rotating Neutron Stars, Pulsars and Supernova Remnants’. *Nature* **219**:145–146.
- N. T. Palliyaguru, et al. (2011). ‘Radio properties of rotating radio transients - I. Searches for periodicities and randomness in pulse arrival times’. *Monthly Notices of the Royal Astronomical Society* **417**:1871–1880.

- C. Patel, et al. (2018). ‘PALFA Single-pulse Pipeline: New Pulsars, Rotating Radio Transients, and a Candidate Fast Radio Burst’. *The Astrophysical Journal* **869**:181.
- G. G. Pavlov & I. A. Shibayev (1978). ‘Thermal emission of an optically thick plasma containing a strong magnetic field’. *Soviet Astronomy* **22**:214–222.
- T. T. Pennucci, et al. (2014). ‘Elementary Wideband Timing of Radio Pulsars’. *The Astrophysical Journal* **790**:93.
- E. Petroff, et al. (2016). ‘FRBCAT: The Fast Radio Burst Catalogue’. *Publications of the Astronomical Society of Australia* **33**:e045.
- E. Petroff, et al. (2019). ‘Fast radio bursts’. **27**(1):4.
- A. Philippov, et al. (2019). ‘Pulsar Radio Emission Mechanism: Radio Nanoshots as a Low Frequency Afterglow of Relativistic Magnetic Reconnection’. *arXiv e-prints* .
- J. A. Phillips & A. W. Clegg (1992). ‘Electron density fluctuations in the local interstellar bubble’. *Nature* **360**:137–139.
- E. Platts, et al. (2018). ‘A Living Theory Catalogue for Fast Radio Bursts’. *arXiv e-prints* p. arXiv:1810.05836.
- M. V. Popov, et al. (2006a). ‘Instantaneous radio spectra of giant pulses from the crab pulsar from decimeter to decameter wavelengths’. *Astronomy Reports* **50**:562–568.
- S. B. Popov, et al. (2006b). ‘A tale of two populations: rotating radio transients and X-ray dim isolated neutron stars’. *Monthly Notices of the Royal Astronomical Society* **369**:L23–L26.
- D. C. Price, et al. (2016). ‘HIPS: A Digital Signal Processor for the Parkes 21-cm Multibeam Receiver’. *Journal of Astronomical Instrumentation* **5**:1641007.

- J. M. Rankin (1986). ‘Toward an empirical theory of pulsar emission. III - Mode changing, drifting subpulses, and pulse nulling’. *The Astrophysical Journal* **301**:901–922.
- J. M. Rankin (1990). ‘Toward an Empirical Theory of Pulsar Emission. IV. Geometry of the Core Emission Region’. *The Astrophysical Journal* **352**:247.
- J. M. Rankin (1993). ‘Toward an empirical theory of pulsar emission. VI - The geometry of the conal emission region’. *The Astrophysical Journal* **405**:285–297.
- S. M. Ransom, et al. (2003). ‘A New Search Technique for Short Orbital Period Binary Pulsars’. *The Astrophysical Journal* **589**:911–920.
- S. M. Ransom, et al. (2002). ‘Fourier Techniques for Very Long Astrophysical Time-Series Analysis’. *The Astronomical Journal* **124**:1788–1809.
- V. Ravi, et al. (2015). ‘A Fast Radio Burst in the Direction of the Carina Dwarf Spheroidal Galaxy’. *The Astrophysical Journal Letters* **799**:L5.
- N. Rea, et al. (2008). ‘On the nature of the intermittent pulsar PSRB1931+24’. *Monthly Notices of the Royal Astronomical Society* **391**:663–667.
- S. L. Redman & J. M. Rankin (2009). ‘On the randomness of pulsar nulls’. *Monthly Notices of the Royal Astronomical Society* **395**:1529–1532.
- A. Reisenegger (2013). ‘Magnetic fields of neutron stars’. In *Magnetic Fields in the Universe IV: From Laboratory and Stars to the Primordial Structures*.
- B. J. Rickett (1977). ‘Interstellar scattering and scintillation of radio waves’. *Annual Review of Astronomy and Astrophysics* **15**:479–504.
- B. J. Rickett (1990). ‘Radio propagation through the turbulent interstellar plasma’. *Annual Review of Astronomy and Astrophysics* **28**:561–605.

- B. J. Rickett, et al. (1984). ‘Slow scintillation in the interstellar medium’. *Astronomy and Astrophysics* **134**:390–395.
- R. T. Ritchings (1976). ‘Pulsar single pulse intensity measurements and pulse nulling’. *Monthly Notices of the Royal Astronomical Society* **176**:249–263.
- R. W. Romani (1987). ‘Model atmospheres for cooling neutron stars’. *The Astrophysical Journal* **313**:718–726.
- R. W. Romani, et al. (1986). ‘Refractive effects in pulsar scintillation’. *Monthly Notices of the Royal Astronomical Society* **220**:19–49.
- A. Rowlinson, et al. (2016). ‘Limits on Fast Radio Bursts and other transient sources at 182 MHz using the Murchison Widefield Array’. *Monthly Notices of the Royal Astronomical Society* **458**:3506–3522.
- J. Roy, et al. (2012). ‘Observations of four glitches in the young pulsar J1833-1034 and study of its glitch activity’. *Monthly Notices of the Royal Astronomical Society* **424**:2213–2221.
- M. A. Ruderman & P. G. Sutherland (1975). ‘Theory of pulsars - Polar caps, sparks, and coherent microwave radiation’. *The Astrophysical Journal* **196**:51–72.
- S. Sallmen, et al. (1999). ‘Simultaneous Dual-Frequency Observations of Giant Pulses from the Crab Pulsar’. *The Astrophysical Journal* **517**:460–471.
- E. E. Salpeter (1969). ‘Pulsar Amplitude Variations’. *Nature* **221**:31–33.
- N. Sartore, et al. (2010). ‘Galactic neutron stars. I. Space and velocity distributions in the disk and in the halo’. *Astronomy and Astrophysics* **510**:A23.
- P. A. G. Scheuer (1968). ‘Amplitude Variations in Pulsed Radio Sources’. *Nature* **218**:920–922.

- P. Scholz, et al. (2016). ‘The Repeating Fast Radio Burst FRB 121102: Multi-wavelength Observations and Additional Bursts’. *The Astrophysical Journal* **833**:177.
- A. D. Seymour & D. R. Lorimer (2013). ‘Evidence for chaotic behaviour in pulsar spin-down rates’. *Monthly Notices of the Royal Astronomical Society* **428**:983–998.
- R. M. Shannon & J. M. Cordes (2010). ‘Assessing the Role of Spin Noise in the Precision Timing of Millisecond Pulsars’. *The Astrophysical Journal* **725**:1607–1619.
- R. M. Shannon & J. M. Cordes (2017). ‘Modelling and mitigating refractive propagation effects in precision pulsar timing observations’. *Monthly Notices of the Royal Astronomical Society* **464**:2075–2089.
- R. M. Shannon, et al. (2018). ‘The dispersion-brightness relation for fast radio bursts from a wide-field survey’. *Nature* **562**(7727):386–390.
- R. M. Shannon, et al. (2014). ‘Limitations in timing precision due to single-pulse shape variability in millisecond pulsars’. *Monthly Notices of the Royal Astronomical Society* **443**(2):1463–1481.
- R. M. Shannon, et al. (2013). ‘Gravitational-wave limits from pulsar timing constrain supermassive black hole evolution.’. *Science* **342**:334–337.
- B. J. Shapiro-Albert, et al. (2018). ‘Radio Properties of Rotating Radio Transients: Single-pulse Spectral and Wait-time Analyses’. *The Astrophysical Journal* **866**:152.
- I. A. Shibanov, et al. (1992). ‘Model atmospheres and radiation of magnetic neutron stars. I - The fully ionized case’. *Astronomy and Astrophysics* **266**:313–320.
- W. Sieber (1973a). ‘Pulsar Spectra’. *Astronomy and Astrophysics* **28**:237.

- W. Sieber (1973b). ‘Pulsar Spectra’. *Astronomy and Astrophysics* **28**:237.
- W. Sieber (1982). ‘Causal relationship between pulsar long-term intensity variations and the interstellar medium’. *Astronomy and Astrophysics* **113**:311–313.
- K. W. Smith & P. W. Terry (2011). ‘Damping of Electron Density Structures and Implications for Interstellar Scintillation’. *The Astrophysical Journal* **730**:133.
- J. M. Smits, et al. (2006). ‘Frequency Dependence of the Drifting Sub-Pulses of PSR B 0031-07’. *Chinese Journal of Astronomy and Astrophysics Supplement* **6**(S2):24–29.
- C. Sobey, et al. (2019). ‘Low-frequency Faraday rotation measures towards pulsars using LOFAR: probing the 3D Galactic halo magnetic field’. *Monthly Notices of the Royal Astronomical Society* **484**:3646–3664.
- C. Sobey, et al. (2015). ‘LOFAR discovery of a quiet emission mode in PSR B0823+26’. *Monthly Notices of the Royal Astronomical Society* **451**:2493–2506.
- V. A. Soglasnov, et al. (2004). ‘Giant Pulses from PSR B1937+21 with Widths  $\leq 15$  Nanoseconds and  $T_b \geq 5 \times 10^{39}$  K, the Highest Brightness Temperature Observed in the Universe’. *The Astrophysical Journal* **616**:439–451.
- M. Sokolowski, et al. (2018). ‘No Low-frequency Emission from Extremely Bright Fast Radio Bursts’. *The Astrophysical Journal Letters* **867**(1):L12.
- M. Sokolowski, et al. (2017). ‘Calibration and Stokes Imaging with Full Embedded Element Primary Beam Model for the Murchison Widefield Array’. *Publications of the Astronomical Society of Australia* **34**:e062.
- M. Sokolowski, et al. (2015). ‘BIGHORNS - Broadband Instrument for Global HydrOgen Reionisation Signal’. *Publications of the Astronomical Society of Australia* **32**:e004.

- C. Sotomayor-Beltran, et al. (2013). ‘Calibrating high-precision Faraday rotation measurements for LOFAR and the next generation of low-frequency radio telescopes’. *Astronomy and Astrophysics* **552**:A58.
- A. Spitkovsky (2006). ‘Time-dependent Force-free Pulsar Magnetospheres: Ax-symmetric and Oblique Rotators’. *The Astrophysical Journal Letters* **648**:L51–L54.
- L. G. Spitler, et al. (2014a). ‘Fast Radio Burst Discovered in the Arecibo Pulsar ALFA Survey’. *The Astrophysical Journal* **790**:101.
- L. G. Spitler, et al. (2014b). ‘Pulse Broadening Measurements from the Galactic Center Pulsar J1745-2900’. *The Astrophysical Journal Letters* **780**:L3.
- L. G. Spitler, et al. (2016). ‘A repeating fast radio burst’. *Nature* **531**:202–205.
- D. H. Staelin & E. C. Reifenstein, III (1968). ‘Pulsating Radio Sources near the Crab Nebula’. *Science* **162**:1481–1483.
- D. H. Staelin & J. M. Sutton (1970a). ‘Observed Shapes of Crab Nebula Radio Pulses’. *Nature* **226**:69–70.
- D. H. Staelin & J. M. Sutton (1970b). ‘Observed Shapes of Crab Nebula Radio Pulses’. *Nature* **226**:69–70.
- B. W. Stappers, et al. (2011). ‘Observing pulsars and fast transients with LOFAR’. *Astronomy and Astrophysics* **530**:A80.
- L. Staveley-Smith, et al. (1996). ‘The Parkes 21 CM multibeam receiver’. *Publications of the Astronomical Society of Australia* **13**:243–248.
- D. R. Stinebring, et al. (2001). ‘Faint Scattering Around Pulsars: Probing the Interstellar Medium on Solar System Size Scales’. *The Astrophysical Journal Letters* **549**:L97–L100.

- D. R. Stinebring, et al. (2019). ‘The Frequency Dependence of Scintillation Arc Thickness in Pulsar B1133+16’. *The Astrophysical Journal* **870**:82.
- G. H. Stokes, et al. (1985a). ‘A survey for short-period pulsars’. *Nature* **317**:787.
- G. H. Stokes, et al. (1985b). ‘A survey for short-period pulsars’. *Nature* **317**:787.
- K. Stovall, et al. (2015). ‘Pulsar Observations Using the First Station of the Long Wavelength Array and the LWA Pulsar Data Archive’. *The Astrophysical Journal* **808**:156.
- A. Sutinjo, et al. (2015). ‘Understanding instrumental Stokes leakage in Murchison Widefield Array polarimetry’. *Radio Science* **50**:52–65.
- G. Swarup (1990). ‘Giant metrewave radio telescope (GMRT) - Scientific objectives and design aspects’. *Indian Journal of Radio and Space Physics* **19**:493–505.
- G. Swarup, et al. (1991). ‘The Giant Metre-Wave Radio Telescope’. *Current Science, Vol. 60, NO.2/JAN25, P. 95, 1991* **60**:95.
- A. Szary, et al. (2015). ‘Two modes of partially screened gap’. *Monthly Notices of the Royal Astronomical Society* **447**:2295–2306.
- T. M. Tauris, et al. (2012). ‘Formation of millisecond pulsars with CO white dwarf companions - II. Accretion, spin-up, true ages and comparison to MSPs with He white dwarf companions’. *Monthly Notices of the Royal Astronomical Society* **425**:1601–1627.
- T. M. Tauris & R. N. Manchester (1998). ‘On the Evolution of Pulsar Beams’. *Monthly Notices of the Royal Astronomical Society* **298**:625–636.
- G. B. Taylor, et al. (2012). ‘First Light for the First Station of the Long Wavelength Array’. *Journal of Astronomical Instrumentation* **1**:50004.

G. B. Taylor, et al. (2016). ‘Observations of Rotating Radio Transients with the First Station of the Long Wavelength Array’. *The Astrophysical Journal* **831**:140.

M. B. Taylor (2006). ‘STILTS - A Package for Command-Line Processing of Tabular Data’. In C. Gabriel, C. Arviset, D. Ponz, & S. Enrique (eds.), *Astronomical Data Analysis Software and Systems XV*, vol. 351 of *Astronomical Society of the Pacific Conference Series*, p. 666.

A. Tchekhovskoy, et al. (2013). ‘Time-dependent 3D magnetohydrodynamic pulsar magnetospheres: oblique rotators’. *Monthly Notices of the Royal Astronomical Society* **435**:L1–L5.

The Astropy Collaboration, et al. (2018). ‘The Astropy Project: Building an Open-science Project and Status of the v2.0 Core Package’. *The Astronomical Journal* **156**:123.

The Astropy Collaboration, et al. (2013). ‘Astropy: A community Python package for astronomy’. *Astronomy and Astrophysics* **558**:A33.

E. Thébault, et al. (2015). ‘International Geomagnetic Reference Field: the 12th generation’. *Earth, Planets, and Space* **67**:79.

D. Thornton, et al. (2013). ‘A Population of Fast Radio Bursts at Cosmological Distances’. *Science* **341**:53–56.

A. N. Timokhin (2010). ‘A model for nulling and mode changing in pulsars’. *Monthly Notices of the Royal Astronomical Society* **408**:L41–L45.

A. N. Timokhin & J. Arons (2013). ‘Current flow and pair creation at low altitude in rotation-powered pulsars’ force-free magnetospheres: space charge limited flow’. *Monthly Notices of the Royal Astronomical Society* **429**:20–54.

- S. J. Tingay, et al. (2013). ‘The Murchison Widefield Array: The Square Kilometre Array Precursor at Low Radio Frequencies’. *Publications of the Astronomical Society of Australia* **30**:e007.
- S. J. Tingay, et al. (2015). ‘A Search for Fast Radio Bursts at Low Frequencies with Murchison Widefield Array High Time Resolution Imaging’. *The Astronomical Journal* **150**:199.
- S. E. Tremblay, et al. (2015). ‘The High Time and Frequency Resolution Capabilities of the Murchison Widefield Array’. *Publications of the Astronomical Society of Australia* **32**:e005.
- C. M. Trott, et al. (2013). ‘Prospects for the Detection of Fast Radio Bursts with the Murchison Widefield Array’. *The Astrophysical Journal Letters* **776**:L16.
- J. Trümper, et al. (1978). ‘Evidence for strong cyclotron line emission in the hard X-ray spectrum of Hercules X-1’. *The Astrophysical Journal Letters* **219**:L105–L110.
- A. J. Turtle, et al. (1987). ‘A prompt radio burst from supernova 1987A in the Large Magellanic Cloud’. *Nature* **327**:38–40.
- V. A. Urpin & D. G. Yakovlev (1980). ‘Thermogalvanomagnetic Effects in White Dwarfs and Neutron Stars’. *Soviet Astronomy* **24**:425.
- S. van der Walt, et al. (2011). ‘The NumPy Array: A Structure for Efficient Numerical Computation’. *Computing in Science & Engineering* **13**(2):22–30.
- M. P. van Haarlem, et al. (2013). ‘LOFAR: The LOw-Frequency ARray’. *Astronomy and Astrophysics* **556**:A2.
- W. van Straten (2004). ‘Radio Astronomical Polarimetry and Point-Source Calibration’. *The Astrophysical Journal Supplement Series* **152**:129–135.
- W. van Straten (2006). ‘Radio Astronomical Polarimetry and High-Precision Pulsar Timing’. *The Astrophysical Journal* **642**:1004–1011.

W. van Straten & M. Bailes (2011). ‘DSPSR: Digital Signal Processing Software for Pulsar Astronomy’. *Publications of the Astronomical Society of Australia* **28**:1–14.

W. van Straten, et al. (2012). ‘Pulsar Data Analysis with PSRCHIVE’. *Astronomical Research and Technology* **9**:237–256.

W. van Straten, et al. (2010). ‘PSRCHIVE and PSRFITS: Definition of the Stokes Parameters and Instrumental Basis Conventions’. *Publications of the Astronomical Society of Australia* **27**:104–119.

M. Vivekanand, et al. (1998). ‘Radio Emission of PSR J0437-4715 at 327 MHz’. *The Astrophysical Journal* **501**:823–829.

M. A. Walker, et al. (2013). ‘Cyclic Spectroscopy of The Millisecond Pulsar, B1937+21’. *The Astrophysical Journal* **779**:99.

N. Wang, et al. (2007). ‘Pulsar nulling and mode changing’. *Monthly Notices of the Royal Astronomical Society* **377**:1383–1392.

R. B. Wayth, et al. (2018). ‘The Phase II Murchison Widefield Array: Design overview’. *Publications of the Astronomical Society of Australia* **35**:33.

J. C. Weatherall (1997). ‘Modulational Instability, Mode Conversion, and Radio Emission in the Magnetized Pair Plasma of Pulsars’. *The Astrophysical Journal* **483**:402–413.

J. C. Weatherall (1998). ‘Pulsar Radio Emission by Conversion of Plasma Wave Turbulence: Nanosecond Time Structure’. *The Astrophysical Journal* **506**:341–346.

J. M. Weisberg, et al. (1999). ‘Arecibo 1418 MHZ Polarimetry of 98 Pulsars: Full Stokes Profiles and Morphological Classifications’. *The Astrophysical Journal Supplement Series* **121**:171–217.

- P. Weltevrede & S. Johnston (2008). ‘Profile and polarization characteristics of energetic pulsars’. *Monthly Notices of the Royal Astronomical Society* **391**:1210–1226.
- P. Weltevrede, et al. (2011). ‘The glitch-induced identity changes of PSR J1119-6127’. *Monthly Notices of the Royal Astronomical Society* **411**:1917–1934.
- P. Weltevrede, et al. (2006a). ‘Is Pulsar B0656+14 a Very Nearby Rotating Radio Transient?’. *The Astrophysical Journal Letters* **645**:L149–L152.
- P. Weltevrede, et al. (2006b). ‘The bright spiky emission of pulsar B0656+14’. *Astronomy and Astrophysics* **458**(1):269–283.
- W. A. Wheaton, et al. (1979). ‘An absorption feature in the spectrum of the pulsed hard X-ray flux from 4U0115 + 63’. *Nature* **282**:240–243.
- M. H. Wieringa (1992). ‘An investigation of the telescope based calibration methods ‘redundancy’ and ‘self-cal’’. *Experimental Astronomy* **2**:203–225.
- I. P. Williamson (1972). ‘Pulse broadening due to multiple scattering in the interstellar medium - I’. *Monthly Notices of the Royal Astronomical Society* **157**:55.
- I. P. Williamson (1973). ‘Pulse broadening due to multiple scattering in the interstellar medium - II’. *Monthly Notices of the Royal Astronomical Society* **163**:345.
- I. P. Williamson (1974). ‘Pulse broadening due to multiple scattering in the interstellar medium - III’. *Monthly Notices of the Royal Astronomical Society* **166**:499–512.
- M. Xue, et al. (2017). ‘A Census of Southern Pulsars at 185 MHz’. *Publications of the Astronomical Society of Australia* **34**:e070.

- M. Xue, et al. (2019). ‘MWA Tied-Array Processing II: Polarimetric Verification and Analysis of two Bright Southern Pulsars’. *arXiv e-prints* p. arXiv:1905.00598.
- J. M. Yao, et al. (2017). ‘A New Electron-density Model for Estimation of Pulsar and FRB Distances’. *The Astrophysical Journal* **835**:29.
- M. D. T. Young, et al. (2010). ‘Pulsar magnetic alignment and the pulsedwidth-age relation’. *Monthly Notices of the Royal Astronomical Society* **402**:1317–1329.
- N. J. Young, et al. (2013). ‘Long-term radio observations of the intermittent pulsar B1931+24’. *Monthly Notices of the Royal Astronomical Society* **429**:2569–2580.
- N. J. Young, et al. (2012). ‘On the pulse intensity modulation of PSR B0823+26’. *Monthly Notices of the Royal Astronomical Society* **427**:114–126.
- N. J. Young, et al. (2014). ‘On the apparent nulls and extreme variability of PSR J1107-5907’. *Monthly Notices of the Royal Astronomical Society* **442**:2519–2533.
- V. E. Zavlin (2009). ‘Thermal emission from isolated neutron stars: theoretical and observational aspects’. In W. Becker (ed.), *Neutron Stars and Pulsars*, vol. 357 of *Astrophysics and Space Science Library*, pp. 181–209. Springer-Verlag Berlin Heidelberg, 1 edn.
- H. Zheng, et al. (2017). ‘An improved model of diffuse galactic radio emission from 10 MHz to 5 THz’. *Monthly Notices of the Royal Astronomical Society* **464**:3486–3497.

Every reasonable effort has been made to acknowledge the owners of copyright material. I would be pleased to hear from any copyright owner who has been omitted or incorrectly acknowledged.